
**Functional mapping of the entorhinal cortex
reveals a hub for synaptic excitability in the young
3xTg mouse model for Alzheimer's disease**

A THESIS SUBMITTED TO THE UNIVERSITY OF MANCHESTER FOR THE
DEGREE OF DOCTOR OF PHILOSOPHY
IN THE FACULTY OF BIOLOGY, MEDICINE AND HEALTH

2019

Francesca Mandino

SCHOOL OF BIOLOGICAL SCIENCES

Neuroscience & Experimental Psychology

Table of Contents

List of Figures.....	5
List of Tables	7
Alternative Format Structure	8
Abstract.....	10
Declaration.....	11
Copyright statement.....	11
Acknowledgements.....	12
List of main abbreviations.....	13
~Chapter 1 ~	15
General Introduction	15
1.1 Alzheimer's disease: a general overview	15
1.1.1 Classification.....	16
1.2 Anatomy of the medial temporal lobe	18
1.2.1 Entorhinal Cortex: function and relevance in AD	20
1.2.2 Lateral entorhinal cortex: cytoarchitecture and projections	21
1.3 Alzheimer's disease	23
1.3.1 Types of AD: Early- and Late-Onset.....	23
1.3.2 Genetic risk factors	24
1.3.3 Molecular hallmarks	25
1.3.4 Unclear aetiology of AD	27
1.4 Animal models in preclinical research	29
1.4.1 Limitations of animal models	31
1.4.2 3xTgAD mouse model	33
1.5 Structure of the present work	35
1.6 Neuroimaging	35
1.6.1 Positron Emission Tomography.....	36
1.6.2 Structural Magnetic Resonance Imaging.....	37
1.6.3 Functional magnetic resonance imaging	38
1.7 Functional Connectivity in Alzheimer's disease.....	40
1.7.1 Evidence from human fMRI	40
1.7.2 Evidence from rodent fMRI	42
1.8 Optogenetics.....	43
1.8.1 Optogenetics in AD	46
1.9 Electrophysiology	47

1.9.1 Fundamentals of electrophysiology	47
1.9.2 Memory formation	49
1.9.3 Neuronal Changes in AD Models.....	50
1.10 Anaesthesia	53
1.11 The present work.....	55
~ Chapter 2 ~	57
General Methods	57
2.1 Animals	57
2.2 fMRI	58
2.2.1 fMRI signal	59
2.2.2 BOLD signal-to-noise.....	59
2.2.3 Animal preparation for imaging.....	60
2.2.4 RsfMRI and ofMRI: data acquisition	61
2.2.5 RsfMRI and ofMRI: data pre-processing.....	62
2.2.6 RsfMRI: data analysis	63
2.2.7 OfMRI: optogenetic surgery	66
2.2.8 OfMRI: stimulation protocols.....	67
2.2.9 OfMRI: data analysis.....	69
2.2.10 Statistics and data availability	69
2.2.11 <i>Ex vivo</i> processing	70
2.3 <i>In vivo</i> electrophysiology.....	74
2.3.1 Anaesthesia and surgery.....	75
2.3.2 Electrode placement.....	76
2.3.3 Stimulation protocols	79
2.3.4 Data analysis	80
2.3.5 Perfusion	83
2.3.6 Histology.....	83
~ Chapter 3 ~	84
Paper 1	84
Rationale behind Paper 1	84
3.1 Abstract.....	86
3.2 Introduction	87
3.3 Method	89
3.3.1 Animals.....	89
3.3.2 Optogenetic surgery	89

3.3.3 Animal preparation for imaging	90
3.3.4 Data acquisition and stimulation protocols	91
3.3.5 fMRI analysis.....	92
3.3.6 <i>Ex vivo</i> processing	93
3.3.7 Statistics and data availability	97
3.4 Results	98
3.4.1 Immunohistochemical validation and ELISA	98
3.4.2 Resting-state fMRI reveals regional homogeneity deficit in 3xTgAD	98
3.4.3 Local FC deficits translates into whole-brain network alterations.....	100
3.4.4 Functional connectome of the ENTl revealed by optogenetics.....	102
3.4.5 Potentiated haemodynamic response and neuronal activity	104
3.5 Discussion.....	107
3.6 Supplementary material	111
~ Chapter 4 ~	123
Paper 2	123
Rationale behind Paper 2	123
4.1 Abstract.....	125
4.2 Introduction.....	126
4.3 Methods.....	129
4.3.1 Animals.....	129
4.3.2 Anaesthesia and surgery.....	129
4.3.3 Surgery	129
4.3.4 Data acquisition.....	131
4.3.5 Stimulation protocols	132
4.3.6 Data analysis	132
4.3.7 Perfusion and histology.....	135
4.4 Results	136
4.4.1 Synaptic strength: current-response input/output.....	136
4.4.2 Paired-pulse stimulation shows hyper-excitability in 3xTgAD	138
4.5 Discussion.....	142
~ Chapter 5 ~	148
General Discussion	148
5.1 Overview	148
5.2 Highlights of the results	150
5.3 The relevance of this study within AD aetiology	157

5.3.1 Beta-amyloid cascade.....	157
5.3.2 Cerebral-amyloid angiopathy	159
5.3.3 Dopaminergic hypothesis.....	160
5.3.4 Axonal degeneration, tauopathy and synaptic deficiency	161
5.4 Limitations and considerations of this study	162
~ Conclusion ~	166
~ References ~	167
~ Appendix 1 ~	199
~ Appendix 2 ~	210
Curriculum Vitae ~	260

Final word count: 41,085

List of Figures

Figure 1.1: Diagram illustrating the characteristic diagnostic features of AD.....	16
Figure 1.2: Diagram showing the main connections across the hippocampal formation and telencephalic regions.....	22
Figure 1.3: Diagram showing the beta-amyloid pathway leading to the accumulation of A β plaques.....	26
Figure 1.4: Formation of neurofibrillary tangles (NFTs).....	27
Figure 1.5: Simplified representation of the balloon model of BOLD signal composition.....	39
Figure 1.6: Illustration of opsin expression through AAV injection.....	46
Figure 1.7: fEPSP responses in DG and BLA following stimulation of the subiculum.....	51
Figure 2.1: Example of ICA components to train a classifier for FIX.....	63
Figure 2.2: Schematics of the principle of optogenetics and combination with fMRI.....	68
Figure 2.3: schematic for electrodes positioning in BLA, ENTl and DG.....	77
Figure 2.4: Histology for the location of the electrodes.....	78
Figure 2.5: An example of the measurement of paired-pulse and I/O slopes in BLA.....	82
Figure 3.1: Resting-state fMRI shows regional homogeneity decrease in 3xTgAD.....	99
Figure 3.2: Optogenetic modulation of the ENTl.....	103
Figure 3.3: Two-sample t-test results, 3 months time-point.....	105
Figure S1: Immunohistochemistry for 3xTgAD characterisation with AT8.....	113
Figure S2: ReHo values extracted in selected ROIs show FC changes in 3xTgAD.....	114
Figure S3: Pair-wise ROI interactions relative to the left-hemisphere ENTl.....	115
Figure S4: Restricted pair-wise ENTl at 3 months of age and 6 months of age overlapped with ReHo.....	116
Figure S5: Whole brain NA at 3 months of age and 6 months of age and overlap with ReHo analysis.....	117
Figure S6: Experimental design for optogenetic stimulation and control validation.....	118
Figure S7: Optogenetic validation of pyramidal neurons in ENTl.....	119
Figure S8: Optogenetically-locked BOLD response in 3xTgAD and overlap with resting-state FC.....	120

Figure S9: Resting-state fMRI with single-loop coil reveals similar patterns of FC deficits in 3xTgAD.....	121
Figure S10: Intrinsic neuronal properties between controls and 3xTgAD.....	122
Figure 4.1: Neuronal circuitry in the medial temporal lobe, electrodes location and CSD.....	134
Figure 4.2: Input/Output curves for BLA and DG response to ENTl stimulation at 3- and 6-months of age show strengthening of synaptic connectivity in 3xTgAD.....	139
Figure 4.3: Paired-pulse stimulation in BLA and DG at 3 and 6 months of age shows increased facilitation in 3xTgAD.....	141
Figure 5.1: Diagram summarising the findings within this work.....	152

List of Tables

Table 2.1: Coordinates for electrodes positioning according to Paxinos atlas.....	76
Table S1: Intrinsic properties of granule cells in dentate gyrus and pyramidal cells in infralimbic cortex.....	111
Table S2: Number of action potential evoked by various current injections.....	112

Alternative Format Structure

This thesis is written in the alternative format structure, to allow for the timely dissemination of my work through publication. Each result chapter is written as a stand-alone research paper. It is my intention, upon completion of my PhD, to submit Paper 1 to *Nature Neuroscience* and Paper 2 to *Hippocampus*. Below, a brief description of the work contained within each chapter and a declaration of the contribution of the authors.

Paper 1

Title: Brain-wide functional mapping of the entorhinal cortex in young 3xTg mouse model for Alzheimer's disease

Authors: Francesca Mandino, Ling Yun Yeow, Chai Lean Teoh, Chun-Yao Lee, Renzhe Bi, Hasan Mohammad, Han Gyu Bae, Seung Hyun Baek, Lee Sejin, Lee Hanqing Jasinda, Mitchell Kim Peng Lai, Sangjong Yung, Yu Fu, John Gigg, Malini Olivo, Joanes Grandjean

Declaration of author contribution: The majority of work and data collection was conducted by Francesca Mandino, with the technical assistance of Ling Yun Yeow and Chai Lean Teoh and Renzhe Bi. The analysis was undertaken by Francesca Mandino and Joanes Grandjean using programs written by Joanes Grandjean. Ex vivo processing of the samples was carried out by internal collaborators in Fu Yu's lab, Chun-Yao Lee, Hasan Mohammad, and in Sangjong Yung's lab, Han Gyu Bae, Seung Hyun Baek, Lee Sejin within SBIC. Additional ex vivo analysis was performed by Lee Hanqing Jasinda and Mitchell Kim Peng Lai, external collaborators at the National University of Singapore. The manuscript composition was done by Francesca Mandino and Joanes Grandjean; critical reading of the manuscript was done by Joanes Grandjean, John Gigg and Malini Olivo.

Paper Overview: Through the implementation of longitudinal rsfMRI and ofMRI I determined how functional changes within the ENTl affect its downstream targets and the rest of the brain in the 3xTg mouse model for AD at 3 and 6 months of age.

Paper 2

Title: 3xTgAD mice express early synaptic hyperexcitability in the amygdala and dentate gyrus following activation of the lateral entorhinal cortex *in vivo*

Authors: Francesca Mandino, Bin Zhu, Marcelo Montemurro, Joanes Grandjean, John Gigg

Declaration of author contribution: The body of work and analyses were conducted by Francesca Mandino under the supervision of John Gigg and Marcelo Montemurro and with the guidance of Bin Zhu. Analyses were undertaken by Francesca Mandino using programs written and developed by Joanes Grandjean.

Paper overview: In light of the results from Paper #1 I performed electrophysiological recordings *in vivo* to investigate changes in synaptic connectivity between ENTl and DG and ENTl and BLA in the 3xTgAD mouse model at 3 and 6 months of age.

Additional work published during the PhD, but that falls outside the scope of this thesis

Besides the work described in this Thesis, additional material acquired during the PhD is collected in the Appendix section. Specifically, during the acquisition of rsfMRI data reported in Chapter 4, one 3xTgAD mouse developed hydrocephalus. Comparative analysis between this hydrocephalic mouse and littermate 3xTgAD controls was carried out highlighting remarkable preservation of FC. The published manuscript is presented in Appendix 1: Mandino, F., Yeow, L.Y., Gigg, J., Olivo, M. and Grandjean, J., 2019. Preserved functional networks in a hydrocephalic mouse. *Matters*, 5(6), p.e201905000001.

Furthermore, a review regarding trends in study design, data acquisition and processing within the animal fMRI community, can be found in Appendix 2 and has been published in *Frontiers in Neuroinformatics*: Mandino, F., Cerri, D.H., Garin, C.M., Straathof, M., van Tilborg, G.A., Chakravarty, M.M., Dhenain, M., Dijkhuizen, R.M., Gozzi, A., Hess, A. and Keilholz, S.D., 2020. Animal Functional Magnetic Resonance Imaging: Trends and Path Toward Standardization. *Frontiers in Neuroinformatics*, 13, p.78.

Doctor of Philosophy, The University of Manchester
Francesca Mandino

Functional mapping of the entorhinal cortex reveals a hub for synaptic excitability in the young 3xTg mouse model for Alzheimer's disease

Abstract

Alzheimer's disease (AD) is the most common form of dementia, resulting in marked neurodegeneration, cognitive decline, memory loss, emotional and behavioural changes. The traditional pathological hallmarks of AD are insoluble beta-amyloid plaques and hyperphosphorylated protein tau tangles. This results in neurodegeneration and brain atrophy, with early damage in major hubs for cognitive function within the medial temporal lobe, particularly the lateral entorhinal cortex, hippocampal formation and basolateral amygdala. Recently, the focus in AD research has shifted attention from end-stage of the disease to the early asymptomatic (prodromal) stages, where an intricate inter-dependency between the timing of plaque and tangle appearance, together with neuronal plasticity changes, might be the initiating events in AD degeneration. Animal models recapitulate partial aspects of the AD *continuum* and may help to understand the underlying mechanisms of AD pathogenesis. The 3xTgAD mouse model is an ideal candidate model to investigate early brain changes at the onset of AD-like pathology, in that it is unique in developing both tangles and plaques late in life yet providing an extended time window with only precursor forms of plaques and tangles. Here, early alterations in the synaptic connectivity among key brain regions for AD progression were assessed through electrophysiological recordings in the amygdala and dentate gyrus of male 3xTgAD mice in response to lateral entorhinal cortex stimulation *in vivo*. We next used longitudinal, whole-brain fMRI to investigate brain-wide functional changes in the 3xTgAD resting-state network. Finally, we used functional mapping of the brain-wide impact of activating entorhinal cortex output by optogenetically exciting entorhinal cortex during simultaneous fMRI recording in 3xTgAD mice.

Electrical stimulation of the lateral entorhinal cortex revealed increased fEPSP responses and short-term synaptic plasticity changes in the basolateral amygdala and dentate gyrus in 3-month old male 3xTgAD mice compared to matched controls. These results demonstrate, for the first time, augmented synaptic excitability in the amygdala and ventral dentate gyrus, which is also affected by pathology progression in older mice. Brain-wide assessment of functional connectivity changes revealed network and localised loss in functional connectivity in regions highly involved in episodic memory, emotional processing and reward. The targeting of specific neuronal populations within the entorhinal cortex by means of optogenetic excitation resulted in a potentiated response in 3xTgAD prefrontal and striatal regions compared to age-matched controls at 3 months of age. This work highlights early alterations in synaptic function within and between disease-relevant brain regions in the 3xTgAD mouse by 3 months of age. Clearly decreased functional coupling during resting-state in 3xTgAD, particularly in the entorhinal cortex, was associated in mice of the same age with increased activity in AD-vulnerable brain regions to direct optogenetic activation of the entorhinal cortex. At first sight these results appear to be in contradiction; however, both effects have been reported in AD patients.

Here, we propose that they can be resolved by considering a state where there is an overall *decrease* in inter-regional axonal connectivity that occurs alongside an *increase* in synaptic strength for the remaining connections in the 3xTgAD model. During endogenous activity, deficits in connectivity could explain the decreased resting-state activity whilst the increased synaptic activity and short-term plasticity produced by exogenous, synchronous activation could potentially explain the apparently incongruous hyperexcitability seen during electrical and optogenetic activation of the entorhinal cortex. Thus, here we demonstrate a brain-wide reorganisation in young 3xTgAD mice, prior to plaques and tangle deposition, in line with clinical evidence and in further support of the 3xTgAD mouse as a valid model for AD.

Declaration

No portion of the work referred to in the thesis has been submitted in support of an application for another degree or qualification of this or any other university or other institute of learning.

Copyright statement

The author of this thesis (including any appendices and/or schedules to this thesis) owns certain copyright or related rights in it (the “Copyright”) and s/he has given The University of Manchester certain rights to use such Copyright, including for administrative purposes.

Copies of this thesis, either in full or in extracts and whether in hard or electronic copy, may be made only in accordance with the Copyright, Designs and Patents Act 1988 (as amended) and regulations issued under it or, where appropriate, in accordance with licensing agreements which the University has from time to time. This page must form part of any such copies made.

The ownership of certain Copyright, patents, designs, trademarks and other intellectual property (the “Intellectual Property”) and any reproductions of copyright works in the thesis, for example graphs and tables (“Reproductions”), which may be described in this thesis, may not be owned by the author and may be owned by third parties. Such Intellectual Property and Reproductions cannot and must not be made available for use without the prior written permission of the owner (s) of the relevant Intellectual Property and/or Reproductions.

Further information on the conditions under which disclosure, publication and commercialisation of this thesis, the Copyright and any Intellectual Property and/or Reproductions described in it may take place is available in the University IP Policy (see <http://documents.manchester.ac.uk/DocuInfo.aspx?DocID=24420>), in any relevant thesis restriction declarations deposited in the University Library, The University Library’s regulations, (see <http://www.library.manchester.ac.uk/about/regulations/>) and in The University’s policy on Presentation of Theses

Acknowledgements

With this PhD coming to an end, there are many people that I would like to thank for their continuous support throughout these four years, across many different countries.

Firstly, I would like to express my deep gratitude to my supervisor Dr John Gigg for the incredible support during my time at The University of Manchester and while overseas. Thank you for your help and guidance throughout this project, the late-night revisions, for visiting me across the globe, and for your continuous encouragement, motivation and meetings/chats in these years and of course for the unlimited coffee supply.

Within the University of Manchester, I would like to thank my second supervisor Dr Marcelo Montemurro, advisor Dr Ingo Schiessl and Dr Jon Turner for their insightful comments and advice. Thank you also to Dr Bin Zhu for his assistance and guidance during my first year, for his help to start my PhD work.

A special thank you to Dr Joanes Grandjean, for your incredible support, patience and for fueling my passion for what we do. I am extremely grateful for having had the opportunity to learn from you. You have helped me shape my scientific mind, 'from simple...to complicated'. Your continuous availability, motivation, incredible music taste and friendship have helped me achieve goals I would not have imagined before joining SBIC.

Thank you to the rest of the neuroimaging group, Ling Yun Yeow for the endless hours doing experiments in the lab, Dr Chai Lean Teoh, Vae Zhang Jiayi, Heidi Foo Jing Ling, Tricia Lim and Nathaniel Low for making such a nice team and for the good memories.

My sincere thanks also go to Prof. Malini Olivo, who provided me with an amazing opportunity to be part of the great LBOI team at Singapore Bioimaging Consortium. Thank you for warmly welcoming me in your lab, for your constant support and for believing in my work and skills. Thank you to Dr Bi Renzhe for your help and expertise during my experiments, to Douglas Goh Wenda, Melvin Wong and Stephanie Lim Hann Qian for your help with admin work.

Thanks to ED Prof Patrick Cozzone for your insightful comments and hard questions. Thanks for your incredible support throughout my PhD and my overseas experiences. Thank you to Cher Meng Chu, Kan Mun Yee Elizabeth Wendy and Jenny See, for your help with bureaucracy and admin paperwork. Thanks to the teams in SBIC and NUS that helped me in my ex vivo data collection. In particular, Dr Fu Yu and his team, especially Dr Chun-Yao Lee and Dr Hasan Mohammad. Dr Jung Sangyong and his team Dr Lee Sejin, Seung Hyun Baek and HanGyu Bae for helping me in my ex vivo data acquisition. Thanks to Dr Mitchell Kim Peng Lai and Dr Lee Hanqing Jasinda at NUS School of Medicine for their collaboration in this project. Thank you also to Dr Beomsue Kim and Dr PARK Sung Jin for helping me getting started with my experimental work.

A big fat thank you goes to the wonderful group of friends that I have had the luck to meet, during my PhD journey. If you are here you know how valuable you are to me (and how little time I have to write this). Thank you to Dr Eleftherios Statharas, Sophie Botsi, Giannis Katsivalis, William Ambler, Elodie Hecq, Joel Antunes, Joseph Wallace, Andrea Vestri, Dr Tatjana Zimasa and Hesham Senih. Thank you for being there when I needed, for listening to my infinite 'mamma mia', for entertaining my late nights at work with your audio files and each of you for your different personalities that made my life outside of work incredible.

Grazie di cuore to Dr Elena Valdambrini, for her true and continuous friendship and constant support during these years. Thank you for taking care of me with your amazing Rescue Kit, for coming all the way to Singapore to visit me and for always being there for me in all sorts of conditions.

A big thank you goes to Richard Clayton for being the constant of this PhD, from the very first day until the last (minute). Thank you for listening to my endless talking, for our food adventures, Kelantan road and Carcassonne, our weird conversations and for your true support in these 4 years of rollercoaster across continents.

Grazie alla mia meravigliosa famiglia, babbo mamma e Aui. Grazie per avermi supportato in questi quattro anni, per aver sopportato la lontananza e per esservi avventurati con me dall'altra parte del mondo. Il vostro sostegno è stato fondamentale e la vostra incredibile forza e determinazione sono fonte di ispirazione ogni giorno.

Thanks to the incredible open-source software and platforms Inkscape Project, R - The R Project for Statistical Computing and OpenNEURO. And finally, thanks to Harry Potter and Jurassic Park film series, for keeping my mind sane when most needed.

List of main abbreviations

3xTgAD	triple transgenic Alzheimer's disease mouse with APPSWE, PS1M146V and TauP130L mutations
129sv/c57bl6	Control mice
AAV	Adeno-associated virus
ACB	Nucleus accumbens
AD	Alzheimer's disease
APP	Amyloid precursor protein
A β	Beta-amyloid
BLA	Basolateral amygdala
BOLD	Blood oxygenation-level dependent
CA1-4	Cornu ammonis fields 1-4
CAA	Cerebral amyloid angiopathy
CaMKII α	Calmodulin-dependent protein kinase II
CBF/V	Cerebral Blood Flow/Volume
ChR2	Channelrhodopsin-2
CSD	Current source density
DA	Dopaminergic
DG	Dentate gyrus
ENTl/m	Entorhinal cortex, lateral/medial
EOAD	Early-onset AD
FC	Functional connectivity
fEPSP	Field excitatory post-synaptic potential
fMRI	Functional Magnetic Resonance Imaging
FTD	Frontotemporal dementia
GABA	Gamma-aminobutyric-acid
HR	Haemodynamic response
I/O	Input/output
ICA	Independent component analysis

ILA	Infralimbic cortex
IOC	Input/output curve
LFP	Local field potential
LOAD	Late-onset AD
LTP	Long-term potentiation
MCI	Mild cognitive impairment
(m)PFC	(medial) prefrontal cortex
MTL	Medial temporal lobe
MUA	Multi-unit array
NA	Network analysis
NFTs	Neurofibrillary tangles
ofMRI	Optogenetics fMRI
P1/P1	Pulse 1/2
PL	Prelimbic cortex
PPF	Paired-pulse facilitation
PPI	Paired-pulse index
PPS	Paired-pulse stimulation
PS1/PS2	Presenilin 1/2
ReHo	Regional homogeneity
ROI	Region of interest
rsfMRI	Resting-state fMRI
RSN	Resting-state network
SSp-bfd	Somatosensory, barrel field cortex
SSp-II	Somatosensory, lower limb
STP	Short-term plasticity
SUA	Single-unit array

~Chapter 1 ~

General Introduction

1.1 Alzheimer's disease: a general overview

Alzheimer's disease (AD) is a neurodegenerative disease, representing the most common type of dementia. AD pathology is characterized by a progressive deterioration of specific regions in the medial temporal lobe (MTL), leading to characteristic deficits in cognitive domains, especially memory and emotion. In 2017, an estimate of 50 million people affected by dementia was released by the Alzheimer's Disease International, with a prediction of an increase of threefold by 2050 (Livingston et al., 2017).

The first attempt to define the cognitive and pathological aspects of the disease was proposed at the beginning of the 20th century by Alois Alzheimer, visiting the now-famous patient Auguste D., who presented diverse symptoms, including progressive impaired memory, paranoia and erratic behaviour (Stelzmann et al., 1995; original article from Alois Alzheimer (Alzheimer, 1907)). In addition, Alzheimer observed the features that traditionally represent the major hallmarks of AD pathology: extracellular deposits, now referred to as plaques of beta-amyloid ($A\beta$; Masters et al., 1985) and neurofibrillary tangles (NFTs), formed by aggregates of hyperphosphorylated tau protein (Braak and Braak, 1991; Goedert et al., 1988; Selkoe, 2011).

It is well accepted that both $A\beta$ plaques and NFTs contribute to progressive synaptic loss, neuronal cell death with microglial activation, inflammation and eventual loss of connectivity across brain regions, particularly in the MTL (Gour et al., 2014; Jack et al., 2010; Scheltens et al., 2016; **Figure 1.1**). This results in general brain atrophy, ventricular enlargement and cortical thinning (Nestor et al., 2008; Singh et al., 2006).

Increasing evidence is also arising for associated vascular changes due to these neurodegenerative processes (Iadecola, 2017; Kisler et al., 2017). The multitude of manifestations characterising AD results in a broad spectrum of changes, ranging from the neuronal level to the whole brain haemodynamic response (HR). As such, the reciprocal interaction between micro- and meso-scale events with brain-wide networks, macro-scale, has kept the mechanisms of AD aetiology out of reach. Cognitive deficits are reported in patients before the accumulation of A β plaques and NFTs, i.e. prodromal stage, thus highlighting the importance of early biomarkers identification (Amieva et al., 2008).

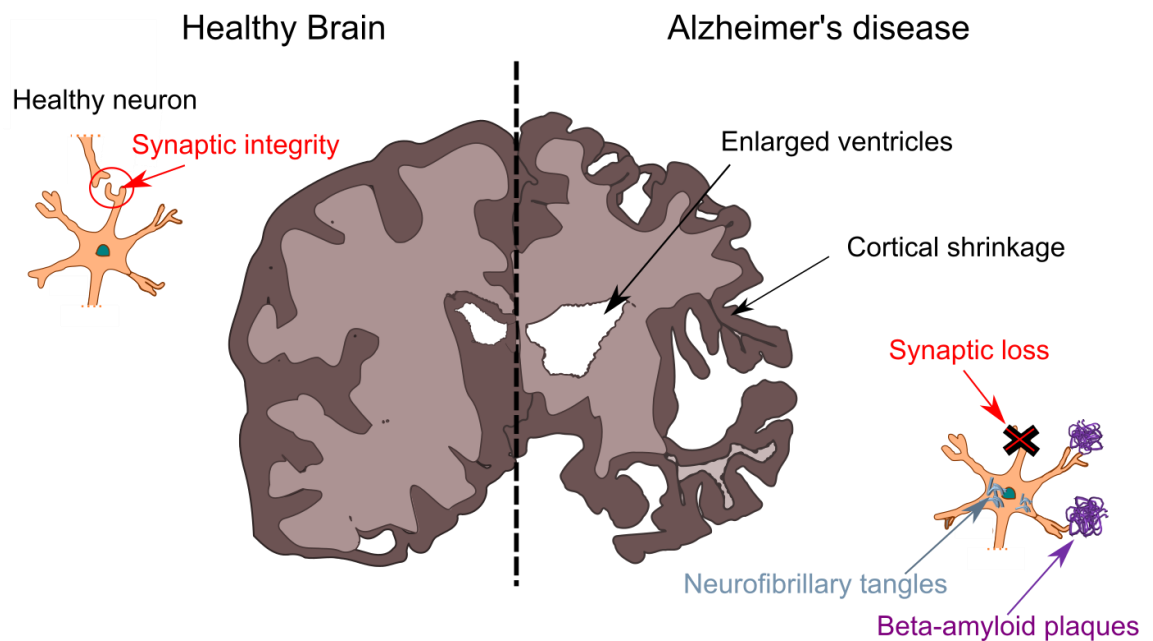


Figure 1.1: Diagram illustrating the characteristic diagnostic features of AD

Left: Representation of a healthy brain and neuron. **Right:** Alzheimer's brain shows advanced brain atrophy with ventricular enlargement and reduction in cortical thickness; moreover, neurons in AD are affected by A β plaques, NFTs and synaptic loss. A β : beta-amyloid; NFTs: neurofibrillary tangles; AD: Alzheimer's disease.

1.1.1 Classification

The classification of AD stages is mostly based on the severity of cognitive decline (Jack et al., 2018) and NFT burden (Braak and Braak, 1995). Preclinical AD is

characterised by no cognitive impairment, whereas clinical AD can be distinguished into prodromal (early stages, no A β plaques or NFTs present) and dementia (advanced AD). With progression of the disease, there is an initial mild cognitive memory impairment (MCI), where the first cognitive function affected is the episodic component of declarative memory, related to the acquisition and recollection of past autobiographical events (place, time, emotions) that occurred in a defined time and place (Bäckman et al., 2001; Greicius et al., 2004; Hodges, 1998). As such, episodic memory deficits represent a defining early cognitive manifestation for AD. Then, in patients that convert from MCI to AD, pathology progression results in increased memory loss, especially emotional memory processes, which can lead to behavioural alterations, such as anxiety, fear and psychosis (advanced AD; Albert et al., 2013; Cohen and Paz, 2015; Dubois et al., 2016; Vermunt et al., 2019a). In a progressed stage of AD, together with the generalised cortical atrophy observed, cholinergic innervation loss and Lewy body manifestation occur (Mesulam, 2004).

There is still no definitive test for AD: patients are diagnosed only upon the clear manifestation of the cognitive symptoms and confirmed only through *post mortem* visualisation of A β plaques and NFTs (Harrison, 2013; Sperling et al., 2011). However, it is now widely accepted that cognitive deficits appear well before the formation of extensive A β plaques and NFTs: MCI patients and cognitively normal subjects have been reported to first present intracellular forms of soluble A β (oligomers representing precursor stages of plaque formation, described in a later section) prior to the manifestation of any cognitive symptoms (Blennow et al., 2015; Jack, 2012; Musiek and Holtzman, 2012). Therefore, a shift of focus, towards the early stages of the disease and the related regions involved, is fundamental in order to identify reliable biomarkers for AD diagnosis.

1.2 Anatomy of the medial temporal lobe

The first region highly affected by AD pathology is the MTL, where the first signs of atrophy occur, due to the progressive nature of neuronal degradation (Scheltens et al., 2016). The MTL comprises a complex ensemble of structures and its boundaries are defined by cortical landmarks: in primates, it presents as foldings and ridges (sulci and gyri) that delimit anatomically and functionally distinct brain regions (Van Hoesen, 1991). Dorsally, the Sylvian fissure separates the MTL from the frontal and parietal lobes. Among its multiple functions, the MTL plays a key role in the representation and integration of sensory inputs, e.g. auditory stimuli are processed in the primary auditory cortex, whereas complex visual cues (e.g., coding of faces) involves the fusiform gyrus. The transverse temporal gyri include the primary auditory cortex, whereas the circular sulcus delimits, anteriorly, the insular cortex – involved in higher sensory processes, emotions, empathy, salience (Gu et al., 2013) – and the amygdala - highly related to fear and emotional processes and described in later sections.

A crucial structure for the functionality of the healthy MTL is the parahippocampal gyrus. This region is highly vulnerable to AD pathology deposition; in particular, the entorhinal and perirhinal subdivisions of the parahippocampal gyrus are thought to be the first targets of the pathological spread (Paola et al., 2007; Khan et al., 2014). The entorhinal cortex represents a specific focus of the current work, therefore, it will be described more in depth, in later sections. The perirhinal cortex is a key region involved in the familiarity aspect of memory formation, for example, perirhinal responses to a particular stimulus often decrease upon repeated presentation of that stimulus (Diana et al., 2007).

One of the most important functions of the MTL is related to the formation of declarative memory, first suggested by the study of the now-famous patient H.M. As a treatment for epilepsy, H.M. was subject to the partial bilateral removal of the amygdala, hippocampus and parahippocampal gyri. This resulted in complete anterograde and partial retrograde declarative amnesia, while the remainder of his behavioural, memory (e.g., procedural memory) and personality aspects were left unchanged (Scoville and Milner, 2000; Penfield and Milner, 1958; Zola-Morgan et al., 1986). Although the anatomy of the MTL was not entirely defined at the time, it was clear that this region was highly relevant for memory processes. More precisely, within the MTL, the main structure related to memory, in addition to the perirhinal and parahippocampal cortices, is the hippocampal formation (Squire and Zola-Morgan, 1991; Tulving and Markowitsch, 1998; Zola-Morgan et al., 1986). In the literature, there is a lack of *consensus* on the exact anatomical composition of the hippocampal formation.

Here, it will be described, and adopted throughout the thesis, as follows. The hippocampal formation includes the entorhinal cortex, which lies at the interface between the dentate gyrus (DG), the neocortex, the subiculum and the hippocampus proper, which is formed by the Cornu Ammonis 1-4 (CA₁₋₄) (Fig. 1.2). The entorhinal cortex, subdivided anatomically into medial (ENT_m) and lateral (ENT_l) aspects, transmits and receives information to and from the hippocampus proper through the DG, creating the canonical, linear trisynaptic circuit EC→DG→CA₃→CA₁ (Andersen et al., 1971). Whilst hippocampal formation connectivity is now known to be much more parallel than this, the term ‘trisynaptic circuit’ still represents a useful approach to understanding hippocampal function. These connectivity pathways within the hippocampal formation will be described further below.

1.2.1 Entorhinal Cortex: function and relevance in AD

The ENT plays a key role in memory and navigation (Fyhn et al., 2004; Hafting et al., 2005). ENTl and ENTm are thought to be functionally different: the former more involved during learning, attention and, particularly, object-in-place recognition tasks, the latter more related to spatial navigation by path integration (Schmidt-Hieber and Häusser, 2013; Tsao et al., 2013). This functional difference is thought to be related to their different connectivity patterns within the brain. The ENTl is the central hub of connection between hippocampal regions, prefrontal regions (mPFC), amygdala (especially the basolateral nucleus, BLA) and the DG. Indeed, anterograde tracers injected in regions highly related to attention, reward, fear and emotional learning processes, such as the BLA, nucleus accumbens (ACB), prelimbic cortex (PL) resulted in ENTl labelled neurons (Ammassari-Teule et al., 2000; Gallagher and Chiba, 1996; Ohara et al., 2018).

Regions correlated with spatial navigation, such as the retrosplenial cortex, were downstream targets of ENTm (**Figure 1.2**; Epstein, 2008; Ohara et al., 2018). Specifically, as the major interface between neocortical regions and the rest of the hippocampal formation, the ENT is crucial for episodic memory (Buzsáki and Moser, 2013; Norman and Eacott, 2004; Squire and Zola-Morgan, 1991). Human AD studies have identified amyloid plaques within ENT, CA1 and subiculum; moreover, high levels of NFTs have been found in the subiculum, CA1, ENT and the amygdala (Arnold et al., 1991). Marked atrophy of the ENT has been correlated with the appearance of episodic memory deficits in AD patients and MCI subjects, suggesting that ENT and hippocampal volume changes are an early biomarker for the conversion from preclinical AD to MCI (Jack et al., 2005; Lacy and Stark, 2012; Paola et al., 2007). Substantial neuronal loss has been reported in multiple studies: advanced AD patients showed $\approx 90\%$ neuronal loss in layer II of the ENT and patients in very early stages showed an alarming 60% loss in the same region, whereas,

prodromal subjects did not show ENT neuronal loss (Gómez-Isla et al., 1996; Price et al., 2001). Evidence shows that, specifically, the ENTl is one of the earliest and most important regions in the early stages of AD (Braak and Braak, 1995; Nakazono et al., 2018; Petrache et al., 2019; Schöll et al., 2016; van Hoesen et al., 1991). Although regions such as the perirhinal cortex also are reported to be highly affected in the early stages of AD (Diana et al., 2007), it is the scope of this thesis to focus on the ENTl and its efferent projections.

1.2.2 Lateral entorhinal cortex: cytoarchitecture and projections

The ENTl is a laminar structure with six-cell layers, located caudally within the MTL. These layers are numbered increasingly from the surface to the inner side of the brain; layers I and IV (molecular layer and lamina dissecans respectively) are poorly populated by cells (Witter, 2007a; Witter et al., 2017). Layer II of ENTl contains gamma-aminobutyric acid (GABA) interneurons, whereas layers III and V are predominantly populated by pyramidal neurons (Canto et al., 2008). Layer V of ENTl can be further subdivided into Va and Vb, where layer Va neurons represent the major projections to cortical and subcortical structures, and layer Vb cells project inputs from the hippocampus proper to the Va (Witter et al., 2017). The main excitatory neurons in the ENTl are stellate and pyramidal cells, but several groups of interneurons can also be found in the ENTl (Canto et al., 2008). The ENTl represents a vital interface between the neocortex and the inner structures, such as the hippocampus proper, the DG and BLA (**Figure 1.2**). The hippocampal memory system is thought to have a dual-nature that places the ENTl as a central hub: information travels out from the hippocampal formation through the ENTl layer V where it can either feed-forward to other cortical sites or travel via deep-to-superficial layer V axon projections to layer II as a feedback loop to the DG, basal ganglia

and striatum (Kloosterman et al., 2003; Ohara et al., 2018; Witter et al., 2017). The DG is a three-layered structure, with molecular, granular cell and polymorphic cell layers (DGmol, DGgc and DGpol respectively). ENTl projects to the DGmol through the perforant pathway, thus, initiating information processing and flow from the neocortex to the hippocampus (Witter et al., 1989; Witter and Amaral, 1991). DG has recently gained attention in dementia research as its function (and disturbance in AD) have been linked to the component of episodic memory, related to pattern separation, whereby similar experiences are represented normally as non-overlapping patterns (Yassa et al., 2010). Moreover, DG shows adult neurogenesis, bringing supporting evidence for its role in memory formation through pattern separation as well as in connecting ENTl and hippocampus proper (Nakashiba et al., 2012; Toda et al., 2019; van Praag et al., 1999).

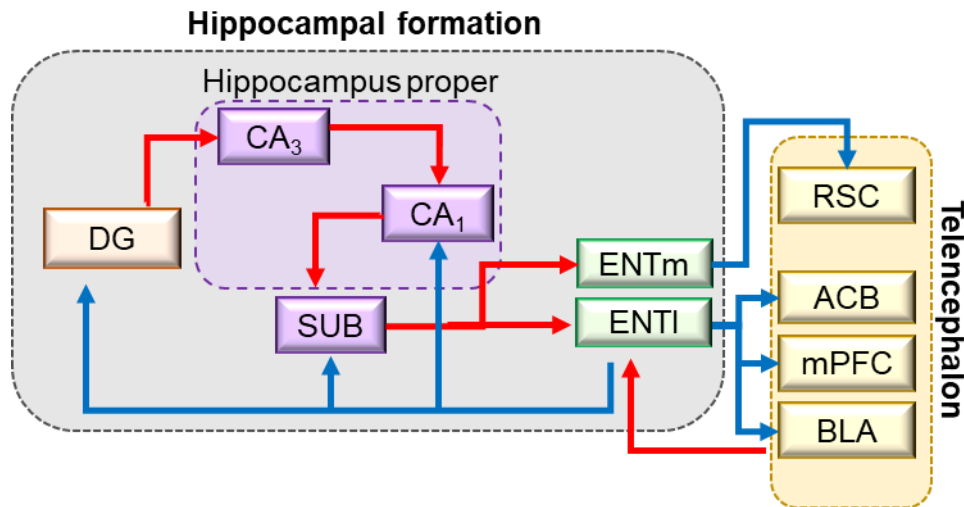


Figure 1.2: Diagram showing the main connections across the hippocampal formation and telencephalic regions

The entorhinal cortex is the connecting hub between the hippocampus proper, the subiculum, the DG and telencephalic regions, such as RSC, ACB, mPFC and BLA. Anatomically and functionally distinct projections arise from the medial and lateral ENT (ENTm and ENTl). ENTm projects mainly to the RSC, region involved in spatial navigation. ENTl projects predominantly to BLA, mPFC and ACB, regions involved in the emotional learning, fear processing and reward system. Within the hippocampal formation, the ENTl projects mono-synaptically to DG (the layer II perforant path), SUB and CA₁ (the layer III temporo-ammonic pathway). ‘Re-entrance’ to the ENTl come from SUB and CA₁ projections to layer V (with a diffuse input to layer III). DG: dentate gyrus; CA₁₋₃: cornu ammonis (subfields 1-3); SUB: subiculum; RSC: retrosplenial cortex; ACB: nucleus accumbens; mPFC: medial prefrontal cortex; BLA: basolateral amygdala.

Another key structure in the MTL, densely connected to the ENTl and declarative and procedural (fear conditioning) memory systems, is the amygdala. The amygdala is most clearly related to emotional memory processes, fear and anxiety (Cohen and Paz, 2015; Paz et al., 2006; Paz and Pare, 2013), as well as emotional learning (Gallagher and Chiba, 1996). Changes within amygdaloid nuclei may contribute to a plethora of neurological diseases, such as temporal lobe epilepsy and schizophrenia (Pitkänen et al., 1998; Reynolds, 1983). Moreover, deficits within the amygdala have been associated with emotional contagion, i.e., empathy, in MCI patients (Sturm et al., 2013), an effect confirmed in rodents (Panksepp and Panksepp, 2013). The major projections from the amygdala to the hippocampal formation arise from the lateral, basal and accessory basal nuclei (Pikkarainen et al., 1999), which together form the BLA (LeDoux, 2007; Savander et al., 1995). The circuit of connections between ENTl, DG and BLA is thought to be highly relevant for declarative and emotional memory (McGaugh, 2002; Squire and Zola-Morgan, 1991; Zola-Morgan et al., 1986).

1.3 Alzheimer's disease

1.3.1 Types of AD: Early- and Late-Onset

AD symptoms appear generally after 65 years of age (late-onset AD, LOAD, also known as sporadic AD), with only a small percentage of cases (< 5%) showing AD symptoms earlier in life (early-onset AD, EOAD, also known as familial AD; Gour et al., 2014; McKhann et al., 1984). In AD research, the earlier manifestation of AD is associated with specific genetic mutations, whereas, later manifestations of the disease are thought to be more related to ageing in tandem with genetic risk factors (Gour et al., 2014). While the aetiology of LOAD is still unknown (Pimplikar, 2009), clear genetic mutations leading to

EOAD have been identified (Goate et al., 1991; Guo et al., 1996). Autosomal dominant mutations in the gene that encodes for amyloid precursor protein (APP) and mutations in the genes encoding for Presenilin 1 and 2 (PS-1, PS-2 related to γ -secretase structure; **Figure 1.3**) are found in patients with EOAD (Guo et al., 1996; Lanoiselée et al., 2017; Weggen and Beher, 2012).

1.3.2 Genetic risk factors

Risk factors for AD have been identified in genes related to lipid metabolism and A β clearance: *CLU*, *PICALM* and, the most commonly investigated, *APOE ϵ 4* (Harold et al., 2009). It is estimated that carrying two copies of the *APOE ϵ 4* variant increases the risk of AD by 12-fold (Spinney, 2014). Recent research shows that the *BACE1* enzyme is significantly involved in the production of A β . Work conducted on APP-overexpressing mice (Tg2576) shows that *BACE1*-deficient mice reported an absence of toxic forms of cleaved APP, compared to Tg2576 mice with regular expression of *BACE1*, thus, opening a new therapeutic direction in *BACE1* inhibitors. These, however, have all failed in clinical trials, perhaps due to being tested only on AD patients at a very late stage of the disease (Liebsch et al., 2019; Luo et al., 2001; Zakaria et al., 2018). Furthermore, recent research from genome-wide association studies (GWAS) has shown a diverse repertoire of genes that may represent risk factors in AD (e.g., *VKORC1* and *ACE* involved in blood coagulation and cerebral blood flow regulation), some of which have been already identified as potential therapeutic targets (Marioni et al., 2018). Although the aetiology of EOAD and LOAD might differ, the development of pathology in both forms is similar, showing the same spatiotemporal pattern of neurological and histological features (Pimplikar, 2009). Hence, research with transgenic animals harbouring mutated human genes associated with EOAD and manifesting AD-like pathology is fundamental for

investigating the onset, cause and possible risk factors of both EOAD and, ultimately, LOAD (Oddo et al., 2003). In this work, the 3xTgAD mouse model will be used to investigate brain changes in the early stages of AD-like pathology (Oddo et al., 2003). First, the main molecular aspects of AD are described below, followed by the mouse model choice.

1.3.3 Molecular hallmarks

The development of A β plaques and NFTs, in AD, typically follows a well-defined spatiotemporal pattern in both EOAD and LOAD (Braak and Braak, 1995; Nelson et al., 2012; Selkoe, 2011). Specifically, within the MTL, A β plaques are seen first in the cortex, specifically ENT (Braak and Braak, 1995) and then later in the amygdala, HF and further structures, whereas, NFTs develop in subcortical regions first, and then later in the cortex (Thal et al., 2002, 2000).

A β plaques

The formation of A β plaques derives from a misprocessing of APP: in the non-pathogenic (non-amyloidogenic) pathway (**Figure 1.3**, left), APP is cleaved by α -secretase in combination with γ -secretase, resulting in the production of soluble forms of APP α (sAPP α), considered to be neuroprotective (Chasseigneaux and Allinquant, 2012), and other non-pathogenic fragments, i.e., P3 and APP intracellular domain (AICD). In the pathogenic (amyloidogenic) pathway (**Figure 1.3**, right), APP is processed with a different combination of enzymes: β -secretase, combined with γ -secretase, leads to the formation of A β peptides of 40 or 42 amino acid length (Kamenetz et al., 2003). Between A β_{1-40} and A β_{1-42} , the latter has more hydrophobic properties and is the major constituent of A β plaques (Iwata et al., 2000). These forms of A β influence negatively neuronal and synaptic

function, initiating a cascade of neuronal degradation, inflammation, formation of reactive oxygen species, activation of astrocytes, eventually leading to neuronal cell death (Hardy, 2006; Johnstone et al., 1999).

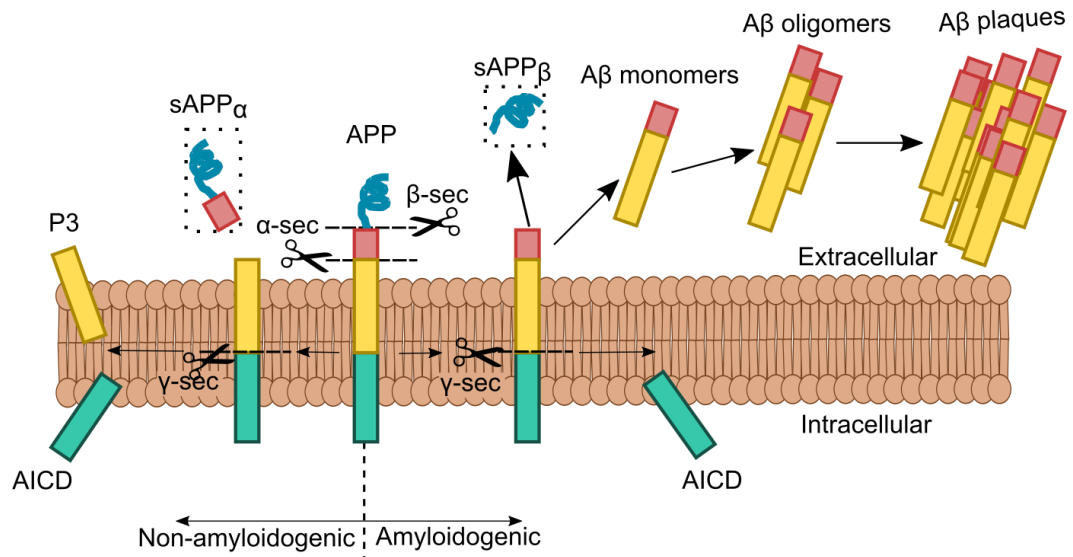


Figure 1.3: Diagram showing the beta-amyloid pathway leading to the accumulation of Aβ plaques

Non-amyloidogenic pathway (**left**): α-secretase and γ-secretase will produce soluble APPα, P3 and AICD, all unrelated to plaque formation. Amyloidogenic pathway (**right**): the action of β-secretase and γ-secretase will lead to the production of sAPPβ, AICD and Aβ₄₀₋₄₂ monomers, which eventually lead to oligomers and plaque formation. sAPP: soluble amyloid precursor protein; AICD: APP intracellular domain; P3: derivative of Aβ-peptide. Aβ: beta-amyloid.

Interestingly, APP, produced in the ENT1 region in AD transgenic mice, is transported through the perforant pathway to the DG (Buxbaum et al., 1998). Lesions in the perforant pathway lead to a decrease of Aβ in the DG, confirming the central role of ENT1 in AD-like pathology (Lazarov et al., 2002).

Neurofibrillary tangles

The second major hallmark in AD is the formation of NFTs from progressive aggregates of hyperphosphorylated protein tau peptides (Brion, 1998). Tau protein is part of the microtubule-associated proteins (MAPS), which are responsible for the stabilization

of microtubules that form the cytoskeleton (Avila et al., 2004; Feinstein and Wilson, 2005). In the non-pathogenic state, protein tau binds/unbinds to the microtubule through phosphorylation/dephosphorylation, helping in the cytoskeleton stabilization and transport. In AD, there is an increase in phosphorylated tau mediated by GSK3 enzyme, leading to the formation of paired helical filaments, which ultimately form aggregates of NFTs (**Figure 1.4**). This chain of events leads to malfunction of the cytoskeleton and ultimately to neuronal degeneration (Avila et al., 2004; Feinstein and Wilson, 2005).

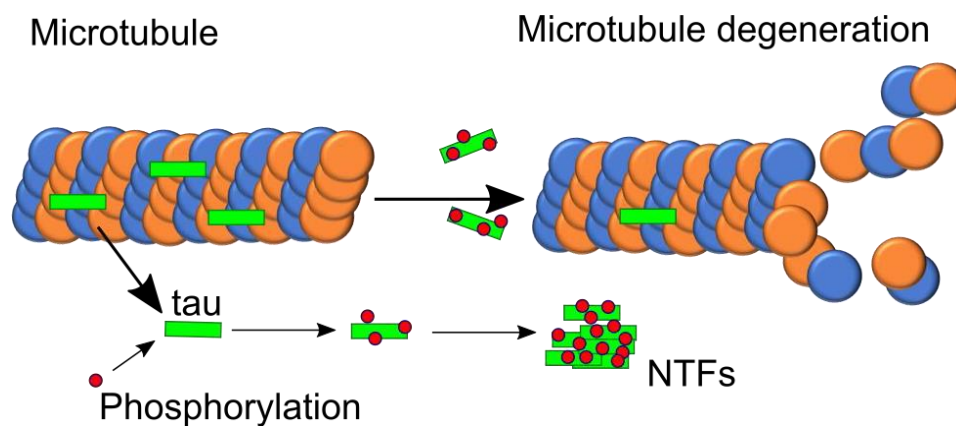


Figure 1.4: Formation of neurofibrillary tangles (NFTs)

The hyperphosphorylation of tau peptides is mediated by GSK3 enzyme and results in the formation of paired helical filaments which subsequently aggregate into NFTs and causes the degeneration of microtubules.

1.3.4 Unclear aetiology of AD

Despite the clear mechanisms for the formation of both A β plaques and NFTs, research on AD has not reached a conclusion on the primary cause leading to AD pathology.

According to the original amyloid cascade hypothesis, A β plaques would be the primary cause, leading to both the formation of NFTs and other AD-related features (Hardy and Higgins, 1992). Furthermore, according to more recent studies, A β

accumulation seems to be the result of a malfunction of its synthesis-to-clearance ratio (Hellström-Lindahl et al., 2008), regulated by enzymes such as β -secretase (*BACE1*) and γ -secretase and *APOE ϵ 4* activities (Evin and Weidemann, 2002).

However, the spatiotemporal deposition of A β plaques does not correlate well with the trajectory of cognitive decline, which is seen to strongly correlate with tau deposition instead (Berg et al., 1998). Several post-mortem studies have highlighted the appearance of NFTs before the presence of A β plaques in AD patients, again challenging the amyloid cascade hypothesis (Schönheit et al., 2004). Moreover, research has shown the presence of A β plaques in healthy subjects with a similar pattern to those found in AD patients, therefore, arguing against the amyloid cascade hypothesis as the fundamental cause of AD (Davis et al., 1999).

The cognitive decline witnessed in MCI patients, i.e., before the appearance of plaques, brings additional evidence against the amyloid cascade hypothesis (Dubois et al., 2016; Jack, 2012). In recent years, evidence for a key role of intracellular forms of A β , i.e. prior to the extracellular aggregation in plaques, has been reported in human studies showing an abundance of A β ₄₂ intracellularly, before the appearance of cognitive deficits (Gouras et al., 2000). As a consequence, synaptic dysfunction and cognitive decline seem to precede the formation of interneuronal plaques and tangles (Billings et al., 2005; LaFerla et al., 2007).

Research on animals (explained further, in later sections) also highlights the appearance of both neuronal dysfunction and memory deficits before the accumulation of A β plaques: for example, the Tg2576 mouse model for AD-like pathology shows spatial memory impairment by 6 months of age where plaques only occur from 18 months of age (Jacobsen et al., 2006). Similarly, the 3xTgAD model mouse shows memory impairments before overt pathology at 2 months, consistent with intraneuronal A β accumulation,

whereas extra-neuronal A β plaques only appear around 10 months (Billings et al., 2005). The LaFerla group originally developed the 3xTgAD model and established the appearance of intraneuronal A β ₄₂ at 4 months of age, together with the development of memory deficits, providing evidence that memory deficits occur before amyloid plaques formation (Davis et al., 2013a, 2013c; Oddo et al., 2003). Additionally, evidence is accumulating on the potential role of neuronal calcium homeostasis dysregulation as a leading factor for the initial stages of AD (Herrup, 2015).

Research in dementia still needs to find conclusive evidence to show AD pathology unravels, and thorough work still needs to be done in establishing the earliest brain changes, in order to have a meaningful therapeutic direction. In the last decade, there has been a shift of focus towards the early stages of the disease in order to develop drugs against prodromal hallmarks of AD pathology, i.e., prior to the appearance of clinical symptoms. Therefore, it is of paramount importance to identify and validate the earliest biomarkers within the prodromal stage (Karran et al., 2011; Vermunt et al., 2019b).

1.4 Animal models in preclinical research

Animal models provide a useful tool to help tackle this issue as they allow invasive experimental access to the microscale of events, e.g., intracranial electrophysiological recordings. Among the variety of animal models created to mimic AD-like pathology, those based on the mouse are most commonly adopted (Elder et al., 2010). Mouse models are relatively inexpensive, the genetic manipulation protocols are well established and they express a similar functional brain connectome to the human and non-human primates (Zerbi et al., 2015); as such, the adoption of mouse models allows a whole-brain, non-invasive, measure of the functional connectome. This provides direct access to neuronal activity and synaptic connectivity in spatially defined brain regions, thus, overcoming the

limitations of techniques such as scalp electroencephalography (EEG) in humans (Beres, 2017).

Furthermore, mouse models for a given pathology represent a fundamental step towards the unravelling of pathological mechanisms: non-invasive techniques, (suitable for patients) and more invasive approaches (information at the neuronal level) can be combined onto the same reference space providing a trans-species translation.

Uncountable advantages arise from the use of rodents in AD research, i.e. the possibility to understand more in depth the pathological role of the different types of beta-amyloid aggregates, from the smallest soluble monomers to extracellular plaques (Elder et al., 2010). Moreover, pharmacological studies, on rodent models for AD, represent one of the initial steps for a drug validation, before trials on higher-order mammals and eventually human trials. The possibility to closely monitor behavioural changes in a mouse, due to acute or chronic drug administration has allowed the discovery of novel treatments, e.g., GABA antagonists to partially restore memory function (Jo et al., 2014). Moreover, the investigation of neuronal circuits and their manipulation *in vivo* has allowed a more fundamental understanding of functional connectivity across brain regions and the different types of signal pathways.

By using an animal model that mirrors human-like pathology, the interpretation of a phenomenon can be easier to make, as the models are purposefully designed to mimic only specific aspects of the pathology. Their shorter lifespan allows to perform longitudinal studies and sample the accelerated unfolding of the pathology over a short period of time. Genetically engineered models can express similar pathology to that affecting humans and may highlight, e.g., by overexpression of a gene, one specific pathological aspect, ultimately helping to unravel intricate pathology-related mechanisms, across several orders of magnitude (Jucker, 2010).

1.4.1 Limitations of animal models

Despite the fundamental contribution of animal models to pre-clinical research and drug development, it is also important to consider the limitations of this approach. A fundamental reason why animal research is generally hard to interpret, and not readily translatable to human findings, is the adoption of anaesthesia in the majority of experimental protocols, where brain status poorly resembles that of the human brain during both the resting- and evoked-state within typical human experiments. Moreover, the great lack of standardisation within experimental protocols, design, hardware, analysis and animal preparation, results in a difficult interpretation of results across laboratories and experimental designs (Mandino et al., 2020). For example, anaesthesia protocol variations (awake, free-breathing, mechanical ventilation) and variations in the anaesthetics used (isoflurane, urethane, medetomidine) do not allow for direct comparison across experiments as these agents elicit different responses in the neurovascular system. For a more detailed discussion on the anaesthetics commonly used, see section 1.10. Moreover, the human brain is dramatically bigger in size compared to the mouse brain; as such, cellular and pathological mechanisms may vary.

The genetically engineered overexpression of a pathological feature does not represent a spontaneous phenomenon; and, it often results in a exaggerated phenotype, which poorly resembles the pathology unfolding in humans. Additionally, mouse models for AD-like pathology mimic FAD type of pathology, which accounts for only 3% of cases, although pathology is essentially identical with SAD. Within the field of AD research, the limitations concern also the genetically modified models' design. To date, the majority of AD-like mouse models are engineered to present over-expression (rather than reduced clearance, as in human patients) of predominantly beta-amyloid constructs (Oddo et al., 2003; Elder et al., 2010).

Careful analysis of these models needs to be promoted, as the phenotype may vary across the models that use the same mutations (APP and PS1; Radde et al., 2006; Holcomb et al., 1998). Moreover, very few transgenic amyloid lines were able to show neurodegeneration and overt NFT formation (Drummond and Wisniewski, 2017; Hodge et al., 2019).

Some mouse models develop NFT and brain atrophy starting from the entorhinal cortex, for example, the PS19 tau mouse (Yoshiyama et al., 2007). Other models such as the 3xTgAD model, report both amyloid plaques and tau tangles (Oddo et al., 2008). However, since no genetic mutations have been linked to tau deposition in AD, these engineered mice derive the tau-related mutation from other pathologies, such as frontotemporal dementia, once again highlighting the difficulties in mirroring the exact spectrum of features of AD (Jankowsky et al., 2017). Models resembling the ‘at risk’ state of AD have also been created, such as the *APOE ϵ 4* (Brecht et al., 2004); however, by representing a ‘increased risk’ to develop AD-like pathology, they do not readily allow for a precise interpretation of the changes and their phenotype may reveal greater variability compared to other models.

Non-human models also have the challenge of replicating the cognitive loss in human patients. For example, episodic memory loss is an early defining symptom in AD but common episodic tests from the clinic cannot be used in the lab as non-human species cannot speak so can only reveal memory through change in their behaviour. However, some progress has been made in this regard, where a task shown to require episodic memory in human (Easton et al. 2012) has been used to reveal episodic-like memory loss in the 3xTg mouse model for AD (Davis et al, 2013).

1.4.2 3xTgAD mouse model

Over the past decades, genetically altered mouse and rat models expressing AD-like pathology have contributed enormously to research into AD pathogenesis, as invasive experiments can be undertaken in these species (LaFerla et al., 2007). The 3xTgAD mouse model was the first to successfully manifest both A β plaques and NFTs (LaFerla et al., 2007; Oddo et al., 2003). The majority of AD rodent models carrying APP/PS transgenes do not show spontaneous NFTs; toxic accumulations are present only in A β -related forms (Duff et al., 1996; Mucke et al., 2000; Oakley et al., 2006), or in a few cases in co-occurring hyperphosphorylated tau, but with no NFT formation (Sturchler-Pierrat et al., 1997). Moreover, models such as the Tg2576 are not able to recapitulate the progressive neuronal loss seen in AD (Janus et al., 2000). The rat TgF344-AD model is one of the first to show NFTs deposition alongside A β plaques and progressive neurodegeneration (Cohen et al., 2013).

This model, however, has an important drawback in that it is based on the Fisher line, which expresses high levels of anxiety, making it difficult to implement the usual spontaneous object recognition tasks used to assess memory most commonly in rodents. As genetic links to tau production in frontotemporal dementia (FTD) are well established, Oddo and colleagues developed and introduced the 3xTgAD mouse by combining EOAD human mutations involved in APP processing (APP_{SWE} and PS1_{M146V}) with a tau transgene from human FTD (Tau_{P301L}; Oddo et al., 2003). Thus, the 3xTgAD mouse was the first model to show both amyloid plaques and tangle pathology in a manner comparable with the respective spatial and temporal pattern in human AD (Delacourte et al., 1999; Frisoni et al., 2010).

3xTgAD mouse model, however, presents some crucial limitations that ought to be considered when planning a study with this mouse line. First of all, the animals present a

shorter life span compared to wild-type with the same genetic background (Rae and Brown, 2015). Additionally, Kitazawa and colleagues have reported a reduction of the pathological features in 3xTgAD, i.e. A β and tau, when the background strain of the 3xTgAD cohort was changed from C57Bl/6 \times 129SvJ to FVB/N, thus, suggesting a probable influence of the genetic background in the resulting development of the pathology (Kitazawa et al., 2012). However, the 3xTgAD mouse model represents a good candidate for investigating the interaction between the two main molecular hallmarks of AD, in that it develops both. Moreover, plaques and tangles, in 3xTgAD mice, appear relatively late in life (~9-11 months old; Mastrangelo and Bowers, 2008), providing a good time window to investigate the initial, prodromal accumulation of intracellular A β , which is thought to play a pivotal role in synaptic changes. Other models of AD (e.g., APP/PS1) show much faster accumulation of extracellular A β plaques (typically within 4 months), so do not have such a wide developmental window over which to research early disease markers for prodromal AD.

Indeed, the 3xTgAD model has helped in understanding how the pathobiology of AD is related to the role of intraneuronal A β_{42} . Evidence in the literature suggests that intracellular A β can be seen by 2 months of age in 3xTgAD amygdala and some parts of the hippocampus proper; at 3 months of age A β appears in superficial ENT; and by 6 months the entire ENT presents A β (Davis et al., 2014; Mastrangelo and Bowers, 2008; McQuiston, 2010). 3xTgAD mice show cognitive impairment from 4 months of age, consistent with high intraneuronal A β levels in hippocampus and amygdala: at that stage, no interneuronal A β depositions or NFTs appear (Billings et al., 2005; Mastrangelo and Bowers, 2008).

Moreover, behavioural experiments by Davis and colleagues show episodic-like memory deficits in 3xTgAD mice compared to controls at 6 months of age, but also

decreased performance already by 3 months (Davis et al., 2013a, 2013c). These deficits may result from the synaptic dysfunction found in 3xTgAD mice by these young ages, e.g., by 4-6 months (Davis et al., 2014; Oddo et al., 2003). Thus, it has been hypothesised that early changes in cognitive performance at 3 months of age in this model could represent the key temporal feature for AD development from MCI stages. In sum, the 3xTgAD mouse represents a good model for investigating the development of AD-like pathology from early into end-stage disease (LaFerla and Oddo, 2005).

1.5 Structure of the present work

In the present thesis, the 3xTgAD mouse model has been studied to investigate the impact of early AD-like pathology on brain function. The main goal of this thesis is to apply techniques that can reveal a better understanding of the pathology, from a whole-brain, macro-scale (Chapter 3), compatible to what is reported in the clinic, to a neuronal level, i.e., micro-scale of events (Chapter 4). Therefore, non-invasive neuroimaging techniques, and their relevance to human research, are described first (sections 1.6-1.7). Secondly, the application of non-invasive neuroimaging techniques in animal models of AD is described (section 1.8), followed by invasive approaches applicable only in animals that can provide a great insight into the underlying phenomena reported in humans (section 1.9).

1.6 Neuroimaging

The devastating progressive pathology of Alzheimer's disease gradually results in generalised brain atrophy, starting within the MTL. As such, the rise of whole-brain, non-invasive neuroimaging techniques in the last twenty years, e.g. positron emission

tomography (PET) and MRI/fMRI, has represented a major step forward in neuroscience and neurology: they provide an accurate and non-invasive mapping of the brain activity and the underlying anatomical structures, and they allow for a longitudinal approach to monitor disease progression. Although PET and fMRI are associated most strongly with investigating the human brain, they can also be applied in animal models, resulting in a useful translational approach. The use of PET and fMRI measures in neuropathological states allows the unbiased measurement of brain-wide alterations that result from the underlying neuronal dysfunctions. Both techniques can also measure the dynamic changes in the brain over time.

1.6.1 Positron Emission Tomography

PET is an imaging technique based on the detection of radioactivity from an injected tracer. It measures blood flow, oxygen consumption, metabolic changes and pathological depositions, e.g. cancerous cells (Berger, 2003). A great advantage of PET is the use of radioisotopes incorporated into biologically relevant molecules, such as carbon radioisotopes for a direct approach *in vivo*. In AD research, the deposition of A β plaques in the human brain can be measured with PET by using, e.g., the radiotracer Pittsburgh Compound-B (PiB) and florbetapir; the accumulation of NFTs can be monitored with flortaucipir tau (Ikonomovic et al., 2008; Pontecorvo et al., 2017). Increased tau has been reported in AD patients by using the tau tracer 18F-AV-1451 (Barret et al., 2017). Strong hypometabolism in frontal, parietal and temporal regions has been reported in AD patients by using [18F]fluoro-deoxyglucose as a measure of local changes in the glucose uptake (Perani et al., 1993).

Higher retention of tau tracer was found in MCI patients in regions encompassing the ENT and was correlated with poor cognitive performance (Neitzel et al., 2019).

Moreover, PET studies in MCI patients have shown that metabolic changes in the ENTl and hippocampus may represent early biomarkers to distinguish patients that progress from MCI to AD, from patients that remain in a stable MCI status (Gao et al., 2018).

1.6.2 Structural Magnetic Resonance Imaging

MRI, compared to PET, offers multiple contrasts, including one for high soft-tissue contrast. Most often, contrast-mechanisms rely on endogenous molecules, which renders molecular imaging more difficult. MRI is commonly based on the interaction of hydrogen particles, present in soft tissue, with a strong magnetic field B_0 , to which the spin of the hydrogen protons are either aligned with or against (Uludag et al., 2015). By using radio frequencies (RF) provided in short pulses orthogonal to B_0 , the hydrogen particles oscillate (precess) within the magnetic field. Whilst, returning to their equilibrium, they emit energy, detected by coils. Subsequent amplification and processing of the signal will result in the detailed images of body tissues (Rawlani and Rawlani, 2014). The two main contrasts used in MRI, based on the magnetisation relaxation, are T1 (grey matter = dark grey, white matter = light grey, ventricles = black) and T2-weighted (grey matter = light grey, white matter = dark grey, ventricles = white); T2* represents T2 contrast whilst accounting for variations in the field inhomogeneity and molecular interactions ($T2^* < T2$).

MRI is routinely adopted to investigate structural changes in AD; it allows to monitor progressive brain atrophy and ventricular enlargement, from preclinical AD to advanced dementia AD cases (Nestor et al., 2008; Vemuri et al., 2009). Indeed, MRI studies on AD patients have reported structural changes in the MTL, specifically in the hippocampus proper and ENT, highlighting the involvement of these regions in AD (for a review Frisoni et al., 2010). Additionally, diffusion-weighted MRI provides information

about connectivity across brain regions by measuring water diffusion along axons (Mori and Barker, 1999; Sandson et al., 1999). Among the variety of applications of MRI, fMRI allows us to determine functional connectivity across brain regions through the haemodynamic response.

1.6.3 Functional magnetic resonance imaging

The traditional fMRI signal relies on neurovascular coupling; increased neuronal activity elicits changes in metabolic demand that, in turn, lead to increased blood flow to that active site (Buxton, 2012; Shmuel, 2019). FMRI is currently playing a central role in the functional mapping of the human brain in both healthy and diseased states, due to its non-invasiveness and its level of spatial resolution that can resolve signals resulting from anatomically-distinct brain regions (Heeger and Ress, 2002; Murphy et al., 2013).

The three main readouts commonly adopted in fMRI are cerebral blood flow (CBF), cerebral blood volume (CBV) and BOLD (Buxton, 2012; Mandeville et al., 1998). CBF is typically acquired through arterial spin labelling, by targeting water protons in arterial blood as an endogenous tracer (Wolf and Detre, 2007). Although it is non-invasive, CBF is relatively challenging to implement: it is based on the difference between a ‘labelled scan’ and a scan without labelling, resulting in relatively slow acquisition; additionally, it presents a lower contrast-to-noise ratio compared to BOLD, which is often preferred (Detre and Wang, 2002; Lu et al., 2003). CBV is a measure of changes in the blood volume across the brain; in human subjects, the most widely used CBV measurement is Vascular-Space-Occupancy (VASO) MRI where the readout is based on T1 changes in the vascular expansion (Lu et al., 2013). However, evidence shows that VASO-MRI lacks sensitivity compared to BOLD in the majority of brain regions, except for the frontal areas (Poser and Norris, 2011).

Another approach used for CBV measures is based on the injection of a paramagnetic contrast agent and monitoring CBV-related changes (Belliveau et al., 1991; Mandeville et al., 1998). However, the need to track an external agent over time, in order to quantify changes, makes this approach less straightforward compared to the BOLD signal, especially for clinical use.

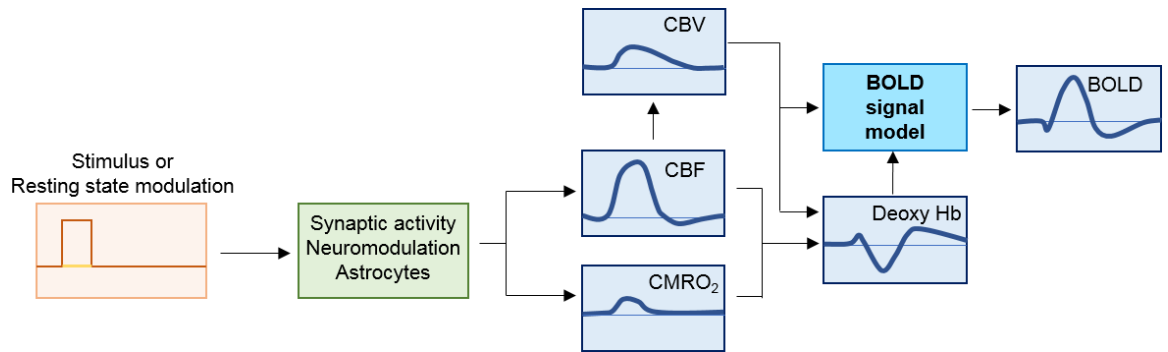


Figure 1.5: Simplified representation of the balloon model of BOLD signal composition

The balloon model highlights the complex interplay between CBV, CMRO₂ and CBF, that gives rise to the BOLD signal. Modulation in neuronal activity elicits changes in CBF and CMRO₂, affecting CBV. The nonlinear combination of changes in CBV and deoxy-haemoglobin concentration results in the BOLD signal of fMRI. CBV: cerebral blood volume; CBF: cerebral blood flow; CMRO₂: cerebral metabolic rate of oxygen consumption; BOLD: blood oxygenation-level dependent.

According to the balloon model (**Figure 1.5**; Buxton, 2012), the BOLD signal results from an intricate interaction between cerebral metabolic rate of oxygen consumption (CMRO₂) and changes in CBF and, thus, CBV, following either resting-state neuronal fluctuations or stimulus-evoked response (Buxton et al., 1998). The BOLD signal is associated with changes in the ratio of oxygenated to deoxygenated haemoglobin during periods of metabolic demand, elicited by prior neuronal activity (Ogawa et al., 1993).

Oxygenated haemoglobin, with no unpaired electrons, is diamagnetic; deoxygenated haemoglobin, however, has unpaired electrons that convey paramagnetic properties. Increase in deoxy-haemoglobin results in a decrease in T₂ and T₂* properties, which is detectable using spin-echo and gradient-echo MRI sequences, respectively.

BOLD signal of fMRI represents a relatively easy measure of the simultaneous activity of one or more brain regions. It can be acquired non-invasively, therefore, aiding translatability across animal models and human brain investigation in healthy and diseased conditions. Functional connectivity (FC) in fMRI derives from the statistical association in multiple brain regions through low-frequency fluctuations in the BOLD signal (Biswal et al., 1995).

1.7 Functional Connectivity in Alzheimer's disease

1.7.1 Evidence from human fMRI

The analysis of FC with fMRI is fundamental for our understanding of temporal synchrony across brain regions and how different brain regions are subdivided into resting-state networks (RSNs). As such, the study of FC in the healthy and diseased brain may contribute enormously in identifying organisational changes within RSNs due to neuropathology. Major initiatives across countries and laboratories have helped in collecting large datasets of human fMRI work on healthy and diseased brain, thus, encouraging meta-analysis approaches, e.g., the UK Biobank initiative, the Human Connectomes Project (Miller et al., 2016; Van Essen et al., 2012) and the Alzheimer's Disease Neuroimaging Initiative (Weiner et al., 2013; Weiner and Veitch, 2015).

Functional impairments in AD patients have been investigated with the use of resting-state fMRI (rsfMRI) and task-based fMRI (Greicius et al., 2004; Johnson et al., 2012). Specifically, rsfMRI studies of AD patients show reduction of FC in some of the major RSNs identified in the human brain, i.e., the default-mode network (DMN), salience network and dorsal attention network (Damoiseaux, 2012; Damoiseaux et al., 2006; Li et al., 2012; Rombouts et al., 2005). The DMN is thought to be active at rest - when subjects are not focused on external stimuli, rather on inner thoughts - and includes the posterior

cingulate cortex, inferior parietal lobe, MTL and mPFC (Raichle, 2015; Raichle et al., 2001). Greicius and colleagues highlighted changes in the DMN even for mild AD, where regions such as the posterior cingulate cortex and the hippocampus showed decreased activation compared to healthy controls (Greicius et al., 2004). Decreased activity in the DMN was associated with enhanced activation of prefrontal regions MCI patients, possibly suggesting a compensatory mechanism (Agosta et al., 2012) and suggesting early synaptic dysfunction before a clear manifestation of the disease (Machulda et al., 2003; Rombouts et al., 2005).

Changes in FC have also been reported in subjects at risk of AD, such as *APOEε4* carriers (Filippini et al., 2009; Sorg et al., 2007), highlighting neuronal alterations decades before disease onset. An increase in activity within MTL regions was present in rsfMRI assessment of young *APOEε4* carriers (Filippini et al., 2009). Changes in the DMN, however, have also been reported in cognitively normal subjects presenting Aβ depositions (Sheline et al., 2010). Importantly, results from multiple fMRI studies on healthy controls, subjects at risk, MCI and AD patients show a similar trend of changes within the DMN: increased FC seems to precede a decrease in FC (Damoiseaux, 2012) and the regions affected in the early stages of AD pathology are highly correlated with the pathological hallmarks highlighted by Braak & Braak (Braak and Braak, 1995).

Task-based (stimulus-evoked) fMRI allows comparison of the haemodynamic response of the brain to specific tasks. Task-based fMRI studies highlighted decrease of fMRI signal in AD patients in regions encompassing the ENTl, parietal cortices and prefrontal cortices, correlated with impaired cognitive performance (Kato et al., 2001; Khan et al., 2014; Small et al., 1999; Sperling, 2003).

However, increased activity was found during memory tasks in MCI patients (Hämäläinen et al., 2007), supporting an initial increase in activity prior to later decrease

(Damoiseaux, 2012). Interestingly, although asymptomatic individuals at risk of AD show no memory impairment in cognitive tests, they display higher activation during a memory task not only in regions related to memory encoding within the MTL (the hippocampal formation) but also in neocortical regions such as the mPFC. This suggests a reallocation of resources as a compensatory mechanism years before disease appearance (Bassett et al., 2006). Additionally, *APOEε4*, non-demented subjects, show a diverse pattern of brain activation during a memory task, compared to controls, again suggesting for a brain-wide compensatory mechanism (Bondi et al., 2005).

1.7.2 Evidence from rodent fMRI

The application of fMRI to rodents represents a great tool for research, as it offers a translational approach to the investigation of corresponding brain changes identified in human pathology. To date, rsfMRI in rodents provides highly comparable results to human rsfMRI and the possibility to anaesthetise and restrain the animal allows for higher control of the signal obtained (Grandjean et al., 2014a). Similarly to human fMRI, fMRI acquired in a paradigm-free setting in mice allows assessment of the synchrony of activity fluctuations in different brain regions (Grandjean et al., 2019b; Guadagno et al., 2018; van Meer et al., 2012; Zhao et al., 2008).

The use of rsfMRI in mouse models for AD-like pathology has highlighted a diverse repertoire of results, which may arise from a combination of effects including the diverse pathological phenotype of each model, presence and type of anaesthesia and acquisition protocols.

A PET-fMRI study in Tg2576 mice highlighted global hypermetabolism by 7 months of age, whereas, no difference in CBV was found, suggesting a compensatory homeostatic mechanism to balance excessive metabolic activity (Luo et al., 2012). A

pioneering study of rsfMRI in the APP/PS1 mouse model for cerebral amyloidosis showed overt plaques throughout the brain, with a reduction in FC in hippocampal areas and somatosensory areas compared to controls (Shah et al., 2013). However, young APP/PS1 mice showed increased FC compared to controls, with older mice showing a decrease in FC, in line with work from Shah (Bero et al., 2012), and resembling the increase prior to decreasing in FC found in AD patients. Changes of CBV in old age (20 months) were found in a mouse model for *APOEε4* gene, observed as an increase in fMRI signal compared to controls predominantly within the ENTl; at younger ages, no difference was reported (Nuriel et al., 2017).

In 3xTgAD, rsfMRI has been performed only once where 2-month-old mice showed decreased interhemispheric FC compared to age-matched controls (Manno et al., 2019); hippocampal structural changes in 3xTgAD have been reported as early as 4 months, as well as memory impairment (Chiquita et al., 2019; Davis et al., 2013b). The variability across animal-laboratories in data acquisition protocols, anaesthesia and animal preparation, prevents, however, to make definitive comparisons and conclusion from the earliest brain changes in mouse models for AD. Further exploration with more standardised methods may result fundamental to aid in cross-laboratories comparison (Grandjean et al., 2019a).

1.8 Optogenetics

Despite the contribution that non-invasive fMRI has brought to clinical and pre-clinical research, it is characterised by mainly three major limitations: its readouts, such as BOLD, are not cell-specific, the time resolution is relatively slow and it provides indirect measures of the underlying neuronal activity.

Indeed, the signal that arises from FC with rsfMRI is derived from the unspecific mixed activity of diverse cell types, e.g., excitatory/inhibitory neurons and glial cells. Labelling techniques such as pharmacological targeting of specific receptors (Ferrari et al., 2012; Jonckers et al., 2015; Razoux et al., 2013), or the more recently developed chemogenetics, allow us to investigate signatures of brain activity coming from the targeting of, for example, a specific neuronal population (Aldrin-Kirk et al., 2018). The administration of drugs to test the pharmacological response of a specific target does not require invasive surgical procedures. It is, however, not advised for prolonged and longitudinal studies, e.g., due to the possible occurrence of desensitisation of activated receptors (Arey, 2014; Berg and Clarke, 2018; Chen et al., 1999).

Pharmacological studies in AD mice have used, for example, bicuculline as GABA_A antagonist, to restore neuronal activity (e.g. in APP23; Mueggler et al., 2002). Chemogenetics is based on the administration of ligands that bind to genetically encoded receptors named Designer Receptors Exclusively Activated by Designer Drugs (DREADDs), thus, ensuring a specific stimulation. Recently, a study with DREADD in APP/PS1 mice, has reported hyperactivity of inhibitory parvalbumin interneurons in the hippocampus already by 4 months of age; a decrease in soluble A β was found, post-treatment (inhibition of the interneurons with DREADD; Hijazi et al., 2019). However, recent evidence has questioned the specificity of the typical ligand used with DREADD, i.e., clozapine-N-oxide (CNO). Evidence suggests that CNO may be metabolised into clozapine which, unlike CNO, is a psychoactive drug, resulting in a possible cascade of unforeseen events (Aldrin-Kirk et al., 2018; Giorgi et al., 2017; Lee et al., 2014; Roth, 2016; Sciolino et al., 2016).

An attractive technique that can genetically-label a specific neuronal population in a targeted brain region is optogenetics (Desai et al., 2011; Grandjean et al., 2019b; Hinz et

al., 2017; Kahn et al., 2013; Leong et al., 2018). Optogenetics is based on the transfection of light-sensitive ion channels into neurons within a predefined region of interest (ROI; Deisseroth, 2011; Lee et al., 2010). The most commonly adopted opsin is the blue-light activated Channelrhodopsin-2 (ChR2), activation of which results in acute excitation and depolarisation of expressing cells (Boyden et al., 2005).

Other opsins such as Halorhodopsin, promote chloride ion influx, therefore, resulting in hyperpolarisation of membrane voltage (Guru et al., 2015; Han, 2012; Kato et al., 2012). Additionally, recently established stabilized step-function opsins (SSFO) allow for a sustained effect over a single brief pulse of light, although these are thought to be extremely sensitive to light, thus additional validation might be necessary (Berndt et al., 2009; Tye and Deisseroth, 2012; Yizhar et al., 2011). Transgenic mouse lines have been developed that can express light-gated ion channels, such as ChR2 (Zeng and Madisen, 2012). However, the traditional method adopted for ChR2 expression in cells is through injection of a viral vector. The simplified viral construct generally contains: a) a targeted promoter to control opsin expression, e.g., calmodulin-dependent protein kinase II (CaMKII α ; Nathanson et al., 2009) which is only expressed by excitatory neurons; b) the opsin part of the construct, e.g., ChR2; and c) a reporter for histological confirmation of the transfection or *ex vivo/in vitro* visualisation (**Figure 1.6**).

Following injection of the viral-vector in the targeted brain region, light-sensitive ion channels are expressed in specific neurons and can be modulated by a specific light-wavelength range (**Figure 1.6b,c**). With the promoter designed to target specific neuronal types, e.g. excitatory CaMKII α -positive neurons, optogenetics represents a great tool to assess the functional contribution of specific neuronal populations.

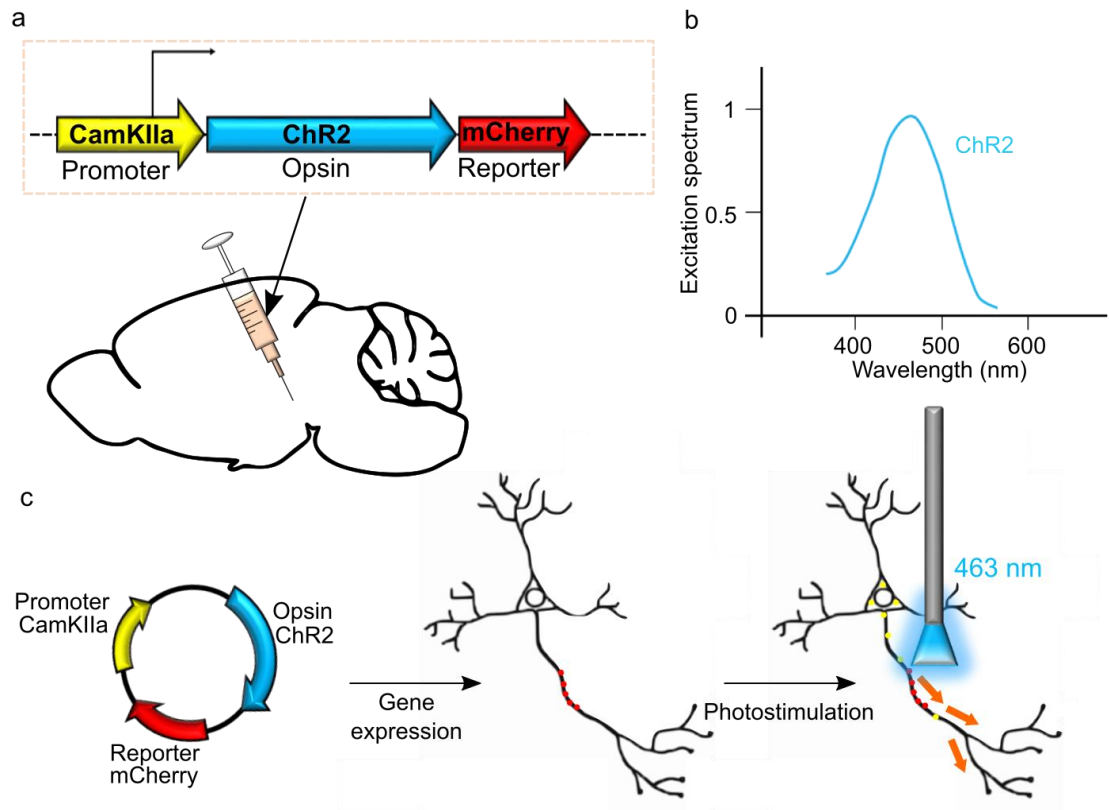


Figure 1.6: Illustration of opsin expression through AAV injection

a) Representation of a viral-vector for ChR2 opsin, with CaMKII α promoter for excitatory neurons and mCherry reporter for histological validation. **b)** The excitation spectrum of ChR2, with peak at 460-480 nm. **c)** AAV including ChR2 opsin is injected in a specific brain region; photostimulation with a specific wavelength results in stimulation-dependent depolarisation of ChR2-positive neurons. CaMKII α : calmodulin-dependent protein kinase II; ChR2: channelrhodopsin-2.

1.8.1 Optogenetics in AD

Prolonged stimulation of the perforant pathway by means of SSFO activation has been shown to produce a 2.5 fold increase in A β accumulation in the DGmol compared to the contralateral side of an APP mouse model for AD-like pathology (Yamamoto et al., 2015). Moreover, A β secretion is activity-dependent, as seen with electrophysiological studies *in vitro* e.g. (Cirrito et al., 2005; Kamenetz et al., 2003). In a study in APP_{SWE}/PS1dE9 mice, low-frequency photostimulation of cortical regions showed a restorative effect on neuronal activity and A β accumulation, highlighting the potential therapeutic use of photostimulation (Kastanenka et al., 2017). Moreover, memory recall

was facilitated through optogenetic stimulation of the ENT in an APP/PS1 mouse model, together with a decrease in DG dendritic spines loss (Roy et al., 2016).

As demonstrated with combined fMRI-electrophysiology in monkeys, the BOLD signal of fMRI is best modelled by changes in LFP rather than action potentials (Logothetis et al., 2001). It is, therefore, the result of a mixed contribution of excitatory and inhibitory neurons, glial cells, etc. and may largely reflect synaptic input activity (Lee et al., 2010). The versatility of fMRI can be further exploited in a preclinical setting by the implementation of stimulus-evoked cellular-specific approaches (Grandjean et al., 2019b). The analysis of whole-brain effects, derived from the optogenetically-driven activity of a specific neuronal population in a brain region, represents the next attractive approach to infer a temporal causality in the cascade of events in brain disease. This can be accomplished by combining optogenetically-induced neuromodulation with fMRI recordings (ofMRI; Albers et al., 2018; Desai et al., 2011). Very recently, optimised protocols for ofMRI have been applied for psychopathologies (Grandjean et al., 2019b). There is, however, a lack of application of ofMRI in AD.

1.9 Electrophysiology

1.9.1 Fundamentals of electrophysiology

Resting state fMRI and ofMRI can be employed to investigate brain changes between healthy and diseased states. One common limitation, however, is the lack of access to direct neuronal activity, i.e., both techniques are based on the BOLD readout, which provides an indirect measure of neuronal activity. Moreover, in the past few decades, most of our understanding of the mechanisms that underlie information transmission and processing in the brain was accomplished through invasive experimental procedures in rodent brains, e.g., electrophysiology *in vivo*. The mechanisms for

information processing in the brain ultimately rely on chemo-electric signal exchange between cells, i.e., action potential propagation, which is based on the sudden change of the electrical potential of a cell which may or may not cause the subsequent depolarisation of a neighbouring cell and, in most cases, chemical synaptic transmission (Buzsáki et al., 2012). Electrophysiology in rodents offers an attractive approach to investigate the electrical properties of single cells and organised circuits in a confined volume (*in vitro* slice electrophysiology) or embedded in the whole brain circuitry (electrophysiology *in vivo*; Buzsáki, 2006; Csicsvari et al., 2003; Henze et al., 2000; Klausberger et al., 2003).

The recording of electrical changes, particularly subthreshold, from a single neuron is most easily accomplished *in vitro*, as the slice format facilitates this methodology. The flow of ions across the cell membrane is recorded from the intracellular level, by disrupting the cellular membrane with a pipette filled with intracellular media (Buzsáki, 2006). Conversely, recordings *in vivo* are mostly undertaken with electrodes placed extracellularly, either as single- or multi-unit Activity (SUA/MUA) or as recordings of Local Field Potential (LFP). Briefly, unit recordings are based on recording of high-frequency voltage ($> 200\text{Hz}$) fluctuations and result in the measurement of the spiking discharge of one or a group of neurons in a specific brain volume. LFP recordings, instead, are based on lower frequencies ($< 200\text{Hz}$) and represent the overall sum of excitatory and inhibitory synaptic activity of a group of neurons (Burns et al., 2010).

One of the advantages of analysing LFP is related to the slower trend of changes in a neuronal population, compared to the rapid excitatory/inhibitory events measured in single neurons, which can result in an annihilation of the signals due to fast asynchrony. The currents recorded with LFP represent slow changes in the overall activity of the targeted extracellular space and will be described as field excitatory postsynaptic potentials (fEPSPs) or field inhibitory postsynaptic potentials (fIPSPs). Interestingly, research using

blood oxygenation-level dependent (BOLD) signal of fMRI (described in later sections) and electrophysiological recordings in monkeys has highlighted that BOLD signal is best described by the course of the LFP rather than single-unit and MUA (Logothetis et al., 2001).

1.9.2 Memory formation

Most of our understanding of the fundamental cellular mechanisms of memory formation comes from electrophysiological recordings performed on animal models. On a physiological level, it is well-established that memory formation and consolidation require changes in synaptic connectivity strength between neurons (Bliss and Collingridge, 1993). Both long-term and short-term synaptic potentiation (LTP and STP, respectively), whilst laboratory phenomena, are mechanisms that share many characteristics with memory formation (Morris et al., 2003). LTP and STP are based on synaptic efficacy changes over different timescales, yet they can be elicited through different cellular pathways (Lamprecht and LeDoux, 2004; Larsen and Jesper Sjöström, 2015). LTP is induced by the application of high-frequency stimulation to a presynaptic target, which leads to a sustained synaptic transmission between pre and postsynaptic neurons (Magee, 1997).

In a classical glutamatergic synapse, rapid and persistent presynaptic glutamate release causes prolonged depolarisation of the postsynaptic membrane, via AMPA (α -amino-3-hydroxy-5-methyl-4-isoxazolepropionic acid) receptor-dependent excitatory postsynaptic currents, resulting in the removal of the magnesium block of N-methyl-D-aspartate (NMDA) receptors. The opening of NMDA receptors allows calcium ion (Ca^{2+}) influx into the postsynaptic cell, ultimately resulting in the short-term phosphorylation of AMPA receptors to increase their conductance together with longer-term up-regulation of AMPA receptor trafficking to the postsynaptic membrane.

There is also evidence that this process results in the presynaptic release of a retrograde transmitter (e.g., nitric oxide) to increase presynaptic glutamate release (Li et al., 2002; Neitz et al., 2011).

Overall, this augmented glutamatergic neurotransmission strength represents a memory for the induction event that persists for hours to months to a lifetime (Bliss and Collingridge, 1993; Bliss and Lomo, 1973; Segal, 2010). As such, LTP is thought to be both a presynaptic and postsynaptic phenomenon. Conversely, STP is induced in response to presynaptic paired-pulse stimulation (PPS) and its duration is tightly linked to the length of the stimulus event (typically less than 1 second); as such STP is thought to be a presynaptic phenomenon, being related to the presynaptic release of neurotransmitters (Shen, 1989).

When a presynaptic neuron is stimulated with a pair of pulses in short sequence, if the presynaptic Ca^{2+} entry, derived from presynaptic depolarisation to the first stimulus (P1), is not entirely buffered away before the arrival of the second stimulus (P2), there is an increase in the release of the presynaptic neurotransmitter to P2 due to a larger Ca^{2+} pulse (combination of residual Ca^{2+} to P1 plus Ca^{2+} entry to P2), resulting in a paired-pulse facilitation (PPF) of the second response compared to the first one (Wu and Saggau, 1994; Zucker, 1989). Thus, STP is purely a presynaptic phenomenon.

1.9.3 Neuronal Changes in AD Models

PPF has been widely investigated in the hippocampal formation *in vitro*, but there are limited studies investigating this form of synaptic plasticity in AD models, particularly with electrophysiological recordings *in vivo*. As mentioned above, early intracellular A β accumulation is correlated with an alteration of synaptic communication (Billings et al., 2005; Davis et al., 2014; Klyubin et al., 2012; Oddo et al., 2003). Interesting results come

from recent electrophysiological studies on transgenic mouse models, where increased excitability is found in hippocampal regions of human-APP (hAPP) mice, probably due to increased presynaptic, A β -modulated, transmitter release *in vivo* (Palop et al., 2007). Moreover, epileptiform activity was found in APdE9 mice (harbouring hAPP_{SWE} and PS1dE9 mutations) for AD, again suggesting neuronal hyperactivity in AD-like pathology (Ziyatdinova et al., 2011). *In vivo* LFP recordings in Tg2576 (Cirrito et al., 2008, 2005) and APP_{SWE} (Kamenetz et al., 2003) models for AD show that A β production is highly correlated with synaptic activity (i.e., activity-dependent), bringing supporting evidence for a crucial role of neuronal activity in A β deposition.

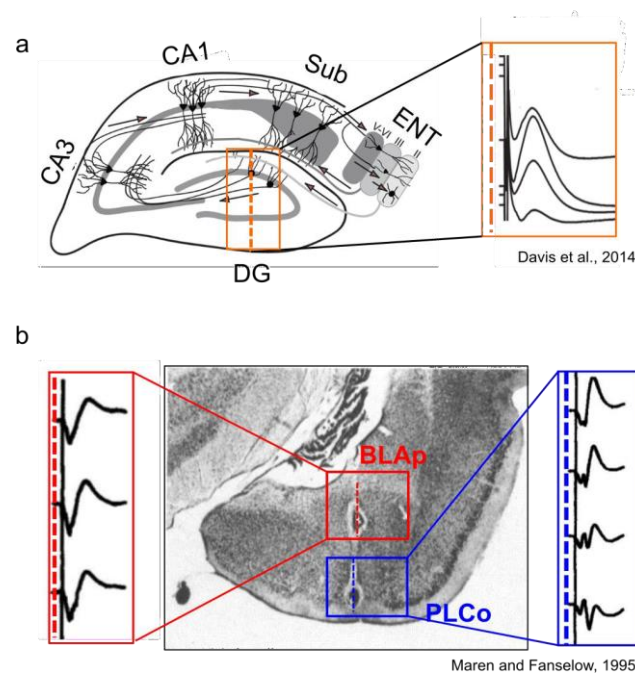


Figure 1.7: fEPSP responses in DG and BLA following stimulation of the subiculum

a) schematics of the hippocampal formation connections; fEPSP recordings of the DG in control mice following perforant path stimulation show a predominant positive-going response; images adapted from (Davis et al., 2014). **b)** histological evidence and representation of recordings along the amygdala region at sequential depths show evoked responses in BLA and PLCo (red and blue sections respectively) in the rat brain. A fast negative-going event is seen firstly in the BLA, whereas, the more ventral PLCo shows a more complex response profile; image adapted from (Maren and Fanselow, 1995). PLCo: posterolateral cortical nucleus; BLA: basolateral amygdala; DG: dentate gyrus; fEPSP: field excitatory postsynaptic potential.

In 3xTgAD mouse, electrophysiology shows evidence for hyperexcitability at a very young age *in vitro* (Kazim et al., 2017). Additionally, electrophysiological studies in the 3xTgAD mouse model show hyperexcitability via PPF changes in CA1 and DG, before plaque formation, *in vivo* (Davis et al., 2014; Oddo et al., 2003). The electrophysiological properties of the dorsal DG have been assessed at 4-6 and 9 months of age in controls and 3xTgAD mouse model *in vivo* (Davis et al., 2014). The cyto-organisation in layers of the DG results in an open field response profile, highlighting a well-structured laminar response, with a positive-going fEPSP response reversal following stimulation of the perforant path (**Figure 1.7a**).

To date, there is a relatively dense body of research on the hippocampal formation circuitry (predominantly *in vitro*); little is known, instead, about the electrophysiological properties of the BLA in mouse models of AD. Given its densely packed cytoarchitecture, fEPSP recordings in the BLA *in vivo* have been reported in line with the characteristics of a closed field (**Figure 1.7b**; Maren and Fanselow, 1995) in healthy control rats. In this pioneering work, the profile response of the BLA to stimulation of the subiculum shows a very fast negative event (fEPSP), followed by a slow positive-going overshoot (presumed feed-forward IPSP). Moreover, recordings from other amygdala nuclei, e.g. the posterolateral cortical nucleus (PLCo), show a sequential depth response profile, highlighting the heterogeneity of the amygdaloid area (**Figure 1.7b**).

To date, no electrophysiological recordings have been investigated in the BLA and DG following stimulation of ENT1, thus these ROIs will be the focus of the electrophysiological part of this work.

1.10 Anaesthesia

In animal research, there are several factors that lead to the almost indispensable use of anaesthetic agents. In the case of invasive procedures, anaesthetic agents are used to elicit unconsciousness and minimise pain and distress associated with electrophysiological recordings in a stereotaxic frame. In the case of neuroimaging such as rsfMRI, besides minimising animal distress, anaesthetic agents may help to exclude confounding signals arising from motion, breathing, heartbeat and to minimise stress-related changes which may affect FC readings (Clement et al., 2008; Grandjean et al., 2014a). If, on the one hand, the employment of anaesthesia is advantageous to experiments, on the other hand, it affects neuronal activity and, thus, the nature of recordings and their interpretation.

It is widely accepted that differences in the pharmacological action of common anaesthetics may produce a corresponding range of effects in the brain (Grandjean et al., 2014a). The results obtained with different anaesthetic regimes cannot be readily compared; indeed, the influence of different anaesthetics on brain activity must be taken into account for a proper interpretation of the results. In different experimental techniques, some anaesthetics are preferred over others, due to the experimental design (Gargiulo et al., 2012). For example, in electrophysiological recordings performed *in vivo*, one of the most commonly adopted anaesthetics is urethane (ethyl carbamate). Urethane is popular as it is thought to reliably mimic a brain state close to physiological sleep (Clement et al., 2008). It has a long-lasting effect (non-recovery) and influences GABAergic transmission only marginally; moreover, it is thought not to affect the respiratory system and to preserve spinal reflexes during surgery (Maggi and Meli, 1986; Soma, 1983). Although largely used in acute experimental conditions, urethane induces progressive cytotoxicity: it is nowadays adopted in experimental designs where recovery is not planned.

In rodent fMRI, research has shown that a variety of anaesthetic regimes result in a similar distribution of common RSNs in the mouse brain (Gozzi and Schwarz, 2016; Grandjean et al., 2019a).

However, different anaesthetics result in variations of FC measurements across the brain, due to their diverse pharmacological pathways. Urethane and isoflurane have been shown to affect striatal FC but preserve cortical and thalamocortical connectivity (Grandjean et al., 2014a; Schwinn et al., 1990). Isoflurane, largely used in imaging studies, has vasodilation properties and targets GABAergic transmission; it allows, however, to a prompt recovery of consciousness soon after cessation of administration, which makes it versatile and low risk. Medetomidine, another widely used anaesthetic, promotes vasoconstriction and subsequent suppression of cortical regions but not striatal areas (Grandjean et al., 2014a). Therefore, a combination of medetomidine at low dose (mixed with a paralytic agent to minimise animal motion) with low dose of isoflurane is thought to affect the brain minimally, thus allowing a state close to waking, to detect cortical and subcortical signal, and the reliable identification of the common RSNs identified in the mouse brain at rest (Grandjean et al., 2014a; Zerbi et al., 2015). Furthermore, one of the most common side-effects of anaesthetics in animal experiments is the risk of hypothermia; in experiments with anaesthetised mice, both in stereotaxic frame or in an MRI-compatible cradle, care must be taken to compensate for heat loss by providing external, homeothermic-regulated heating through a heating pad or cradle (Caro et al., 2013).

1.11 The present work

From the research conducted so far, both on humans and mouse models for AD-like pathology, the pivotal role of the ENT1, in the early stages of AD, emerges. Research on animal models, designed to mimic human pathologies, allows us to obtain information from the neuronal micro-scale to the whole-brain macro-scale, as both invasive and non-invasive approaches can be adopted. The general aim of this project is, therefore, to rely on the advantages of several techniques to investigate brain changes in the early stages of AD-like pathology in a mouse model.

The integration of information gained across different scales will help in overcoming the unavoidable limitations of each technique if used in isolation.

Therefore, the experimental programme focused on:

- 1) rsfMRI to provide a non-invasive, brain-wide measure of the network organisation in the healthy and diseased state, although its signature is not a direct measure of the underlying neuronal activity;
- 2) optogenetics to manipulate the activity of a specific neuronal population in a determined region, in combination with fMRI to investigate the haemodynamic response of the whole brain following the initial stimulation of a functionally and spatially defined neuronal population;
- 3) *in vivo* electrophysiology to provide information about neuronal connectivity changes emerging in pathology, although limited regions can be investigated and the signal recorded is not cell-specific.

In this work, I hypothesised that the neuronal hyperexcitability of ENT1 affects its postsynaptic targets and results in a global network excitatory-inhibitory imbalance in the early stages of AD-like pathology in the 3xTg mouse model for AD. In order to assess

early events in pathology progression, the two time-points of 3 and 6 months of age were investigated throughout the work.

The specific aims were to measure:

Brain-wide functional changes within, and relative to, the ENTl during the resting-state, by performing rsfMRI on 3xTgAD and control animals longitudinally at 3 and 6 months of age.

Whole-brain response with fMRI, following photostimulation of light-sensitive excitatory neurons within the ENTl of 3xTgAD and age-matched control mice. This will also be conducted longitudinally, on a second cohort, at 3 and 6 months of age.

Synaptic changes in the early stages of AD-like pathology in the downstream targets of the lateral entorhinal cortex. This will be accomplished through the assessment of synaptic short-term plasticity and functional connectivity between (i) ENTl and DG and (ii) ENTl and BLA through electrophysiological recordings *in vivo*.

~ Chapter 2 ~

General Methods

All the *in vivo* electrophysiological experiments described in this thesis were conducted at the University of Manchester between September 2015 and October 2016; the fMRI experiments (rsfMRI and ofMRI) were carried out in Singapore at the Singapore Bioimaging Consortium (SBIC) A*STAR between January 2017 and June 2019.

2.1 Animals

Experiments were conducted on male 129sv/c57bl6 (controls) and 3xTgAD mouse model for Alzheimer's disease on the same genetic background, where the original breeding pairs were donated by the LaFerla lab (University of California, USA; Oddo et al., 2003). The mouse model is a triple-transgenic, carrying the human familial AD transgenes for APP, Swedish mutation (APP_{SWE}), PS1_{M146V} mutation and the P301L mutation for tau from frontotemporal dementia. 3xTgAD mice are born pathology-free and start to develop cognitive deficits around 4 months of age (Clinton et al., 2007). Therefore, all experiments conducted in this thesis refer to 3 and 6 months of age time-points, as these timepoints provide a good window to investigate prodromal pathology development (Davis et al., 2014; Mastrangelo and Bowers, 2008).

All procedures conducted in the UK were performed in accordance with the UK Animals (Scientific Procedures) Act 1986 and the University of Manchester Ethical Review Panel under Home Office license PPL 70/7843. All experiments performed in Singapore Bioimaging Consortium, A*STAR, Singapore, were in accordance with the ethical standards of the Institutional Animal Care and Use Committee (A*STAR Biological Resource Centre, Singapore, IACUC #171203).

In both locations, the 3xTgAD and the control colonies were maintained ‘in-house’ through the pairing of homozygous individuals. Mice were housed in cages of up to five, with same-sex and genotype cage-mates in a pathogen-free environment, kept at a 45-65% humidity, under a 12:12-hour light-dark cycle and room temperature, with ad-libitum access to food and water.

2.2 fMRI

Data collection for the fMRI part was done at Singapore Bioimaging Consortium (SBIC, A*STAR). BOLD measures of fMRI were performed in rsfMRI experiments and fMRI combined with optogenetics (ofMRI) experiments. Within the rsfMRI experiments, male controls (total N = 10) and 3xTgAD (total N = 19) were used for all the experiments. Specifically, a cohort of controls and 3xTgAD mice underwent a rsfMRI imaging session at 3 months of age ($N_{\text{controls}} = 10$ and $N_{3\text{xTgAD}} = 19$) and then at 6 months of age ($N_{\text{controls}} = 10$ and $N_{3\text{xTgAD}} = 13$).

For ofMRI experiments, a pilot group of $N_{\text{controls}} = 25$ mice were first used to optimise stereotaxic surgery procedures and successful injection and expression of AAV for Channelrhodopsin in the ENTl. Once faithful and reproducible results were obtained, a cohort of controls (N = 10) and 3xTgAD (N = 12) mice underwent optogenetic surgery for opsin transfection at 2 months of age, combined with optic fibre implant after which ofMRI sessions followed at 3 months of age and 6 months of age ($N_{\text{controls}} = 8$ and $N_{3\text{xTgAD}} = 10$). Additionally, one cohort of controls (N = 9) underwent optogenetic surgery with an injection of mCherry (no opsin), combined with optic fibre implant and subsequent ofMRI session at 3 months of age, as a control experiment.

2.2.1 fMRI signal

The signature of functional MRI (BOLD, CBV or CBF) describes changes in the hemodynamic response of the brain. There are techniques that allow us to gain more specific information about the neuronal response, for example, manganese-enhanced fMRI; however, due to the lack of sensitivity, they have been sparsely used and CBV, CBF and BOLD represent the most commonly adopted fMRI readouts (Lin and Koretsky, 1997; Silva, 2012). The BOLD signal is based on the coupling of the vascular response of the brain with the underlying neuronal changes, CBV measures the amount of blood present in a given volume and CBF measures the blood supply in a given time window (Buxton, 2012). CBV, with the injection of iron-oxide-based compounds for contrast enhancement, represents a more sensitive measure of the hemodynamic response of the brain compared to BOLD, particularly at lower magnetic fields (Mandeville et al., 2004). However, due to its non-invasiveness, the BOLD signal is the most widely used fMRI readout to investigate the healthy and diseased brain. Therefore, in this work, thanks to the adoption of an ultra-high magnetic field and in order to minimize invasiveness, BOLD signal was adopted throughout the experiments.

2.2.2 BOLD signal-to-noise

Compared to the much larger human brain, functional imaging of the mouse brain requires higher spatial resolution, in order to distinguish anatomical structures and to map onto them the relative changes of the haemodynamic response of the different brain regions. Thus, a crucial requirement for imaging the small rodent brain is a high signal-to-noise ratio (SNR), which results in enhanced sensitivity to detect BOLD fluctuations (Baltes et al., 2010). As mentioned earlier, increasing the static magnetic field, B_0 , represents one strategy to enhance BOLD fMRI sensitivity in rodents (Gati et al., 1997).

Moreover, a significant enhancement of sensitivity can be accomplished by minimising the amount of noise affecting the signal. Specifically, one of the main forms of noise influencing the BOLD fMRI signal is thermal noise derived by the coils within the system. By using cryogenic probes, a substantial increase in SNR has been reported (Darrasse and Ginefri, 2003). Therefore, for the rsfMRI experiments in this project, a cryogenic receiver surface coil (2x2 phased-array receiver only coil), provided with a liquid helium cooling system, was adopted.

Due to the constraints caused by the fibre optic implant, a room temperature single-loop surface coil was used for the ofMRI experimental mice imaging sessions. Another primary source of noise in fMRI signal derives from animal motion and physiological changes, e.g., heart and respiration rates (Grandjean et al., 2014a). To address this, an anaesthesia protocol that included a paralytic agent, to minimize animal motion and physiological changes, was adopted as described below.

2.2.3 Animal preparation for imaging

Animal preparation followed (Grandjean et al., 2014a) for both rsfMRI and ofMRI experiments. Anaesthesia was induced with 4% isoflurane; subsequently, animals were endotracheally intubated, placed on an MRI-compatible cradle and artificially ventilated (90 breaths/minute; Kent Scientific Corporation, Torrington, Connecticut, USA). A bolus with a mixture of medetomidine (Dormitor, Elanco, Greenfield, Indiana, USA) and Pancuronium Bromide (muscle relaxant, Sigma-Aldrich Pte Ltd, Singapore) was administered subcutaneously (0.05 mg/kg), followed by a maintenance infusion (0.1 mg/kg/hr) administered 5 minutes later while isoflurane was simultaneously reduced and then kept at 0.5%. Functional MRI was acquired 20 min following maintenance infusion

onset to allow for the animal state to stabilize. Care was taken to maintain the temperature of the animals at 37°C.

2.2.4 RsfMRI and ofMRI: data acquisition

Data were acquired on an 11.75 T scanner (Bruker BioSpin MRI, Ettlingen, Germany) equipped with a BGA-S gradient system, a 72 mm linear volume resonator coil for transmission. A 2×2 phased-array cryogenic surface receiver coil was adopted for the rsfMRI experiment (N = 29), whereas the surface coil for ofMRI (N = 31) experiments was substituted with a 10 mm single loop surface coil.

For rsfMRI data acquisition, an anatomical reference scan was acquired using a spin-echo turboRARE sequence: field of view (FOV) = 17×9 mm², FOV saturation slice masking non-brain regions, number of slices = 28, slice thickness = 0.35, slice gap = 0.05 mm, matrix dimension (MD) = 200×100, repetition time (TR) = 2750 ms, echo time (TE) = 30 ms, RARE factor = 8, number of averages = 2. Functional scans were acquired using a gradient-echo echo-planar imaging (EPI) sequence with the same geometry as the anatomical: MD = 90×60, TR = 1000 ms, TE = 15 ms, flip angle = 50°, volumes = 600, bandwidth = 250 kHz.

Parameters for ofMRI data acquisition were adapted to the lower sensitivity of the room temperature receiver coil. The anatomical reference scan was acquired using FOV = 20×10 mm², number of slices = 34, slice thickness = 0.35, slice gap = 0 mm, MD = 200 × 100, TR = 2000 ms, TE = 22.5 ms, RARE factor = 8, number of averages = 2. Functional scans were acquired using FOV = 17×9 mm², FOV saturation slice masking non-brain regions, number of slices = 21, slice thickness = 0.45, slice gap = 0.05 mm, MD = 60 x 30, TR = 1000 ms, TE = 11.7 ms, flip angle = 50°, volumes = 720, bandwidth = 119047 Hz.

Field inhomogeneity was corrected using MAPSHIM protocol. Images were acquired using Paravision 6.0.1 software.

2.2.5 RsfMRI and ofMRI: data pre-processing

Images were processed using a protocol optimized for the mouse. Images were corrected for spikes (*3dDespike*, *AFNI*; Cox, 1996), motion (*mcflirt*, *FSL*; Smith et al., 2004), and B₁ field inhomogeneity (*fast*). Automatic brain masking was carried out on the EPI using *bet*, following smoothing with a 0.3 mm² kernel (*susan*), and a 0.01 Hz high-pass filter (*fslmaths*).

Nuisance regression was performed using FIX (FMRIB's -Functional MRI of the Brain-ICA-based -Independent Component Analysis-~~X~~noiseifier; Zerbi et al., 2015): FIX is an approach based on the fragmentation of the time-series into independent components and the subsequent classification of the components into true signal and noise; by training a classifier, it is then possible to remove only the noise components from the true signal. Illustrated below an example of noise (**Figure 2.1a,c**) and an example of true signal (**Figure 2.1b,d**) in relation to the ofMRI dataset. Separate classifiers were generated for rsfMRI and ofMRI.

The EPIs were registered to the Allen Institute for Brain Science (AIBS) reference template ccfv3 using SyN diffeomorphic image registration (*antsIntroduction.sh*, *ANTs*; Avants et al., 2009).

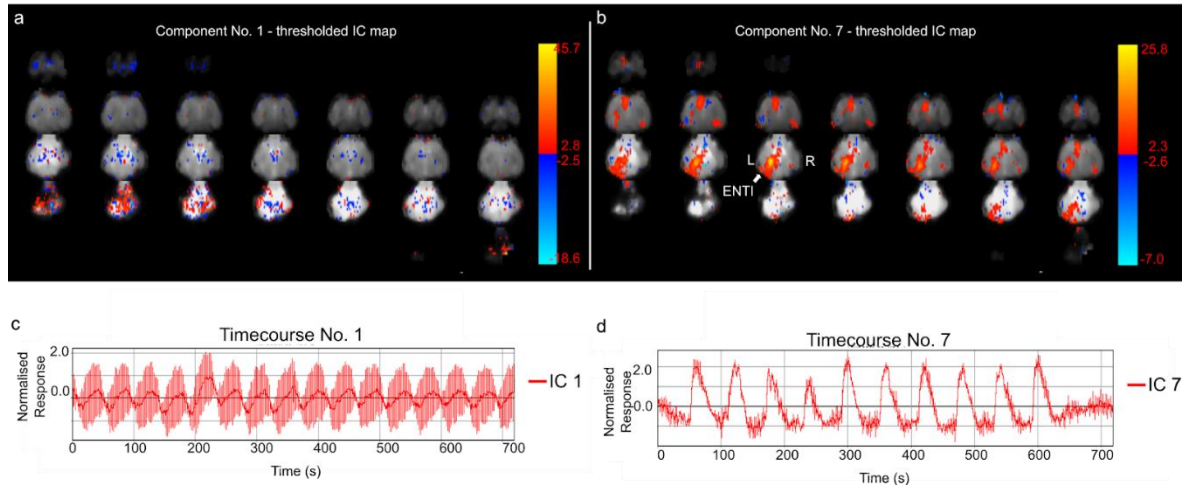


Figure 2.1: Example of ICA components to train a classifier for FIX

Fragmentation of the time courses into multiple components allows to distinguish noise **(a)** from true signal **(b)**. The visualisation of the signal over time allows to detect noisy signal **(c)** from BOLD response relative to optogenetic stimulation **(d)**.

2.2.6 RsfMRI: data analysis

By being estimated in a paradigm-free setting, resting-state FC is based on intrinsic models of connectivity; as such, many approaches can be used to analyse it, by adopting a data-driven or hypothesis-driven approach. A few examples are outlined below.

Seed-Based Analysis

Seed-based analysis (SBA) is one of the most commonly adopted hypothesis-driven approaches. A ROI (seed) is first selected, often a result of a manually-drawn cluster of voxels, and its averaged time course is correlated with voxels across the brain, resulting in a connectivity map in relation to the selected ROI (Pawela et al., 2008; Sforazzini et al., 2014a; Zerbi et al., 2015).

Independent Component Analysis

ICA is another widely adopted approach (Hutchison et al., 2010; Sforazzini et al., 2014). Unlike SBA, ICA is a data-driven, hypothesis-free method to investigate connectivity networks across the brain. Through ICA, the time course is divided into separate components, identifying statistically-independent networks. With ICA it is crucial to carefully consider the number of components to use, as some RSNs could be fragmented if a high number of components is adopted (Sforazzini et al., 2014). To facilitate the selection of ICA components, guidelines with inclusion/exclusion general criteria have been outlined recently for the mouse brain (Zerbi et al., 2015).

Regional Homogeneity analysis

Regional homogeneity (ReHo) is a low-parameter method that is increasingly being adopted to study local FC changes. In this thesis, local connectivity was assessed with ReHo (*3dReHo*; Wu et al., 2017; Zang et al., 2004). ReHo does not provide information on distal connections (Zang et al., 2004) but rather allows inference about local connectivity changes; it is relatively simple to interpret and has been applied successfully into resting-state FC using rodents and higher animal models (Li et al., 2018; Rao et al., 2017; Wu et al., 2017). ReHo is often used to measure changes in the local functional connectivity of the brain at rest, in that it measures the temporal correlation between one voxel and its neighbours. The coefficient W describes ReHo values ranging from 0 to 1, where higher value represents a higher correlation across two voxels.

The formula for obtaining W coefficients is described below (1).

(1)

$$W = \frac{\sum(R_i)^2 - n(\bar{R})^2}{\frac{1}{12}K^2(n^3 - n)}$$

The parameter W for ReHo values is, therefore, described by the sum rank of the i th time-point (R_i), the number of time-series within a cluster (K), the mean across them (\bar{R}) and the number of ranks (n). ReHo is a hypothesis-free, data-driven and non-user biased approach that provides information on local FC changes (Zang et al., 2004).

Whole-Brain network analysis & pair-wise analysis

A method to analyse resting-state FC across the whole brain is based on establishing the correlation of pairs of ROIs across brain regions, as defined through the brain atlas. The lines in the matrix resulting from this analysis show the correlation of a single ROI with all the other ROIs in each line. Here, a whole-brain network analysis was carried out to infer FC over spatially distinct brain regions.

Besides carrying out a ReHo analysis to assess local FC changes, and whole-brain network analysis to infer on brain-wide FC, a hypothesis-driven approach was then adopted to further investigate the rsfMRI data, in order to assess FC in the diseased brain, in relation to the ROI ENTl. Therefore, although ReHo analysis is crucial to determine local changes in FC, graph theoretical approaches reveal whole-brain functional network changes by analysing the pair-wise correlation of resting-state FC between spatially distinct brain regions (Bullmore and Sporns, 2009; Sanz-Arigita et al., 2010). According to the graph theory of network analysis, a functional network is characterised by multiple nodes interconnected by edges. Pair-wise ROI analysis was carried out with respect to ROIs defined in the AIBS atlas. Time series extracted with the atlas were cross-correlated to the time series from the ENTl using Pearson's correlation.

2.2.7 OfMRI: optogenetic surgery

In order to investigate the embedding of ENTl functional changes within the whole brain, light pulse stimulation of pyramidal neurons in the ENTl, by means of optogenetics was combined with the fMRI BOLD readout. Optogenetics is based on the dynamic control of a genetically-defined group of neurons (Deisseroth, 2011; Lee et al., 2010). By injection of an adeno-associated viral vector (AAV) containing the sequence for opsin and a neuronal-type specific promoter, a specific neuronal population is transfected for the expression of a light-gated ion channel. In this project, ENTl was transfected with the Channelrhodopsin-2 (ChR2; Nagel et al., 2003) opsin including a CaMKII α promoter for excitatory neurons (Nathanson et al., 2009). Transfected neurons express light-gated cation channels (Na⁺) sensitive to a specific wavelength (473 nm) of light, which results in the opening of the ion channels with subsequent depolarization of the membrane (**Figure 2.2**). Male controls (N = 25 pilot with ChR2-mCherry, N = 10 experimental ChR2-mCherry, and N = 9 controls with no opsin expression, only mCherry) and 3xTgAD (N = 12) mice (~30 g) were anaesthetised with Ketamine/Xylazine mixture (Ketamine 75 mg/kg, Xylazine 10 mg/kg).

The head was shaved and cleaned with three wipes of Betadine® and ethanol (70%) and lidocaine (1-8 mg/kg) was administered subcutaneously *in situ*. Each animal was kept on a homoeothermic heating pad to prevent hypothermia, the head was positioned in a stereotaxic frame and protective ophthalmic gel was applied to each eye to avoid dryness. A portion of the skin from the scalp was removed to expose the skull. Perforation of the skull was performed with a hand-held surgical drill (drill bit tip Ø 0.9 mm²) to create a small craniotomy -2.8 mm from bregma and +4.2 mm left from the middle line. Virus

injection was carried through the craniotomy at -2.8 to -2.7 mm from the brain surface and the cannula tip position was adjusted to -2.6 mm from the surface.

Coordinates were taken from the Paxinos mouse brain atlas (Paxinos and Franklin, 2004). An injection of adeno-associated virus (AAV) was performed in the target location through a precision pump (KD Scientific Inc., Harvard Bioscience) with a 10 μ l NanoFil syringe and 33-gauge beveled needle (NF33BV-2). The AAVs used (AAV5-CaMKII α -hChR2 (H134R)-mCherry, AAV5-CaMKII α -mCherry, titer $1-8 \times 10^{12}$ vg/ml) were acquired from Vector Core at the University of North Carolina (USA). A volume of 0.75 μ l of the viral vector was injected in each mouse at a rate of 0.15 μ l/min. The needle was kept in location for 10 minutes after the injection was completed, to exclude backflow. After needle extraction, a fibre optic cannula (\varnothing 200 μ m, 0.39 NA, length according to injection site, \varnothing 1.25 mm ceramic ferrule) was lowered to the target region (Laser 21 Pte Ltd, Singapore; Hangzhou Newdoon Technology Co. Ltd, China). The cannula was fixed in place with dental cement (Meliodent rapid repair, Kulzer). Buprenorphine (0.05-0.1 mg/kg) was administered post-surgically to each animal for three days. Animal recovery took place on a warm pad.

2.2.8 OfMRI: stimulation protocols

Animals underwent the first ofMRI session at least 3 weeks after virus injection. ChR2 stimulation was provided through a blue light laser (473 nm, LaserCentury, Shanghai Laser & Optic Century Co., Ltd) controlled by LabVIEW (National Instruments, USA) using a customised script. The power of the laser, in continuous mode, was 15 mW/mm². Within the pilot study (N = 25), two main stimulation protocols were used to assess the faithfulness of the evoked BOLD response: 40 blocks with 2 s ON and 10 s OFF and 10 blocks of 10 s ON and 50 s OFF (**Figure 2.2c,d,e**).

In both cases, an initial 50 s of baseline was applied. **Figure 2.2** shows an example of two scans using both stimulation protocols: 40 blocks of 2 s stimulation each (**Figure 2.2c**) and 10 blocks of 10 s stimulation (**Figure 2.2d**). The evoked response was faithful to the stimulation protocol in each case (**Figure 2.2e**). As the BOLD signal is characterised by a 1-2 s delay of response to the stimulus, and a 5-6 s dispersion period after the peak of amplitude, the 10 s ON and 50 s OFF protocol was adopted for the experimental work described in Chapter 3 in order to guarantee a complete return to baseline of the BOLD signal (Buxton, 2012). Specifically, after an initial 50 s of rest as a baseline, 10 s of either 5, 10 or 20 Hz light pulses were followed by 50 s rest period in a 10-block design. An additional 50 s of rest was recorded after the last block of stimulation.

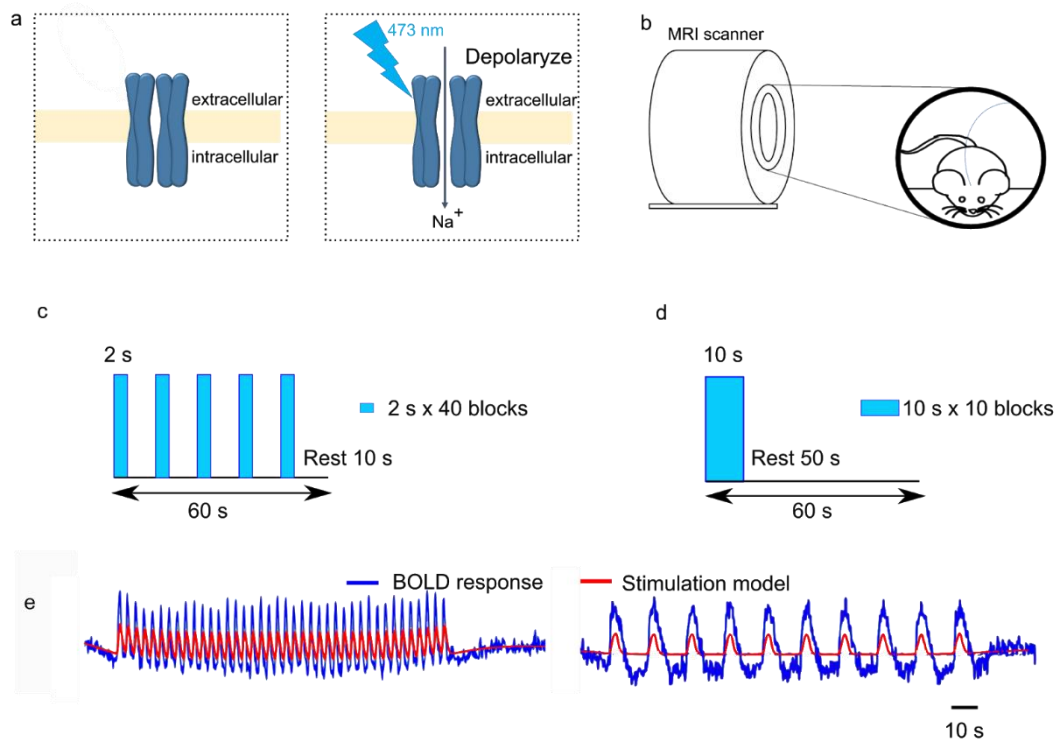


Figure 2.2: Schematics of the principle of optogenetics and combination with fMRI

a) Blue light-activated channelrhodopsin (473 nm) results in neuronal depolarisation following photostimulation. **b)** ofMRI design: the mouse is positioned onto a MRI-compatible cradle, and receives external photostimulation through an optic fibre. **c,d)** Different stimulation designs with 40 blocks of 2 s of stimulation and 10 blocks with 10 seconds of stimulation **(e)** corresponding BOLD responses, left and right respectively.

Experimental and control groups underwent the same imaging protocol, i.e., one resting-state scan followed by randomized 5 Hz, 10 Hz and 20 Hz evoked fMRI scans. Additionally, in order to exclude abnormal behaviour induced by the photostimulation protocol (Weitz et al., 2015), all animals underwent the three stimulation sessions (5 Hz, 10 Hz and 20 Hz) again while awake and freely walking in a behaviour-chamber.

2.2.9 OfMRI: data analysis

Data for the ofMRI experiments was pre-processed identically to the rsfMRI data, as described in section 2.2.5. The ofMRI response was analysed using a general linear model (GLM) framework (*fsl_glm*). The stimulation paradigm and its first derivative were convolved using the default gamma function and used as regressors in the analysis, with motion parameters as covariates.

2.2.10 Statistics and data availability

For both the rsfMRI and ofMRI datasets, descriptive statistics are given as mean difference and 95th confidence interval, unless stated otherwise, and graphically represented as ‘Gardner–Altman plots’ (<https://www.estimationstats.com/>; Ho et al., 2019). If not specified, descriptive statistics are provided for left-hemisphere ROIs. The statistical threshold for significance was set at $p < 0.05$, two-tailed. The voxel-wise analysis was carried out with a non-parametric, permutation-based (5000 permutations) test (*randomize*). Cluster correction was carried out with threshold-free cluster enhancement (tfce). Thresholded t-statistics for one- and two-sample t-tests ($p < 0.05$, tfce corrected) are shown as a colour-coded overlay on the AIBS template. ROI analysis was carried out with a linear mixed model using genotype and age as fixed effects and individual intercepts as

random effects, using *lme4* package (1.1-21) for R (<https://cran.r-project.org/>, 3.5.3, “Great Truth”). Significance was assessed with general linear hypothesis tests implemented in *multcomp* (1.4-10) package and corrected with false discovery rate. Both the rsfMRI and ofMRI datasets are publicly available on <https://openneuro.org/>; **Project IDs: Mouse_rest_3xTG, Mouse_opto_3xTG.**

2.2.11 *Ex vivo* processing

All the *ex vivo* processing of the experimental mice brains has been conducted through external collaboration with staff @ SBIC, A*STAR and the National University of Singapore. Specifically, Dr Sejin Lee and Mr Hangyu Bae in the Neuromodulation and Neurocircuitry group @ SBIC have carried out slice electrophysiology in 8 experimental mice ($N_{\text{controls}} = 4$ and $N_{3\text{xTgAD}} = 4$). Mr Seung Hyun Baek has carried out the immunohistochemistry stainings. Dr Chun-Yao Lee in Neuro Plasticity Group (NPG) @ SBIC has carried out the sliced optogenetics stimulation ($N_{\text{controls}} = 1$ and $N_{3\text{xTgAD}} = 1$). Dr Jasinda Lee @ NUS has carried out ELISA assays.

Patch-clamp recordings for ChR2 expression

Experiments were performed on acute brain slices. Mouse brains were rapidly removed after decapitation and placed in high sucrose ice-cold oxygenated artificial cerebrospinal fluid (ACSF) containing the following (in mM): 230 sucrose, 2.5 KCl, 10 MgSO₄, 0.5 CaCl₂, 26 NaHCO₃, 11 glucose, 1 kynurenic acid, pH 7.3, 95% O₂ and 5% CO₂. Coronal brain slices were cut at a thickness of 250 µm using a vibratome (VT1200S; Leica Biosystems) and immediately transferred to an incubation chamber filled with ACSF containing the following (in mM): 119 NaCl, 2.5 KCl, 1.3 MgCl₂, 2.5 CaCl₂, 1.2 NaH₂PO₄, 26 NaHCO₃, and 11 glucose, pH 7.3, equilibrated with 95% O₂ and 5% CO₂.

Slices were allowed to recover at 32°C for 30 minutes and then maintained at room temperature. Experiments were performed at room temperature.

Whole-cell patch-clamp recordings were performed on CaMKII α -positive ENT1 cells expressing ChR2-mCherry and were visualized using a CCD camera and monitor. Pipettes used for recording were pulled from thin-walled borosilicate glass capillary tubes (length 75 mm, outer diameter 1.5 mm, inner diameter 1.1 mm, WPI) using a DMZ Ziets-Puller (Zeitz).

Patch pipettes (2–4 M Ω) were filled with internal solution containing (in mM): 105 K-gluconate, 30 KCl, 4 MgCl₂, 10 HEPES, 0.3 EGTA, 4 Na-ATP, 0.3 Na-GTP, and 10 Na₂-phosphocreatine (pH 7.3 with KOH; 295 mOsm), for both voltage- and current-clamp recordings. Photostimulation (460 nm) was delivered by LED illumination system (pE-4000). Several trains of square pulses of 20 ms duration with 5, 10, and 20 Hz, were delivered respectively under current-clamp mode ($I = 0$) to examine whether the neurons were able to follow high-frequency photostimulation.

After different frequencies of photostimulation were completed, neurons were shifted to voltage-clamp mode (at -60 mV), and a prolonged square pulse of 500 ms duration was delivered, to further confirm whether ChR2-induced current could be seen on the recording neurons. The access resistance, membrane resistance, and membrane capacitance were consistently monitored during the experiment to ensure the stability and the health of the cell.

Whole-cell current-clamp recordings

After undergoing the scan at 6-months of age 8 mice ($N_{\text{controls}} = 4$, $N_{3\times\text{TgAD}} = 4$) from the ofMRI experimental mice were used for whole-cell patch recording in brain slices. An overdose of Ketamine/Xylazine (0.1 ml/kg) was administered prior to cardiac

perfusion with ice-cold, oxygenated (95% O₂ and 5% CO₂) NMDG-HEPES solution consisting of NMDG 93, KCl 2.5, NaH₂PO₄ 1.2, NaHCO₃ 30, HEPES 20, glucose 25, sodium ascorbate 5, thiourea 2, sodium pyruvate 3, MgSO₄ 10, CaCl₂ 0.5 (in mM, pH 7.3-7.4, 300-310 mOsm). After perfusion, the brain was sliced coronally at 350 µm thickness using a VT-1000 vibratome (Leica, Germany) in ice-cold, oxygenated NMDG-HEPES solution. Brain slices were transferred to pre-warmed NMDG-HEPES solution and recovered for 35 min with constant oxygenation at 37°C. During the recovery, 250, 250, 500, 1000, 2000 µL of 2 M NaCl solution were added at 10, 15, 20, 25 and 30 min, respectively, into 150 ml of the recovery solution.

After recovery, brain slices were placed in HEPES-holding solution consisting NaCl 92, KCl 2.5, NaH₂PO₄ 1.2, NaHCO₃ 30, HEPES 20, glucose 25, sodium ascorbate 5, thiourea 2, sodium pyruvate 3, MgSO₄ 2, CaCl₂ 2 (in mM, pH 7.3-7.4, 300-310 mOsm; Ting et al., 2018) at room temperature. For recording, brain slices were transferred to a recording chamber and perfused with ACSF solution consisting of NaCl 124, KCl 2.5, NaH₂PO₄ 1.2, NaHCO₃ 24, HEPES 5, glucose 12.5, MgSO₄ 2, CaCl₂ 2 (in mM, pH 7.3-7.4, 300-310 mOsm) at room temperature. Recording pipettes were prepared from borosilicate glass pipette using a P-1000 (Sutter instrument, USA) to 4-7 MΩ impedance.

The current clamp recording was performed in infralimbic cortex layer 2/3 and dentate gyrus using recording pipettes filled with an internal solution consisting K-gluconate 130, EGTA 0.1, MgCl₂ 1, HEPES 10, NaCl 5, KCl 11, phosphocreatine 5, Mg-ATP 2, Na-GTP 0.3 (in mM, pH 7.3-7.4, 300-310 mOs). The data were collected and recorded by Multiclamp 700A amplifier (Axon Instruments, USA), Digidata 1550B (Axon Instruments, USA), pCLAMP v10 (Molecular Devices, USA), and HEKA ECP10 USB (HEKA Elektronik, Germany), PatchMaster v2x90.2. Only data that met the criteria (Leakage current, < 100 pA; R-series, <30 MΩ) were used for further analysis.

Neuronal intrinsic properties were analysed using AxoGraph X and statistical analysis conducted using Prism 7.0. The data was plotted by the mean number of action potential with SEM. The statistical significance was presented with asterisks (* $p < 0.05$, ** $p < 0.01$ by Mann-Whitney U test).

Immunohistochemistry

Immunohistochemical analyses were performed as described previously (Baek et al., 2017). Briefly, brains of $N_{\text{controls}} = 3$ controls (3, 6 and 10 months of age) and $N_{3\text{xTgAD}} = 3$ (3, 6 and 10 months of age) were fixed by perfusion with 4% PFA in phosphate buffer saline (PBS) and then in PFA and 30% sucrose for 48 h at 4°C. Fixed brains were cut on a microtome (CM3050S, Leica Microsystems, Nussloch, Germany) as 45 μm -thick sections and collected into a cold cryoprotectant solution (80 mM K_2HPO_4 , 20 mM KH_2PO_4 , 154 mM NaCl, 0.3 g/ml sucrose, 0.01 g/ml polyvinylpyrrolidone, 30% vol/vol ethylene glycol).

Sections were washed 5 times for 3 minutes in 1 x PBS and blocked in 5% FBS with 0.1% Triton X-100 for 1 hour, followed by overnight incubation with the primary antibody in blocking solution at 4°C.

The brain sections were immunostained with primary antibodies against A β (6e10, Covance Research Products Inc Cat #SIG-39300-1000 RRID: AB_10175637) and phospho-tau (AT8 ThermoFisher Scientific, Cat. #MN1020). After the primary antibody binding step sections were washed 5 times in 1 x PBS for 3 min and then incubated with anti-mouse Alexa 488 or anti-rabbit Alexa 594 for 2 hours followed by washing 3 times with 1 x PBS for 3 minutes.

Sections were then mounted with DAPI plus mounting media on slides. All pictures were taken by using a confocal microscope with a 40 \times objective.

ELISA diagnostic assay

Briefly, brains were homogenized in Tris-HCl buffer and agitated for 30 minutes before centrifugation at 6000 g. The supernatant was used for the detection of soluble A β ₄₀₋₄₂ and the pellet was re-suspended in Tris-HCl and 10 μ l was used for further processing for insoluble A β ELISA as recommended by the ELISA kit (incubation with 5 M Guanidine to solubilize any aggregates and diluted before adding into ELISA plates). Samples were diluted only when necessary (phospho-tau and total tau were diluted 2x, no dilution for A β ELISAs). As readings may be affected by how much of the sample was loaded into each well, we normalized ELISA results to protein assay results of the same fraction, hence, the final units are in picogram of A β or tau in per milligram of protein (pg/mg protein).

Ex vivo histology for mCherry expression

After the completion of experiments, animals were injected with an overdose of Ketamine/Xylazine and transcardially perfused with PBS, 0.01 M followed by 4% PFA in 0.01 M PBS. After extraction, the brain was post-fixed in 4% PFA overnight. Brain sections of 50 μ m were cut with a vibratome (VBT1200s, Leica); fluorophore expression, together with Hoechst staining, was checked through a confocal microscope Ti-E; DS-Qi2; Fluorescence, SBIC-Nikon Imaging Center, Singapore) for anatomical confirmation of viral infection and fibre optic cannula positioning.

2.3 *In vivo* electrophysiology

Acute *in vivo* electrophysiology to record electrically-evoked Local Field Potentials (LFP; 0.1 to 200 Hz) was carried out on 3xTgAD mice and age-matched controls to assess functional connectivity (input-output function) and synaptic short-term plasticity (paired-

pulse facilitation) at two age points: 3-4 and 6-7 months of age. Male controls (total N = 11) and 3xTgAD (total N = 10) were used for all experiments. Specifically, $N_{\text{controls}} = 7$ and $N_{3\text{xTgAD}} = 6$ underwent 3 months old time-point experiments. Additionally, $N_{\text{controls}} = 4$ and $N_{3\text{xTgAD}} = 4$ mice underwent 6 months old time-point experiments.

2.3.1 Anaesthesia and surgery

All *in vivo* electrophysiological experiments were conducted using urethane general anaesthesia via single intraperitoneal (i.p.) injection (1.5-1.7 g/kg of urethane as a 30 % w/v solution prepared in 0.9% saline; ethyl carbamate Sigma, UK). An additional dose was administered after 40 minutes in cases of non-complete areflexia (50 μ l of 10 % w/v urethane solution prepared in 0.9 % saline). Body temperature was maintained at 37°C throughout the duration of the whole experiment with the use of a homoeothermic blanket (Harvard, UK) connected to a thermistor placed underneath the abdomen. Once fully anaesthetized mice were mounted and fixed into a stereotaxic frame (Kopf 1430, USA), through the use of ear and mouth bars, prior to surgery. Care was taken to position the skull on a horizontal plane connecting Bregma and Lambda.

For each mouse, in order to expose the skull, a midline incision was made and the scalp retracted. After identifying Bregma and Lambda, the distance between the two landmarks was measured and compared to the standard 4.2 mm reported in the mouse brain atlas (Paxinos and Franklin, 2004). Scaling between the two measurements allowed an adjustment for the coordinates of the craniotomies, in order to improve the accuracy of electrode placement. Craniotomies were drilled over the left hemisphere using a 0.9 mm drill bit (Fine Science Tools, Germany) and a high-speed hand-held drill (Foredom, USA). Care was taken to maintain the brain and the craniotomy sites moist during the whole surgery procedure with sterile saline.

2.3.2 Electrode placement

The skull was marked relative to Bregma and the midline for craniotomies in the left hemisphere above BLA, ENTl and DG (**Table 2.1**). The first recording electrode was lowered 4 mm into the brain to enter BLA at an angle of 15° from vertical in the coronal plane. Then the recording electrode for the DG region was lowered for 4 mm vertically into the brain. Finally, the stimulating electrode was placed in the ENTl region, starting at a depth of 3 mm. The stimulation electrode depth was then adjusted according to the response strength obtained during test 50 ms interval paired-pulse stimulation at 0.33 Hz (**Figure 2.3**).

Table 2.1: Coordinates for electrodes positioning according to Paxinos atlas. AP: anterior-posterior; ML: medio-lateral; DV: dorso-ventral

	BLA	ENTl	DG
AP (mm)	-2.5	-2.8	-3.5
ML (mm)	+2	+4.2	+2.5
DV (mm)	-4	-2.6	-4
Angle (°)	15°	0°	0°

The recording electrodes were 2 x 16 32-contact probes (A2x16-10-100-500-413, NeuroNexus Technologies, MI). Each electrode consisted of 2 shanks, each containing 16 signal recording electrode contacts (numbered 1-16 and 17-32), which will be called ‘channels’ in the rest of the work. The distance between the two shanks was 500 µm, the 16 channels per shank were distributed over 1500 µm of length as the channels were

separated by 100 μm (**Figure 2.3a,b,c**). The area of each recording contact was 413 μm^2 . Recording electrodes were coated in Vibrant CM-DiI (Sigma, UK) cell-labelling solution prior to insertion for their post-mortem localisation by fluorescence microscopy.

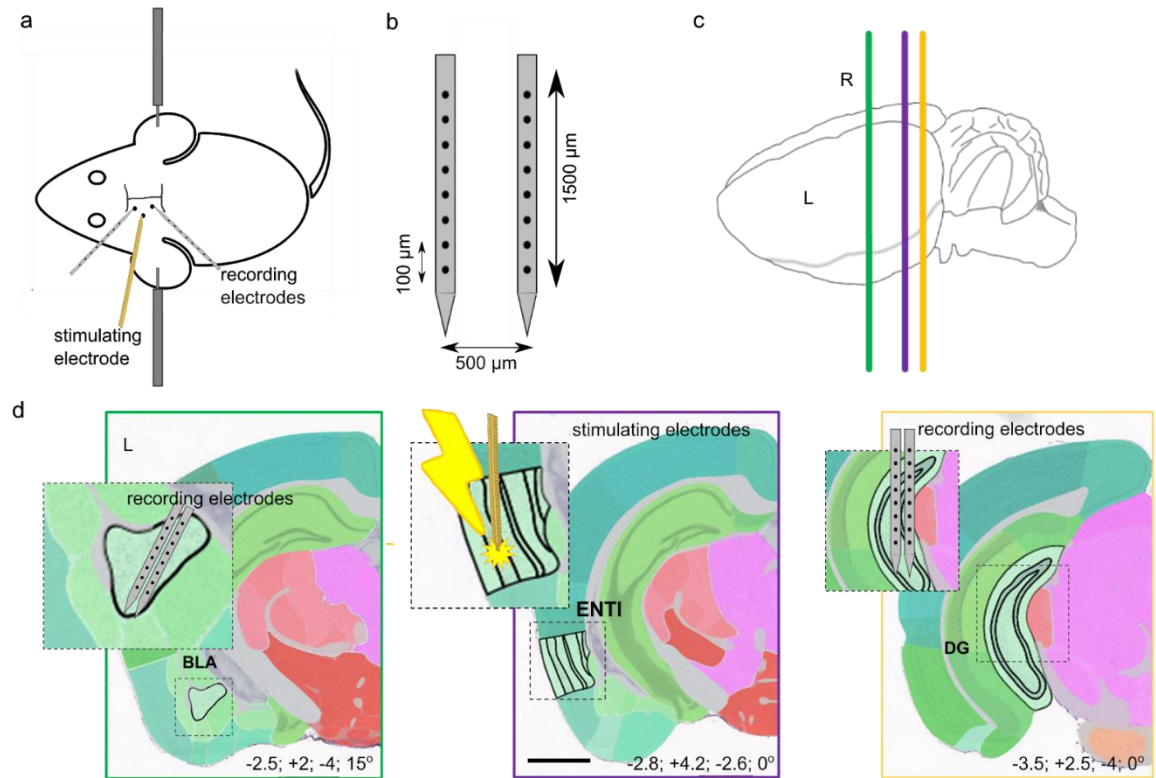


Figure 2.3: schematic for electrodes positioning in BLA, ENTl and DG

a) Setup for *in vivo* electrophysiological recordings in DG and BLA, and stimulation in ENTl in the left hemisphere. **b)** Representation of the Neuronexus 2 x 16 32-contact probes. Distance between the twin shanks = 500 μm , length of each shank 1500 μm , distance across channels = 100 μm . Only 8 of 16 contacts shown for clarity. **c)** Sagittal view of the three ROIs: BLA (green section), ENTl (purple section), DG (yellow section). **d)** Coronal sections of the ROIs: diagram to show target locations for recording electrodes in BLA, and DG (left and right panels) and stimulating electrode in ENTl (middle panel). Coordinates per each location are given in mm in each panel as anterior-posterior; medio-lateral; dorso-ventral; angle of the electrode. scale bar: 1000 μm

The electrodes were used to record evoked responses during electrical stimulation patterns. Graphics for electrodes position is shown in **Figure 2.3d** and histological evidence for the final placement of the recording electrodes and stimulating electrode are

shown in **Figure 2.4**. A bipolar stimulating electrode (twisted 125 μ m diameter Teflon-insulated stainless-steel wires; Advent RM, UK) was positioned at the surface of the cortex and then slowly lowered during stimulus delivery until the ENTl was reached and a characteristic evoked laminar profile was seen (reported in Chapter 3). Stimuli were 0.2 ms duration and delivered via a constant-current device (DS3, Digitimer, UK).

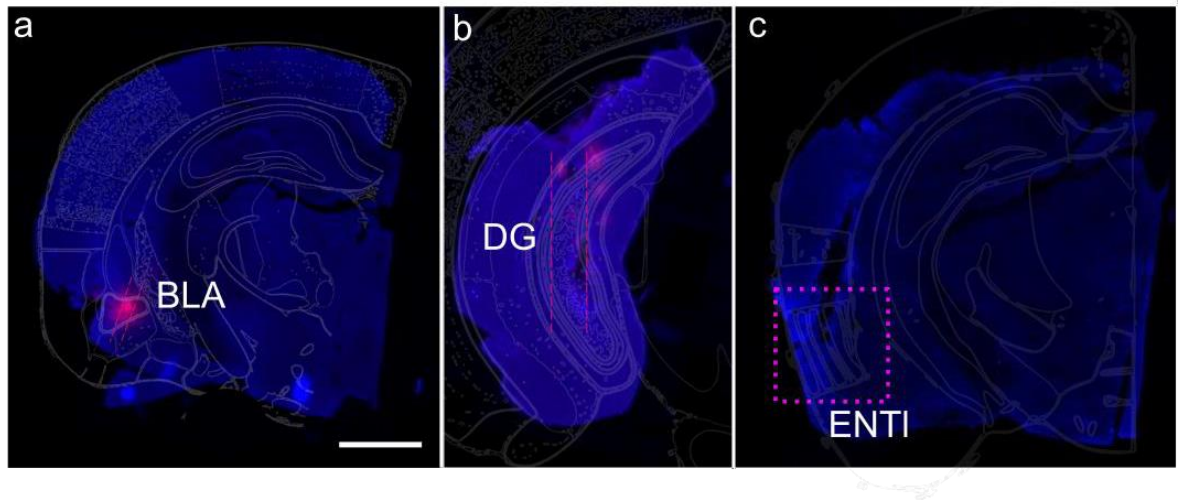


Figure 2.4: Histology for the location of the electrodes

DiI fluorescence showing the electrode location within the BLA and DG regions (**a,b**) respectively. **c**) Final placement of the stimulating electrode targeting the ENTl. scale bar: 1000 μ m

Stimulus patterns included paired-pulses (pairs of stimuli provided at varying intervals; see below) to measure both short-term plasticity (STP) over a range of inter-pulse intervals (see below) and functional connectivity (input/output; I/O) over a range of stimulus intensities (see below). Electrical stimuli were triggered by analogue 5 V square wave pulses from a PCI card (PCI-6071E, National Instruments, UK). Stimulation patterns were implemented with custom-designed programs written in LabVIEW (v8, National Instruments, UK). Data were recorded to disk as PLX/DDT files (Plexon data file types; Plexon, USA) using a Recorder64 system (Plexon, USA) after digitization at 10 kHz (12-bit A/D) per channel and bandpass filtering (0.1 - 1 kHz). Amplification was normally

500x overall via a 20x headstage amplifier and further amplification set via software on the PC-mounted Recorder64 system PCI data acquisition card. To confirm that electrodes were accurately placed within DG and BLA, single stimulus pulses (300 μ A) were applied to the ENTl until characteristic evoked response profiles were detected.

2.3.3 Stimulation protocols

Input/output curve (IOC)

After obtaining a typical response profile in DG and BLA through stimulation of ENTl, the I/O curve (IOC) was constructed by applying pairs of pulses at 50 ms interval, characterised by increasingly strong stimulation to assess how the recorded response changed as a function of input strength. Stronger stimulation should recruit more fibres/synapses and result in a larger response; thus, the IOC reflects the effective range of synaptic connectivity. The range of current intensities was 180, 300, 450 and 600 μ A. Stimuli at each intensity were delivered 20 times with an inter-stimulus interval of 3 s. Evoked responses were considered to be monosynaptic field excitatory postsynaptic potential (fEPSP) as these were consistent with previous literature (Davis et al., 2014; Maren and Fanselow, 1995). The initial fEPSP slope to each first stimulus of each pair was measured using a custom script in R (**Figure 2.5**). The input current parameter for the Paired-Pulse recordings was then set to that which produced the half-maximal response on the IOC (i.e., 50% of the current required to elicit a maximal fEPSP). In the majority of cases, the 50% value was 300 μ A.

Paired-Pulse stimulation (PPS)

Paired-pulses were delivered with a current intensity of 300 μ A (50 % of IOC), changing the interval within the pair every 20 repetitions. The range of intervals was 20,

50, 100, 200, 500 and 1000 ms. A custom-made R script was used to measure the initial slopes of the fEPSP for pulses 1 and 2 (P1 and P2 respectively), averaged across the 20 pairs, in order to detect any paired-pulse facilitation or depression (**Figure 2.5**). Depression (PPD) could be identified by a decrease in the response to the second pulse, i.e., P2 would be less steep than P1, and *vice versa* for paired-pulse facilitation (PPF). PPF/PPD provides an index for the capacity of synaptic connections to express short-term plasticity, a form ‘memory’ for prior synaptic activity that only persists for the duration of the stimulus (Zucker, 1989).

2.3.4 Data analysis

All data were imported offline into Spike2 (CED Cambridge, UK) and saved as text files to be processed with custom made R scripts.

Current source density

In order to obtain a spatiotemporal map of synaptic activity along each shank in BLA and DG, current source density (CSD) analysis was carried out, which allowed us to establish local presence and direction of current flow. This technique helps to ensure that recorded potentials are being generated from activated tissue local to the electrode rather than being volume conducted purely via the extracellular space from synaptic activation at a distance. The latter would have zero value in a CSD analysis. Calculated non-zero CSD values are thought to represent current flow into and out of local neurons as a result of locally-active synapses (producing removal (sink) or addition (source) of currents from activation of those synapses).

The analysis of CSD assumes that the tissue conductivity within the ROI is homogeneous.

The general formula for computing CSD values is:

$$\text{CSD}(h, t) = \sigma_h (\Phi(h - n\Delta h, t) - 2\Phi(h, t) + \Phi(h + n\Delta h, t)) / (n\Delta h)^2 \quad (2)$$

Where σ_h is the tissue conductivity (assumed to be constant), $\Phi(h, t)$ is the field potential at a given time (t) and depth (h), Δh is equal to the distance between channels in one electrode, i.e. 100 μm for neighbouring electrodes, and n corresponds to the spatial smoothing value (Freeman and Nicholson, 1975). In these experiments, we chose to calculate the CSD from neighbouring channels, so our spatial smoothing factor was 1. The PPS recording for 50 ms interval was selected for CSD analysis, from each animal. The 20 pairs of stimuli were averaged and a contour plot for CSD values was performed in Origin®. Current sources in the CSD analysis were visualized in red, whereas sinks in blue and zero-value regions in green. The CSD visualization per each shank per each mouse provided an informative overview of the current sources and sinks anatomically aligned with the 16 channels in each electrode's shank, facilitating the choice of the channels to analyse for IOC and PPS protocols.

IOC and PPS

For IOC, used to assess changes in functional connectivity (FC), the slope of the average P1 fEPSP in each pair was used to plot the curve. For PPS, in order to measure the value of PPF or PPD short-term plasticity, the paired-pulse index (PPI) was calculated using P1 and P2 initial fEPSP slopes with the following formula (**Figure 2.5**).

$$\text{PPI} = (P2 - P1) / P1 \quad (3)$$

As a result, $PPI > 0$ represents enhanced short-term plasticity ($P2 > P1$), defined as PPF; $PPI < 0$ represents a depression of short-term plasticity, therefore PPD ($P2 < P1$). Responses to the IOC (initial slope for P1) and PPI (ratio between P2 and P1) paradigms, in BLA and DG at the two age groups, were analysed separately with a linear mixed model analysis, using ROI, age, genotype, amplitude or intervals (for IOC and PPS respectively), and their mutual interactions as fixed effects; animal intercepts and repetitions of stimulation (20 times each) as random effects using R package *lme4*.

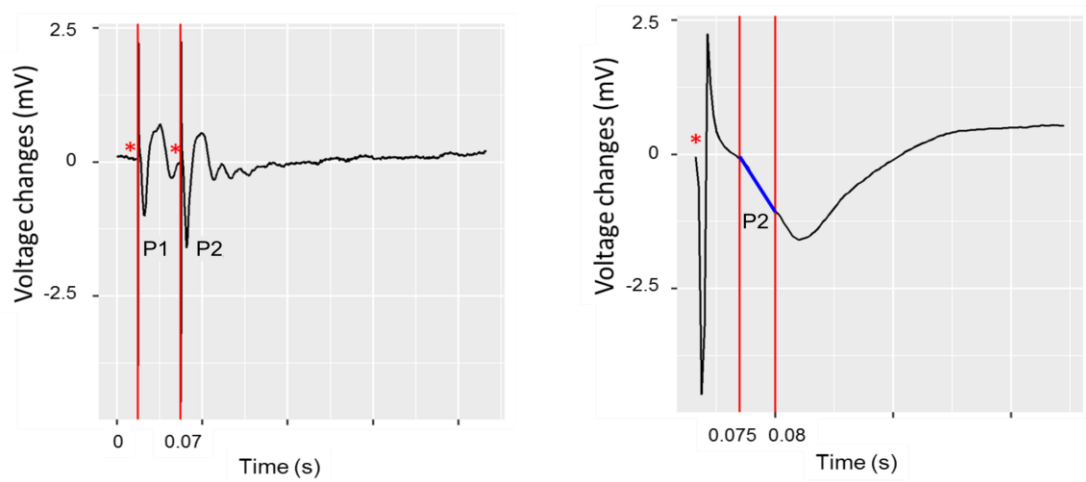


Figure 2.5: An example of the measurement of paired-pulse and I/O slopes in BLA

Left: example of one paired-pulse response in 3xTgAD mouse (3 months old, 50 ms PPS interval). P1 indicates the slope for the fEPSP response to Pulse 1, P2 indicates the second response, i.e. slope for the response to Pulse 2. The red lines indicate the two stimuli. **Right:** expanded view of P2; here, the red lines define the interval, for measuring the fEPSP slope; the blue line indicates the portion of the response measured as the initial slope of the fEPSP. This value was calculated as the slope of the blue line. This was always taken from the straightest portion of the initial responses.

Interaction effects were determined using a likelihood ratio test. A post-hoc analysis was performed after a general linear hypothesis test using contrast to determine genotype effects at each stimulation amplitude or interval. Correction for multiple comparisons was implemented during the contrast analysis using the R package *multcomp* (Bates et al., 2015; Bretz et al., 2016). Data are plotted as mean \pm standard error (SEM).

2.3.5 Perfusion

At the end of the experiment, an additional volume of anaesthesia with urethane (30%) was administered to the animals (i.e., terminal anaesthesia). The animals were then transcardially perfused with 0.9 % saline, followed by 4 % paraformaldehyde (PFA). The brain was then extracted and stored in 4 % PFA in a refrigerator for at least 24 hours. Prior to sectioning, the brain was transferred into a 30 % sucrose solution until it sank for cryoprotection.

2.3.6 Histology

Once sunk in sucrose the left hemisphere was removed, mounted in Tissue-Tek (source) on a freezing stage and coronal sections 50 μm thick were made using a microtome (Leica, UK). Slices were then mounted on subbed slides and allowed to dry overnight in absence of light. Finally, the slices were sent to the Bioimaging Centre in the Faculty of Biology, Medicine and Health at the University of Manchester and photographed using a 3D Histech, Pannoramic 250 Flash III digital slide scanner system (3DHistech, Hungary). The images were viewed using CaseViewer software (3DHistech, Hungary) in order to detect the fluorescence from the electrode tracks.

~ Chapter 3 ~

Paper 1

Rationale behind Paper 1

The project described in this thesis was made possible through a multi-site collaboration, between the University of Manchester and the Singapore Bioimaging Consortium. The major advantage of this collaboration was the ability to adopt different techniques to investigate the early stages of AD-like pathology in the young 3xTgAD mouse model. The overall aim of this project was to integrate a variety of techniques in order to exploit their relative advantages and to overcome their limitations, by combining the different readouts in the same framework.

Thus, firstly, fMRI recordings of the resting-state brain were acquired. Although this is not cell-specific and only reports neuronal activity indirectly, resting-state fMRI is beneficial in that it provides non-invasive information about FC in both healthy and diseased brain states. The non-invasive nature of fMRI renders it a fundamental tool for translation between pre-clinical and clinical research: when applied to an animal model, it can bring crucial insight into the pathological changes in FC and, by extension, can aid the interpretation of FC changes in the human brain.

A great advantage of using animal models is that fMRI can be used during invasive manipulation of specific neuronal populations, which is unachievable in patients. To take advantage of this my second step in this Paper was to optogenetically-induce manipulation of excitatory neurons in the left ENTl in combination with whole-brain fMRI readout. This was a logical subsequent step that provided further information on the relationship of BOLD fMRI signal to synaptic activity (the latter will be further probed directly with *in vivo* electrophysiology in Paper 2, Chapter 4).

Title: Brain-wide functional mapping of the entorhinal cortex in young 3xTg mouse model for Alzheimer's disease

Francesca Mandino^{*ab}, Ling Yun Yeow^a, Renzhe Bi^a, Lee Sejin^a, Han Gyu Bae^{ac}, Seung Hyun Baek^a, Chun-Yao Lee^a, Hasan Mohammad^a, Chai Lean Teoh^a, Jasinda H. Lee^d, Mitchell K. P. Lai^d, Sangyong Jung^a, Yu Fu^a, Malini Olivo^a, John Gigg^b, Joanes Grandjean^{ae}

a Singapore Bioimaging Consortium, Agency for Science, Technology and Research, Singapore

b Faculty of Biology, Medicine and Health, The University of Manchester, Manchester, United Kingdom

c Department of Life Sciences, Yeungnam University, Gyeongsan, Gyeongsangbuk-do 38541, South Korea

d Department of Pharmacology, Yong Loo Lin School of Medicine, National University of Singapore

e Department of Radiology and Nuclear Medicine & Donders Institute for Brain, Cognition, and Behaviour, Donders Institute, Radboud University Medical Centre

Corresponding author

Francesca Mandino,

Faculty of Biology, Medicine and Health, The University of Manchester, Manchester, United Kingdom mandino.francesca@gmail.com

Keywords: 3xTgAD, mouse, Alzheimer's disease, electrophysiology, *in vivo*

3.1 Abstract

Alzheimer's disease is the most common cause of dementia and is distinguished by the progressive accumulation of toxic neuritic plaques and neurofibrillary tangles in the brain. Recently, research has shifted the attention towards investigating the early pre-plaque stage of pathology. Animal models, which recapitulate aspects of this pathology, have proven useful in exploring underlying mechanisms associated with the disease, such as depicting functional changes in the brain with ultra-high field fMRI.

Here, we firstly assessed spontaneous activity in the 3xTgAD mouse model for cerebral amyloidosis and tau hyperphosphorylation, at 3 and 6 months of age. We hypothesised that functional connectivity would decrease within, and in relation to, orthologous areas to the human temporal lobes, which are the earliest cortical areas to be affected in pre-AD subjects. Secondly, we combined optogenetic stimulation with fMRI in order to gather neuronal-specific signatures from the BOLD signal of fMRI. Resting-state fMRI results confirmed a loss of local functional connectivity in 3xTgAD mice compared to controls, and a decrease in functional connectivity encompassing distal brain regions, relative to the entorhinal cortex. The optogenetic activation of entorhinal pyramidal neurons showed, instead, increased responses in 3xTgAD compared to controls, at both ages.

We conclude that, by 3 months of age, 3xTgAD mice show decreased functional coupling in the entorhinal cortex during spontaneous activity. This converts to increased activity in major hubs for cerebral amyloidosis upon strong experimental activation, thus suggesting an increase in metabolic demand in pathology, possibly as a result of heightened synaptic activity. This study brings supporting evidence for a functional reorganization of the brain within the early stages of AD-like pathology, in line with several empirical findings in humans at risk of developing AD.

3.2 Introduction

Alzheimer's disease (AD) is a neurodegenerative disease characterised by progressive cognitive decline and pathological accumulation of beta-amyloid ($A\beta$) products and phosphorylated tau protein in the brain as $A\beta$ plaques and neurofibrillary tangles (NFTs), respectively (Braak and Braak, 1995, 1991). Cognitive decline in AD patients is initially manifested through episodic memory deficits and then progresses to emotional memory and learning impairment, fear, anxiety (Bäckman and Small, 2007; Dere et al., 2010; Gilboa et al., 2006; Paz and Pare, 2013). With currently no effective treatment, AD is predicted to affect 75.6 million people worldwide by 2030 and has a significant patient and economic impact (Mount and Downton, 2006; Vradenburg, 2015). AD development is manifested as progressive brain atrophy detectable with structural MRI and $A\beta$ deposition revealed by PET (Jack et al., 2010).

Growing evidence indicates that functional magnetic resonance imaging (fMRI) markers, either acquired at rest (rsfMRI) or evoked during tasks, provide one of the earliest indicators of pathology and may predict disease progression (Sperling et al., 2011). Functional biomarkers are sensitive to mild cognitive impairment (MCI) and also seen in groups at risk of AD, such as mid-life *APOE ϵ 4* carriers (Chen et al., 2013; Filippini et al., 2009). However, variability in study methodology, exclusion/inclusion criteria, presentation of co-morbidities and limitations in performing invasive experiments in humans highlight the difficulties in obtaining a clear understanding of the functional landscape in the early stages of the pathology.

To address some of these limitations we first sought to investigate the relationship between the multitude of functional readouts derived from fMRI (Buxton, 2012; Smitha et al., 2017) during the early stages of cerebral amyloidosis and tau pathology. Secondly, we sought to reveal the neuronal substrate underlying these functional alterations. Finally, we

tested for disease-relevant enabling factors whose expression correlated with functional deficits concurrently with the AD-associated molecular substrate. To address these outstanding questions, we measured fMRI both at rest (rsfMRI; Gozzi and Schwarz, 2016; Grandjean et al., 2014b) and concurrently with optogenetics (ofMRI; Grandjean et al., 2019b; Lee et al., 2010) in the 3xTgAD model. This model expresses human PS1_{M146V}, APP_{SWE} and tau_{P301L} mutations (Oddo et al., 2003), thus recapitulating major aspects of AD. In particular, it displays a prolonged pre-plaque stage of intracellular A β accumulation in AD-related regions (hippocampal formation, amygdala and cortex) with the appearance of both cognitive impairment and synaptic dysfunction at a young age (Billings et al., 2005). A β plaques and NFTs aggregates appear later in the life cycle, often from approximately 9-10 months of age.

This model was selected as its behavioural profile replicates cognitive symptoms found in MCI, namely, perturbed emotion and episodic-like memory at young ages (Billings et al., 2005; Davis et al., 2013b; España et al., 2010). For these reasons, we hypothesize that functional changes would be present within, and relative to, the lateral entorhinal cortex (ENTl), a region at the interface between neocortex and hippocampus proper, fundamental for the formation, retrieval and consolidation of memories (Palop et al., 2006; Petrache et al., 2019).

The ENTl has been shown to be among the earliest targets of AD development (Van Hoesen et al., 1991). In animals, it represents one of the earliest regions affected by neuronal hyperexcitability and synaptic imbalance in mouse models for AD, such as the knock-in model *APPNL-F/NL-F* (Petrache et al., 2019). Hence, we hypothesized that in the early stages of cerebral amyloidosis and tau pathology 3xTgAD mice would result in functional connectivity changes in this region at rest and this would be further potentiated by optogenetic activation of ENTl projections to drive global neuronal network imbalance.

3.3 Method

3.3.1 Animals

All applicable international, national, and/or institutional guidelines for the care and use of animals were followed. All procedures performed in studies involving animals were in accordance with the ethical standards of the Institutional Animal Care and Use Committee (A*STAR Biological Resource Centre, Singapore, IACUC #171203). Male 129sv/c57bl6 controls (total N = 29) and 3xTgAD (total N = 31) were used for all the experiments. Specifically, $N_{\text{controls}} = 10$ and $N_{3\text{xTgAD}} = 19$ underwent rsfMRI experiments. Additionally, $N_{\text{controls}} = 19$ and $N_{3\text{xTgAD}} = 12$ mice underwent ofMRI experiments. Specific breakdown of animals group sizes is found per experiment.

3.3.2 Optogenetic surgery

Male 129sv/c57bl6 and 3xTgAD mice (~30 g, N = 19, N = 12 respectively) were anaesthetised with a mixture of Ketamine/Xylazine (Ketamine 75 mg/kg, Xylazine 10 mg/kg). The scalp was shaved and then cleaned with Betadine® and ethanol (70%). Lidocaine was administered subcutaneously, *in situ*. Each animal was kept on a warm pad to prevent hypothermia, and the head was positioned in a stereotaxic frame with protective ophthalmic gel applied to avoid corneal drying. A portion of the skin from the scalp was removed to expose the skull. Perforation of the skull was performed with a hand-held surgical drill (drill bit tip Ø .9 mm²) to create a small craniotomy -2.8 mm from bregma and +4.2 mm left from the middle line.

Virus injection was carried through the craniotomy at -2.8 to -2.7 mm from the brain surface and the cannula tip position was adjusted to -2.6 mm from the surface. Coordinates were taken from the Paxinos mouse brain atlas (Paxinos and Franklin, 2004). An injection of adeno-associated virus (AAV) was performed at the target through a

precision pump (KD Scientific Inc., Harvard Bioscience) with a 10 μ l NanoFil syringe with a 33-gauge beveled needles (NF33BV-2). The injected AAVs were AAV5-CaMKII α -hChR2 (H134R)-mCherry ($N_{\text{controls}} = 10$, $N_{3\times\text{TgAD}} = 12$) or AAV5-CaMKII α -mCherry ($N_{\text{controls-mCherry}} = 9$ with no opsin), titer $1-8 \times 10^{12}$ vg/ml, acquired from Vector Core at the University of North Carolina (USA).

A total volume of 0.75 μ l of AAV was injected in each mouse at a rate of 0.15 μ l/min. The injection needle was kept in location for 10 minutes after the injection was completed, to exclude backflow. After the needle extraction, a fibre optic cannula (\varnothing 200 μ m, 0.39 NA, length according to injection site, \varnothing 1.25 mm ceramic ferrule) was lowered to the region targeted for AAV (Laser 21 Pte Ltd, Singapore; Hangzhou Newdoon Technology Co. Ltd, China). The cannula was fixed in place with dental cement (Meliodent rapid repair, Kulzer). Buprenorphine was administered post-surgery to each animal. Animal recovery took place on a warm pad.

3.3.3 Animal preparation for imaging

Animal preparation followed (Grandjean et al., 2014a). Anaesthesia was induced with 4% isoflurane; subsequently, the animals were endotracheally intubated, placed on an MRI-compatible cradle and artificially ventilated (90 breaths/minute; Kent Scientific Corporation, Torrington, Connecticut, USA). A bolus with a mixture of medetomidine (Dormitor, Elanco, Greenfield, Indiana, USA) and Pancuronium Bromide (muscle relaxant, Sigma-Aldrich Pte Ltd, Singapore) was administered subcutaneously (0.05 mg/kg), followed by a maintenance infusion (0.1 mg/kg/hr) administered 5 minutes later while isoflurane was simultaneously reduced and kept to 0.5%. Functional MRI was acquired 20 min following maintenance infusion onset to allow for the animal state to stabilize. Care was taken to maintain the temperature of the animals at 37°C.

3.3.4 Data acquisition and stimulation protocols

Data were acquired on an 11.75 T (Bruker BioSpin MRI, Ettlingen, Germany) equipped with a BGA-S gradient system, a 72 mm linear volume resonator coil for transmission. A 2×2 phased-array cryogenic surface receiver coil was adopted for the rsfMRI experiment (N = 29) and a 10 mm single loop surface coil for ofMRI experiments (N = 31). Images were acquired using Paravision 6.0.1 software.

For the rsfMRI data acquisition, an anatomical reference scan was acquired using a spin-echo turboRARE sequence: field of view (FOV) = 17×9 mm², FOV saturation slice masking non-brain regions, number of slices = 28, slice thickness = 0.35, slice gap = 0.05 mm, matrix dimension (MD) = 200×100, repetition time (TR) = 2750 ms, echo time (TE) = 30 ms, RARE factor = 8, number of averages = 2. Functional scans were acquired using a gradient-echo echo-planar imaging (EPI) sequence with the same geometry as the anatomical: MD = 90×60, TR = 1000 ms, TE = 15 ms, flip angle = 50°, volumes = 600, bandwidth = 250 kHz.

Parameters for the ofMRI data acquisition were adapted to the lower sensitivity of the room-temperature receiver coil. The anatomical reference scan was acquired using FOV = 20×10 mm², number of slices = 34, slice thickness = .35, slice gap = 0 mm, MD = 200×100, TR = 2000 ms, TE = 22.5 ms, RARE factor = 8, number of averages = 2.

Functional scans were acquired using FOV = 17×9 mm², FOV saturation slice masking non-brain regions, number of slices = 21, slice thickness = 0.45, slice gap = 0.05 mm, MD = 60×30, TR = 1000 ms, TE = 11.7 ms, flip angle = 50°, volumes = 720, bandwidth = 119047 Hz. Field inhomogeneity was corrected using MAPSHIM protocol. ChR2 stimulation was provided through a blue-light laser (473 nm, LaserCentury, Shanghai Laser & Optic Century Co., Ltd) controlled by in-house software (LabVIEW, National Instruments).

The power of the laser (measured in continuous mode) was of 15 mW/mm². After an initial 50 s of rest as a baseline, 10 s of 5, 10 or 20 Hz light pulses were followed by 50 s of rest period, in a 10-block design fashion. An additional 60 s of rest was recorded after the last block of stimulation.

Experimental and control groups underwent the same imaging protocol, i.e., one resting-state scan followed by randomized 5 Hz, 10 Hz, 20 Hz evoked fMRI scans. Additionally, to exclude any abnormal behaviour induced by the photostimulation protocol (Weitz et al., 2015), all animals underwent the three stimulation sessions (5 Hz, 10 Hz and 20 Hz) again while awake and freely walking in a behaviour-chamber.

3.3.5 fMRI analysis

Images were processed using a protocol optimized for the mouse. Images were corrected for spikes (*3dDespike*, *AFNI*; Cox, 1996), motion (*mcflirt*, *FSL*; Smith et al., 2004), and B₁ field inhomogeneity (*fast*). Automatic brain masking was carried out on the EPI using *bet*, following smoothing with a 0.3 mm² kernel (*susan*), and a 0.01 Hz high-pass filter (*fslmaths*). Nuisance regression was performed using FIX (Zerbi et al., 2015). Separate classifiers were generated for rsfMRI and ofMRI. The EPIs were registered to the Allen Institute for Brain Science (AIBS) reference template ccfv3 using SyN diffeomorphic image registration (*antsIntroduction.sh*, *ANTs*; Avants et al., 2009).

Local connectivity was assessed with Regional Homogeneity (ReHo, *3dReHo*; Wu et al., 2017; Zang et al., 2004). Pair-wise region-of-interest (ROI) analysis was carried out with respect to ROIs defined in the AIBS atlas. Time series extracted with the atlas were cross-correlated to the time series from the ENTl using Pearson's correlation. ofMRI response was examined using a general linear model (GLM) framework (*fsl_glm*).

The stimulation paradigm and its first derivative were convolved using the default gamma function and used as regressors in the analysis, with motion parameters as co-variates.

3.3.6 *Ex vivo* processing

Patch-clamp recordings for ChR2 expression

Experiments were performed on acute brain slices. Mouse brains were rapidly removed after decapitation and placed in high sucrose ice-cold oxygenated artificial cerebrospinal fluid (ACSF) containing the following (in mM): 230 sucrose, 2.5 KCl, 10 MgSO₄, 0.5 CaCl₂, 26 NaHCO₃, 11 glucose, 1 kynurenic acid, pH 7.3, 95% O₂ and 5% CO₂. Coronal brain slices were cut at a thickness of 250 μ m using a vibratome (VT1200S; Leica Biosystems) and immediately transferred to an incubation chamber filled with ACSF containing the following (in mM): 119 NaCl, 2.5 KCl, 1.3 MgCl₂, 2.5 CaCl₂, 1.2 NaH₂PO₄, 26 NaHCO₃, and 11 glucose, pH 7.3, equilibrated with 95% O₂ and 5% CO₂. Slices were allowed to recover at 32° C for 30 minutes and then maintained at room temperature. Experiments were performed at room temperature.

Whole-cell patch-clamp recordings were performed on CaMKII α -positive ENT1 cells expressing ChR2-mCherry and were visualized using a CCD camera and monitor.

Pipettes used for recording were pulled from thin-walled borosilicate glass capillary tubes (length 75 mm, outer diameter 1.5 mm, inner diameter 1.1 mm, WPI) using a DMZ Ziets-Puller (Zeitz). Patch pipettes (2–4 M Ω) were filled with internal solution containing (in mM): 105 K-gluconate, 30 KCl, 4 MgCl₂, 10 HEPES, 0.3 EGTA, 4 Na-ATP, 0.3 Na-GTP, and 10 Na₂-phosphocreatine (pH 7.3 with KOH; 295 mOsm), for both voltage- and current-clamp recordings. Photostimulation (460 nm) was delivered by LED illumination system (pE-4000). Several trains of square pulses of 20 ms duration with 5, 10, and 20 Hz,

were delivered respectively under current-clamp mode ($I = 0$) to examine whether the neurons were able to follow high-frequency photostimulation. After different frequencies of photostimulation were completed, neurons were shifted to voltage-clamp mode (at -60 mV), and a prolonged square pulse of 500 ms duration was delivered, to further confirm whether ChR2-induced current could be seen on the recording neurons. The access resistance, membrane resistance, and membrane capacitance were consistently monitored during the experiment to ensure the stability and the health of the cell.

Whole-cell current-clamp recordings in the infralimbic cortex and dentate gyrus

After undergoing the scan at 6-months of age 8 mice ($N_{\text{controls}} = 4$, $N_{3\times\text{TgAD}} = 4$) from the ofMRI experimental mice were used for whole-cell patch recording in brain slices. An overdose of Ketamine/Xylazine (0.1 ml/kg) was administered prior to cardiac perfusion with ice-cold, oxygenated (95% O_2 and 5% CO_2) NMDG-HEPES solution consisting of NMDG 93, KCl 2.5, NaH_2PO_4 1.2, NaHCO_3 30, HEPES 20, glucose 25, sodium ascorbate 5, thiourea 2, sodium pyruvate 3, MgSO_4 10, CaCl_2 0.5 (in mM, pH 7.3 - 7.4, 300-310 mOsm).

After perfusion, the brain was sliced coronally at 350 μm thickness using a VT-1000 vibratome (Leica, Germany) in ice-cold, oxygenated NMDG-HEPES solution. Brain slices were transferred to pre-warmed NMDG-HEPES solution and recovered for 35 min with constant oxygenation at 37°C. During the recovery, 250, 250, 500, 1000, 2000 μL of 2 M NaCl solution were added at 10, 15, 20, 25 and 30 min, respectively, into 150 ml of the recovery solution. After recovery, brain slices were placed in HEPES-holding solution consisting NaCl 92, KCl 2.5, NaH_2PO_4 1.2, NaHCO_3 30, HEPES 20, glucose 25, sodium ascorbate 5, thiourea 2, sodium pyruvate 3, MgSO_4 2, CaCl_2 2 (in mM, pH 7.3 - 7.4, 300-310 mOsm; Ting et al., 2018) at room temperature.

For recording, brain slices were transferred to a recording chamber and perfused with ACSF solution consisting of NaCl 124, KCl 2.5, NaH₂PO₄ 1.2, NaHCO₃ 24, HEPES 5, glucose 12.5, MgSO₄ 2, CaCl₂ 2 (in mM, pH 7.3-7.4, 300-310 mOsm) at room temperature. Recording pipettes were prepared from borosilicate glass pipette using a P-1000 (Sutter instrument, USA) to 4-7 M Ω impedance. The current clamp recording was performed in infralimbic cortex layer 2/3 and dentate gyrus using recording pipettes filled with an internal solution consisting K-gluconate 130, EGTA 0.1, MgCl₂ 1, HEPES 10, NaCl 5, KCl 11, phosphocreatine 5, Mg-ATP 2, Na-GTP 0.3 (in mM, pH 7.3-7.4, 300-310 mOsm). The data were collected and recorded by Multiclamp 700A amplifier (Axon Instruments, USA), Digidata 1550B (Axon Instruments, USA), pCLAMP v10 (Molecular Devices, USA), and HEKA ECP10 USB (HEKA Elektronik, Germany), PatchMaster v2x90.2. Only data that met the criteria (Leakage current, < 100 pA; R-series, < 30 M Ω) were used for further analysis. Neuronal intrinsic properties were analysed using AxoGraph X and statistical analysis conducted using Prism 7.0. The data were plotted as the mean of the number of action potential with SEM. The statistical significance was presented with asterisks (*p<0.05, **p<0.01 by Mann-Whitney U test).

Immunohistochemistry

Immunohistochemical analyses were performed as described previously (Baek et al., 2017). Briefly, brains of N_{controls} = 3 (3, 6 and 10 months of age) and N_{3xTgAD} = 3 (3, 6 and 10 months of age) were fixed by perfusion with 4% PFA in phosphate buffer saline (PBS) and then in PFA and 30% sucrose for 48 h at 4°C. Fixed brains were cut on a microtome (CM3050S, Leica Microsystems, Nussloch, Germany) as 45 μ m-thick sections and collected into a cold cryoprotectant solution (80 mM K₂HPO₄, 20 mM KH₂PO₄, 154 mM NaCl, 0.3 g/ml sucrose, 0.01 g/ml polyvinylpyrrolidone, 30% vol/vol ethylene glycol).

Sections were washed 5 times for 3 minutes in 1 x PBS and blocked in 5% FBS with 0.1% Triton X-100 for 1 hour, followed by overnight incubation with the primary antibody in blocking solution at 4°C. The brain sections were immunostained with primary antibodies against A β (6e10, Covance Research Products Inc Cat #SIG-39300-1000 RRID: AB_10175637) and phospho-tau (AT8 ThermoFisher Scientific, Cat. #MN1020). After the primary antibody binding step sections were washed 5 times in 1 x PBS for 3 min and then incubated with anti-mouse Alexa 488 or anti-rabbit Alexa 594 for 2 hours followed by washing 3 times with 1 x PBS for 3 minutes. Sections were then mounted with DAPI plus mounting media on slides. All pictures were taken by using a confocal microscope with a 40 \times objective.

ELISA diagnostic assay

Briefly, brains were homogenized in Tris-HCl buffer and agitated for 30 minutes before centrifugation at 6000 g. The supernatant was used for the detection of soluble A β ₄₀₋₄₂ and the pellet was re-suspended in Tris-HCl and 10 μ l was used for further processing for insoluble A β ELISA as recommended by the ELISA kit (incubation with 5 M Guanidine to solubilize any aggregates and diluted before adding into ELISA plates). Samples were diluted only when necessary (ptau and total tau were diluted 2x, no dilution for A β ELISAs). As readings may be affected by how much of the sample was loaded into each well, we normalized ELISA results to protein assay results of the same fraction, hence, the final units are in picogram of A β or tau in per milligram of protein (pg/mg protein).

Ex vivo histology for mCherry expression

After the completion of experiments, animals were injected with an overdose of Ketamine/Xylazine and transcardially perfused with PBS, 0.01 M followed by 4% paraformaldehyde (PFA) in 0.01 M PBS. After extraction, the brain was post-fixed in 4% PFA overnight. Brain sections of 50 μ m were cut with a vibratome (VBT1200s, Leica); fluorophore expression, together with Hoechst staining, was checked through a confocal microscope Ti-E; DS-Qi2; Fluorescence, SBIC-Nikon Imaging Center, Singapore) for anatomical confirmation of viral infection and fibre optic cannula positioning.

3.3.7 Statistics and data availability

Descriptive statistics are given as mean difference and [95th confidence interval], unless stated otherwise, and graphically represented as ‘Gardner–Altman plots’, (<https://www.estimationstats.com/>; Ho et al., 2019). If not specified, descriptive statistics are provided for left-hemisphere ROIs. The statistical threshold for significance was set at $p < 0.05$, two-tailed. Voxel-wise was carried out with non-parametric permutation-based (5000 permutations) test (*randomize*). Cluster correction was carried out with threshold-free cluster enhancement (tfce). Thresholded t-statistic for one-sample and two-sample t-tests ($p < 0.05$, tfce corrected) are shown as a colour-coded overlay on the AIBS template. ROI analysis was carried out with a linear mixed model using genotype and age as fixed effects and individual intercepts as random effects, using *lme4* package (1.1-21) for R (<https://cran.r-project.org/>, 3.5.3, “Great Truth”). Significance was assessed with general linear hypothesis tests implemented in *multcomp* (1.4-10) package and corrected with false discovery rate. Both the rsfMRI and ofMRI datasets are made publicly available on <https://openneuro.org/> **Project IDs: Mouse_rest_3xTG, Mouse_opto_3xTG.**

3.4 Results

3.4.1 Immunohistochemical validation and ELISA

Firstly, immunohistochemical staining and ELISA for A β and tau were performed at 3, 6 and 10 months of age in 3xTgAD and age-matched controls. Analyses showed no plaques or NFTs at 3 or 6 months of age, confirming that these ages represent early stages of pathology progression (Clinton et al., 2007; Mastrangelo and Bowers, 2008);

Supplementary Figure S1). Indeed, tau-pathology in 3xTgAD mice was present as phosphorylated tau by 3 months of age in the amygdaloid nuclei and the hippocampus proper and DG by 6 months when revealed by AT8 staining (**Supplementary Figure S1a,b**). Probable NFTs accumulation was, instead, found only in older mice (**Supplementary Figure S1c**).

Control animals showed no staining with AT8 (data not shown). ELISA results confirmed an increase of total tau in 3xTgAD compared to controls (for example, 6 month-old 3xTgAD mice showed values of *circa* 212,000 pg/mg and controls 6,600 pg/mg; Hampel and Teipel, 2004). ELISA showed no detectable difference between 3xTgAD and controls at any time point for insoluble A β ₄₀; soluble A β ₄₀ was reported \approx 1.3-fold increase by 3 months of age (3xTgAD = 16,000 pg/mg; controls = 12,000 pg/mg) and \approx 1.7-fold increase in 3xTgAD compared to controls at 6 months of age (3xTgAD = \approx 16,100 pg/mg; controls = 9,120 pg/mg). From ELISA and immunohistochemical examination at these ages, there was no evidence for an increase in A β ₄₂ or plaques in 3xTgAD compared to controls.

3.4.2 Resting-state fMRI reveals regional homogeneity deficit in 3xTgAD

We recorded rsfMRI in male 3xTgAD (N = 19) and control mice on the same background strain (129sv/c57bl6); N = 10) at 3 and 6 months of age (N_{3xTgAD} = 13, N_{controls}

= 10). The rsfMRI protocol employed here was recently compared to others in a multi-center study. The latter indicated elevated sensitivity and specificity to RSN detected in this dataset relative to other protocols, including an awake mouse protocol (Grandjean et al., 2019a). One 3xTgAD mouse developed hydrocephalus, which, despite the acute condition, only marginally affected FC (Mandino et al., 2019). This animal was removed from this study following our *a priori* exclusion criteria.

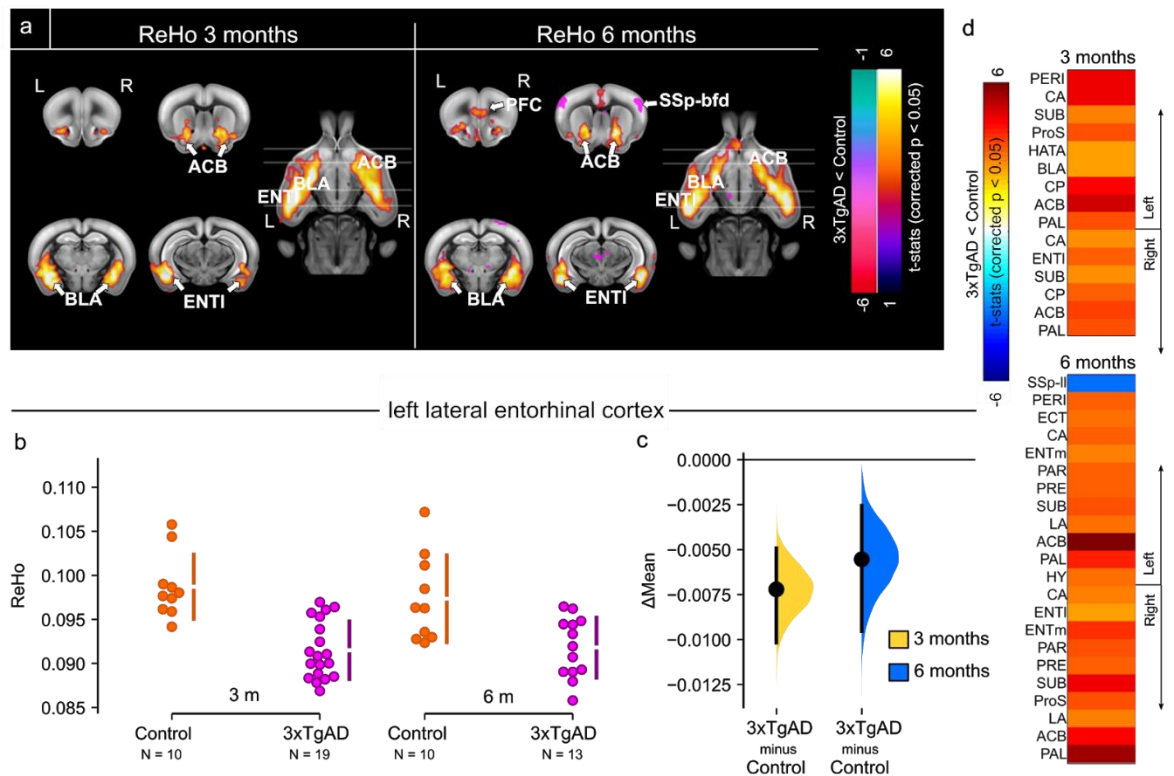


Figure 3.1: Resting-state fMRI shows regional homogeneity decrease in 3xTgAD

a) Regional Homogeneity (ReHo) shown as thresholded group analysis for 3 months and 6 months of age at left and right, respectively. 3xTgAD mice show a significant decrease in ReHo by 3 months of age within the ENTI, ACB and BLA. 3xTgAD shows increased ReHo values for SSp-bfd, by 6 months of age. **b,c)** A significant decrease in ReHo was found at 3 and 6 months of age in the ENTI. **d)** Pair-wise ROI interactions relative to the left ENTI shows decrease of FC in right ENTI, ACB, BLA. Increase in FC was found again in somatosensory regions. SSp-II: somatosensory area, lower limb; PERI: perirhinal area; ECT: entorhinal area; CA: cornu ammonis; ENTm: medial entorhinal cortex; PAR: parasubiculum; PRE: presubiculum; SUB: subiculum; ProS: prosubiculum; HATA: hippocampal-amygdalar transition area; LA: lateral amygdalar nucleus; BLA: basolateral amygdala; CP: caudoputamen; ACB: nucleus accumbens; PAL: pallidum; HY: hypothalamus; ENTI: lateral entorhinal cortex.

Five 3xTgAD mice could not be included in the second time point scan, leading to the following group sizes $N_{3xTgAD} = 19$, $N_{controls} = 10$ at 3 months; $N_{3xTgAD} = 13$, $N_{controls} = 10$ at 6 months. 3xTgAD mice presented a deficit in ReHo compared to controls, at both age groups (**Figure 3.1a**), localized ventrally within the brain.

These included the ENTl ($\Delta mean_{3months} = -0.007$ [-0.010, -0.005], $\Delta mean_{6months} = -0.006$ [-0.010, -0.003], **Figure 3.1bc**) within the retrohippocampal area, the nucleus accumbens (ACB, $\Delta mean_{3months} = -0.003$ [-0.005, -0.001], $\Delta mean_{6months} = -0.005$ [-0.007, -0.003], **Supplementary Figure S2a**) in the ventral striatum, the basolateral amygdala (BLA, $\Delta mean_{3months} = -0.018$ [-0.024, -0.014], $\Delta mean_{6months} = -0.015$ [-0.020, -0.011], **Supplementary Figure S2b**) within the amygdaloid area. Moreover, deficits in ReHo were also found in 3xTgAD in the medial prefrontal cortex (mPFC), such as the prelimbic cortex (PL, $\Delta mean_{3months} = -0.004$ [-0.015, -0.005], $\Delta mean_{6months} = -0.016$ [-0.032, -0.005], **Supplementary Figure S2c**).

Concurrently, 3xTgAD exhibited enhanced ReHo in somatosensory areas, such as barrel field cortex (SSp-bfd, $\Delta mean_{3months} = 0.122$ [0.005, 0.020], $\Delta mean_{6months} = 0.017$ [0.006, 0.035], **Supplementary Figure S2d**). In summary, the 3xTgAD model, similar to other transgenic models, e.g. PSAPP, ArcA β (Grandjean et al., 2016; Shah et al., 2016, 2013), presents functional alterations that precede A β deposition. The functional deficits hotspots overlapped with the amygdaloid-striatal-ventral system, early sites of tau aggregation, thus conferring this model with added relevance to the study of early emotional-memory deficits found in MCI patients.

3.4.3 Local FC deficits translates into whole-brain network alterations

The ENTl is a major hub involved in early stages of AD pathology in humans and AD-pathology in mice; as such, it was targeted as a major focus for further analysis. To

examine distal FC alterations at rest, we assessed pair-wise ROI interactions relative to the left-hemisphere ENTl. FC to the ENTl was decreased in the retrohippocampal and hippocampal regions (**Figure 3.1d, Supplementary Figure S3**, e.g. ENTl right hemisphere: $\Delta\text{mean}_{3\text{months}} = -0.114$ [-0.193, -0.035], $\Delta\text{mean}_{6\text{months}} = -0.127$ [-0.205, -0.058], **Supplementary Figure S3a**), ventral striatum (ACB: $\Delta\text{mean}_{3\text{months}} = -0.110$ [-0.154, -0.068], $\Delta\text{mean}_{6\text{months}} = -0.152$ [-0.199, -0.107], **Supplementary Figure S3b**), and amygdala (BLA: $\Delta\text{mean}_{3\text{months}} = -0.066$ [-0.110, -0.025], $\Delta\text{mean}_{6\text{months}} = -0.061$ [-0.115, -0.011], **Supplementary Figure S3c**). Similarly, an increase in FC relative to the somatosensory cortex was presented (SSp-II: $\Delta\text{mean}_{3\text{months}} = 0.0833$ [0.0192, 0.149], $\Delta\text{mean}_{6\text{months}} = 0.112$ [0.0587, 0.157], **Supplementary Figure S3d**). These results focusing on the ENTl-specific network show similarities to the whole brain FC changes assessed with ReHo, presented in an overlapped design in **Supplementary Figure S4**.

In an exploratory analysis, we examined whole-brain network deficits in 3xTgAD mice at 3 and 6 months of age, summarised in **Supplementary Figure S5a** (left and right respectively) in a half-matrix format. Alterations were consistent between both age-groups, localized within and between regions highlighted in the ReHo analysis, namely, in the amygdaloid/cerebral nuclei (including BLA and ACB) and the hippocampal formation, e.g. ENTl (**Figure 3.1a, Supplementary Figure S5b**).

These results indicated that local FC deficits translated into distal FC deficits and transpired into greater network dysfunction. Moreover, regions highlighted in the pair-wise correlation analysis were also found to be enriched in tau aggregates later in the disease progression (amygdala and hippocampal formation, **Supplementary Figure S1c**, left and right respectively), consistent with tau dispersions within functionally connected networks (Franzmeier et al., 2019).

3.4.4 Functional connectome of the ENTl revealed by optogenetics

The ENTl was revealed to be a major hub region affected in 3xTgAD at rest. To explore its functional connectome, we used ofMRI (Deisseroth, 2011; Lee et al., 2010) to visualize the haemodynamic response to a 10-block design photostimulation of ChR2-transfected CaMKII α -positive (AAV5-CaMKII α -hChR2 (H134R)-mCherry) ENTl neurons ($N_{\text{controls}} = 10$, $N_{3\text{xTgAD}} = 12$; **Figure 3.2a**; **Supplementary Figure S6a**). Anatomical imaging of the fibre revealed that the ENTl was accurately targeted (**Supplementary Figure S6b**). Transfection led to robust expression at the target site (**Figure 3.2b**, **Supplementary Figure S7a**). Cell bodies of transfected neurons were consistent with those of pyramidal cells (**Figure S7b**). ENTl neurons faithfully responded to 5 and 20 Hz pulse trains in both controls and 3xTgAD (**Figure 3.2d** and **Supplementary Figure S7c**, respectively). Prolonged photostimulation (500 ms) applied to the patched neurons confirmed an effective ChR2-induced inward current on both control and 3xTgAD mice (**Supplementary Figure S7d**). There was no evidence of aberrant spontaneous behaviour to photostimulation protocols in freely walking mice, unlike seizures previously reported following photostimulation of the hippocampus in rats (Weitz et al., 2015).

The haemodynamic response was significantly associated with our modelled response in controls (**Figure 3.2e**, left and middle panels) and 3xTgAD (**Supplementary Figure S8**, left and middle panels) in an unbiased GLM analysis in several regions, including: the hippocampal formation (hippocampus proper, ENTl, DG, SUB), the amygdaloid area (e.g. BLA), the ventral striatum (ACB), the prefrontal and the insular areas at both time points. Interestingly, optogenetically-evoked activity was mostly confined to the ipsilateral hemisphere, despite the presence of contralateral projections, as predicted by viral tracers (**Figure 3.2e** left panel, spatial correlation $R = 0.36$). This supports the presence of neuronal mechanisms that silence the response contralaterally but

not ipsilaterally to artificially generated neuronal activity, perhaps via feed-forward active inhibition (Histed, 2018).

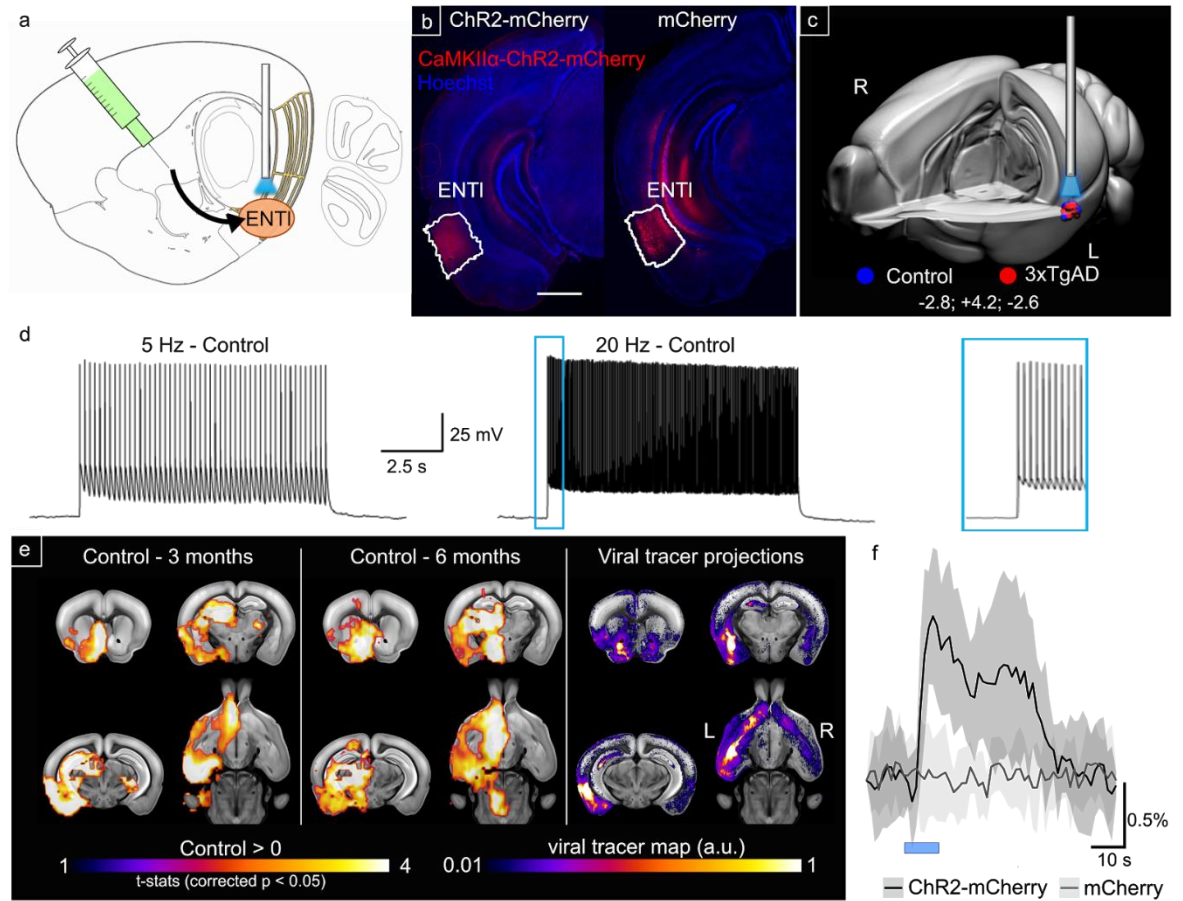


Figure 3.2: Optogenetic modulation of the ENTl

a) Diagram of stereotaxic injection and fiber optic implantation. **b)** ChR2-mCherry/Hoechst co-labelling in one ChR2-mCherry control (left panel) and one mCherry control (right panel) mouse indicate successful targeting of the ENTl and stable transfection. Scale bar: 1000 μm . **c)** 3D rendering of fiber tip position for each experimental animal, red dots indicate 3xTgAD subjects ($N = 12$) and blue dots indicate controls ($N = 10$). Coordinates of ENTl injection site are reported in mm from Bregma: AP: -2.8; ML: +4.2; DV: -2.6. **d)** Optogenetic stimulation of ChR2-transfected neurons at 5 Hz and 20 Hz shows frequency-locked spiking activity *in vitro*. **e)** Optogenetically-locked BOLD response overlaps with density projection maps. Left and middle panels indicating one-sample t-test for stimulation-locked BOLD response in the control group and 3xTgAD mice ($N = 10$, $N = 12$, respectively; $p < 0.05$ corrected) highlighting activation in key regions related to ENTl projections, i.e. BLA, ACB. AIBS tracer projection density map with injection in ENTl (experiment ID: #114472145; right panel). **f)** BOLD response profile, averaged across 10 blocks, following stimulation at 20 Hz of control mice injected with ChR2-mCherry ($N = 10$) and control mice injected with mCherry only ($N = 9$) shows opsin-dependent BOLD response. AP: anterior-posterior; ML: medio-lateral; DV: dorso-ventral.

The response elicited through photostimulation of ENT1 was comparable between 3 and 6 months, indicating a stable expression allowing for longitudinal analysis (**Figure 3.2e** left and middle panels for controls, and **Supplementary Figure S8** for 3xTgAD 3 and 6 months, left and middle panels respectively).

A negative control carried out in controls (N = 9) transfected with mCherry alone (**Figure 3.2b**) did not reveal the presence of a light response, except for a visual-associated response of the lateral geniculate nucleus and superior colliculus, probably due to fibre illumination perceived as visual stimulus (**Figure 3.2f**). Hence, we concluded that the response recorded with ofMRI was not associated with potential heating and/or vascular photoreactivity artefacts (Christie et al., 2013; Rungta et al., 2017; Schmid et al., 2017).

Photostimulation at frequencies ranging from 5 to 20 Hz indicated spatially overlapping results (**Supplementary Figure S6d**), in contrast to (Chan et al., 2017). In fact, the visually-associated response amplitude was stronger at lower frequencies (**Supplementary Figure S6c** upper panel), while the opsin-associated response was more marked at 20 Hz (**Figure 4.3e**, **Supplementary Figure S8**). The visual response, elicited with 5 Hz stimulation, was subsequently masked from our results and the remainder of the analysis is focused on the 20 Hz paradigm (**Supplementary Figure S6c** upper panel).

3.4.5 Potentiated haemodynamic response and neuronal activity

To assess response differences across the whole brain, a non-parametric second-level analysis comparing the amplitude of activation between 3xTgAD and controls was carried out (**Figure 3.3a**). A few animals could not be scanned at the 6-months time-point due, for example, to the detachment of the implant. Therefore, group sizes differ between 3 months ($N_{\text{controls}} = 10$, $N_{3\text{xTgAD}} = 12$) and 6 months ($N_{\text{controls}} = 8$, $N_{3\text{xTgAD}} = 10$) of age. At 3 months of age, 3xTgAD mice showed significantly larger responses across several regions

compared to controls, including the ipsilateral dorsal hippocampus proper and DG, ACB, PL, ILA, cingulate retrosplenial areas, and contralateral ENTl. The presence of an effect at the 6 months time-point could not be inferred, potentially due to the reduced group size, or to a normalization of the response at a later age.

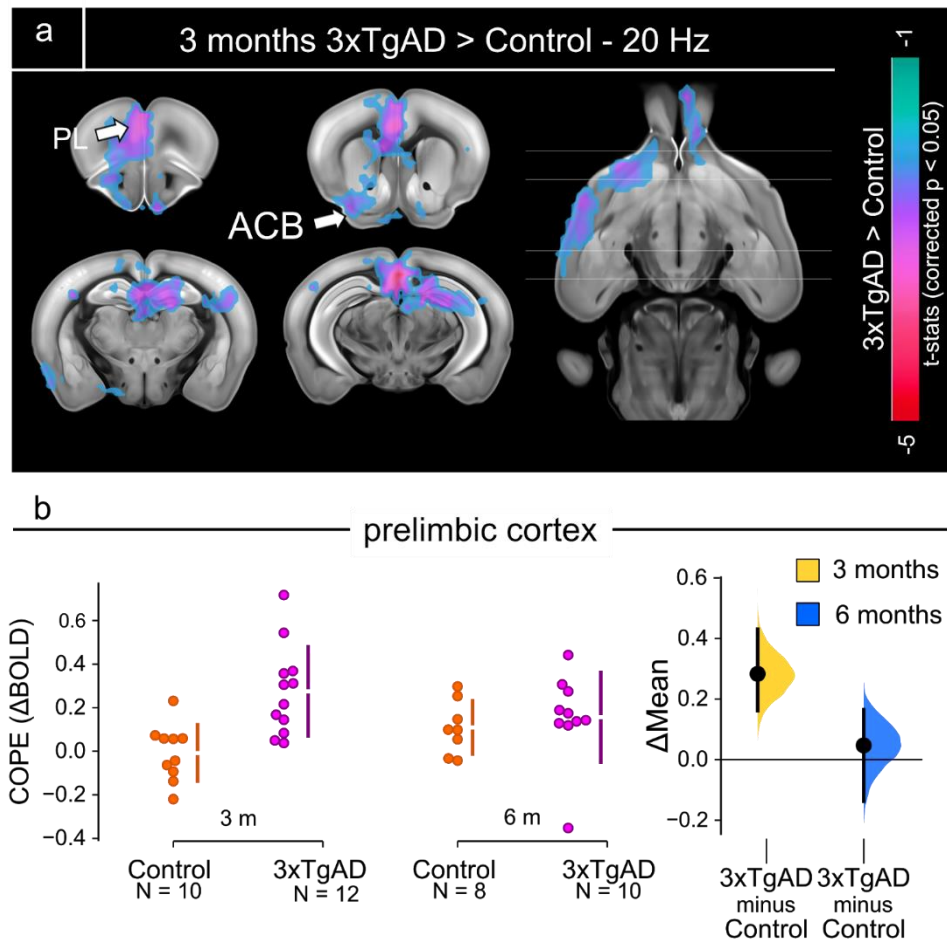


Figure 3.3: Two-sample t-test results, 3 months time-point

a) Two-sample t-test showing significantly higher response ($p < 0.05$, corrected) in 3xTgAD compared to controls in regions encompassing the prefrontal cortex, such as PL, and ventral striatum (ACB). **b,c)** COPE extracted from the PL as example of potentiated response in 3xTgAD compared to age-matched controls, at 3 and 6 months of age. PL: prelimbic cortex; COPEs: contrast of parameter estimates.

To examine local response amplitude, contrast of parameter estimates (COPEs)

were extracted from ROIs highlighted in the voxel-wise comparison: ENTl ($\Delta\text{mean}_{3\text{months}} = 0.044$, [0.022, 0.070]), ACB ($\Delta\text{mean}_{3\text{months}} = 0.15$ [0.0106, 0.298]) and PL (shown in

Figure 3.3b as example, $\Delta\text{mean}_{3\text{months}} = 0.283$ [0.161, 0.431]). Similar results were present at lower stimulation frequencies, although the more distal regions lacked an effect at lower frequencies (example for 10 Hz, ENTl: $\Delta\text{mean}_{3\text{months}} = 0.008$, [-0.08, 0.09]). Data acquired at rest, prior to optogenetic stimulation, with the single loop coil, indicated ReHo deficits converging with that acquired in the previous dataset (i.e. with cryogenic coil), replicating our observations above (**Figure 3.1a, Supplementary Figure S9**). Acute slice electrophysiology indicated that both hippocampal and prefrontal excitatory neurons of 3xTgAD were prone to hyperactivity following current injection compared to controls (**Supplementary Figure S10; Supplementary Table S1**), while the shape of the spikes was otherwise mostly unaltered (**Supplementary Table S2**).

To examine how the functional alterations of the ENTl functional projectome at 3 months relate to loss of connections at rest, we projected the two responses onto the same template (**Supplementary Figure S8c**). There, we found that several of the ROIs presenting a decreased FC at rest were responding with greater amplitude to an optogenetically-driven neuronal activity. This was the case for regions encompassing the ventral striatum (ACB), the dorsal DG within the hippocampal formation and prefrontal regions. We concluded, therefore, that disturbed distal connectivity at rest translated to heightened haemodynamic response to elicited neuronal activity with optogenetics, and that this response is accompanied with hyperactivity of the embedded neurons within the affected circuits, while their intrinsic spiking properties remained unaltered.

3.5 Discussion

The entorhinal and associated hippocampal areas form a fundamental network for memory encoding and retrieval (van Strien et al., 2009). Specifically, the lateral entorhinal cortex is crucial for episodic memory (Buzsáki and Moser, 2013) and is one of the primary areas affected in human AD (Van Hoesen et al., 1991) and the 3xTgAD model of cerebral amyloidosis and tauopathy (Oddo et al., 2003). Here, we demonstrate that local FC disruption in 3xTgAD mice translates into larger network dysfunction as seen by a general reduction in resting-state activity (**Figure 3.1**). Moreover, network dysfunction at rest further translated into the aberrant response to optogenetically-driven neuronal activity, highlighting a possible increase in neuronal excitability following stimulation (**Figure 3.3a, Supplementary Figure S8** right panel).

The dichotomy of the direction of these changes in resting and evoked activity, specifically within the ENTl network, mirrors several findings in preclinical and mild AD patients. Decreased FC is found in mild AD patients at rest, in areas related to the DMN, including the hippocampal formation (Greicius et al., 2004; Wang et al., 2006). However, task-based fMRI studies show increased activity in memory-related areas in subjects at risk of AD but cognitively still normal (e.g. *APOE* ϵ 4 carriers), suggesting a possible dichotomy in network organisation of the brain at rest and in engaged status (Bookheimer et al., 2000).

Taken together, our findings thus seem to reconcile apparent discordant results put forward in early-AD subjects (Braskie et al., 2012; Filippini et al., 2009; Sheline et al., 2010). This was, however, not systematically consistent throughout dementia research literature. Studies with both memory-task and resting-state in *APOE* ϵ 4 carriers show increased activity both at rest and during task-based fMRI (Filippini et al., 2009). This may be due to different stages into the pathology or analysis parameters. Alternatively, this

could be related to network-specific alterations. We report here elevated ReHo and distal FC in the somatosensory networks, indicating that not all circuits are affected in the same manner. Indeed, the presence of phospho-tau was found in regions presenting decrease in FC regions (**Supplementary Figure S1**), highlighting the selective vulnerability of the amygdaloid area and hippocampal formation in AD-pathology, resulting in local loss of coherence.

Considering the above, we propose that the dichotomy of decreased spontaneous co-activation and increased evoked response suggests localized circuit disorganization within AD-vulnerable networks. At rest, decrease of inter-regional connectivity is predominant, and leads to impoverished network efficiency. During acute modulated stimulation, instead, we assist at an increase in synaptic activity, thus resulting in increased metabolic demand. This circuit disorganisation may be the result of synaptic dysfunction, neuronal morphology changes and aberrant neuronal excitation (Šišková et al., 2014).

The electrophysiological evidence reported here from DG and prefrontal areas confirms aberrant spiking activity, highlighting a possible excitatory/inhibitory (E/I) imbalance in early stages of AD-like pathology. Previous evidence in hAPP mice highlights a causal cascade of events with synaptic dysfunction and consequent neuronal hyperexcitation as key causes. The administration of the anti-epileptic drug Levetiracetam for a prolonged period resulted in amelioration of behavioural and synaptic transmission deficits, confirming an E/I imbalance (Lipton and Sanz-Blasco, 2012). Overall, this loss of efficiency and local circuit disruption results in increased metabolic requirements during tasks, to overcome inappropriate signal transmission and processing leading to aggravated pathology later in life (Bero et al., 2011). Under this model, functional alterations become both an important biomarker and a target for early interventions aimed at restoring normal synaptic transmission in local circuitry (Canter et al., 2016). This is an increasingly

important approach, as network dysfunction and corresponding tau pathology are thought to propagate from dysfunctional hub to hub (Braak and Braak, 1995). Hence, early detection with functional biomarkers would be a vital tool in early prevention schemes.

Beyond the ENT1, the ventral amygdaloid-striatal system, including the BLA and ACB, presented localized FC deficits. This is consistent with behavioural results in young 3xTgAD, where fear and emotional processes are highly affected (España et al., 2010). Moreover, evidence from animal research shows that the modulation of fear conditioning in the BLA is regulated by prefrontal regions, in a ‘top-down’ inhibitory fashion. Lesions in the infralimbic cortex (ILA) are thought to disrupt fear memory extinction processes, thus highlighting the delicate balance between these regions for a healthy processing of emotional control (for a review Etkin et al., 2011). Indeed, emotional control, regulated by the ventral hippocampal-prefrontal-amygdaloid system, is also affected in pre-AD patients (LaBar and Cabeza, 2006; Sturm et al., 2013).

Interestingly, a central hub highlighted in our analysis is the ACB of the ventral striatum. ACB expresses a high tau load in AD patients in the later stages of the disease. This, together with the evidence in the BLA, suggests a ventrally-oriented vulnerability of pathology spread (Selden et al., 1994). ACB is thought to be related to dopaminergic (DA) systems regulating reward (Salamone et al., 2005). Loss of DA neurons and DA signalling pathway dysfunction have been associated with memory loss in AD patients (Koch et al., 2014) and AD-like mouse models (Cordella et al., 2018). Moreover, loss of DA receptors, especially D2, has been shown in areas such as the hippocampal formation, prefrontal cortices and BLA (Joyce et al., 1993; Kemppainen et al., 2003) in AD patients. Our results, therefore, bring supporting evidence for a disruption in the DAergic system associated with early cerebral amyloidosis and tauopathy, which leads to synaptic dysfunction in ACB, BLA and prefrontal projection sites. Therefore, the dysfunction of DA transmission in

distal targets, prior to amyloid plaque accumulation, may contribute to the initial pathogenesis of AD.

In sum, functional deficits found within and relative to the temporal and ventral areas in 3xTgAD mice recapitulate several important effects described with functional neuroimaging in pre- and early stages of AD. Importantly, we highlight a possible loss of local coherence derived from aberrant neuronal activity in AD-vulnerable regions, before the appearance of overt A β plaques and NFTs. Aberrant neuronal activity, in turn, might be due to a reduced inhibition or to a loss of connectivity which results in an enriched excitatory synaptic response as a potential compensatory mechanism for decreased synaptic connectivity.

Moreover, our results are consistent with disruption in DA signalling pathways involving ACB, BLA and prefrontal regions as one of the earliest features characterising AD development. Finally, photostimulation of ENTl pyramidal cells leads to a marked increase in BOLD response in several important projection areas, which seems to mirror several empirical findings in humans at risk of developing AD. This apparent dichotomy between resting- and evoked- functional responses can be seen during the early stages of cerebral amyloidosis and tauopathy in 3xTgAD and is in line with several empirical findings in humans at risk of developing AD. Our results highlight the central role of the ENTl as a hub for AD-like pathogenesis and provide an understanding of the underlying mechanisms leading to functional deficits preceding this devastating neurodegenerative disorder.

3.6 Supplementary material

3.6.1 Supplementary tables

Table S1: Intrinsic properties of granule cells in dentate gyrus and pyramidal cells in infralimbic cortex

Rheobase, threshold, AP latency, AP amplitude, AHP, AHP latency, half width of AP were measured from the first trace showing action potential (Rheobase trace). The values represent mean value with SEM and the statistical significance was presented with asterisk ($p < 0.05$, $p^{**} < 0.01$ by Mann-Whitney U test; N = number of animals, n = number of cells).

Table 1. Intrinsic properties						
	dentate gyrus			Infralimbic cortex		
	control (N = 4, n = 29)	3xTgAD (N = 5, n = 18)	p value (M-W)	control (N = 4, n = 10)	3xTgAD (N = 5, n = 11)	p value (M-W)
Rm (mV)	-74.54 ±0.7242	-76.66±1.029	ns	-52.42±2.827	-54.71±3.149	ns
Rheobase (pA)	79.83±6.231	69.44±6.591	ns	37±8.95	24.55±3.659	ns
Threshold (mV)	-33.38±1.554	-36.38±1.919	ns	-35.69±0.5727	-34.58±1.228	ns
AP latency (ms)	238±40.01	343.3±56.88	ns	94.81±28.06	174.2±33.35	ns
AP Amplitude (mV)	97.06±2.129	91.59±2.219	ns	72.99±2.284	70.34±2.871	ns
AHP (mV)	-11.35±0.8297	-10.17±1.241	ns	-10.9±1.653	-10.73±0.9142	ns
AHP latency (ms)	5.015±0.2014	4.794±0.3514	ns	16.88±3.091	55.6±13.21	0.0028 (**)
Half-width (ms)	1.321±0.0424	1.242±0.0472	ns	2.27±0.1154	2.862±0.2157	0.0079 (**)

Table S2: Number of action potential evoked by various current injections

The number of action potentials was counted in granule cells in dentate gyrus and pyramidal cells in infralimbic cortex from various current injection (20 – 140 pA). The values represent mean value with SEM and the statistical significance was presented with asteriska (*p<0.05, **p<0.01 by Mann-Whitney U test; N = number of animals, n = number of cells).

Table 2. Number of Action potential (Hz)							
	dentate gyrus				infralimbic cortex		
Current injection (pA)	control (N = 4, n = 29)	3xTgAD (N = 5, n=18)	p value (M-W)		control (N = 4, n = 10)	3xTgAD (N = 5, n = 11)	p value (M-W)
20	na	na	na		1.8±0.7572	2.182±0.6851	ns
40	0.1034±0.076	1.556±0.879	ns		4±1.229	6±0.9723	ns
60	0.5517±0.2359	3.556±1.322	0.029 (*)		6.2±1.724	9.636±0.8008	ns
80	2.621±0.5985	6.056±1.652	ns		7.8±1.825	11.45±0.9757	ns
100	4.345±0.7773	8.5±1.801	ns		9.2±1.611	12.55±1.012	ns
120	5.241±1.013	10.39±1.91	0.0214 (*)		8±1.366	13.82±1.094	0.0036 (**)
140	6.138±1.24	10.83±1.526	0.0078 (**)		8.4±1.392	13.45±1.268	0.0204 (*)

3.6.2 Supplementary figures

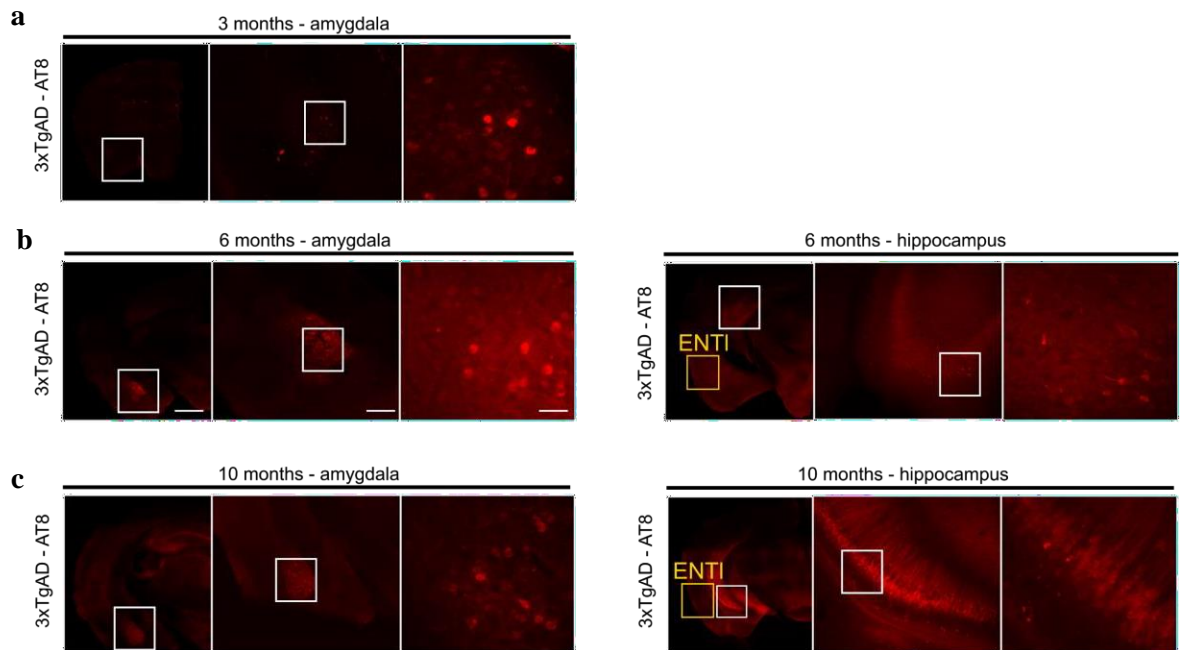


Figure S1: Immunohistochemistry for 3xTgAD characterisation with AT8

a) 3xTgAD mice show positive staining for phosphorylated tau in the amygdaloid area by 3 months. **b)** 6 months old 3xTgAD mice show tau-positive labelling in the amygdala (white square, left panel) and extended to the hippocampus proper (white square, right panel); within the hippocampal formation, the ENT1 (yellow squares) shows no apparent pathology. **c)** 10 months old 3xTgAD mice show tau-positive staining in the amygdala (white square, left panel) and hippocampus proper (white square, right panel). Within the hippocampal formation, the ENT1 (yellow square, right panel) however does not show positive response to AT8. Left panels 1000 μm , middle panels 500 μm , right panels 100 μm .

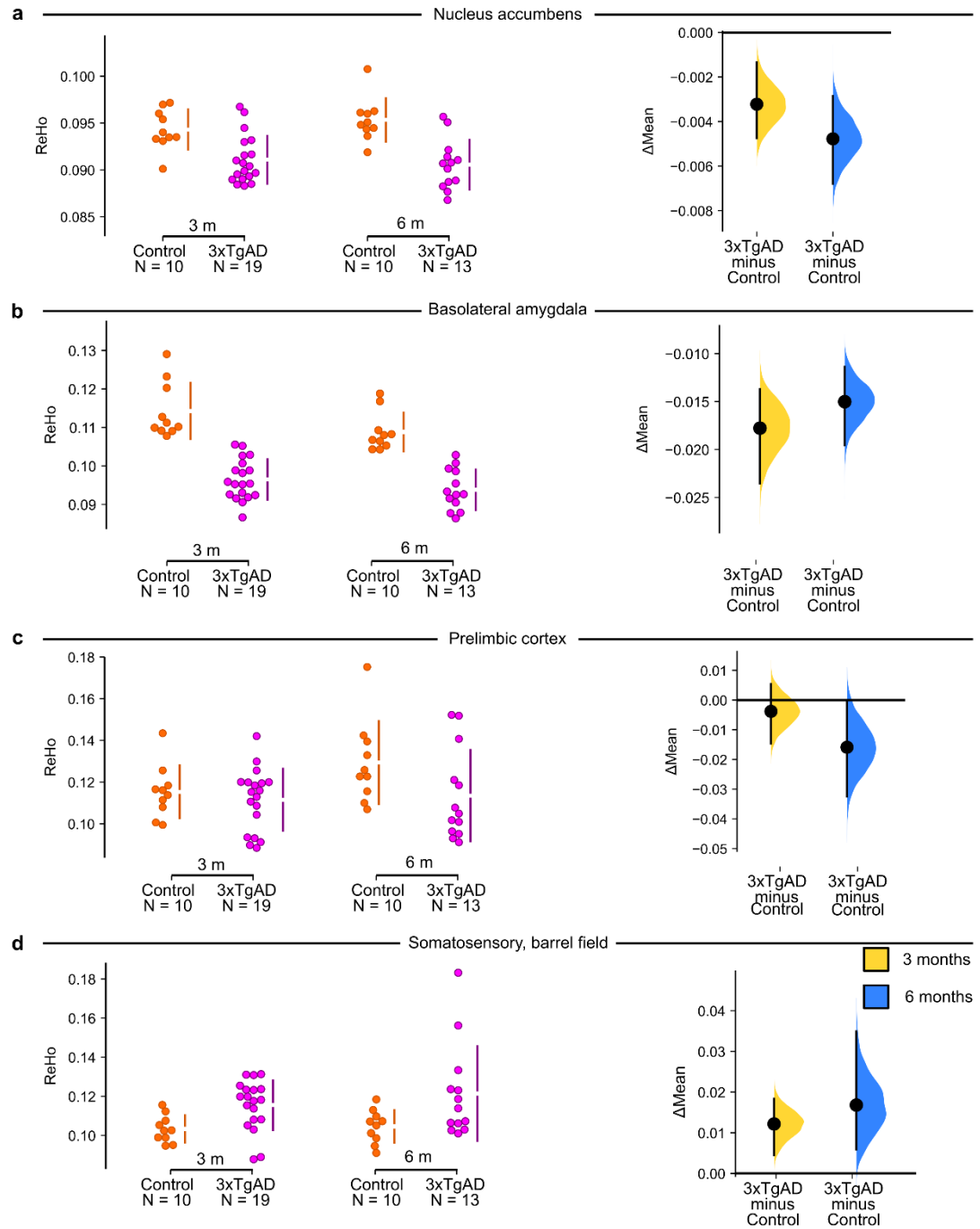


Figure S2: ReHo values extracted in selected ROIs show FC changes in 3xTgAD

3xTgAD mice show deficits in ReHo in regions encompassing the ACB (**a**), the BLA (**b**) and the PL (**c**). Increase in ReHo was found in somatosensory areas (SSp-bfd) suggests that FC deficits in 3xTgAD might be network-specific to AD-vulnerable regions (**d**). ACB: nucleus accumbens; BLA: basolateral amygdala; PL: prelimbic cortex; ReHo: regional homogeneity.

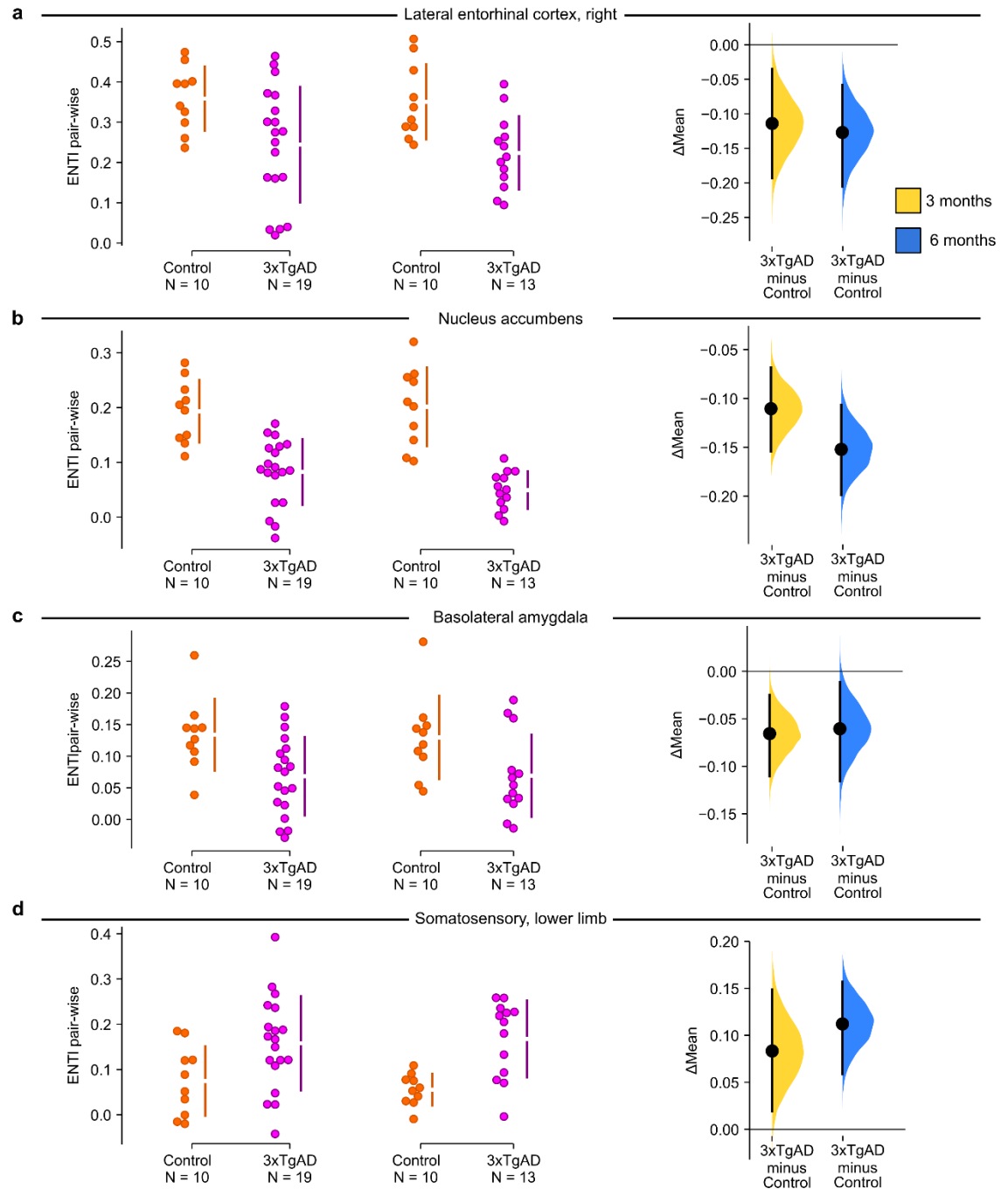


Figure S3: Pair-wise ROI interactions relative to the left-hemisphere ENTl

Compared to the left ENTl, 3xTgAD mice show a decrease in FC in right ENTl (**a**), ACB (**b**) and BLA (**c**). These results show consistent trend as in whole-brain ReHo, highlighting the relevance of ENTl as central hub for FC changes in 3xTgAD. **d**) FC in somatosensory regions is increased in 3xTgAD compared to controls, in pair-wise interaction with left ENTl.

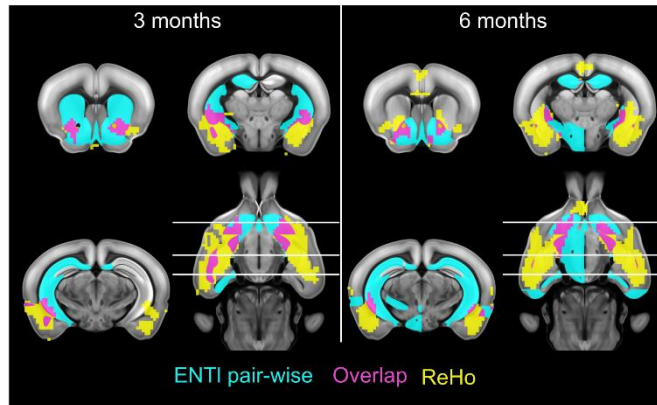


Figure S4: Restricted pair-wise ENTl at 3 months of age and 6 months of age overlapped with ReHo

Overlap between ReHo (yellow) and pair-wise interactions between ENTl and whole-brain regions (cyan) resulted in major hotspots of interest, consistent across ages.

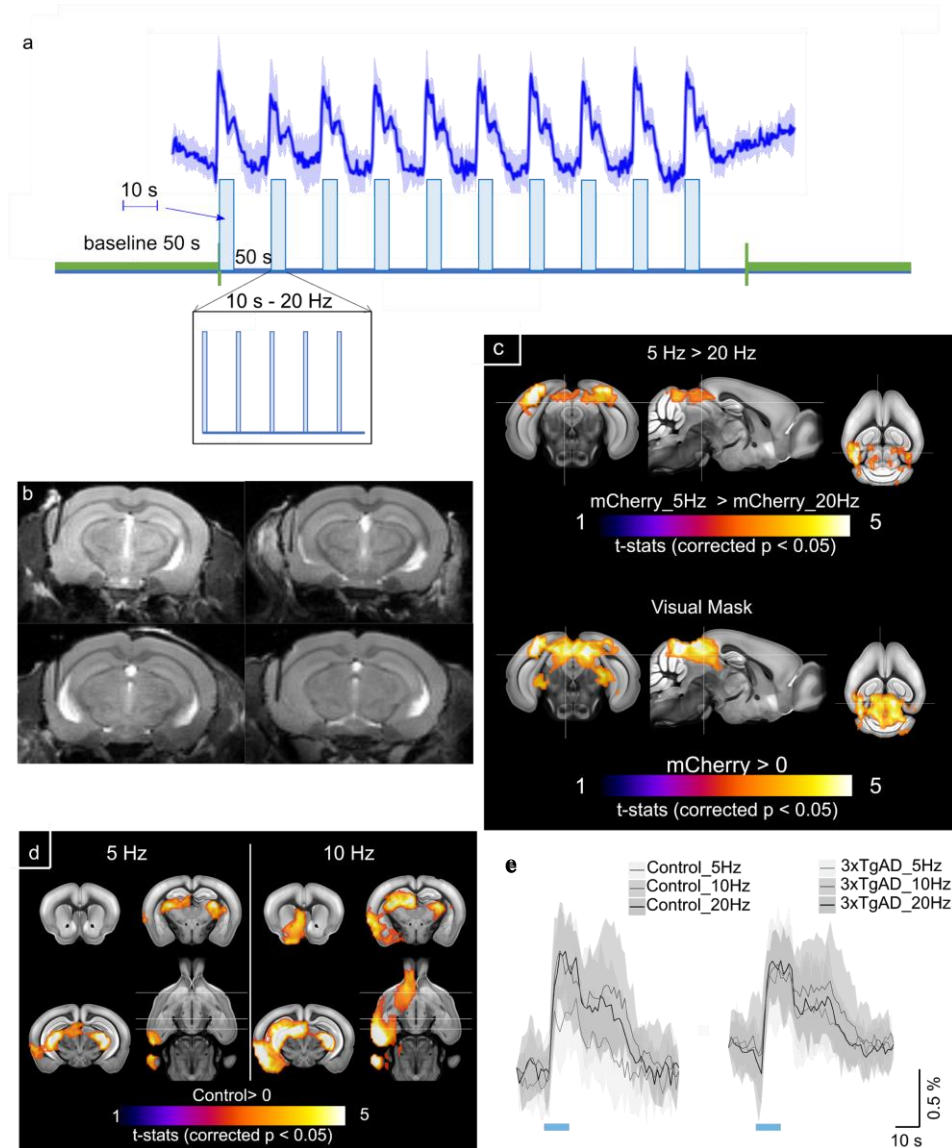


Figure S6: Experimental design for optogenetic stimulation and control validation

a) Stimulation design consisted of 50 s baseline and subsequent 10 blocks of 5, 10 or 20 Hz-pulses for 10 s, alternated by 50 s of rest with no stimulation; stimulation protocols were provided in random order. **b)** Anatomical scan shows the fiber positioning in 4 mice from the experimental group. **c) Top:** Two-sample t-test in mice transfected with mCherry shows that only lower frequencies, i.e., 5 Hz, engage a stronger response in the visual system, compared to 20 Hz stimulation. **Bottom:** Response derived from 5 Hz stimulation protocol was used to mask the regions that responded positively to visual stimulation. **d)** Mice injected with ChR2 show response to low frequencies, i.e. 5 and 10 Hz, here shown as the control group at 3 months of age. The response to 20 Hz stimulation was chosen for the rest of the analyses. **e)** Average BOLD response for the 10 blocks of stimulation across frequencies for controls and 3xTgAD (left and right respectively), represented in mean \pm SD.

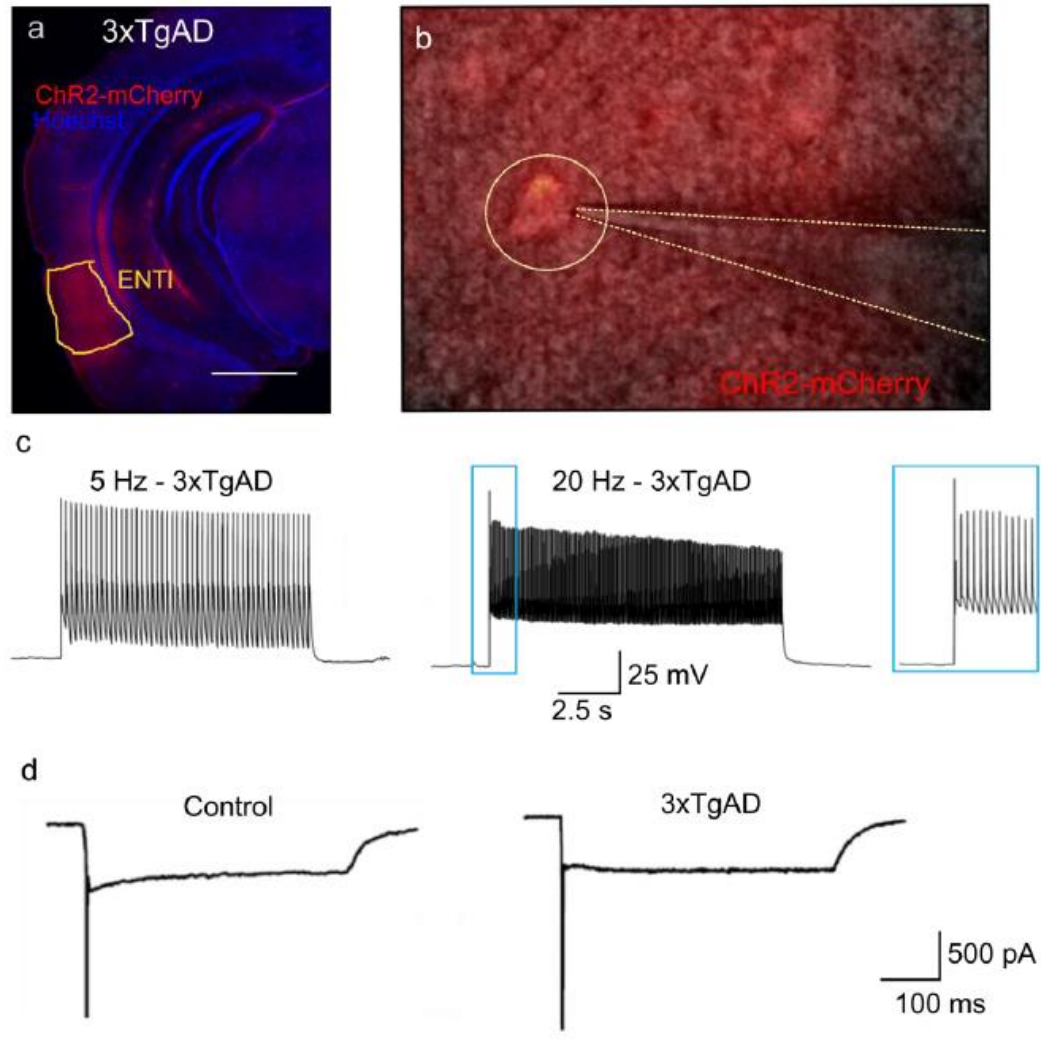


Figure S7: Optogenetic validation of pyramidal neurons in ENT1

Histological evidence for opsin expression in 3xTgAD mice co-stained with Hoechst neuronal cell bodies. whole-cell patch-clamping in a ChR2-expressing pyramidal neuron in the ENT1. **c)** 5 and 20 Hz stimulation of the patched neuron show faithful frequency-gated activity. **d)** Prolonged photostimulation (500 ms) applied under voltage-clamp mode (-60 mV) shows an initial action potential spike and a ChR2-induced inward current.

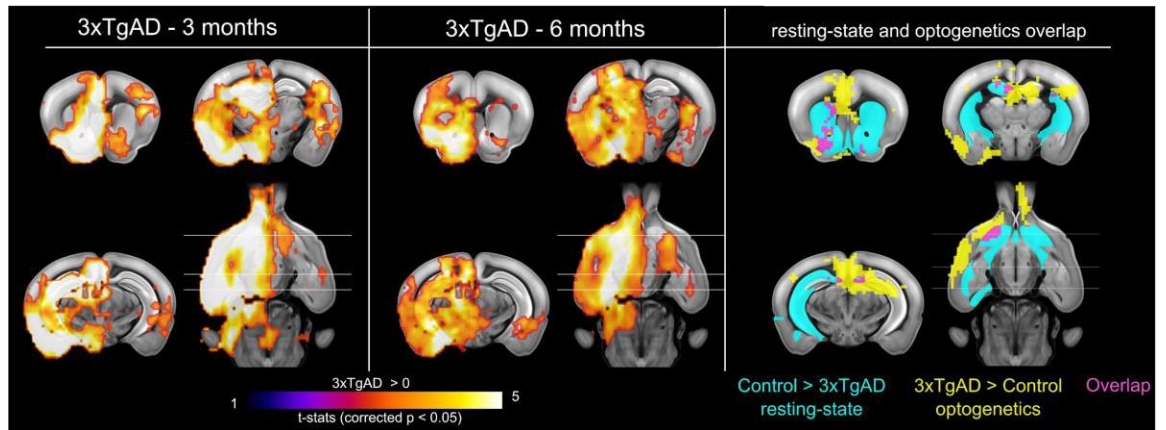


Figure S8: Optogenetically-locked BOLD response in 3xTgAD and overlap with resting-state FC

Left and middle panels indicating one-sample t-test for stimulation-locked BOLD response in the 3xTgAD mice ($p < 0.05$ corrected) at 3 ($N = 12$) and 6 ($N = 10$) months of age highlighting activation in key regions related to ENT1 projections, i.e. HIP, BLA, ACB. Right panel indicating resting-state FC analysis (cyan) and optogenetically evoked response (yellow) highlights overlapping *loci* for decrease in FC at rest and potentiated response during stimulation (pink).

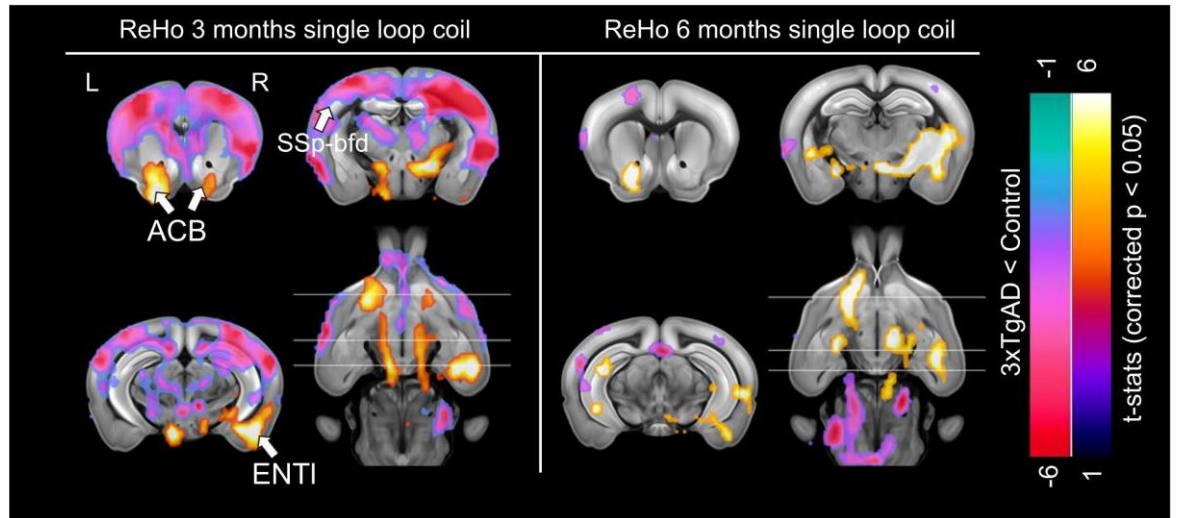


Figure S9: Resting-state fMRI with single-loop coil reveals similar patterns of FC deficits in 3xTgAD

ReHo analysis of rsfMRI with single-loop coil, acquired before the ofMRI protocols, reveals similar loss of coherence in AD-vulnerable brain regions, e.g. ENTl, ACB. Increase in ReHo in somatosensory areas is also in line with the results reported with the cryogenic coil. ENTl: lateral entorhinal cortex; ACB: nucleus accumbens; SSp-bfd: somatosensory barrel field cortex; ReHo: regional homogeneity.

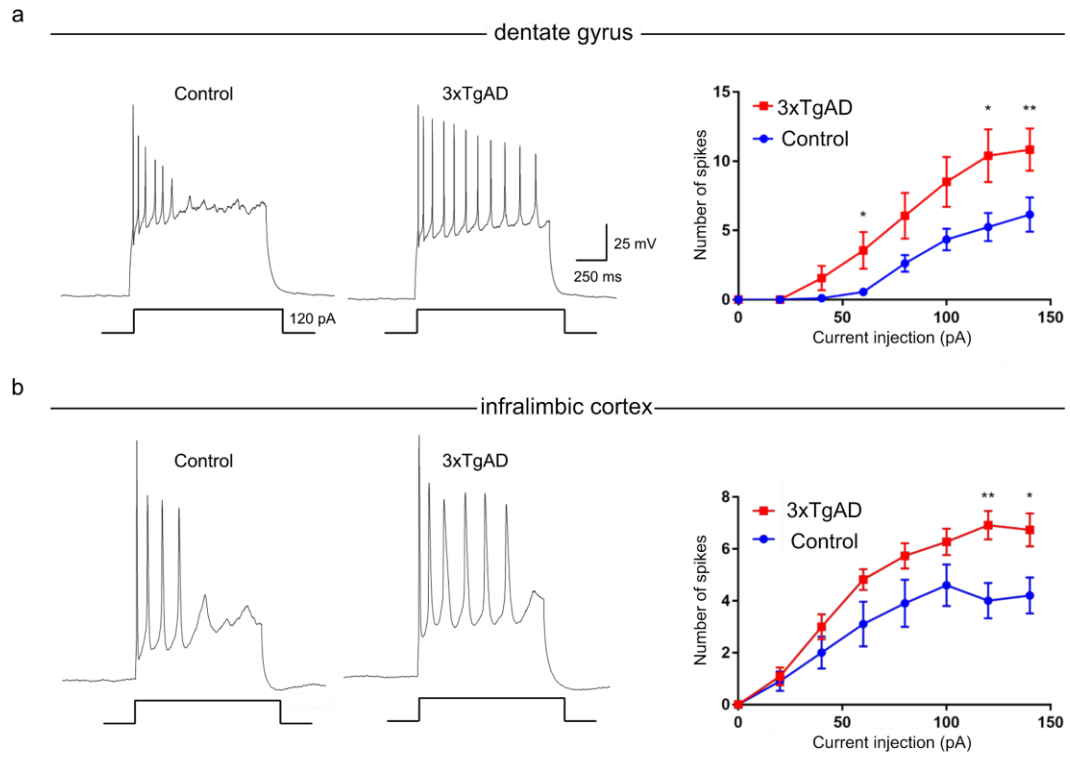


Figure S10: Intrinsic neuronal properties between controls and 3xTgAD

Representative firing pattern of action potential with 120 pA injection on **(a)** granule cells of dentate gyrus (controls: N = 4, n = 29 / 3xTgAD: N = 5, n = 18) and **(b)** pyramidal cells of infralimbic cortex (controls: N = 4, n = 10 / 3xTgAD: N = 4, n = 11) from each mouse line were shown, left side of each panel. The number of action potential spikes was counted from various injected currents on **(a)** granule cells in dentate gyrus and **(b)** pyramidal cells in infralimbic cortex, right side of each panel. The data were plotted by mean number of action potential with SEM. The statistical significance was presented with asterisk (* $p < 0.05$, ** $p < 0.01$ by Mann-Whitney U test; N = number of animals, n = number of cells).

~ Chapter 4 ~

Paper 2

Rationale behind Paper 2

With the work conducted in Paper #1, whole-brain FC changes in the young 3xTgAD mouse have been reported by means of high-field fMRI. Specifically, FC decrease in areas vulnerable to tau deposition were evident by 3 months of age. Conversely, with optogenetically-driven stimulation of the excitatory neurons in the ENTl, an increase in BOLD signal was identified in downstream targets of the ENTl. The dichotomic relationship observed between resting-state and evoked-state conditions cannot be readily interpreted, as the fMRI readouts (in both circumstances) are a product of the underlying neurovascular coupling. As such, the aim of the second part of this project was to gain information on the neuronal scale of events, carried out through electrophysiological recording and stimulation *in vivo*.

In order to achieve the above aim, electrophysiological recordings were analysed in the same mouse model at the same age-points to gain insight into the underlying synaptic physiology within disease-relevant regions of interest displaying AD-like pathology. Although a major disadvantage of targeted electrophysiology *in vivo* is the limited ‘field of view’, by choosing the same target regions as in fMRI, i.e., the activation of ENTl (Paper 1), it is possible to investigate further the evoked-state, already reported with ofMRI. Electrophysiological recordings *in vivo*, therefore, provide further insight in the underlying physiological mechanisms that result in the FC changes seen with rsfMRI and ofMRI (Paper 1).

Title: 3xTgAD mice express early synaptic hyperexcitability in the amygdala and dentate gyrus following activation of the lateral entorhinal cortex *in vivo*

Francesca Mandino^{ab*}, Bin Zhu^a, Marcelo Montemurro^a, Joanes Grandjean^c, John Gigg^a

a Faculty of Biology, Medicine and Health, The University of Manchester, Manchester, United Kingdom

b Singapore Bioimaging Consortium, Agency for Science, Technology and Research, 11 Biopolis Way, Singapore 138667, Singapore

c Department of Radiology and Nuclear Medicine & Donders Institute for Brain, Cognition, and Behaviour, Donders Institute, Radboud University Medical Centre

Corresponding author

Francesca Mandino,

Faculty of Biology, Medicine and Health, The University of Manchester, Manchester, United Kingdom mandino.francesca@gmail.com

Keywords: 3xTgAD, mouse, Alzheimer's disease, electrophysiology, *in vivo*

4.1 Abstract

Alzheimer's disease (AD) is a neurodegenerative state resulting in memory loss, emotional changes such as heightened aggression and a later gradual decline in executive function.

This pathology targets preferentially the hippocampal formation and amygdala within the medial temporal lobes of patients. This can be visualised as the gradual accumulation of insoluble beta-amyloid plaques and hyperphosphorylated protein tau aggregates, resulting in progressive neuronal cell death and brain atrophy. Changes in synaptic integrity among the key hubs expressing this pathology are thought to be one of the major factors for AD symptom development.

Mouse models engineered to recapitulate AD features represent a fundamental step to establish early prodromal disease markers, giving access to direct neuronal measurements. Indeed, there is growing evidence that an early marker in these models and AD patients is synaptic hyperexcitability, perhaps resulting from intracellular, particularly presynaptic, accumulation of soluble beta-amyloid. The 3xTg mouse model for AD shows cognitive deficits already by 3-4 months of age, that is before overt amyloid accumulations are found in the brain. Here, we investigated synaptic circuit integrity over this age range among key regions for AD progression, through electrophysiological recordings *in vivo*. Electrical stimulation of the lateral entorhinal cortex revealed increased neuronal connectivity with both mid-septo-temporal dentate gyrus and basolateral amygdala in 3-month old male 3xTgAD mice. Moreover, increased short-term synaptic plasticity in 3xTgAD mice was also found in these two connections at 3-months, which was also seen in a 6-months age group. These results demonstrate increased facilitation in the amygdala for the first time in an AD model and extend the presence of similar changes to more ventral dentate gyrus. Overall, our work further supports the view that synaptic changes are among the earliest markers of AD-like pathology the 3xTgAD mouse and further support the translational relevance of this model to AD patients.

4.2 Introduction

Alzheimer's disease (AD) is the most common form of dementia and it is commonly associated with the overt accumulation of beta-amyloid (A β) plaques and neurofibrillary tangles of hyperphosphorylated tau protein aggregates (NFTs; Selkoe, 2008, 1997). The typical phenotype of AD results in a progressive cognitive loss, starting with episodic memory (Bäckman et al., 2004) and progressing to emotional memory and emotional learning, fear and anxiety (Cohen and Paz, 2015; Gallagher and Chiba, 1996; Paz and Pare, 2013). It has been shown, however, that cognitive deficits are poorly correlated with A β plaque load in AD patients (Berg et al., 1998). Furthermore, studies on subjects suffering from mild cognitive impairment (MCI), a precursor to AD in many cases, show episodic memory deficits before pre-plaques appearance, i.e., at stages where only soluble intracellular A β forms are found (Selkoe, 2008, 1997). Thus, there is a growing interest and focus on the role of soluble A β oligomers as a key culprit for early cognitive decline in AD. AD is commonly correlated with synaptic transmission changes in local and distributed circuits within the hippocampal formation, which may result in the reported memory deficits (Selkoe, 2002).

However, the genotype-to-phenotype physiological mechanisms underlying cognitive decline are still not fully understood: the functional synaptic connectivity across the earliest targets of AD pathology, leading to memory deficits, needs further exploration. The key regions affected in early AD progression encompass the medial temporal lobe (Jobst et al., 1994). Specifically, the entorhinal cortex (lateral part, ENTl) is one of the first regions to show pathology in human AD (Braak and Braak, 1995) and is a vital interface between the hippocampal formation and the neocortex, playing a key role in memory encoding and retrieval (Buckmaster, 2004; van Groen et al., 2003). ENTl layer II is

monosynaptically connected with the dentate gyrus (DG) of the hippocampal formation through the perforant pathway (Hyman et al., 1986).

Together, ENTl and DG, represent the first node of the trisynaptic circuit (Witter, 2007b). Recent work has shown that DG may contribute to memory formation, through neurogenesis (Toda et al., 2019; van Praag et al., 1999), as well as working as a hub between ENTl and hippocampus proper (i.e. Cornu Ammonis fields; Nakashiba et al., 2012). The function of DG is often related to pattern separation, particularly to disambiguate episodic memories that share elements such as different events that occur in the same encoding context (Yassa et al., 2010).

Additionally, the amygdala, particularly the basolateral nucleus (BLA), is a central hub for emotional memory, fear and anxiety processing and is a key region in facilitating declarative memory encoding in situations with high emotional arousal (Bazelot et al., 2015; Paz and Pare, 2013; Roozendaal and McGaugh, 2011). The BLA and ENTl are some of the earliest targets for toxicity in AD (Booth et al., 2016; Khan et al., 2014; Nelson et al., 2018). The deep layers of the ENTl receive monosynaptic inputs from the BLA (Brothers and Finch, 1985; Maren and Quirk, 2004; Xu et al., 2016) and strong connections are also seen from ENTl to BLA in rat (Agster et al., 2016; Ferry et al., 2006; Tomás Pereira et al., 2016). **Figure 3.1a** represents a schematic of the main circuitry involving BLA, ENTl and DG.

Animal models such as transgenic mice overexpressing human genes associated with familial AD represent an important approach to investigate the neuronal changes caused by AD-like pathology. The 3xTgAD mouse model carries transgenes for human PS1M146V, APPSWE and TauP130L. It recapitulates the major features of AD development in a similar spatiotemporal fashion to that seen in AD patients, in that it develops both A β plaques and NFTs later in life (Mastrangelo and Bowers, 2008).

Moreover, 3xTgAD mice show cognitive deficits prior to plaque deposition, rendering this a good candidate model to investigate prodromal stages of AD-like pathology (Davis et al., 2013b; Marchese et al., 2013; Mastrangelo and Bowers, 2008). Changes in synaptic activity and connectivity have been found in hippocampal regions including the ENT in transgenic mouse models, compared to healthy controls, such as the PDAPP mouse model for AD-like pathology or rTg4510 model for tauopathy (Booth et al., 2016; Larson et al., 1999; Moechars et al., 1999).

To date, the majority of studies investigating neuronal excitability and synaptic connectivity have been conducted *in vitro*, by performing electrophysiological recording on isolated brain regions; these have highlighted a disruption in neuronal connectivity in several mouse lines for AD-like pathology (Chapman et al., 1999; Fitzjohn et al., 2001). Electrophysiological recordings in slices of the 3xTgAD mouse model bring supporting evidence for a loss of synaptic transmission assessed *in vitro* (Oddo et al., 2003).

Conversely, work *in vivo* highlights hyper-excitatory behaviour in 3xTgAD hippocampal regions (Davis et al., 2014; Palop et al., 2007). It is, therefore, necessary to investigate further the synaptic changes in a specific brain region whilst embedded within the brain, in order to preserve the bidirectional cortical connectivity, crucial for memory encoding and retrieval. Here for the first time in 3xTgAD mouse, we investigated synaptic integrity between ENTl and its BLA and DG post-synaptic targets *in vivo*. We hypothesised a genotype effect on synaptic integrity in the regions of interest (ROIs) in 3xTgAD mice compared to matched controls. By performing evoked Local Field Potential (LFP) recordings in BLA and DG following electrical stimulation of the ENTl, we assessed synaptic integrity and short-term plasticity in 3xTgAD mice at 3 and 6 months of age, in order to study prodromal stages of AD-like pathology.

4.3 Methods

4.3.1 Animals

All procedures were performed in accordance with the UK Animals (Scientific Procedures) Act 1986. Male 3xTgAD and control mice on the same background strain (129sv/c57bl6) aged either 3-4 months (N = 6 and N = 7, respectively) or 6-7 months old (N = 4 and N = 4, respectively) were used for these experiments to monitor the impact of early stages of AD-like pathology (Billings et al., 2005; Davis et al., 2013b; Mastrangelo and Bowers, 2008). Mice were housed as 5 cage-mates by sex and genotype in a pathogen-free environment on a 12 h light: dark cycle with food and water available *ad libitum*.

4.3.2 Anaesthesia and surgery

Anaesthesia was induced via intraperitoneal (i.p) injection of urethane (1.5-1.7 g/kg of 30% w/v solution prepared in 0.9% saline; ethyl carbamate Sigma, UK). An additional dose of urethane (50 µl of 10% w/v urethane solution prepared in 0.9 % saline) was administered if complete areflexia was not reached after 40 minutes from the first injection. Mice were mounted and fixed in a stereotaxic frame and mouse adapter (Kopf 1430, USA) to immobilise the head prior to surgery. Body temperature was maintained around 37°C throughout the duration of the whole experiment with the use of a homoeothermic blanket (Harvard, UK) and a rectal thermistor probe placed underneath the abdomen.

4.3.3 Surgery

A midline scalp incision was made and the skin retracted to expose the skull. After identifying Bregma and Lambda, the distance between these two landmarks was measured and compared to the standard 4.2 mm reported in the mouse brain atlas (Paxinos and

Franklin, 2004). Differences between the two measurements allowed a proportional adjustment for craniotomy coordinates to improve the accuracy of electrode placement. Craniotomies were made above the left hemisphere using a 0.9 mm drill bit (Fine Science Tools, Germany) and a high-speed handheld drill (Foredom, USA). Care was taken to maintain the craniotomy sites moist during the whole surgery procedure. Coordinates for craniotomy and electrode placement were marked onto the skull, relative to Bregma and the midline for recording in BLA (Bregma: AP -2.5 mm, ML: 2 mm) and DG (Bregma: AP -3.5 mm, ML: 2.5 mm), as well as stimulation of ENTl (Bregma: AP -2.8 mm, ML: 4.2 mm). Recording electrodes consisted of 32-contact probes, each laid out as 2 shanks of 16 electrodes that were 500 μ m apart with 100 μ m between recording points (A2x16-10-500-100-413, NeuroNexus Technologies, MI).

These were first lowered to target locations (BLA target was 4 mm ventral from brain surface at a 15° angle from vertical in the coronal plane; the DG target was also 4 mm ventral to brain surface but along a vertical plane) and then used to record brain activity during different stimulation protocols. The 2 recording electrode shanks were coated in Vibrant CM-DiI (Sigma, UK) cell-labelling solution to allow post-mortem localisation of their location with *post hoc* fluorescence microscopy.

The stimulation electrode consisted of twisted, 125 μ m diameter Teflon-insulated stainless-steel wires (Advent RM, UK) and was inserted an initial 3 mm from the brain surface in one step and then slowly lowered further during continuous application of stimulating pulses (50 ms paired-pulse stimulation (PPS), 300 μ A) until the expected responses in DG and BLA were seen on an oscilloscope. The inter-regional connectivity across the ROIs targeted is shown in **Figure 4.1**, together with the final placements for recording electrodes.

4.3.4 Data acquisition

All data were recorded on a Recorder64 system (Plexon Inc, USA), and saved for offline analysis. Electrodes were connected to a headstage (fixed gain of x20) and then to a preamplifier for a total gain of x500. LFP were recorded at a sampling rate of 5 or 10 kHz using a 12-bit A/D converter and then stored for offline analysis. A low pass filter (1 kHz) was applied to remove spiking activity. Responses on up to 4 electrodes could be visualised during the experiment on an oscilloscope (HAMEG Instruments GmbH, US).

Electrical stimuli were delivered by a constant-current stimulator (DS3, Digitimer, UK), triggered by analogue 5 V square wave pulses from a National Instruments PCI card (PCI-6071E). Timings and types of stimuli to be delivered were controlled through custom-written programs in LabVIEW (v8, National Instruments). Stimulus duration was fixed at 200 μ s throughout each protocol. Firstly, the stimulating electrode was lowered gradually into position whilst PPS was applied (interval 50ms, 3s between pairs) until the typical evoked field excitatory postsynaptic potential (fEPSP) responses for BLA and DG were established.

Specifically, a fast negative fEPSP was detected in the BLA, peaking around 4-5 ms after the stimulus, followed by a slower positive overshoot, consistent with previous literature (Maren and Fanselow, 1995). Within DG, a positive initial fEPSP response, typical of the molecular layer of DG, was recorded in each mouse (**Figure 4.1b**, left inset). The dotted line in left and right panels of **Figure 4.1b** represents examples of the initial fEPSP response slope in both DG and BLA, respectively, measured during these experiments. Once a typical fEPSP response profile was obtained in both BLA and DG, two different protocols of stimulation were performed: Input/Output (I/O) and PPS. In each mouse, the channel with the most distinctive response (as revealed through current source density analysis *post hoc*; see below) was selected for further analysis.

4.3.5 Stimulation protocols

Input/output curve

The IOC reflects the functional strength of synaptic connectivity: by applying different current intensities, it is possible to analyse how the response (Output) changes as a function of input strength (Input). The range of current intensities used here was 180, 300, 450 and 600 μA .

Paired-pulse stimulation

To measure short-term synaptic plasticity, stimulus current was set to half-maximum of the response obtained in the BLA I/O paradigm, i.e., c.300 μA , and paired-pulses were delivered at this current with different paired-pulse intervals (PPI) for 20 repetitions each. The range of intervals was 20, 50, 100, 200, 500 and 1000 ms.

4.3.6 Data analysis

Current source density

Once all data were collected, current source density analysis (CSD) was carried out in each mouse to facilitate the selection of the optimal response channels in each ROI (**Figure 4.1c**). CSD analysis provides a spatio-temporal map of the various current sinks and sources recorded throughout tissue sampled by the electrodes (Freeman and Nicholson, 1975). As such, sources are plotted in red colour representing negative CSD values (positive current), sinks are plotted in blue to indicate positive CSD values (negative current) and neutral regions are visualised in green. Through CSD analysis it was possible to isolate the shortest latency electrode responses corresponding to the strongest source/sink signal, therefore, allowing for further analysis as the contact most likely to lie next to excitatory synaptic active zones. **Figure 4.1c** reports an example of CSD for one

3xTgAD and one control mouse at 3 months of age: qualitative analysis highlights stronger CSD values in 3xTgAD in both BLA and DG (**Figure 4.1c**, right section of both left and right images) compared to age-matched controls.

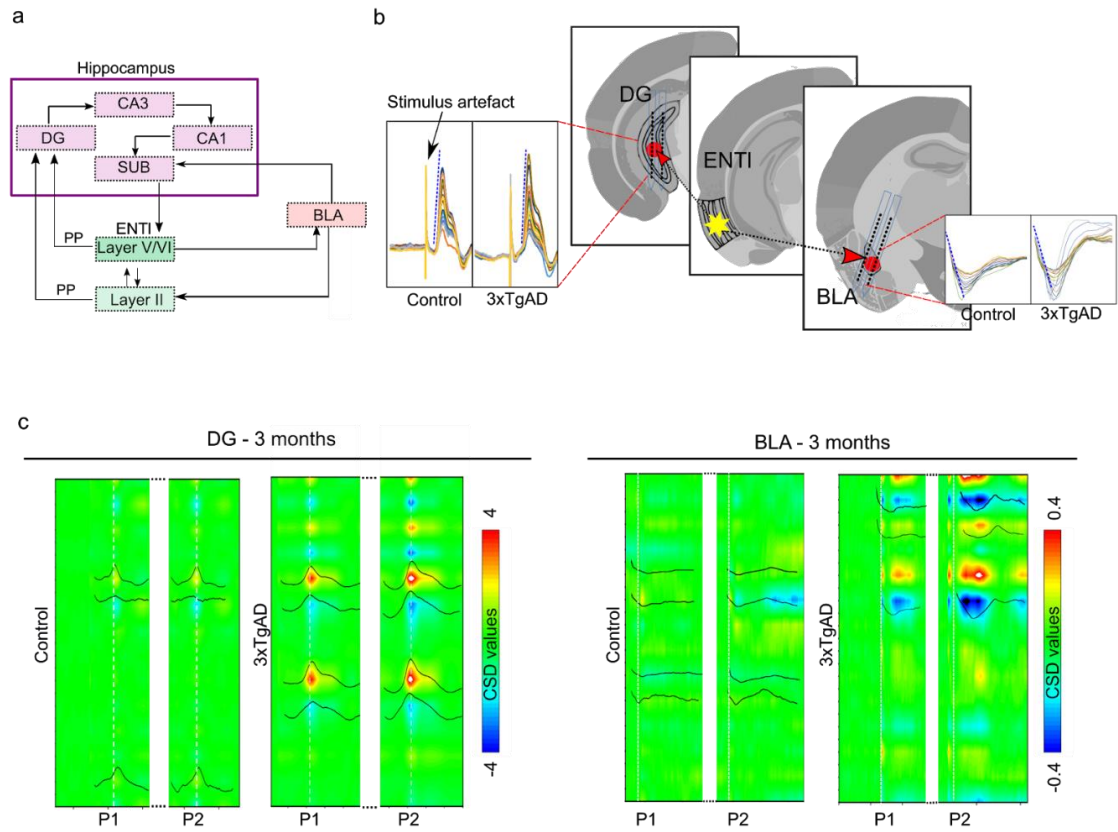


Figure 4.1: Neuronal circuitry in the medial temporal lobe, electrodes location and CSD

a) Schematic view of the synaptic connections among the ENTl, within the hippocampal formation, and BLA. ENTl is connected mono-synaptically to the DG through the PP and from layers V and VI to the BLA. **b)** Representation of the stimulating and recording electrodes and raw data. The stimulating electrode was targeted to ENTl with recording electrodes in DG and BLA. Left and right insets show raw fEPSPs recorded in one control and one 3xTgAD mouse for DG and BLA, respectively, at 3 months. No major differences could be seen between the spatial distribution of sinks and sources in response profiles between transgenic and control mice. The fEPSP response in DG results showed a positive-going response, whereas, that for BLA showed a fast, negative-going event. **c)** CSD analysis for one control and one 3xTgAD at 3 months with current sources (red) and sinks (blue). Green indicates neutral regions. Left panels represent CSD values in DG while those on the right are from BLA. Both panels represent fEPSPs evoked by 50 ms paired-pulse stimulation. ENTl: lateral Entorhinal Cortex; DG: Dentate Gyrus; CA: Cornus Ammonis; SUB: Subiculum; BLA: Basolateral Amygdala; PP: perforant pathway; P1: Pulse 1; P2: Pulse 2; CSD: Current Source Density; fEPSP: field excitatory postsynaptic potential.

The different cyto-architecture of BLA and DG may result in their different CSD profiles, with BLA showing a more localised (closed-field) CSD signal than the DG, which has a more laminar structure (open-field).

IOC and PPS statistics

For the IOC protocol, stimulation at each current intensity was repeated 20 times (runs), the initial slope of the fEPSP response measured for each repetition and then these 20 values were averaged. The mean response to each current step for each mouse was used to plot the I/O curve of response to current intensity by genotype, age and ROI. For the PPS protocol, the slope for the initial fEPSP response on a selected channel was measured for both stimuli (P1, P2) in each pair. For each pair, the fEPSP response to the second stimulus (P2) was normalised to that of the first (P1) and expressed as a ratio, such that positive values indicate synaptic paired-pulse facilitation (PPF) and negative values synaptic PP depression (PPD).

$$PPI = (P2 - P1) / P1 \quad (3)$$

In the case of synaptic facilitation $PPI > 0$, whereas, $PPI < 0$ for synaptic depression.

For both the IOC and PPS results, statistical analysis was performed using the statistical software R 3.6.1 (The R Foundation for Statistical Computing). Responses to the I/O (initial slope for P1) and PPI (ratio between P2 and P1) paradigms in BLA and DG at the two age groups were analysed separately with a linear mixed model analysis, using ROI, age, genotype, amplitude/intervals (amplitude for IOC and interval for PPS), and their mutual interactions as fixed effects and animal intercepts and runs repeats as random

effects using R package *lme4*. Interaction effects were determined using a likelihood ratio test. A *post hoc* analysis was performed after a general linear hypothesis test using contrast to determine genotype effects at each stimulation amplitude or interval. Correction for multiple comparisons was implemented during the contrast analysis using the R package *multcomp* (Bates et al., 2015; Bretz et al., 2016). Data are plotted as mean \pm standard error (SEM).

4.3.7 Perfusion and histology

At the end of the experiment, an additional dose of urethane (30%) was administered to the animals (i.e., terminal anaesthesia); the animals were then transcardially perfused with 0.9% saline, followed by 4% paraformaldehyde (PFA). The brain was then extracted, placed in 4% PFA and refrigerated for 24 hours. After this, the brain was then transferred to 30% sucrose solution until it sank. After the fixation of the brain and sinking in sucrose, the left hemisphere was removed and coronal sections 50 μ m thick were made using a freezing microtome (Leica, UK). Sections were mounted onto subbed slides and allowed to dry overnight in the dark. Finally, they were imaged using a 3D Histech, Panoramic 250 Flash III digital slide scanner system (3DHistech, Hungary). The images were viewed using CaseViewer software (3DHistech, Hungary) for visualization of DiI.

4.4 Results

To investigate synaptic integrity in the early stages of AD-like pathology in the 3xTgAD mouse model, we recorded evoked fEPSPs in the DG and BLA following electrical stimulation of ENTl inputs. In both ROIs it was possible to establish a typical response profile: BLA showed an initial negative fEPSP, whereas, DG was characterised by a steep positive fEPSP. In both ROIs, the general response profile was not altered by genotype: suggesting a relatively spatiotemporally preserved input from the ENTl to both DG and BLA at these age points.

Once a typical response profile was established in each ROI, electrical stimulation with multiple stimulation paradigms (IOC and PPS) was performed to test for synaptic integrity between ENTl and post-synaptic targets. Specifically, stimulation of the ENTl was firstly performed with varying current intensities, ranging from 180 μ A to 600 μ A (IOC). Subsequently, pairs of stimuli at 50% of the maximum response size on the IOC were provided at different time intervals, ranging from 20 ms to 1000 ms, in order to assess short-term synaptic plasticity (PPS).

4.4.1 Synaptic strength: current-response input/output

In the IOC analysis for synaptic strength, a quadruple interaction effect was reported between ROIs, age, genotype, stimulation amplitude: $F(35,32) = 108.31$, $p < 0.001$. Additionally, the field response to increasing current amplitudes was analysed in both BLA and DG (**Figure 4.2a,b** respectively) at 3 months ($N_{\text{controls}} = 5$, $N_{3\text{xTgAD}} = 4$, **Figure 4.2** left panels) and 6 months (controls $N_{\text{controls}} = 4$, $N_{3\text{xTgAD}} = 3$, **Figure 4.2** right panels).

BLA I/O curve

No significant aging effect was found in control BLA between 3 and 6 months of age. There was, instead, a significant effect of ageing in 3xTgAD mice between 3 and 6 months of age for currents $> 180 \mu\text{A}$ (**Figure 4.2a**). Hence, 6-month-old 3xTgAD mice showed larger responses compared to 3 month-old 3xTgAD mice at $300 \mu\text{A}$ ($z = -2.65$, $p < 0.05$), $450 \mu\text{A}$ ($z = -3.25$, $p < 0.005$) and $600 \mu\text{A}$ ($z = -3.19$, $p < 0.005$). At 3 months of age, there was no significant difference in response between controls and 3xTgAD ($p > 0.5$; **Figure 4.2a**, left panel). A strong difference in response was instead found at 6 months of age, where 3xTgAD mice had significantly larger responses than controls at $180 \mu\text{A}$ (z-score -3.381 , $p < 0.005$), $300 \mu\text{A}$ ($z = -6.23$, $p < 0.001$), $450 \mu\text{A}$ ($z = -6.64$, $p < 0.001$) and $600 \mu\text{A}$ ($z = -7.1$, $p < 0.001$; **Figure 4.2a**, right panel).

DG I/O curve

Interestingly, whilst there was no significant aging effect in 3xTgAD between 3 and 6 months of age, there was a significant effect in controls: 3-month-old controls showed significantly weaker responses to $180 \mu\text{A}$ compared to 6 months ($z = 2.32$, $p < 0.05$). Across genotypes, 3xTgAD mice showed larger responses than controls by 3 months of age (**Figure 4.2b** left panel; $300 \mu\text{A}$ z-score = 2.36 , $p < 0.05$; $450 \mu\text{A}$ z-score = 2.6 , $p < 0.05$ and $600 \mu\text{A}$ z-score = 2.93 , $p < 0.005$; $180 \mu\text{A}$ n.s.), whereas, at 6-months of age there was a significant difference between genotypes only for the strongest current stimulus ($600 \mu\text{A}$, z-score = 2.12 , $p < 0.05$), although there was a trend for increased facilitation in 3xTgAD mice compared to controls (**Figure 4.2b** right panel).

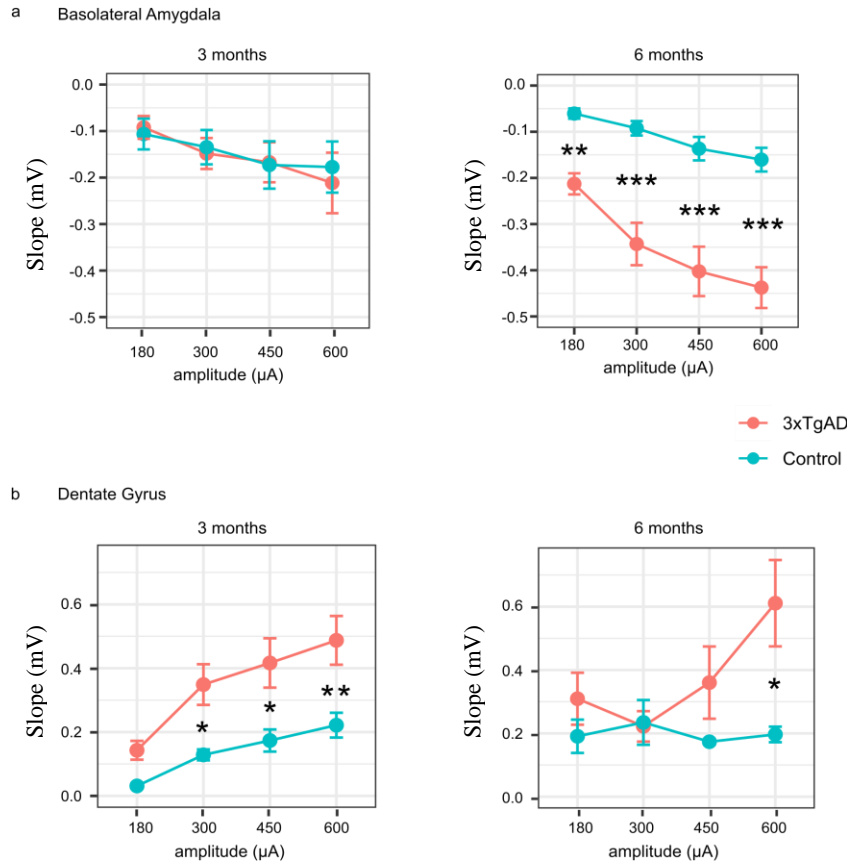


Figure 4.2: Input/Output curves for BLA and DG response to ENTl stimulation at 3- and 6-months of age show strengthening of synaptic connectivity in 3xTgAD

a,b) I/O curve for 3 (left) and 6 (right) month-old 3xTgAD mice and matched controls in BLA (top) and DG (bottom). Data are plotted as mean initial fEPSP slope values \pm SEM. * $p < 0.05$, ** $p < 0.005$, *** $p < 0.001$. ENTl: lateral entorhinal cortex, BLA: basolateral amygdala; DG: dentate gyrus; I/O: input/output; SEM: standard error of the mean.

4.4.2 Paired-pulse stimulation shows hyper-excitability in 3xTgAD

Short-term plasticity was assessed with paired-pulse stimulation at varying intra-pair intervals. The current intensity was set to 300 μ A, corresponding to approximately half-maximum of the stimulus current intensity performed with IOC in the majority of the regions and ages. As for IOC results, a quadruple effect between ROI, age, genotype and intervals was found for the PPS paradigm: $F_{(51,46)} = 28.135$, $p = 3.425e-05$.

Paired-pulse stimulation in BLA

Interestingly, an ageing effect was found in the BLA responses of controls for 50 ms PPS, where 3 month-old controls showed PPF and 6 month-old controls showed depression ($z = 3.22$, $p < 0.01$). By 3 months of age, control animals showed facilitation in BLA at intervals > 20 ms; for the shortest interval of 20 ms, there was, instead, evidence for paired-pulse depression (**Figure 4.3a** left panel), which suggests an initial inhibitory effect via GABA_A receptors. For the longest intervals of 500 and 1000 ms, there was no difference between P1 and P2 in controls. 3xTgAD mice showed the greatest facilitation to shorter intervals with no facilitation for intervals of 500 and 1000 ms. A significant genotype effect was seen in the BLA by 3 months of age at the shorter intervals, where a significant increase in PPF was found in 3xTgAD compared to controls (20 ms, z -score = -3.96, $p < 0.001$; 50 ms, z -score = -3.11, $p < 0.05$; **Figure 4.3a** left panel). 3 month- and 6 month-old 3xTgAD mice showed increased facilitation compared to age-matched controls at the shorter intervals (20 ms, z -score = -3.33, $p < 0.005$; 50 ms, z -score = -4.34, $p < 0.001$; **Figure 4.3a** right panel), therefore, bringing supporting evidence for a genotype effect affecting short-term plasticity.

Paired-pulse stimulation in DG

In control animals, there was a significant aging effect at 100 ms, where 3 months-old mice showed facilitation and 6 months-old mice showed depression. However, the trend at both ages highlighted only weak facilitation or depression in controls. No aging effect was seen in the 3xTgAD responses, with animals showing increased facilitation at shorter intervals compared to controls at both 3 months of age (20 ms, z -score = -3.16, $p < 0.01$; 50 ms, z -score = -4.54, $p < 0.001$; **Figure 4.3b** left panel) and 6 months of age (20

ms, z-score = -3.5, $p < 0.001$; 50 ms, z-score = -3.6, $p < 0.001$; 100 ms, z-score = -3.2, $p < 0.01$; 200 ms, z-score = -2.3, $p < 0.05$; **Figure 4.3b** right panel).

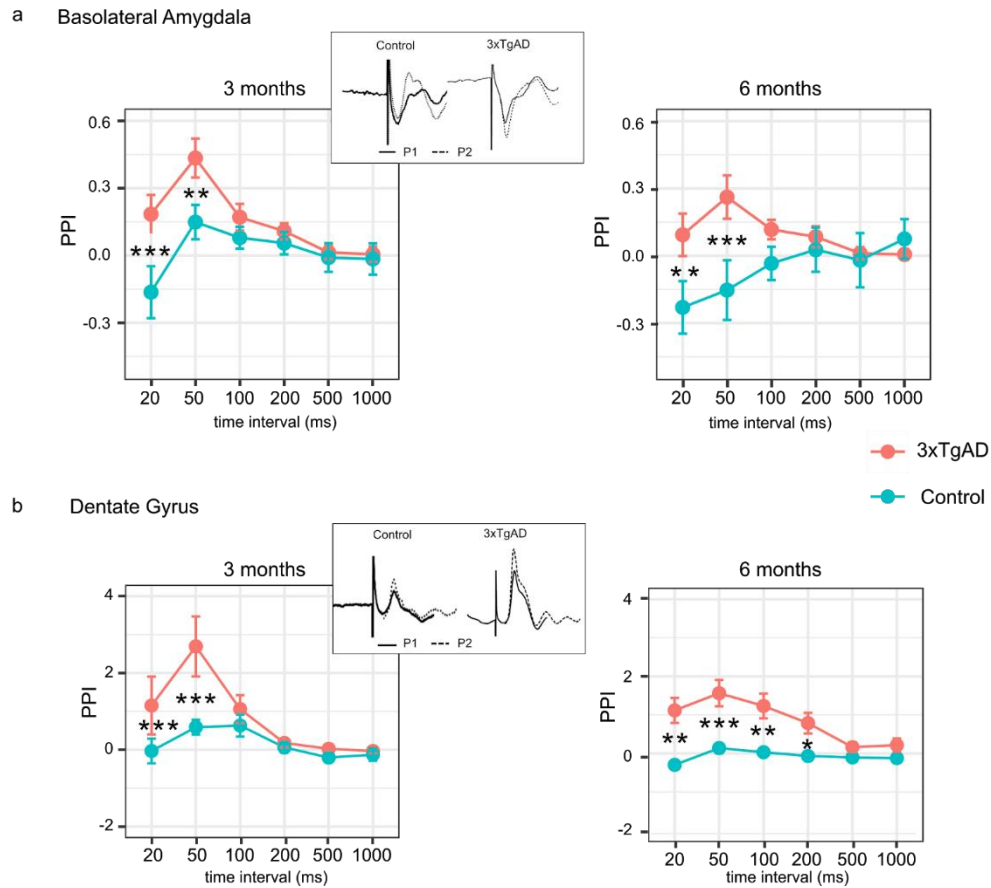


Figure 4.3: Paired-pulse stimulation in BLA and DG at 3 and 6 months of age shows increased facilitation in 3xTgAD

a,b) Response to ENTl stimulus pairs (PPS) with intervals of 20, 50, 100, 200, 500 and 1000 ms. fEPSP response to PPS recorded in BLA (top) and DG (bottom) curve in 3 (left) and 6 (right) month-old 3xTgAD mice and matched controls showed a significant increase in facilitation at short intervals: 20 ms, 50 ms. DG shows a genotype effect in intervals of 100 and 200 ms at 6 months. Data are plotted as mean \pm SEM. * $p < 0.05$, ** $p < 0.005$, *** $p < 0.001$. PPS: paired-pulse stimulation. ENTl: lateral entorhinal cortex, BLA: basolateral amygdala; DG: dentate gyrus; PPS: paired-pulse stimulation; fEPSP: field excitatory postsynaptic potential; SEM: standard error of the mean.

Results from the PPS highlight strong synaptic facilitation in 3xTgAD at short PP intervals in both BLA and DG at 3 months of age, also supporting synaptic hyperexcitability in this mouse model at this pre-plaque stage. Indeed, the synaptic

depression evident in controls at 20 ms PPI in BLA is transformed into clear synaptic facilitation in 3xTgAD.

4.5 Discussion

Alzheimer's disease (AD), in its early stages, is characterized phenotypically by impaired episodic memory that progresses in later stages to include emotional memory, aggression, reduced executive function, poor spatial navigation and increased anxiety, accompanied by the pathological formation of A β plaques and tau tangles (Bäckman and Small, 2007; Ringman, 2005). The effect of this pathology on medial temporal lobe structures plays a key role in the appearance of the cognitive deficits in AD. Specifically, ENTl and DG are crucial for episodic memory, pattern separation and the amygdala represents a crucial locus for fear and emotional processes related to emotional memory encoding (España et al., 2010; Jagust, 2018; Khan et al., 2014).

Synaptic circuitry changes are key for memory formation, suggesting that mechanisms for this are deficient in AD (Selkoe, 2008, 2002). Animal models for AD-like pathology can shed light onto the link between the memory deficits typical of AD and the underlying neuronal changes, as they allow us to study changes in neuronal activity and excitability in anatomically and functionally distinct brain regions *in vivo*. The 3xTg mouse model for AD shows clear deficits in episodic-like memory at a young age, in parallel with hippocampal excitability changes (Davis et al., 2014, 2013b) and well before the accumulation of A β plaques and NFTs (Mastrangelo and Bowers, 2008). To date, however, little is known about the preservation of synaptic circuits in 3xTgAD and other AD mouse models, as only a few studies have been carried out *in vivo*, i.e., whilst preserving distal and local neural connections (Davis et al., 2014). Growing evidence suggests the fundamental role of the ENTl as one of the earliest targets for AD. Therefore, further research exploiting the ENTl and its downstream projections, particularly towards the emotional hub (BLA) and pattern separation deficits (DG) is necessary.

Here, we aimed to test whether neuronal circuits involved in emotional and episodic-like memory present synaptic changes in young 3xTgAD mice. We investigated synaptic connectivity and short-term plasticity with recordings of electrically-evoked fEPSPs from male 3xTgAD mice, at 3 and 6 months of age *in vivo*. Neuronal connectivity between ENTl and BLA did not differ between 3xTgAD and controls during increasing stimulation of the ENTl in mice aged 3 months: the response profiles showed a parallel, moderate, increase in response with increased stimulus intensity, indicating no change of basal connectivity in 3xTgAD mice at this age. However, by 6 months of age, 3xTgAD mice revealed a strong, intensity-dependent increase in the BLA response to ENTl activation compared to controls, suggesting a strengthening of ENTl connectivity to the BLA with age and, presumably, pathological progression. Interestingly, the response to increased stimulation in DG was already larger by 3 months of age in 3xTgAD compared to age-matched controls, hinting towards an earlier manifestation of an enhanced neuronal connectivity strengthening between ENTl and DG compared to that for BLA.

This phenomenon could be induced by a potentiation of remaining synaptic connections, through a decrease of feed-forward inhibition from the ENTl to its downstream targets (Palop and Mucke, 2010a, 2010b). In order to test changes in presynaptic release probability, short-term synaptic plasticity was analysed with a paired-pulse paradigm, where electrical stimuli were provided in pairs with a variable interval within these stimulus pairs. Overall, 3xTgAD mice showed facilitation for shorter intra-pulse intervals (e.g., 20 and 50 ms) in both BLA and DG, at both 3 and 6 months of age, in general agreement with previous evidence investigating more dorsal hippocampal formation pathways (Davis et al., 2014).

Generally, synaptic facilitation seen at short intervals is thought to derive from a plethora of phenomena that result in increased glutamate release at the presynaptic terminal

(Berretta and Jones, 1996a, 1996b; Zucker, 1989). When stimuli are delivered at longer inter-pulse intervals (e.g., 500 or 1000ms), the residual Ca^{2+} responsible for facilitation at short intervals will have been already cleared through presynaptic buffering, thus, resulting in no difference between postsynaptic response slope or amplitude to the first and second pulses of each pair. However, for short intervals (e.g., 20 or 50 ms), the response to the second pulse occurs when residual presynaptic Ca^{2+} is still present from the depolarisation evoked by the first pulse, therefore, synaptic release to the second pulse is facilitated. Here, we demonstrated that 3xTgAD mice show short-term neuronal plasticity changes well before the appearance of plaques and tangles.

The increased facilitation reported in the DG by 6 months, even for longer intervals, i.e., 100 and 200 ms (**Figure 4.3b** right) seems to bring supporting evidence for synaptic plasticity changes in line with neuronal connectivity strengthening found with IOC. These results agree with previous work showing a similar increase in dorsal DG and CA1 of female 3xTgAD mice over a similar age range (Davis et al., 2014) and epileptiform behaviour and increased activity in the hippocampal formation in other mouse models for AD-like pathology (Palop et al., 2007). Moreover, evidence from *APOE ϵ 4* mice suggests excitatory synaptic activity in the BLA (Klein et al., 2014). Increased epileptiform behaviour has been encountered in AD patients (Lozsadi and Larner, 2006; Mendez and Lim, 2003) and is often treated with antiepileptic drugs (AEDs) that predominantly act on glutamate release, to modulate neuronal hyperactivity (Vossel et al., 2017). Thus, the hyperactivity and enhanced neuronal connectivity reported here and in other literature, may result from a compensatory mechanism to progressive disruption of inter-regional connectivity, which then elicits a strengthening in the remaining connection: increased activity is needed in order to balance the progressive insult, in order to result in the same information transmission (Davis, 2006).

Our results highlight that the increased excitatory state appears prior to A β plaques and NFTs accumulation, in AD-sensitive brain regions. Yet, the exact temporal unravelling of the intricate cascade of events involving A β and tau accumulation, synaptic loss and hyperactivity, is not fully understood. It is well established that overt plaques and NFTs contribute to loss of synaptic connectivity and neuronal cell death (Palop and Mucke, 2010b; Selkoe, 2008, 2002). However, the focus has shifted towards earlier manifestations of these molecular hallmarks: soluble forms of tau and oligomers of A β are thought to play a critical role in synaptic degeneration (Green et al., 2019; Ittner et al., 2010; Pooler et al., 2014). Specifically, progressive accumulation of tau results in epileptiform activity in neurons, the latter is reduced in studies where tau accumulation is genetically modulated, thus confirming its crucial role in mechanisms underlying hyperactivity (DeVos et al., 2013). There is also a strong case for aberrant A β in early stages of AD-like pathology increasing presynaptic transmitter release, thus, also promoting – here – ENT1 excitability (Palop and Mucke, 2016, 2010b). At the same time, the accumulation of A β and tau highly dependent on neuronal activity (DeVos et al., 2013; Noebels, 2011; Palop and Mucke, 2010b; Wu et al., 2016). Moreover, growing evidence highlights the interdependence of tau and A β production, e.g. dendritic tau modulates the toxicity of postsynaptic A β accumulations (Ittner et al., 2010; Roberson et al., 2007).

Thus, the inter-dependency between increased activity and tau/A β accumulation leads to a spiralling circuit driven by positive feedback that eventually results in neurodegeneration and cognitive decline. Indeed, our results bring supporting evidence for the first appearance of neuronal plasticity changes during very early stages of AD-like pathology, when A β plaques and NFTs are not yet seen in 3xTgAD. Recently, new evidence highlights that increased excitability may also be caused by a loss of local inhibition, in order to maintain the excitatory-inhibitory (E/I) balance, as suggested by

other neuropsychiatric states such as schizophrenia and sclerosis (Bateup et al., 2013; Gao and Penzes, 2015). Evidence from *APOEε4* mice showed increased activity in the ENTl as a major effect, and this may be derived by a loss of inhibition mediated by GABAergic circuitry (Nuriel et al., 2017). Work on the entorhinal cortex epileptiform activity in rats has also shown a decrease in inhibitory inputs to the layer II of the region *in vitro*, again suggesting a downstream deficit in inhibition in this area (Kumar, 2006). ENTl predominantly projects to the DG through layer II fibres, therefore, the increased response seen in DG in this work might result from a loss of inhibitory projections from the ENTl to the DG.

Increased excitability in DG may contribute to a breakdown in pattern separation (Nakashiba et al., 2012; Yassa et al., 2010), which would, in turn, potentially cause the confusion seen in MCI and AD patients and impairment in memory for life events. Poor pattern separation has been correlated with an increase in DG/CA3 activity in MCI patients (Yassa et al., 2010). Moreover, the hippocampal-amygdala connection is highly involved in emotional memory formation; particularly, GABAergic activity to modulate the response within the BLA is beneficial for a healthy control of emotional memory processes; aberrant activity within the amygdala might, therefore, result in deficits related to increased emotional contagion, fear, aggression and anxiety reported already in MCI patients (Bienvenu et al., 2012; Nava-Mesa et al., 2014; Sturm et al., 2013; Trzepacz et al., 2013).

Taken together, these results bring supporting evidence for neuronal hyperactivity and synaptic plasticity changes in 3xTgAD mice, compared to healthy controls already by a very young age, in agreement with documented cognitive decline already by 3/4 months of age (Billings et al., 2005; Davis et al., 2017, 2013a, 2013b). We, therefore, suggest that a hyperactive behaviour due to network remodelling, e.g., synaptic plasticity changes,

and/or loss of inhibition from interneurons, may play a key role in the earliest stages of AD-like pathology, and may be present even before extracellular amyloid and tau accumulation.

~ Chapter 5 ~

General Discussion

5.1 Overview

Alzheimer's disease (AD) is a devastating neurodegenerative disease and the most common cause of dementia (McKhann et al., 1984; Stelzmann et al., 1995). AD pathology presents as a continuous decline with very typical features in late stages. However, research in the last decades has concentrated on early stages of the disease, where treatment development may reverse completely its occurrence and may prevent the devastating memory and personality loss reported in later stages (Jack et al., 2010). AD presents initially with a mild memory deficit, clinically diagnosed as mild cognitive impairment (MCI). This deficit is first seen for declarative memory, particularly the episodic component (Paola et al., 2007; Tulving and Markowitsch, 1998), which represents one of the earliest cognitive biomarkers for AD diagnosis. Specifically, studies in AD patients and animal models for AD-like pathology have highlighted the central role of medial temporal lobe (MTL) structures in the early stages of AD, which agrees well with the central role for this region as a vital hub for declarative memory formation (Gour et al., 2014; Thal et al., 2000).

The lateral entorhinal cortex (ENTl) within the MTL is thought to be highly relevant in the early stages of pathology, as an interface between the neocortex and the rest of the hippocampal formation, thus, fundamental for information processing and exchange (Braak and Braak, 1991; Eichenbaum, 2000). Atrophy and functional changes in AD and MCI patients have been reported in the ENTl, highlighting its potential relevance as an early biomarker for AD. Moreover, evidence arising from animal work highlights an intricate network of episodic memory modulation mediated by fear, emotional memory,

and/or the reward system of the brain (Carlezon and Thomas, 2009; Dere et al., 2010; España et al., 2010; Paz and Pare, 2013), thus, involving the hippocampal formation, amygdaloid area and striatal areas.

To date, very little is known about the aetiology of AD: accumulation of beta-amyloid (A β) plaques and neurofibrillary tangles (NFTs) of hyperphosphorylated protein tau represent the main hallmarks of the pathology; however, cognitive, functional and neuronal changes are reported prior to plaque and tangle formation (Green et al., 2019; Oddo et al., 2003; Selkoe, 2008).

Despite the extensive body of literature on AD molecular mechanisms, the precise cascade of events is still not fully understood, as is their impact on brain physiology. Evidence coming from early-onset AD (EOAD) cohorts and frontotemporal dementia patients has identified genetic mutations and risk factors linked to the aberrant production of plaques and tangles (Selkoe, 1997). Although late-onset AD (LOAD) cohorts represent the majority of AD cases (> 90%) and their exact pathogenesis is still unknown (Small and Duff, 2008), it is widely accepted that beta-amyloid is the key culprit underlying the brain degeneration in EOAD (Goate et al., 1991). Moreover, the spatiotemporal progression of AD pathology in the brains of EOAD and LOAD patients is similar. Therefore, modelling AD in rodents, harbouring EOAD-relevant human genetic mutations, has provided useful insights into the progression of neuronal, functional and behavioural deficits in AD.

The predictable stages of the pathology in AD model systems has greatly aided the investigation of brain changes in human AD. However, preclinical models for AD-like pathology fail to fully recapitulate the entire spectrum of AD features, as their genotypic manifestations are based mostly on engineered non-spontaneous overexpression of AD-like features. Models for AD-like pathology differ in pathological manifestations, e.g., mice

with APP mutations fail to develop NFTs and very few models show neuronal loss (Billings et al., 2005; Cohen et al., 2013; Oddo et al., 2003). Nevertheless, preclinical research has helped tremendously to both understand the causal cascade of events happening in each genotypic model and develop the major hypotheses for AD pathology. In this study, the triple transgenic mouse model (3xTg) for AD was adopted, as it offers a relatively broad interval where only precedent forms of NFTs and A β plaques are present, providing a long developmental window where these mice exhibit typical prodromal AD (pre-plaque and pre-NFT) symptoms only (Oddo et al., 2003).

5.2 Highlights of the results

In this work, 3xTgAD mice show aberrant phospho-tau protein in the BLA by 3 months of age that extends to the hippocampal regions by 6 months; however, no NFTs could be detected at these ages. Unfortunately, no definitive conclusion could be drawn on whether these animals also presented intracellular forms of toxic A β ₄₂ or extracellular insoluble plaques. However, previous characterisation of the pathological profile of this mouse model shows the presence of plaques only after 9 months of age, thus, at the age points investigated here (< 7 months old) it is highly likely that mice had intracellular soluble forms of toxic A β without extracellular plaques (LaFerla et al., 2007; Mastrangelo and Bowers, 2008; Oddo et al., 2003). This thesis aimed to investigate early stages of AD-like pathology in 3xTgAD mouse and specifically how neuronal and synaptic changes in young 3xTgAD are embedded in brain-wide network reorganisation and plasticity.

The specific aims of the project were:

1. To establish how the progression of AD-like pathology impacts brain-wide network organisation. This has been carried out with rsfMRI in a longitudinal study on anaesthetised 3xTgAD mice and age-matched controls.

2. To further explore brain-wide functional mapping under AD-like pathology by stimulation of excitatory neurons in the ENTl. This was done by means of optogenetics in an fMRI setting, to longitudinally assess (in 3 and 6-month old animals) how pathology affects the evoked haemodynamic response of the brain.

3. To determine disease-relevant changes in synaptic strength and plasticity within (i) ENTl to BLA and (ii) ENTl to DG circuitry in 3xTgAD mice. This was achieved through *in vivo* assessment of synaptic connectivity (IOC) and short-term synaptic plasticity (PPS). This was carried out on cohorts of urethane-anaesthetised male mice at 3 and 6 months of age, to investigate for age-related pathological changes in neuronal activity and how these relate to fMRI changes in Aims 1 and 2 above.

A summary of the findings from this thesis is outlined in **Figure 5.1**.

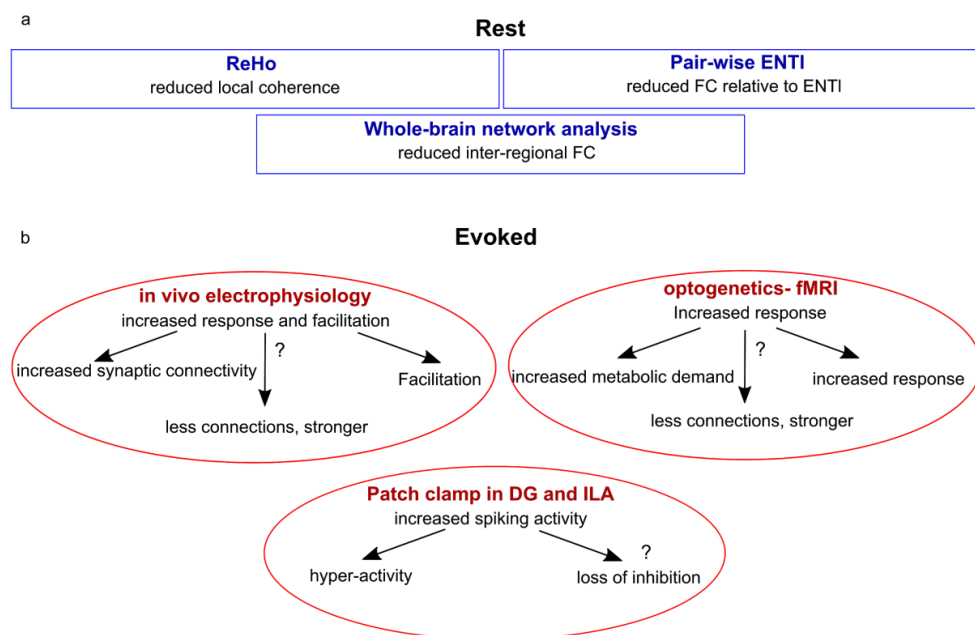


Figure 5.1: Diagram summarising the findings within this work.

a) 3xTgAD mice present whole-brain FC deficits at rest and loss of regional homogeneity in AD-vulnerable brain regions, which are also down-stream targets of the ENTl. Pair-wise analysis of FC relative to the ENTl confirms marked deficits in FC in 3xTgAD at rest. **b)** Decreased FC at rest co-exists with enhanced response during stimulation of the ENTl by means of optogenetics or electrophysiology *in vivo*. Hyper-excitability of the down-stream targets of the ENTl is also found with electrophysiology *in vitro*.

The longitudinal assessment of FC changes, during the resting-state of the brain, highlighted loss in regional homogeneity (ReHo) in regions highly involved in AD patients, namely ENTl, BLA, ACB and prefrontal cortices. There was, however, increased ReHo in somatosensory regions, suggesting that loss of local coherence might be network specific. This, together with the evidence of phospho-tau in BLA and hippocampal regions, suggests that local loss of coherence might be related to regions vulnerable for AD-hallmark deposition (**Figure 5.1a**). Moreover, resting-state FC analysis in relation to the ENTl (with pair-wise connectivity analysis) and as hypothesis-free assessment (whole-brain network analysis) revealed the marked involvement of hippocampal, striatal and amygdaloid areas showing decrease in FC at rest. Therefore, the analysis with whole-brain network connectivity and ReHo shows that local loss of coherence, within a confined region, may result in distal connectivity deficits.

The neuroimaging experiments carried out with rsfMRI and ofMRI highlighted a dichotomic modulation within the brain of 3xTgAD mice, already by 3 months of age. As explained above, FC analyses restricted to ENTl have highlighted a decrease in connectivity in 3xTgAD (supported by whole-brain ReHo analyses). However, the photostimulation of excitatory neurons in the entorhinal cortex, shows that the response in 3xTgAD is potentiated compared to controls at 3 months of age, thus suggesting an increased metabolic demand (possibly due to enhanced underlying neuronal connectivity) in pathology, compared to the healthy state.

The *in vivo* assessment of synaptic strength and short-term plasticity conducted between ENTl and BLA/DG has highlighted evidence for increased functional synaptic response and synaptic facilitation in these monosynaptic connections (**Figure 5.1**). Therefore, a key finding from these experiments is the presence of neuronal plasticity changes in the absence of overt plaques and tangles. This could be due to increased fibre

recruitment, presynaptic facilitation of neurotransmitter release and/or loss of early inhibition.

3xTgAD mice show a marked increase in facilitation compared to controls evident by 3 months of age in both *loci* of the recordings, possibly due to a presynaptic hyper-active state in ENTl projections. The clear molecular mechanisms behind plasticity changes and aberrant neuronal activity in AD are not fully understood. However, a healthy brain can dynamically maintain an excitatory/inhibitory (E/I) balance that provides beneficial homeostasis. Thus, a disruption in E/I *equilibrium*, either by excitatory or inhibitory changes, may elicit a compensatory mechanism to temporarily restore correct function. As such, the electrophysiological evidence from this work shows that the hyper-excitability reported may be due to either excessive presynaptic glutamate release and/or decreased feed-forward inhibition in the regions recorded.

The synaptic and neuronal changes affecting 3xTgAD mice in the early stages of pathology have a brain-wide impact. In support of potentiation in the neuronal response, increased neuronal excitability was found with *in vitro* (in DG and ILA) electrophysiological recordings. This suggests that aberrant neuronal activity may represent the underpinning mechanisms resulting in localised loss of coherence and brain-wide network-specific dysfunction, at rest. Thus, I speculate that the increased neuronal activity is affecting functional connectivity both locally and distally, producing defects in FC (ReHo, pair-wise, network analysis) but also inducing a potentiated response in the downstream targets of the ENTl, once this is stimulated (electrophysiology *in vivo*/ofMRI). These results highlight the complexity of the phenomena underpinning the early stages of AD-like pathology in 3xTgAD.

This work shows that distal connectivity disturbances could be explained by local connectivity deficits. The evidence on the micro-scale, i.e. electrophysiology *in vivo* and *ex*

vivo, taken together with the fMRI results, highlights that FC deficits are rooted in a deeper physiological context; this supports the trans-species relevance of our results. Moreover, staging the disease progression has been an important question in AD in order to understand mechanisms and to improve diagnostics (Selkoe et al., 2012). Here, 3xTgAD presented phospho-tau spreading from 3 to 10 months and this was associated with long-range connectivity deficits in young model animals. This suggests tight coupling between functional connectivity and tau progression (Franzmeier et al., 2019), supported by molecular work by others (Clavaguera et al., 2013). The results highlighted in this work can be further connected to other models of axonal degeneration and inflammatory response (Krstic & Knuesel, 2013), thus, providing a coherent description of the pathophysiology process taking place in AD.

The contribution of different A β species (soluble oligomers, fibrils, plaques) represents a crucial focus of AD-research. The present work highlights FC changes in the absence of amyloid plaques and detectable elevated A β levels, similar to previous results in other models (Bero et al., 2012; Shah et al., 2013). Importantly, these results are in line with evidence from studies on subjects at risk of developing AD (Sheline et al., 2010; Filippini et al., 2009); as such, young 3xTgAD mice at 3 months of age may represent the early stages of AD, as they recapitulate features of subjects at risk of AD; thus, they can bring insights into the pre-clinical stage of disease-relevant pathology.

The dichotomy of the direction of these changes in resting and evoked activity, specifically within the ENTl network, mirrors several findings in preclinical and early AD patients. Decreased functional connectivity is found in mild AD patients at rest, in areas related to the DMN, including the hippocampal formation (Greicius et al., 2004). However, task-based fMRI studies show increased activity in memory-related areas in subjects at risk of AD but cognitively still normal (e.g. APOE ϵ 4 carriers) suggesting a possible dichotomy

in network organization of the brain at rest and in engaged status (Bookheimer et al., 2000). Taken together, our findings, thus, provide a potential reconciliation for discordant results put forward in early-AD subjects.

Importantly, the results reported here fit into modern hypotheses for the amyloid cascade. Buckner and colleagues demonstrated that network dysfunction overlapped and preceded amyloid deposition, as revealed with PET (Buckner et al., 2005). Bero and colleagues demonstrated in APP transgenic models that hyper-connectivity patterns at a young age correlated with amyloid plaque distribution later in life (Bero et al., 2012). As such, the present results support the notion that local and distal network dysfunction at rest impairs information transmission and processing. This leads to increased metabolic demand during evoked activity, which putatively leads to circuit exhaustion and further accumulation of A β species through increased neuronal activity (Bero et al., 2011). It will be important to confirm this model prediction in older 3xTgAD mice.

Indeed, further experiments towards the validation of the specific profile of the ENTl response might help shed light onto the cascade of events reported here. For example, the marked increased neuronal response in the ventral dentate gyrus assessed with electrophysiology *in vivo*, is not fully recapitulated with ofMRI, where the effect of the stimulation is found more dorsally. This might be due to the discrepancy in the stimulation provided, where optogenetic labelling of ENTl neurons might result in a wider stimulated area, compared to the more localised stimulation elicited with electric pulses.

Evidence on the mapping of the perforant pathway connectivity between ENTl and DG highlights differences in medial and lateral perforant pathway involvement, with facilitation seen in the former and depression in the latter (McNaughton, 1980). This may suggest a more specific stimulation of the medial perforant pathway with electrophysiology, and a simultaneous stimulation of both parts with optogenetics,

resulting in a weakened effect. The targeting of specific layers of the ENTl through optogenetics, e.g. with retrograde AAV injected in the DG, may also help in understanding the contribution of specific sections of the perforant pathway to ofMRI signal (Rowland et al., 2013).

Moreover, performing electrophysiological recordings of the DG during optogenetic stimulation of the ENTl pyramidal neurons might also produce further insight into the underlying mechanisms found in this work. This would also allow to overcome the major limitation of the time resolution difference between the BOLD-evoked signal (in order of seconds) and the millisecond time-scale of events recorded with electrophysiology.

Furthermore, the employment of simulation analysis to modulate connection strength and excitability in silico, thus modelling the networks investigated here, may help to reproduce the dichotomic trend of results seen in this work, and in AD patients with rsfMRI and task-based fMRI (Braskie et al., 2012; Filippini et al., 2009; Sheline et al., 2010).

Additionally, information theory has helped in neuroscience field to understand if, when analysing evoked neuronal activity resulting from repeated stimuli, there is a difference in the quantity and quality of information extracted when considering the timing of spikes relative to the oscillatory background activity, compared to information extraction by spikes alone (Kayser et al., 2009; Montemurro et al., 2008). The calculation of Shannon entropy values provides an approach to assess mutual information between two signals (Shannon, 1948) in that Shannon entropy measures the uncertainty in a system (when the probability of each outcome is equally distributed, entropy, hence uncertainty, is maximised). Hence, a future application of transfer entropy analyses might help to gain additional quantitative and causal information on synaptic transfer.

Taken together, the results from these diverse approaches demonstrate local dysfunction in neuronal circuits in confined brain regions, vulnerable to phospho-tau occurrence. Local loss of coherence results in increased synaptic activity, thus in increased metabolic demand in response to input, which is seen by the optogenetic results and electrophysiology. The identification of overlapping functional hubs that present loss of FC but enhanced response following ENT1 stimulation may suggest the relevance of these projection areas in the early stages of AD-like pathology in 3xTgAD mouse.

5.3 The relevance of this study within AD aetiology

In past decades, continuous research has tried to identify the molecular mechanisms underpinning AD pathogenesis. Whilst the aetiology of EOAD is quite clear, the triggers for LOAD initial changes are still obscure. The controlled manipulation of genetically engineered animal models, although genotypically closer to the EOAD profile, might aid in the identification of LOAD pathogenesis. Different mouse models and AD cohorts have led to the identification of a diverse repertoire of hypotheses for AD pathogenesis. Here, I attempt to place my results within these major theories for AD development and how this work may provide a further contribution to their development and refinement.

5.3.1 Beta-amyloid cascade

The beta-amyloid cascade hypothesis places the development of toxic A β plaques as the trigger for a consequential cascade of events where gradual plaque deposition elicits a neuroinflammatory response, together with synaptic dysfunction and altered neuronal activity, eventually resulting in neuronal cell death and cognitive decline (Hardy and Higgins, 1992). However, the amyloid cascade hypothesis has been challenged in the past as, for example, level of plaque deposition correlates poorly with the spatiotemporal

pattern of cognitive decline, which instead is highly correlated with NFT deposition (Braak and Braak, 1995; Nelson et al., 2012). Therapeutic strategies have to date mostly focused on targeting A β ; however, these have all been disappointingly unsuccessful (Cummings et al., 2014). Moreover, the presence of A β and absence of NFTs and neuronal degeneration in healthy individuals further challenges the A β cascade hypothesis and highlights the crucial role of axonal morphological changes in AD (Serrano-Pozo et al., 2011). There is, however, strong evidence for a bidirectional dependency of neuronal activity and beta-amyloid deposition: the latter has been shown to be activity-dependent, but, on the other hand, increase of amyloid levels are thought to elicit epileptiform activity (Cirrito et al., 2005; Kamenetz et al., 2003).

Interestingly, mice overexpressing APP in the ENTl result in increased A β within the DG, and ablation of the perforant pathway results in a decrease in hippocampal accumulation of A β . This strongly supports a sequential spread of pathology through axonal transport and synaptic connections and for a crucial role of ENTl in early stages of AD-like pathology (Harris et al., 2010; Lazarov et al., 2002). Our results are in line with a strong involvement of the ENTl in the early stages of AD-like pathology in 3xTgAD, as it is a key region for APP synthesis (Lazarov et al., 2002). However, we could not conclude that 3xTgAD mice at 3 or 6 months of age presented A β nor NFTs, although we saw the presence of phosphorylated tau in AD-sensitive brain regions and the presence of non-toxic A β ₄₀. Evidence from previous characterisation of the pathological profile of 3xTgAD mode shows A β ₄₂ plaques accumulated extracellularly after 9 months of age; as such, the mice used in this work could present intracellular forms of toxic A β extracellular insoluble plaques (LaFerla et al., 2007; Mastrangelo and Bowers, 2008; Oddo et al., 2003).

Phospho-tau in our data is present in amygdaloid and hippocampal areas, regions highly involved in the first cognitive deficits in AD patients, i.e., episodic and emotional

memory. Here, we see marked abnormal effects in the ENTl projection areas in both electrophysiological experiments and rsfMRI/ofMRI. Furthermore, we see changes in the electrophysiological properties of neurons before any overt accumulation of toxic plaques. Therefore, our work is supporting evidence for A β as a concomitant factor in AD-like pathology in 3xTgAD, but not as the initial trigger for the cascade of events seen, which, instead, might be a neuronal remodelling through synaptic plasticity, which results in loss of local FC and increased metabolic demand during stimulation.

5.3.2 Cerebral-amyloid angiopathy

In AD, the accumulation of plaques around or within the blood vessels is a common phenomenon, reported in more than 80% of advanced AD cases, resulting in cerebral amyloid angiopathy (CAA (Vinters, 1987)). The high incidence of CAA in AD cases renders the separation between vasculopathy and AD pathology challenging, especially in human studies relying on the haemodynamic response of the brain. As such, the HR of the brain is influenced by a wide spectrum of components, such as vascular tone, reactivity, size, and blood oxygenation. Thus, brain disorders presenting a vascular component, such as Alzheimer's disease, metabolic disorders and vascular dementia, may affect the HR in addition to neural metabolism (D'Esposito et al., 2003). Non-invasive animal imaging in mouse models for AD, e.g., the APP23 mouse (Beckmann et al., 2011), has proven useful to monitor changes in CAA characteristics over time.

The specific distribution of deficits highlighted in this work does not support the presence of CAA, as the latter is thought to primarily affect cortical capillaries in occipital areas (Serrano-Pozo et al., 2011). However, the deficits in FC seen at rest in 3xTgAD could still have a vascular contribution. As such, the major unresolved limitation of the fMRI BOLD signal is the impossibility to fully extract the underlying neuronal signature.

By using fMRI in combination with direct neuronal recordings, i.e. electrophysiology or calcium photometry, it is possible to produce haemodynamic-independent readouts, which would allow for a more informative interpretation of haemodynamic changes in AD-like pathology. For example, calcium fibre-photometry measures changes in intracellular calcium concentration, an indicator of direct neuronal activity, in a specific group of neurons (e.g. glutamatergic), generally using a calcium reporter protein expressed via an AAV injection (Schulz et al., 2012). Thus, future work in the direction of identifying the neural underpinnings of CAA and AD-like pathology may rely on the combination of fMRI with calcium photometry.

5.3.3 Dopaminergic hypothesis

Interestingly, recent evidence has suggested a new contribution of the DAergic system in AD neuronal changes (Martorana et al., 2009; Martorana and Koch, 2014; Salamone et al., 2005). As well as for the toxic effects of A β in the acetylcholine pathway, new evidence suggests an interaction between A β and dopamine that may produce loss of DA neurons and DAergic signalling pathway dysfunction, associated with memory loss in AD patients (Koch et al., 2014; Martorana et al., 2009) and AD-like mouse models (Cordella et al., 2018). Moreover, loss of DA receptors, especially D2, has been shown in areas such as the hippocampal formation, prefrontal cortices and BLA (Joyce et al., 1993; Kemppainen et al., 2003) in AD patients. PET studies on Alzheimer's patients also confirm a loss of striatal D2-like receptors (Tanaka et al., 2003). Additionally, recent studies have shown that DAergic signalling in the hippocampal formation plays a pivotal role in the distal connections with the ACB in mouse models for AD-like pathology, such as the Tg2576 mouse model (Cordella et al., 2018).

Our results are in line with a probable disruption of the DAergic system in early stages of AD-like pathology in 3xTgAD. DAergic neuronal degeneration may be the result of regional loss of coherence in ACB, prefrontal and amygdaloid regions. Therefore, the dysfunction of DAergic transmission in distal targets, prior to amyloid plaque accumulation, may represent one of the causes for AD aetiology (Krashia et al., 2019). The optogenetic targeting of DAergic neurons in 3xTgAD, such as within the ventral tegmental area, might help shed light on the contribution of the DAergic system degeneration onto the early network alterations.

5.3.4 Axonal degeneration, tauopathy and synaptic deficiency

Our work shows localized deficits in phospho-tau enriched brain regions. Moreover, the acute excitation of ENT1 by means of electrical or optogenetic stimulation elicited an aberrant response in postsynaptic targets, suggesting a potentiation of the response in 3xTgAD. Neuronal degeneration and correlated synaptic dysfunction may be early prerequisites for AD development, as supported by the axonal degeneration hypothesis of AD (Salvadores et al., 2017; Serrano-Pozo et al., 2011). In recent years, a new hypothesis for the pathological cascade of events underlying AD development has placed axonal degeneration as one of the earliest events leading to AD (Kanaan et al., 2013). Evidence from a backward directionality of neuronal degeneration, starting from the axon progressing to the soma, has recently arisen (Kneynsberg et al., 2017). The tau protein plays a crucial role in axonal structural stability and function through maintaining the microtubules that form the axonal cytoskeleton and transport mechanisms (Roberson et al., 2007; Vossel et al., 2010).

Tau misfolding is one of the leading causes for axonal disruption and, ultimately, aberrant synaptic activity and neuronal degeneration that leads to cognitive deficits

(Adalbert and Coleman, 2013). The results shown in this work may suggest a potential role of axonal morphology in AD-like pathology in 3xTgAD. Indeed, long-distance transport is highly correlated to axonal integrity. Evidence from studies on 3xTgAD mice shows defective myelination prior to plaques and NFTs appearance, which supports our findings of a probable neuronal degeneration affecting the synaptic activity and long-distance axonal integrity (Desai et al., 2009). The application of diffusion-weighted MRI would represent a logical next step to undertake in a future investigation on this mouse model, in order to infer for white matter and axonal integrity. White matter changes have been reported in AD patients and a strong deficit in myelination has been reported in 3xTgAD mice already by 2 months of age in the hippocampus proper, thus further confirming a probable neuronal degeneration in this mouse model (Desai et al., 2009; Roher et al., 2002).

5.4 Limitations and considerations of this study

The work described in Chapters 3 and 4 (Papers 1 and 2, respectively) has been the result of a collaboration between laboratories and across technical approaches and levels of analysis. Functional brain changes of one specific mouse model, 3xTgAD, were evaluated using different modalities, spanning from the micro- to the meso- and macro-scale of events. The work conducted in both laboratories has allowed insight into early brain changes in 3xTgAD mice at the whole-brain level, firstly at rest, with rsfMRI; the whole-brain functional mapping of the ENTI projections subsequently highlighted differences in responses compared to wild-type, suggesting enhanced synaptic changes due to increased metabolic load. This has been further confirmed with electrophysiological recordings *in vivo* and *ex vivo*, where synaptic hyperexcitability at 3 and 6 months of age was revealed. It

is, however, necessary to take into consideration the limitations that this work might present.

Firstly, the different anaesthesia protocols used for the neuroimaging experiments and the electrophysiological recordings *in vivo*: the former was conducted with isoflurane under ventilation and a mix of medetomidine and a muscle relaxant, with the latter conducted via systemic injection of urethane. As reported in section 1.10, anaesthetic agents may each affect the brain and the vascular system differently. Therefore, a straightforward interpretation of the results obtained in Chapters 3 and 4 cannot be drawn. Whilst it is possible to perform rsfMRI and ofMRI experiments with the adoption of an awake imaging protocol (Desai et al., 2011), this is not possible for the acute electrophysiology study, where an anaesthetised state of the animal is required. As such, the adoption of standardised protocols with the application of one singular anesthesia compound is recommended for future studies.

Secondly, careful consideration regarding the limitations of the animal model used are needed. As reported in section 1.4.1, the 3xTgAD mouse model is the result of an overexpression of three mutations (with one of these not related to AD) leading to the formation of plaques and tau aggregates in a disease-relevant spatial and temporal manner. As per the majority of the AD-like models that overexpress mutations, they all represent mutations linked to FAD. Although the aetiology of FAD is well described, mechanisms that result in SAD still need investigation. As such, the relevance of data from a FAD-related mouse model to the interpretation of SAD is not straightforward. A possible suggestion for future studies could include the adoption of a risk-model, such as the *APOE ϵ 4* mouse, where the phenotype may be closer to SAD than 3xTgAD or APP/PS1 models, for example.

One major limitation that arises from this work (and animal models in pre-clinical research more generally) is the relative translatability of the findings. As mentioned above, although the use of rodents allows the advantageous invasive study of neuronal changes (which is not possible on humans) it requires the animal to be anaesthetised. The anaesthetised brain may resemble the REM/non-REM condition of the human brain (Clement et al., 2008), but it cannot be readily compared to the resting-state of the human brain during rsfMRI, nor to the evoked-state of the human brain during task-based fMRI. As mentioned previously, awake protocols would be the best suit for results to be more readily translatable, but this is not possible within an acute paradigm and the awake preparation sacrifices sophisticated experimental control compared to the anaesthetised condition.

The analytical approach to investigate FC changes represents another aspect that needs careful consideration and may result in a limitation rather than an advantage, especially in the analysis of the neuroimaging work. By adopting similar analytical approaches to human fMRI research, the analyses performed on rodents can be interpreted more easily. In the rsfMRI work presented here a limited set of FC analyses was carried out, namely, ReHo, network analysis and pair-wise correlation. It is important to note that ReHo analysis, although well-established in the rodent brain and fairly easy to interpret, is not yet part of the common analytical protocols adopted in human brain imaging. It is, therefore, reasonable, perhaps in future studies, to further exploit these results with another data-driven approach more common in clinical research, such as Independent Component Analysis (ICA), (Deng et al., 2016). Data-driven analyses represent a fundamental approach to investigate broad, whole-brain changes in FC. However, hypothesis driven approaches with a more planned comparison basis may help shed light onto a specific biological question; for example, in human fMRI research a seed-based approach is often

used. Seed-based analysis (SBA) entails the identification of a user-drawn ROI and the voxel-wise correlation to that ROI, on a whole-brain level. Here, SBA was not performed; however, a comparable metric of analysis was conducted by means of pair-wise correlation: the ‘seed’ chosen was the anatomical ROI of the left ENTl and the ROI to ROI correlations of the whole-brain were computed and reported in **Figure 3.1b**.

A crucial aspect that needs further discussion is the nature of the BOLD signal itself. The BOLD readout of fMRI is relatively easy to obtain and represents the most commonly adopted metric in rodent fMRI. However, it is highly sensitive to the vasculature and the physiological condition of the animal. Whilst the adoption of BOLD is still recommended for this project as a common readout, translatable to human fMRI, care must be taken in order to minimise confounding variables in the experimental setting. As such, careful monitoring of the physiological parameters of the animal is crucial: here, the breathing rhythm was controlled through a ventilation pump and the animal temperature was monitored continuously. Moreover, in order to exclude any fluctuations related to anaesthesia administration, a 20 minute pause was given between the injection of the anaesthetic and the first EPI recorded.

Despite the above considerations the present work brings novel insights into the pre-clinical field of AD research; these results may help shed light onto the early stages of AD pathology. The work described in this thesis, however, is based on a broad variety of methods, each with specific limitations and advantages. As such, the present work is insightful, but it will require further validation and careful consideration of the limits of the techniques and the settings adopted, in order to provide the scientific community with valuable information.

~ Conclusion ~

This thesis shows evidence for early functional alterations in brain-wide neuronal circuits of the 3xTg mouse model for AD. These changes as measured by resting-state MRI (rsfMRI), are apparent by 3 months of age, that is, well before these mice present with overt A β plaques and neurofibrillary tangles.

The decrease in functional coupling in the lateral entorhinal cortex (ENTl) at rest in rsfMRI co-exists with a potentiated response in ENTl and ENTl synaptic targets to direct optogenetic stimulation (ofMRI). This is further supported by *in vivo* direct neuronal recordings of the neuronal pathway between ENTl and key hubs in AD pathology, DG and BLA. The regions affected in the dichotomic response present phospho-tau enrichment, therefore, suggesting a functional-pattern of tau deposition. We suggest that the co-existence of both increased and decreased functional connectivity in 3xTgAD mice under different experimental conditions can be explained in the following way. The decrease in rsfMRI may be due to reduced synaptic connectivity whilst the synaptic hyperexcitability in response to direct stimulation can be explained by upregulation of synaptic excitability within the remaining intact connections.

To conclude, this work brings supporting evidence for a brain-wide network reorganisation in 3xTgAD mice, prior to overt pathology development, highlighting that plasticity changes within and down-stream of the lateral entorhinal cortex may represent an early biomarker for AD-like pathology. Determining the earliest changes in the time course of AD-like pathology by means of invasive and non-invasive techniques will result fundamental for finally unravelling AD pathogenesis.

~ References ~

1. Adalbert, R., Coleman, M.P., 2013. Review: Axon pathology in age-related neurodegenerative disorders. *Neuropathology and Applied Neurobiology*. <https://doi.org/10.1111/j.1365-2990.2012.01308.x>
2. Agosta, F., Pievani, M., Geroldi, C., Copetti, M., Frisoni, G.B., Filippi, M., 2012. Resting-state fMRI in Alzheimer's disease: beyond the default mode network. *Neurobiol. Aging* 33, 1564–1578.
3. Agster, K.L., Tomás Pereira, I., Saddoris, M.P., Burwell, R.D., 2016. Subcortical connections of the perirhinal, postrhinal, and entorhinal cortices of the rat. II. efferents. *Hippocampus* 26, 1213–1230.
4. Albers, F., Schmid, F., Wachsmuth, L., Faber, C., 2018. Line scanning fMRI reveals earlier onset of optogenetically evoked BOLD response in rat somatosensory cortex as compared to sensory stimulation. *Neuroimage* 164, 144–154.
5. Albert, M.S., DeKosky, S.T., Dickson, D., Dubois, B., Feldman, H.H., Fox, N.C., Gamst, A., Holtzman, D.M., Jagust, W.J., Petersen, R.C. and Snyder, P.J., 2011. The diagnosis of mild cognitive impairment due to Alzheimer's disease: recommendations from the National Institute on Aging-Alzheimer's Association workgroups on diagnostic guidelines for Alzheimer's disease. *Alzheimer's & dementia*, 7(3), pp.270-279.
6. Aldrin-Kirk, P., Heuer, A., Rylander Ottosson, D., Davidsson, M., Mattsson, B., Björklund, T., 2018. Chemogenetic modulation of cholinergic interneurons reveals their regulating role on the direct and indirect output pathways from the striatum. *Neurobiol. Dis.* 109, 148–162.
7. Alzheimer, A., 1907. Über eine eigenartige Erkrankung der Hirnrinde [article in German]. *Allg Z Psych Psych-gerich Med* 64, 146–148.
8. Amieva, H., Le Goff, M., Millet, X., Orgogozo, J.M., Pérès, K., Barberger-Gateau, P., Jacqmin-Gadda, H., Dartigues, J.F., 2008. Prodromal Alzheimer's disease: successive emergence of the clinical symptoms. *Ann. Neurol.* 64, 492–498.
9. Ammassari-Teule, M., Passino, E., Restivo, L., De Marsanich, B., 2000. Fear conditioning in C57/BL/6 and DBA/2 mice: variability in nucleus accumbens function according to the strain predisposition to show contextual- or cue-based responding. *European Journal of Neuroscience*. <https://doi.org/10.1111/j.1460-9568.2000.01333>.
10. Andersen, P., Bliss, T. V. P., & Skrede, K. K., 1971. Lamellar organization of hippocampal excitatory pathways. *Experimental Brain Research*, 13, 222-238.
11. Arey, B.J., 2014. An Historical Introduction to Biased Signaling. *Biased Signaling in Physiology, Pharmacology and Therapeutics*. <https://doi.org/10.1016/b978-0-12-411460-9.00001-x>
12. Arnold, S.E., Hyman, B.T., Flory, J., Damasio, A.R., Van Hoesen, G.W., 1991. The topographical and neuroanatomical distribution of neurofibrillary tangles and neuritic plaques in the cerebral cortex of patients with Alzheimer's disease. *Cereb. Cortex* 1, 103–116.
13. Avants, B.B., Tustison, N., Song, G., 2009. Advanced normalization tools (ANTS). *Insight J.* 2, 1–35.

14. Avila, J., Pérez, M., Lucas, J.J., Gómez-Ramos, A., Santa María, I., Moreno, F., Smith, M., Perry, G., Hernández, F., 2004. Assembly in vitro of tau protein and its implications in Alzheimer's disease. *Curr. Alzheimer Res.* 1, 97–101.
15. Bäckman, L., Jones, S., Berger, A.-K., Laukka, E.J., Small, B.J., 2004. Multiple cognitive deficits during the transition to Alzheimer's disease. *J. Intern. Med.* 256, 195–204.
16. Bäckman, L., Small, B.J., 2007. Cognitive deficits in preclinical Alzheimer's disease and vascular dementia: patterns of findings from the Kungsholmen Project. *Physiol. Behav.* 92, 80–86.
17. Bäckman, L., Small, B.J., Fratiglioni, L., 2001. Stability of the preclinical episodic memory deficit in Alzheimer's disease. *Brain* 124, 96–102.
18. Baek, S.H., Park, S.J., Jeong, J.I., Kim, S.H., Han, J., Kyung, J.W., Baik, S.-H., Choi, Y., Choi, B.Y., Park, J.S., Bahn, G., Shin, J.H., Jo, D.S., Lee, J.-Y., Jang, C.-G., Arumugam, T.V., Kim, J., Han, J.-W., Koh, J.-Y., Cho, D.-H., Jo, D.-G., 2017. Inhibition of Drp1 Ameliorates Synaptic Depression, A β Deposition, and Cognitive Impairment in an Alzheimer's Disease Model. *The Journal of Neuroscience*. <https://doi.org/10.1523/jneurosci.2385-16.2017>
19. Baltes, C., Bosshard, S., Mueggler, T., Ratering, D., Rudin, M., 2010. Increased blood oxygen level-dependent (BOLD) sensitivity in the mouse somatosensory cortex during electrical forepaw stimulation using a cryogenic radiofrequency probe. *NMR in Biomedicine*. <https://doi.org/10.1002/nbm.1613>
20. Barret, O., Alagille, D., Sanabria, S., Comley, R.A., Weimer, R.M., Borroni, E., Mintun, M., Seneca, N., Papin, C., Morley, T., Marek, K., Seibyl, J.P., Tamagnan, G.D., Jennings, D., 2017. Kinetic Modeling of the Tau PET Tracer F-AV-1451 in Human Healthy Volunteers and Alzheimer Disease Subjects. *J. Nucl. Med.* 58, 1124–1131.
21. Bassett, S.S., Yousem, D.M., Cristinzio, C., Kusevic, I., Yassa, M.A., Caffo, B.S., Zeger, S.L., 2006. Familial risk for Alzheimer's disease alters fMRI activation patterns. *Brain* 129, 1229–1239.
22. Bates, D., Mächler, M., Bolker, B., Walker, S., 2015. Fitting Linear Mixed-Effects Models Using lme4. *Journal of Statistical Software*. <https://doi.org/10.18637/jss.v067.i01>
23. Bateup, H.S., Johnson, C.A., Deneffrio, C.L., Saulnier, J.L., Kornacker, K., Sabatini, B.L., 2013. Excitatory/inhibitory synaptic imbalance leads to hippocampal hyperexcitability in mouse models of tuberous sclerosis. *Neuron* 78, 510–522.
24. Bazelot, M., Bocchio, M., Kasugai, Y., Fischer, D., Dodson, P.D., Ferraguti, F., Capogna, M., 2015. Hippocampal Theta Input to the Amygdala Shapes Feedforward Inhibition to Gate Heterosynaptic Plasticity. *Neuron* 87, 1290–1303.
25. Beckmann, N., Gerard, C., Abramowski, D., Cannet, C., Staufenbiel, M., 2011. Noninvasive Magnetic Resonance Imaging Detection of Cerebral Amyloid Angiopathy-Related Microvascular Alterations Using Superparamagnetic Iron Oxide Particles in APP Transgenic Mouse Models of Alzheimer's Disease: Application to Passive A Immunotherapy. *Journal of Neuroscience*. <https://doi.org/10.1523/jneurosci.4936-10.2011>
26. Belliveau, J.W., Kennedy, D.N., Jr, McKinstry, R.C., Buchbinder, B.R., Weisskoff, R.M., Cohen, M.S., Vevea, J.M., Brady, T.J., Rosen, B.R., 1991. Functional mapping of the human visual cortex

- by magnetic resonance imaging. *Science* 254, 716–719.
27. Beres, A.M., 2017. Time is of the Essence: A Review of Electroencephalography (EEG) and Event-Related Brain Potentials (ERPs) in Language Research. *Appl. Psychophysiol. Biofeedback* 42, 247–255.
 28. Berger, A., 2003. Positron emission tomography. *BMJ*. <https://doi.org/10.1136/bmj.326.7404.1449>
 29. Berg, K.A., Clarke, W.P., 2018. Making Sense of Pharmacology: Inverse Agonism and Functional Selectivity. *Int. J. Neuropsychopharmacol.* 21, 962–977.
 30. Berg, L., McKeel, D.W., Jr, Miller, J.P., Storandt, M., Rubin, E.H., Morris, J.C., Baty, J., Coats, M., Norton, J., Goate, A.M., Price, J.L., Gearing, M., Mirra, S.S., Saunders, A.M., 1998. Clinicopathologic studies in cognitively healthy aging and Alzheimer's disease: relation of histologic markers to dementia severity, age, sex, and apolipoprotein E genotype. *Arch. Neurol.* 55, 326–335.
 31. Berndt, A., Yizhar, O., Gunaydin, L.A., Hegemann, P., Deisseroth, K., 2009. Bi-stable neural state switches. *Nat. Neurosci.* 12, 229–234.
 32. Bero, A.W., Bauer, A.Q., Stewart, F.R., White, B.R., Cirrito, J.R., Raichle, M.E., Culver, J.P., Holtzman, D.M., 2012. Bidirectional Relationship between Functional Connectivity and Amyloid-Deposition in Mouse Brain. *Journal of Neuroscience*. <https://doi.org/10.1523/jneurosci.5845-11.2012>
 33. Bero, A.W., Yan, P., Roh, J.H., Cirrito, J.R., Stewart, F.R., Raichle, M.E., Lee, J.-M., Holtzman, D.M., 2011. Neuronal activity regulates the regional vulnerability to amyloid- β deposition. *Nat. Neurosci.* 14, 750–756.
 34. Berretta, N., Jones, R.S., 1996a. Tonic facilitation of glutamate release by presynaptic N-methyl-D-aspartate autoreceptors in the entorhinal cortex. *Neuroscience* 75, 339–344.
 35. Berretta, N., Jones, R.S., 1996b. A comparison of spontaneous EPSCs in layer II and layer IV-V neurons of the rat entorhinal cortex in vitro. *J. Neurophysiol.* 76, 1089–1100.
 36. Bienvenu, T.C.M., Busti, D., Magill, P.J., Ferraguti, F., Capogna, M., 2012. Cell-type-specific recruitment of amygdala interneurons to hippocampal theta rhythm and noxious stimuli *in vivo*. *Neuron* 74, 1059–1074.
 37. Billings, L.M., Oddo, S., Green, K.N., McGaugh, J.L., LaFerla, F.M., 2005. Intraneuronal A β Causes the Onset of Early Alzheimer's Disease-Related Cognitive Deficits in Transgenic Mice. *Neuron*. <https://doi.org/10.1016/j.neuron.2005.01.040>
 38. Biswal, B., Yetkin, F.Z., Haughton, V.M., Hyde, J.S., 1995. Functional connectivity in the motor cortex of resting human brain using echo-planar MRI. *Magn. Reson. Med.* 34, 537–541.
 39. Blennow, K., Mattsson, N., Schöll, M., Hansson, O., Zetterberg, H., 2015. Amyloid biomarkers in Alzheimer's disease. *Trends Pharmacol. Sci.* 36, 297–309.
 40. Bliss, T.V., Collingridge, G.L., 1993. A synaptic model of memory: long-term potentiation in the hippocampus. *Nature* 361, 31–39.

41. Bliss, T.V., Lomo, T., 1973. Long-lasting potentiation of synaptic transmission in the dentate area of the anaesthetized rabbit following stimulation of the perforant path. *J. Physiol.* 232, 331–356.
42. Bondi, M.W., Houston, W.S., Eyler, L.T., Brown, G.G., 2005. fMRI evidence of compensatory mechanisms in older adults at genetic risk for Alzheimer disease. *Neurology* 64, 501–508.
43. Bookheimer, S.Y., Strojwas, M.H., Cohen, M.S., Saunders, A.M., Pericak-Vance, M.A., Mazziotta, J.C., Small, G.W., 2000. Patterns of brain activation in people at risk for Alzheimer's disease. *N. Engl. J. Med.* 343, 450–456.
44. Booth, C.A., Ridler, T., Murray, T.K., Ward, M.A., de Groot, E., Goodfellow, M., Phillips, K.G., Randall, A.D., Brown, J.T., 2016. Electrical and Network Neuronal Properties Are Preferentially Disrupted in Dorsal, But Not Ventral, Medial Entorhinal Cortex in a Mouse Model of Tauopathy. *J. Neurosci.* 36, 312–324.
45. Boyden, E.S., Zhang, F., Bamberg, E., Nagel, G., Deisseroth, K., 2005. Millisecond-timescale, genetically targeted optical control of neural activity. *Nat. Neurosci.* 8, 1263–1268.
46. Braak, H., Braak, E., 1995. Staging of Alzheimer's disease-related neurofibrillary changes. *Neurobiol. Aging* 16, 271–8; discussion 278–84.
47. Braak, H., Braak, E., 1991. Neuropathological staging of Alzheimer-related changes. *Acta Neuropathologica*. <https://doi.org/10.1007/bf00308809>
48. Braskie, M.N., Medina, L.D., Rodriguez-Agudelo, Y., Geschwind, D.H., Macias-Islas, M.A., Cummings, J.L., Bookheimer, S.Y., Ringman, J.M., 2012. Increased fMRI signal with age in familial Alzheimer's disease mutation carriers. *Neurobiology of Aging*. <https://doi.org/10.1016/j.neurobiolaging.2010.09.028>
49. Brecht, W.J., Harris, F.M., Chang, S., Tesseur, I., Yu, G.Q., Xu, Q., Fish, J.D., Wyss-Coray, T., Buttini, M., Mucke, L. and Mahley, R.W., 2004. Neuron-specific apolipoprotein e4 proteolysis is associated with increased tau phosphorylation in brains of transgenic mice. *Journal of Neuroscience*, 24(10), pp.2527-2534.
50. Bretz, F., Hothorn, T., Westfall, P., 2016. Multiple Comparisons Using R. CRC Press.
51. Brion, J.P., 1998. Neurofibrillary tangles and Alzheimer's disease. *Eur. Neurol.* 40, 130–140.
52. Brothers, L.A., Finch, D.M., 1985. Physiological evidence for an excitatory pathway from entorhinal cortex to amygdala in the rat. *Brain Res.* 359, 10–20.
53. Buckmaster, C.A., 2004. Entorhinal Cortex Lesions Disrupt the Relational Organization of Memory in Monkeys. *Journal of Neuroscience*. <https://doi.org/10.1523/jneurosci.1532-04.2004>
54. Bullmore, E., Sporns, O., 2009. Complex brain networks: graph theoretical analysis of structural and functional systems. *Nat. Rev. Neurosci.* 10, 186–198.
55. Burns, S.P., Xing, D., Shapley, R.M., 2010. Comparisons of the dynamics of local field potential and multiunit activity signals in macaque visual cortex. *J. Neurosci.* 30, 13739–13749.
56. Buxbaum, J.D., Thinakaran, G., Koliatsos, V., O'Callahan, J., Slunt, H.H., Price, D.L., Sisodia, S.S., 1998. Alzheimer amyloid protein precursor in the rat hippocampus: transport and processing

- through the perforant path. *J. Neurosci.* 18, 9629–9637.
56. Buxton, R.B., 2012. Dynamic models of BOLD contrast. *Neuroimage* 62, 953–961.
 57. Buxton, R.B., Wong, E.C., Frank, L.R., 1998. Dynamics of blood flow and oxygenation changes during brain activation: the balloon model. *Magn. Reson. Med.* 39, 855–864.
 58. Buzsáki, G., 2006. Rhythms of the Brain.
<https://doi.org/10.1093/acprof:oso/9780195301069.001.0001>
 59. Buzsáki, G., Anastassiou, C.A., Koch, C., 2012. The origin of extracellular fields and currents-- EEG, ECoG, LFP and spikes. *Nat. Rev. Neurosci.* 13, 407–420.
 60. Buzsáki, G., Moser, E.I., 2013. Memory, navigation and theta rhythm in the hippocampal-entorhinal system. *Nat. Neurosci.* 16, 130–138.
 61. Canter, R.G., Penney, J., Tsai, L.-H., 2016. The road to restoring neural circuits for the treatment of Alzheimer's disease. *Nature* 539, 187–196.
 62. Canto, C.B., Wouterlood, F.G., Witter, M.P., 2008. What does the anatomical organization of the entorhinal cortex tell us? *Neural Plast.* 2008, 381243.
 63. Carlezon, W.A., Jr, Thomas, M.J., 2009. Biological substrates of reward and aversion: a nucleus accumbens activity hypothesis. *Neuropharmacology* 56 Suppl 1, 122–132.
 64. Caro, A.C., Hankenson, F.C., Marx, J.O., 2013. Comparison of thermoregulatory devices used during anesthesia of C57BL/6 mice and correlations between body temperature and physiologic parameters. *J. Am. Assoc. Lab. Anim. Sci.* 52, 577–583.
 65. Chan, R.W., Leong, A.T.L., Ho, L.C., Gao, P.P., Wong, E.C., Dong, C.M., Wang, X., He, J., Chan, Y.-S., Lim, L.W., Wu, E.X., 2017. Low-frequency hippocampal–cortical activity drives brain-wide resting-state functional MRI connectivity. *Proceedings of the National Academy of Sciences.*
<https://doi.org/10.1073/pnas.1703309114>
 66. Chapman, P.F., White, G.L., Jones, M.W., Cooper-Blacketer, D., Marshall, V.J., Irizarry, M., Younkin, L., Good, M.A., Bliss, T.V.P., Hyman, B.T., Younkin, S.G., Hsiao, K.K., 1999. Impaired synaptic plasticity and learning in aged amyloid precursor protein transgenic mice. *Nature Neuroscience.* <https://doi.org/10.1038/6374>
 67. Chasseigneaux, S., Allinquant, B., 2012. Functions of A β , sAPP α and sAPP β : similarities and differences. *J. Neurochem.* 120 Suppl 1, 99–108.
 68. Chen, C.-J., -J. Chen, C., -C. Chen, C., Wu, D., -F. Chi, N., -C. Chen, P., -P. Liao, Y., -W. Chiu, H., -J. Hu, C., 2013. Effects of the Apolipoprotein E ϵ 4 Allele on Functional MRI during n-Back Working Memory Tasks in Healthy Middle-Aged Adults. *American Journal of Neuroradiology.*
<https://doi.org/10.3174/ajnr.a3369>
 69. Chen, Y.I., Brownell, A.L., Galpern, W., Isacson, O., Bogdanov, M., Beal, M.F., Livni, E., Rosen, B.R., Jenkins, B.G., 1999. Detection of dopaminergic cell loss and neural transplantation using pharmacological MRI, PET and behavioral assessment. *Neuroreport* 10, 2881–2886.
 70. Chiquita, S., Ribeiro, M., Castelhana, J., Oliveira, F., Sereno, J., Batista, M., Abrunhosa, A.,

- Rodrigues-Neves, A.C., Carecho, R., Baptista, F., Gomes, C., Moreira, P.I., Ambrósio, A.F., Castelo-Branco, M., 2019. A longitudinal multimodal *in vivo* molecular imaging study of the 3xTg-AD mouse model shows progressive early hippocampal and taurine loss. *Hum. Mol. Genet.* 28, 2174–2188.
71. Christie, I.N., Wells, J.A., Southern, P., Marina, N., Kasparov, S., Gourine, A.V., Lythgoe, M.F., 2013. fMRI response to blue light delivery in the naïve brain: implications for combined optogenetic fMRI studies. *Neuroimage* 66, 634–641.
 72. Cirrito, J.R., Kang, J.-E., Lee, J., Stewart, F.R., Verges, D.K., Silverio, L.M., Bu, G., Mennerick, S., Holtzman, D.M., 2008. Endocytosis Is Required for Synaptic Activity-Dependent Release of Amyloid- β *In vivo*. *Neuron*. <https://doi.org/10.1016/j.neuron.2008.02.003>
 73. Cirrito, J.R., Yamada, K.A., Finn, M.B., Sloviter, R.S., Bales, K.R., May, P.C., Schoepp, D.D., Paul, S.M., Mennerick, S., Holtzman, D.M., 2005. Synaptic Activity Regulates Interstitial Fluid Amyloid- β Levels *In vivo*. *Neuron*. <https://doi.org/10.1016/j.neuron.2005.10.028>
 74. Clavaguera, F., Akatsu, H., Fraser, G., Crowther, R.A., Frank, S., Hench, J., Probst, A., Winkler, D.T., Reichwald, J., Staufenbiel, M. and Ghetti, B., 2013. Brain homogenates from human tauopathies induce tau inclusions in mouse brain. *Proceedings of the National Academy of Sciences*, 110(23), pp.9535-9540.
 75. Clement, E.A., Richard, A., Thwaites, M., Ailon, J., Peters, S., Dickson, C.T., 2008. Cyclic and sleep-like spontaneous alternations of brain state under urethane anaesthesia. *PLoS One* 3, e2004.
 76. Clinton, L.K., Billings, L.M., Green, K.N., Caccamo, A., Ngo, J., Oddo, S., McGaugh, J.L., LaFerla, F.M., 2007. Age-dependent sexual dimorphism in cognition and stress response in the 3xTg-AD mice. *Neurobiol. Dis.* 28, 76–82.
 77. Cohen, R.M., Rezai-Zadeh, K., Weitz, T.M., Rentsendorj, A., Gate, D., Spivak, I., Bholat, Y., Vasilevko, V., Glabe, C.G., Breunig, J.J., Rakic, P., Davtyan, H., Agadjanyan, M.G., Kepe, V., Barrio, J.R., Bannykh, S., Szekely, C.A., Pechnick, R.N., Town, T., 2013. A transgenic Alzheimer rat with plaques, tau pathology, behavioral impairment, oligomeric $a\beta$, and frank neuronal loss. *J. Neurosci.* 33, 6245–6256.
 78. Cohen, Y., Paz, R., 2015. It All Depends on the Context, but Also on the Amygdala. *Neuron*. <https://doi.org/10.1016/j.neuron.2015.08.012>
 79. Cordella, A., Krashia, P., Nobili, A., Pignataro, A., La Barbera, L., Viscomi, M.T., Valzania, A., Keller, F., Ammassari-Teule, M., Mercuri, N.B., Berretta, N., D’Amelio, M., 2018. Dopamine loss alters the hippocampus-nucleus accumbens synaptic transmission in the Tg2576 mouse model of Alzheimer’s disease. *Neurobiol. Dis.* 116, 142–154.
 80. Cox, R.W., 1996. AFNI: software for analysis and visualization of functional magnetic resonance neuroimages. *Comput. Biomed. Res.* 29, 162–173.
 81. Csicsvari, J., Henze, D.A., Jamieson, B., Harris, K.D., Sirota, A., Barthó, P., Wise, K.D., Buzsáki, G., 2003. Massively Parallel Recording of Unit and Local Field Potentials With Silicon-Based Electrodes. *Journal of Neurophysiology*. <https://doi.org/10.1152/jn.00116.2003>
 82. Cummings, J.L., Morstorf, T., Zhong, K., 2014. Alzheimer’s disease drug-development pipeline: few candidates, frequent failures. *Alzheimer’s Research & Therapy*. <https://doi.org/10.1186/alzrt269>

83. Damoiseaux, J.S., 2012. Resting-state fMRI as a biomarker for Alzheimer's disease? *Alzheimer's Research & Therapy*. <https://doi.org/10.1186/alzrt106>
84. Damoiseaux, J.S., Rombouts, S.A.R.B., Barkhof, F., Scheltens, P., Stam, C.J., Smith, S.M., Beckmann, C.F., 2006. Consistent resting-state networks across healthy subjects. *Proc. Natl. Acad. Sci. U. S. A.* 103, 13848–13853.
85. Darrasse, L., Ginefri, J.-C., 2003. Perspectives with cryogenic RF probes in biomedical MRI. *Biochimie* 85, 915–937.
86. Davis, D.G., Schmitt, F.A., Wekstein, D.R., Markesbery, W.R., 1999. Alzheimer neuropathologic alterations in aged cognitively normal subjects. *J. Neuropathol. Exp. Neurol.* 58, 376–388.
87. Davis, G.W., 2006. Homeostatic control of neural activity: from phenomenology to molecular design. *Annu. Rev. Neurosci.* 29, 307–323.
88. Davis, K.E., Burnett, K., Gigg, J., 2017. Water and T-maze protocols are equally efficient methods to assess spatial memory in 3xTg Alzheimer's disease mice. *Behav. Brain Res.* 331, 54–66.
89. Davis, K.E., Eacott, M.J., Easton, A., Gigg, J., 2013a. Episodic-like memory is sensitive to both Alzheimer's-like pathological accumulation and normal ageing processes in mice. *Behavioural Brain Research*. <https://doi.org/10.1016/j.bbr.2013.03.009>
90. Davis, K.E., Easton, A., Eacott, M.J., Gigg, J., 2013b. Episodic-like memory for what-where-which occasion is selectively impaired in the 3xTgAD mouse model of Alzheimer's disease. *J. Alzheimers. Dis.* 33, 681–698.
91. Davis, K.E., Fox, S., Gigg, J., 2014. Increased hippocampal excitability in the 3xTgAD mouse model for Alzheimer's disease *in vivo*. *PLoS One* 9, e91203.
92. Deisseroth, K., 2011. Optogenetics. *Nat. Methods* 8, 26.
93. Delacourte, A., David, J.P., Sergeant, N., Buee, L., Wattez, A., Vermersch, P., Ghazali, F., Fallet-Bianco, C., Pasquier, F., Lebert, F., Petit, H., Di Menza, C., 1999. The biochemical pathway of neurofibrillary degeneration in aging and Alzheimer's disease. *Neurology*. <https://doi.org/10.1212/wnl.52.6.1158>
94. Deng, L., Sun, J., Cheng, L. and Tong, S., 2016. Characterizing dynamic local functional connectivity in the human brain. *Scientific reports*, 6, p.26976.
95. Dere, E., Pause, B.M., Pietrowsky, R., 2010. Emotion and episodic memory in neuropsychiatric disorders. *Behav. Brain Res.* 215, 162–171.
96. Desai, M., Kahn, I., Knoblich, U., Bernstein, J., Atallah, H., Yang, A., Kopell, N., Buckner, R.L., Graybiel, A.M., Moore, C.I., Boyden, E.S., 2011. Mapping brain networks in awake mice using combined optical neural control and fMRI. *J. Neurophysiol.* 105, 1393–1405.
97. Desai, M.K., Sudol, K.L., Janelins, M.C., Mastrangelo, M.A., Frazer, M.E., Bowers, W.J., 2009. Triple-transgenic Alzheimer's disease mice exhibit region-specific abnormalities in brain myelination patterns prior to appearance of amyloid and tau pathology. *Glia*. <https://doi.org/10.1002/glia.20734>

98. D'Esposito, M., Deouell, L.Y., Gazzaley, A., 2003. Alterations in the BOLD fMRI signal with ageing and disease: a challenge for neuroimaging. *Nat. Rev. Neurosci.* 4, 863– 872.
99. Detre, J.A., Wang, J., 2002. Technical aspects and utility of fMRI using BOLD and ASL. *Clin. Neurophysiol.* 113, 621–634.
100. DeVos, S.L., Goncharoff, D.K., Chen, G., Kebodeaux, C.S., Yamada, K., Stewart, F.R., Schuler, D.R., Maloney, S.E., Wozniak, D.F., Rigo, F., Bennett, C.F., Cirrito, J.R., Holtzman, D.M., Miller, T.M., 2013. Antisense reduction of tau in adult mice protects against seizures. *J. Neurosci.* 33, 12887–12897.
101. Diana, R.A., Yonelinas, A.P., Ranganath, C., 2007. Imaging recollection and familiarity in the medial temporal lobe: a three-component model. *Trends Cogn. Sci.* 11(9):379–86
102. Drummond, E., Wisniewski, T., 2017. Alzheimer's disease: experimental models and reality. *Acta Neuropathologica*. <https://doi.org/10.1007/s00401-016-1662-x>
103. Dubois, B., Hampel, H., Feldman, H.H., Scheltens, P., Aisen, P., Andrieu, S., Bakardjian, H., Benali, H., Bertram, L., Blennow, K., Broich, K., Cavado, E., Crutch, S., Dartigues, J.-F., Duyckaerts, C., Epelbaum, S., Frisoni, G.B., Gauthier, S., Genthon, R., Gouw, A.A., Habert, M.-O., Holtzman, D.M., Kivipelto, M., Lista, S., Molinuevo, J.-L., O'Bryant, S.E., Rabinovici, G.D., Rowe, C., Salloway, S., Schneider, L.S., Sperling, R., Teichmann, M., Carrillo, M.C., Cummings, J., Jack, C.R., Jr, Proceedings of the Meeting of the International Working Group (IWG) and the American Alzheimer's Association on 'The Preclinical State of AD'; July 23, 2015; Washington DC, USA, 2016. Preclinical Alzheimer's disease: Definition, natural history, and diagnostic criteria. *Alzheimers. Dement.* 12, 292–323.
104. Duff, K., Eckman, C., Zehr, C., Yu, X., Prada, C.-M., Perez-tur, J., Hutton, M., Buee, L., Harigaya, Y., Yager, D., Morgan, D., Gordon, M.N., Holcomb, L., Refolo, L., Zenk, B., Hardy, J., Younkin, S., 1996. Increased amyloid- β 42 (43) in brains of mice expressing mutant presenilin 1. *Nature*. <https://doi.org/10.1038/383710a0>
105. Easton, A., Webster, L.A. and Eacott, M.J., 2012. The episodic nature of episodic-like memories. *Learning & Memory*, 19(4), pp.146-150.
106. Eichenbaum, H., 2000. A cortical-hippocampal system for declarative memory. *Nat. Rev. Neurosci.* 1, 41–50.
107. Elder, G.A., Gama Sosa, M.A. and De Gasperi, R., 2010. Transgenic mouse models of Alzheimer's disease. *Mount Sinai Journal of Medicine: A Journal of Translational and Personalized Medicine: A Journal of Translational and Personalized Medicine*, 77(1), pp.69-81.
108. Epstein, R.A., 2008. Parahippocampal and retrosplenial contributions to human spatial navigation. *Trends in Cognitive Sciences*. <https://doi.org/10.1016/j.tics.2008.07.004>
109. España, J., Giménez-Llort, L., Valero, J., Miñano, A., Rábano, A., Rodríguez-Alvarez, J., LaFerla, F.M., Saura, C.A., 2010. Intraneuronal β -Amyloid Accumulation in the Amygdala Enhances Fear and Anxiety in Alzheimer's Disease Transgenic Mice. *Biol. Psychiatry* 67, 513–521.
110. Etkin, A., Egner, T., Kalisch, R., 2011. Emotional processing in anterior cingulate and medial prefrontal cortex. *Trends Cogn. Sci.* 15, 85–93.

111. Evin, G., Weidemann, A., 2002. Biogenesis and metabolism of Alzheimer's disease Abeta amyloid peptides. *Peptides* 23, 1285–1297.
112. Feinstein, S.C., Wilson, L., 2005. Inability of tau to properly regulate neuronal microtubule dynamics: a loss-of-function mechanism by which tau might mediate neuronal cell death. *Biochimica et Biophysica Acta (BBA) -Molecular Basis of Disease*.
<https://doi.org/10.1016/j.bbadis.2004.07.002>
113. Ferrari, L., Turrini, G., Crestan, V., Bertani, S., Cristofori, P., Bifone, A., Gozzi, A., 2012. A robust experimental protocol for pharmacological fMRI in rats and mice. *J. Neurosci. Methods* 204, 9–18.
114. Ferry, B., Ferreira, G., Traissard, N., Majchrzak, M., 2006. Selective involvement of the lateral entorhinal cortex in the control of the olfactory memory trace during conditioned odor aversion in the rat. *Behavioral Neuroscience*. <https://doi.org/10.1037/0735-7044.120.5.1180>
115. Filippini, N., MacIntosh, B.J., Hough, M.G., Goodwin, G.M., Frisoni, G.B., Smith, S.M., Matthews, P.M., Beckmann, C.F., Mackay, C.E., 2009. Distinct patterns of brain activity in young carriers of the APOE-epsilon4 allele. *Proc. Natl. Acad. Sci. U. S. A.* 106, 7209–7214.
116. Fitzjohn, S.M., Morton, R.A., Kuenzi, F., Rosahl, T.W., Shearman, M., Lewis, H., Smith, D., Reynolds, D.S., Davies, C.H., Collingridge, G.L., Seabrook, G.R., 2001. Age-Related Impairment of Synaptic Transmission But Normal Long-Term Potentiation in Transgenic Mice that Overexpress the Human APP695SWE Mutant Form of Amyloid Precursor Protein. *The Journal of Neuroscience*.
<https://doi.org/10.1523/jneurosci.21-13-04691.2001>
117. Franzmeier, N., Rubinski, A., Neitzel, J., Kim, Y., Damm, A., Na, D.L., Kim, H.J., Lyoo, C.H., Cho, H., Finsterwalder, S., Duering, M., Seo, S.W., Ewers, M., for the Alzheimer's Disease Neuroimaging Initiative, 2019. Functional connectivity associated with tau levels in ageing, Alzheimer's, and small vessel disease. *Brain*. <https://doi.org/10.1093/brain/awz026>
118. Freeman, J.A., Nicholson, C., 1975. Experimental optimization of current source-density technique for anuran cerebellum. *Journal of Neurophysiology*. <https://doi.org/10.1152/jn.1975.38.2.369>
119. Frisoni, G.B., Fox, N.C., Jack, C.R., Scheltens, P., Thompson, P.M., 2010. The clinical use of structural MRI in Alzheimer disease. *Nature Reviews Neurology*.
<https://doi.org/10.1038/nrneurol.2009.215>
120. Fyhn, M., Molden, S., Witter, M.P., Moser, E.I., Moser, M.-B., 2004. Spatial representation in the entorhinal cortex. *Science* 305, 1258–1264.
121. Gallagher, M., Chiba, A.A., 1996. The amygdala and emotion. *Curr. Opin. Neurobiol.* 6, 221–227.
Gao, N., Tao, L.-X., Huang, J., Zhang, F., Li, X., O'Sullivan, F., Chen, S.-P., Tian, S.-J., Mahara, G., Luo, Y.-X., Gao, Q., Liu, X.-T., Wang, W., Liang, Z.-G., Guo, X.-H., 2018. Contourlet-based hippocampal magnetic resonance imaging texture features for multivariant classification and prediction of Alzheimer's disease. *Metab. Brain Dis.* 33, 1899–1909.
122. Gao, R., Penzes, P., 2015. Common Mechanisms of Excitatory and Inhibitory Imbalance in Schizophrenia and Autism Spectrum Disorders. *Current Molecular Medicine*.
<https://doi.org/10.2174/1566524015666150303003028>
123. Gargiulo, S., Greco, A., Gramanzini, M., Esposito, S., Affuso, A., Brunetti, A., Vesce, G., 2012.

- Mice anesthesia, analgesia, and care, Part I: anesthetic considerations in preclinical research. *ILAR J.* 53, E55–69.
124. Gati, J.S., Menon, R.S., Ugurbil, K., Rutt, B.K., 1997. Experimental determination of the BOLD field strength dependence in vessels and tissue. *Magn. Reson. Med.* 38, 296– 302.
 125. Gilboa, A., Winocur, G., Rosenbaum, R.S., Poreh, A., Gao, F., Black, S.E., Westmacott, R., Moscovitch, M., 2006. Hippocampal contributions to recollection in retrograde and anterograde amnesia. *Hippocampus* 16, 966–980.
 126. Giorgi, A., Migliarini, S., Galbusera, A., Maddaloni, G., Mereu, M., Margiani, G., Gritti, M., Landi, S., Trovato, F., Bertozzi, S.M., Armirotti, A., Ratto, G.M., De Luca, M.A., Tonini, R., Gozzi, A., Pasqualetti, M., 2017. Brain-wide Mapping of Endogenous Serotonergic Transmission via Chemogenetic fMRI. *Cell Rep.* 21, 910–918.
 127. Goate, A., Chartier-Harlin, M.C., Mullan, M., Brown, J., Crawford, F., Fidani, L., Giuffra, L., Haynes, A., Irving, N., James, L., 1991. Segregation of a missense mutation in the amyloid precursor protein gene with familial Alzheimer's disease. *Nature* 349, 704– 706.
 128. Goedert, M., Wischik, C.M., Crowther, R.A., Walker, J.E., Klug, A., 1988. Cloning and sequencing of the cDNA encoding a core protein of the paired helical filament of Alzheimer disease: identification as the microtubule-associated protein tau.
 129. Proceedings of the National Academy of Sciences. <https://doi.org/10.1073/pnas.85.11.4051>
 130. Gómez-Isla, T., Price, J.L., McKeel, D.W., Jr., Morris, J.C., Growdon, J.H., Hyman, B.T., 1996. Profound Loss of Layer II Entorhinal Cortex Neurons Occurs in Very Mild Alzheimer's Disease. *The Journal of Neuroscience*. <https://doi.org/10.1523/jneurosci.16-14-04491.1996>
 131. Gouras, G.K., Tsai, J., Naslund, J., Vincent, B., Edgar, M., Checler, F., Greenfield, J.P., Haroutunian, V., Buxbaum, J.D., Xu, H., Greengard, P., Relkin, N.R., 2000. Intraneuronal A β 42 Accumulation in Human Brain. *The American Journal of Pathology*. [https://doi.org/10.1016/s0002-9440\(10\)64700-1](https://doi.org/10.1016/s0002-9440(10)64700-1)
 132. Gour, N., Felician, O., Didic, M., Koric, L., Gueriot, C., Chanoine, V., Confort-Gouny, S., Guye, M., Ceccaldi, M., Ranjeva, J.P., 2014. Functional connectivity changes differ in early and late-onset Alzheimer's disease. *Hum. Brain Mapp.* 35, 2978–2994.
 133. Gozzi, A., Schwarz, A.J., 2016. Large-scale functional connectivity networks in the rodent brain. *Neuroimage* 127, 496–509.
 134. Grandjean, J., Canella, C., Anckaerts, C., Ayrancı, G., Bougacha, S., Bienert, T., Buehlmann, D., Coletta, L., Gallino, D., Gass, N., Garin, C.M., Nadkarni, N.A., Hübner, N., Karatas, M., Komaki, Y., Kreitz, S., Mandino, F., Mechling, A.E., Sato, C., Sauer, K., Shah, D., Strobelt, S., Takata, N., Wank, I., Wu, T., Yahata, N., Yeow, L.Y., Yee, Y., Aoki, I., Mallar Chakravarty, M., Chang, W.-T., Dhenain, M., von Elverfeldt, D., Harsan, L.-A., Hess, A., Jiang, T., Keliris, G.A., Lerch, J.P., Okano, H., Rudin, M., Sartorius, A., Van der Linden, A., Verhoye, M., Weber-Fahr, W., Wenderoth, N., Zerbi, V., Gozzi, A., 2019a. Common functional networks in the mouse brain revealed by multi-centre resting-state fMRI analysis. *bioRxiv*. <https://doi.org/10.1101/541060>
 135. Grandjean, J., Corcoba, A., Kahn, M.C., Upton, A.L., Deneris, E.S., Seifritz, E., Helmchen, F., Mann, E.O., Rudin, M., Saab, B.J., 2019b. A brain-wide functional map of the serotonergic responses to acute stress and fluoxetine. *Nat. Commun.* 10, 350.

136. Grandjean, J., Derungs, R., Kulic, L., Welt, T., Henkelman, M., Nitsch, R.M., Rudin, M., 2016. Complex interplay between brain function and structure during cerebral amyloidosis in APP transgenic mouse strains revealed by multi-parametric MRI comparison. *Neuroimage* 134, 1–11.
137. Grandjean, J., Schroeter, A., Batata, I., Rudin, M., 2014a. Optimization of anesthesia protocol for resting-state fMRI in mice based on differential effects of anesthetics on functional connectivity patterns. *Neuroimage* 102 Pt 2, 838–847.
138. Grandjean, J., Schroeter, A., He, P., Tanadini, M., Keist, R., Krstic, D., Konietzko, U., Klohs, J., Nitsch, R.M., Rudin, M., 2014b. Early Alterations in Functional Connectivity and White Matter Structure in a Transgenic Mouse Model of Cerebral Amyloidosis. *The Journal of Neuroscience*. <https://doi.org/10.1523/jneurosci.4762-13.2014>
139. Green, C., Sydow, A., Vogel, S., Anglada-Huguet, M., Wiedermann, D., Mandelkow, E., Mandelkow, E.-M., Hoehn, M., 2019. Functional networks are impaired by elevated tau-protein but reversible in a regulatable Alzheimer's disease mouse model. *Mol. Neurodegener.* 14, 13.
140. Greicius, M.D., Srivastava, G., Reiss, A.L., Menon, V., 2004. Default-mode network activity distinguishes Alzheimer's disease from healthy aging: evidence from functional MRI. *Proc. Natl. Acad. Sci. U. S. A.* 101, 4637–4642.
141. Gu, X., Hof, P.R., Friston, K.J. and Fan, J., 2013. Anterior insular cortex and emotional awareness. *Journal of Comparative Neurology*, 521(15), pp.3371-3388.
142. Guadagno, A., Kang, M.S., Devenyi, G.A., Mathieu, A.P., Rosa-Neto, P., Chakravarty, M., Walker, C.-D., 2018. Reduced resting-state functional connectivity of the basolateral amygdala to the medial prefrontal cortex in preweaning rats exposed to chronic early-life stress. *Brain Struct. Funct.* 223, 3711–3729.
143. Guo, Q., Furukawa, K., Sopher, B.L., Pham, D.G., Xie, J., Robinson, N., Martin, G.M., Mattson, M.P., 1996. Alzheimer's PS-1 mutation perturbs calcium homeostasis and sensitizes PC12 cells to death induced by amyloid beta-peptide. *Neuroreport* 8, 379– 383.
144. Guru, A., Post, R.J., Ho, Y.-Y., Warden, M.R., 2015. Making Sense of Optogenetics. *Int. J. Neuropsychopharmacol.* 18, yv079.
145. Hafting, T., Fyhn, M., Molden, S., Moser, M.-B., Moser, E.I., 2005. Microstructure of a spatial map in the entorhinal cortex. *Nature* 436, 801–806.
146. Hämäläinen, A., Pihlajamäki, M., Tanila, H., Hänninen, T., Niskanen, E., Tervo, S., Karjalainen, P.A., Vanninen, R.L., Soininen, H., 2007. Increased fMRI responses during encoding in mild cognitive impairment. *Neurobiol. Aging* 28, 1889–1903.
147. Hampel, H., Teipel, S.J., 2004. Total and phosphorylated tau proteins: evaluation as core biomarker candidates in frontotemporal dementia. *Dement. Geriatr. Cogn. Disord.* 17, 350–354.
148. Han, X., 2012. *In vivo* application of optogenetics for neural circuit analysis. *ACS Chem. Neurosci.* 3, 577–584.
149. Hardy, J., 2006. The Amyloid Hypothesis: history and alternatives. *Alzheimer: 100 Years and Beyond*. https://doi.org/10.1007/978-3-540-37652-1_15

150. Hardy, J., Higgins, G., 1992. Alzheimer's disease: the amyloid cascade hypothesis. *Science*. <https://doi.org/10.1126/science.1566067>
151. Harold, D., Abraham, R., Hollingworth, P., Sims, R., Gerrish, A., Hamshere, M.L., Pahwa, J.S., Moskvina, V., Dowzell, K., Williams, A., Jones, N., Thomas, C., Stretton, A., Morgan, A.R., Lovestone, S., Powell, J., Proitsi, P., Lupton, M.K., Brayne, C., Rubinsztein, D.C., Gill, M., Lawlor, B., Lynch, A., Morgan, K., Brown, K.S., Passmore, P.A., Craig, D., McGuinness, B., Todd, S., Holmes, C., Mann, D., David Smith, A., Love, S., Kehoe, P.G., Hardy, J., Mead, S., Fox, N., Rossor, M., Collinge, J., Maier, W., Jessen, F., Schürmann, B., van den Bussche, H., Heuser, I., Kornhuber, J., Wiltfang, J., Dichgans, M., Frölich, L., Hampel, H., Hüll, M., Rujescu, D., Goate, A.M., Kauwe, J.S.K., Cruchaga, C., Nowotny, P., Morris, J.C., Mayo, K., Sleegers, K., Bettens, K., Engelborghs, S., De Deyn, P.P., Van Broeckhoven, C., Livingston, G., Bass, N.J., Gurling, H., McQuillin, A., Gwilliam, R., Deloukas, P., Al-Chalabi, A., Shaw, C.E., Tsolaki, M., Singleton, A.B., Guerreiro, R., Mühleisen, T.W., Nöthen, M.M., Moebus, S., Jöckel, K.-H., Klopp, N., Wichmann, H.-E., Carrasquillo, M.M., Shane Pankratz, V., Younkin, S.G., Holmans, P.A., O'Donovan, M., Owen, M.J., Williams, J., 2009. Erratum: Genome-wide association study identifies variants at CLU and PICALM associated with Alzheimer's disease. *Nature Genetics*. <https://doi.org/10.1038/ng1009-1156d>
152. Harris, J.A., Devidze, N., Verret, L., Ho, K., Halabisky, B., Thwin, M.T., Kim, D., Hamto, P., Lo, I., Yu, G.-Q., Palop, J.J., Masliah, E., Mucke, L., 2010. Transsynaptic progression of amyloid- β -induced neuronal dysfunction within the entorhinal-hippocampal network. *Neuron* 68, 428–441.
154. Harrison, J., 2013. Cognitive Approaches to Early Alzheimer's Disease Diagnosis. *Medical Clinics of North America*. <https://doi.org/10.1016/j.mcna.2012.12.014>
155. Heeger, D.J., Ress, D., 2002. What does fMRI tell us about neuronal activity? *Nat. Rev. Neurosci.* 3, 142–151.
156. Hellström-Lindahl, E., Ravid, R., Nordberg, A., 2008. Age-dependent decline of neprilysin in Alzheimer's disease and normal brain: inverse correlation with A β levels. *Neurobiol. Aging* 29, 210–221.
157. Henze, D.A., Borhegyi, Z., Csicsvari, J., Mamiya, A., Harris, K.D., Buzsáki, G., 2000. Intracellular features predicted by extracellular recordings in the hippocampus *in vivo*. *J. Neurophysiol.* 84, 390–400.
158. Herrup, K., 2015. The case for rejecting the amyloid cascade hypothesis. *Nature Neuroscience*. <https://doi.org/10.1038/nn.4017>
159. Hijazi, S., Heistek, T.S., Scheltens, P., Neumann, U., Shimshek, D.R., Mansvelder, H.D., Smit, A.B., van Kesteren, R.E., 2019. Early restoration of parvalbumin interneuron activity prevents memory loss and network hyperexcitability in a mouse model of Alzheimer's disease. *Molecular Psychiatry*. <https://doi.org/10.1038/s41380-019-0483-4>
160. Hinz, R., Peeters, L., Li, C., Van Der Linden, A., Keliris, G., 2017. A comparison of BOLD response between optogenetic and visual stimulation of the lateral Geniculate Nucleus. *Frontiers in Neuroscience*. <https://doi.org/10.3389/conf.fnins.2017.94.00059> Histed, M.H., 2018. Feedforward Inhibition Allows Input Summation to Vary in Recurrent Cortical Networks. *eNeuro* 5. <https://doi.org/10.1523/ENEURO.0356-17.2018>

161. Hodge, R.D., Bakken, T.E., Miller, J.A., Smith, K.A., Barkan, E.R., Graybuck, L.T., Close, J.L., Long, B., Johansen, N., Penn, O., Yao, Z., Eggermont, J., Höllt, T., Levi, B.P., Shehata, S.I., Aevermann, B., Beller, A., Bertagnolli, D., Brouner, K., Casper, T., Cobbs, C., Dalley, R., Dee, N., Ding, S.-L., Ellenbogen, R.G., Fong, O., Garren, E., Goldy, J., Gwinn, R.P., Hirschstein, D., Keene, C.D., Keshk, M., Ko, A.L., Lathia, K., Mahfouz, A., Maltzer, Z., McGraw, M., Nguyen, T.N., Nyhus, J., Ojemann, J.G., Oldre, A., Parry, S., Reynolds, S., Rimorin, C., Shapovalova, N.V., Somasundaram, S., Szafer, A., Thomsen, E.R., Tieu, M., Quon, G., Scheuermann, R.H., Yuste, R., Sunkin, S.M., Lelieveldt, B., Feng, D., Ng, L., Bernard, A., Hawrylycz, M., Phillips, J.W., Tasic, B., Zeng, H., Jones, A.R., Koch, C., Lein, E.S., 2019. Conserved cell types with divergent features in human versus mouse cortex. *Nature* 573, 61–68.
162. Ho, J., Tumkaya, T., Aryal, S., Choi, H., Claridge-Chang, A., 2019. Moving beyond P values: data analysis with estimation graphics. *Nat. Methods* 16, 565–566.
163. Hodges, J., 1998. The amnesic prodrome of Alzheimer's disease. *Brain*. <https://doi.org/10.1093/brain/121.9.1601>
164. Holcomb L, Gordon MN, McGowan E, Yu X, Benkovic S, Jantzen P, Saad WK, Mueller R, Morgan D, Sanders S et al (1998) Accelerated Alzheimer-type phenotype in transgenic mice carrying both mutant amyloid precursor protein and presenilin 1 transgenes. *Nat Med* 4:97–100
165. Hutchison, R.M., Mirsattari, S.M., Jones, C.K., Gati, J.S., Leung, L.S., 2010. Functional networks in the anesthetized rat brain revealed by independent component analysis of resting-state FMRI. *J. Neurophysiol.* 103, 3398–3406.
166. Hyman, B.T., Van Hoesen, G.W., Kromer, L.J., Damasio, A.R., 1986. Perforant pathway changes and the memory impairment of Alzheimer's disease. *Ann. Neurol.* 20, 472–481.
167. Iadecola, C., 2017. The Neurovascular Unit Coming of Age: A Journey through Neurovascular Coupling in Health and Disease. *Neuron* 96, 17–42.
168. Ikonomic, M.D., Klunk, W.E., Abrahamson, E.E., Mathis, C.A., Price, J.C., Tsopelas, N.D., Lopresti, B.J., Ziolk, S., Bi, W., Paljug, W.R., Debnath, M.L., Hope, C.E., Isanski, B.A., Hamilton, R.L., DeKosky, S.T., 2008. Post-mortem correlates of *in vivo* PiB-PET amyloid imaging in a typical case of Alzheimer's disease. *Brain*. <https://doi.org/10.1093/brain/awn016>
169. Ittner, L.M., Ke, Y.D., Delerue, F., Bi, M., Gladbach, A., van Eersel, J., Wölfling, H., Chieng, B.C., Christie, M.J., Napier, I.A., Eckert, A., Staufenbiel, M., Hardeman, E., Götz, J., 2010. Dendritic Function of Tau Mediates Amyloid- β Toxicity in Alzheimer's Disease Mouse Models. *Cell*. <https://doi.org/10.1016/j.cell.2010.06.036>
170. Iwata, N., Tsubuki, S., Takaki, Y., Watanabe, K., Sekiguchi, M., Hosoki, E., Kawashima-Morishima, M., Lee, H.-J., Hama, E., Sekine-Aizawa, Y., Saido, T.C., 2000. Identification of the major A β 1–42-degrading catabolic pathway in brain parenchyma: Suppression leads to biochemical and pathological deposition. *Nature Medicine*. <https://doi.org/10.1038/72237>
171. Jack, C.R., 2012. Alzheimer Disease: New Concepts on Its Neurobiology and the Clinical Role Imaging Will Play. *Radiology*. <https://doi.org/10.1148/radiol.12110433>
172. Jack, C.R., Bennett, D.A., Blennow, K., Carrillo, M.C., Dunn, B., Haeberlein, S.B., Holtzman, D.M., Jagust, W., Jessen, F., Karlawish, J., Liu, E., Molinuevo, J.L., Montine, T., Phelps, C., Rankin, K.P., Rowe, C.C., Scheltens, P., Siemers, E., Snyder, H.M., Sperling, R., Elliott, C.,

- Masliah, E., Ryan, L., Silverberg, N., 2018. NIA-AA Research Framework: Toward a biological definition of Alzheimer's disease. *Alzheimer's & Dementia*.
<https://doi.org/10.1016/j.jalz.2018.02.018>
173. Jack, C.R., Jr, Knopman, D.S., Jagust, W.J., Shaw, L.M., Aisen, P.S., Weiner, M.W., Petersen, R.C., Trojanowski, J.Q., 2010. Hypothetical model of dynamic biomarkers of the Alzheimer's pathological cascade. *Lancet Neurol.* 9, 119–128.
 174. Jack, C.R., Shiung, M.M., Weigand, S.D., O'Brien, P.C., Gunter, J.L., Boeve, B.F., Knopman, D.S., Smith, G.E., Ivnik, R.J., Tangalos, E.G., Petersen, R.C., 2005. Brain atrophy rates predict subsequent clinical conversion in normal elderly and amnesic MCI. *Neurology*.
<https://doi.org/10.1212/01.wnl.0000180958.22678.91>
 175. Jacobsen, J.S., -C. Wu, C., Redwine, J.M., Comery, T.A., Arias, R., Bowlby, M., Martone, R., Morrison, J.H., Pangalos, M.N., Reinhart, P.H., Bloom, F.E., 2006. Early-onset behavioral and synaptic deficits in a mouse model of Alzheimer's disease. *Proceedings of the National Academy of Sciences*. <https://doi.org/10.1073/pnas.0600948103>
 176. Jagust, W., 2018. Following the pathway to Alzheimer's disease. *Nat. Neurosci.* Janus, C., Azhar Chishti, M., Westaway, D., 2000. Transgenic mouse models of Alzheimer's disease. *Biochimica et Biophysica Acta (BBA) -Molecular Basis of Disease*. [https://doi.org/10.1016/s0925-4439\(00\)00033-8](https://doi.org/10.1016/s0925-4439(00)00033-8)
 177. Jankowsky, J.L. and Zheng, H., 2017. Practical considerations for choosing a mouse model of Alzheimer's disease. *Molecular neurodegeneration*, 12(1), p.89.
 178. Jo, S., Yarishkin, O., Hwang, Y.J., Chun, Y.E., Park, M., Woo, D.H., Bae, J.Y., Kim, T., Lee, J., Chun, H. and Park, H.J., 2014. GABA from reactive astrocytes impairs memory in mouse models of Alzheimer's disease. *Nature medicine*, 20(8), p.886.
 179. Jobst, K.A., Smith, A.D., Szatmari, M., Esiri, M.M., Jaskowski, A., Hindley, N., McDonald, B., Molyneux, A.J., 1994. Rapidly progressing atrophy of medial temporal lobe in Alzheimer's disease. *Lancet* 343, 829–830.
 180. Johnson, K.A., Fox, N.C., Sperling, R.A., Klunk, W.E., 2012. Brain imaging in Alzheimer disease. *Cold Spring Harb. Perspect. Med.* 2, a006213.
 181. Johnstone, M., Gearing, A.J.H., Miller, K.M., 1999. A central role for astrocytes in the inflammatory response to β -amyloid; chemokines, cytokines and reactive oxygen species are produced. *Journal of Neuroimmunology*. [https://doi.org/10.1016/s0165-5728\(98\)00226-4](https://doi.org/10.1016/s0165-5728(98)00226-4)
 182. Jonckers, E., Shah, D., Hamaide, J., Verhoye, M., Van der Linden, A., 2015. The power of using functional fMRI on small rodents to study brain pharmacology and disease. *Front. Pharmacol.* 6, 231.
 183. Joyce, J.N., Kaeger, C., Ryoo, H., Goldsmith, S., 1993. Dopamine D2 receptors in the hippocampus and amygdala in Alzheimer's disease. *Neurosci. Lett.* 154, 171–174.
 184. Jucker, M., 2010. The benefits and limitations of animal models for translational research in neurodegenerative diseases. *Nat. Med.* 16, 1210–1214.
 185. Kahn, I., Knoblich, U., Desai, M., Bernstein, J., Graybiel, A.M., Boyden, E.S., Buckner, R.L.,

- Moore, C.I., 2013. Optogenetic drive of neocortical pyramidal neurons generates fMRI signals that are correlated with spiking activity. *Brain Res.* 1511, 33–45.
186. Kamenetz, F., Tomita, T., Hsieh, H., Seabrook, G., Borchelt, D., Iwatsubo, T., Sisodia, S., Malinow, R., 2003. APP processing and synaptic function. *Neuron* 37, 925–937.
187. Kanaan, N.M., Pigino, G.F., Brady, S.T., Lazarov, O., Binder, L.I., Morfini, G.A., 2013. Axonal degeneration in Alzheimer's disease: when signaling abnormalities meet the axonal transport system. *Exp. Neurol.* 246, 44–53.
188. Karran, E., Mercken, M., De Strooper, B., 2011. The amyloid cascade hypothesis for Alzheimer's disease: an appraisal for the development of therapeutics. *Nature Reviews Drug Discovery*. <https://doi.org/10.1038/nrd3505>
189. Kastanenka, K.V., Hou, S.S., Shakerdige, N., Logan, R., Feng, D., Wegmann, S., Chopra, V., Hawkes, J.M., Chen, X., Bacskai, B.J., 2017. Optogenetic Restoration of Disrupted Slow Oscillations Halts Amyloid Deposition and Restores Calcium Homeostasis in an Animal Model of Alzheimer's Disease. *PLOS ONE*. <https://doi.org/10.1371/journal.pone.0170275>
190. Kato, H.E., Zhang, F., Yizhar, O., Ramakrishnan, C., Nishizawa, T., Hirata, K., Ito, J., Aita, Y., Tsukazaki, T., Hayashi, S., Hegemann, P., Maturana, A.D., Ishitani, R., Deisseroth, K., Nureki, O., 2012. Crystal structure of the channelrhodopsin light-gated cation channel. *Nature* 482, 369–374.
191. Kato, T., Knopman, D., Liu, H., 2001. Dissociation of regional activation in mild AD during visual encoding: a functional MRI study. *Neurology* 57, 812–816.
192. Kayser, C., Montemurro, M.A., Logothetis, N.K., Panzeri, S., 2009. Spike-phase coding boosts and stabilizes information carried by spatial and temporal spike patterns. *Neuron* 61, 597–608.
193. Kazim, S.F., Chuang, S.-C., Zhao, W., Wong, R.K.S., Bianchi, R., Iqbal, K., 2017. Early-Onset Network Hyperexcitability in Presymptomatic Alzheimer's Disease Transgenic Mice Is Suppressed by Passive Immunization with Anti-Human APP/A β Antibody and by mGluR5 Blockade. *Frontiers in Aging Neuroscience*. <https://doi.org/10.3389/fnagi.2017.00071>
194. Kemppainen, N., Laine, M., Laakso, M.P., Kaasinen, V., Någren, K., Vahlberg, T., Kurki, T., Rinne, J.O., 2003. Hippocampal dopamine D2 receptors correlate with memory functions in Alzheimer's disease. *Eur. J. Neurosci.* 18, 149–154.
195. Khan, U.A., Liu, L., Provenzano, F.A., Berman, D.E., Profaci, C.P., Sloan, R., Mayeux, R., Duff, K.E., Small, S.A., 2014. Molecular drivers and cortical spread of lateral entorhinal cortex dysfunction in preclinical Alzheimer's disease. *Nature Neuroscience*. <https://doi.org/10.1038/nn.3606>
196. Kisler, K., Nelson, A.R., Montagne, A., Zlokovic, B.V., 2017. Cerebral blood flow regulation and neurovascular dysfunction in Alzheimer disease. *Nat. Rev. Neurosci.* 18, 419–434.
197. Klausberger, T., Magill, P.J., Márton, L.F., Roberts, J.D.B., Cobden, P.M., Buzsáki, G., Somogyi, P., 2003. Brain-state- and cell-type-specific firing of hippocampal interneurons *in vivo*. *Nature*. <https://doi.org/10.1038/nature01374>
198. Kitazawa, M., Medeiros, R. and M LaFerla, F., 2012. Transgenic mouse models of Alzheimer disease: developing a better model as a tool for therapeutic interventions. *Current pharmaceutical*

design, 18(8), pp.1131-1147.

199. Klein, R.C., Acheson, S.K., Mace, B.E., Sullivan, P.M., Moore, S.D., 2014. Altered neurotransmission in the lateral amygdala in aged human apoE4 targeted replacement mice. *Neurobiol. Aging* 35, 2046–2052.
200. Kloosterman, F., van Haeften, T., Witter, M.P., da Silva, F.H.L., 2003. Electrophysiological characterization of interlaminar entorhinal connections: an essential link for re-entrance in the hippocampal-entorhinal system. *European Journal of Neuroscience*. <https://doi.org/10.1111/j.1460-9568.2003.03046.x>
201. Klyubin, I., Mably, A., Minogue, A., Hu, N.-W., Farrell, M., Walsh, D., Rowan, M., 2012. Alzheimer's disease human brain beta-amyloid-containing extracts inhibit hippocampal long-term potentiation in rats *in vivo* : Relationship between soluble and insoluble preparations. *Alzheimer's & Dementia*. <https://doi.org/10.1016/j.jalz.2012.05.1735>
202. Kneynsberg, A., Combs, B., Christensen, K., Morfini, G., Kanaan, N.M., 2017. Axonal Degeneration in Tauopathies: Disease Relevance and Underlying Mechanisms. *Front. Neurosci.* 11, 572.
203. Koch, G., Di Lorenzo, F., Bonni, S., Giacobbe, V., Bozzali, M., Caltagirone, C., Martorana, A., 2014. Dopaminergic Modulation of Cortical Plasticity in Alzheimer's Disease Patients. *Neuropsychopharmacology*. <https://doi.org/10.1038/npp.2014.119>
204. Krashia, P., Nobili, A., D'Amelio, M., 2019. Unifying Hypothesis of Dopamine Neuron Loss in Neurodegenerative Diseases: Focusing on Alzheimer's Disease. *Frontiers in Molecular Neuroscience*. <https://doi.org/10.3389/fnmol.2019.00123>
205. Krstic, D. and Knuesel, I., 2013. Deciphering the mechanism underlying late-onset Alzheimer disease. *Nature Reviews Neurology*, 9(1), p.25.
206. Kumar, S.S., 2006. Hyperexcitability, Interneurons, and Loss of GABAergic Synapses in Entorhinal Cortex in a Model of Temporal Lobe Epilepsy. *Journal of Neuroscience*. <https://doi.org/10.1523/jneurosci.0064-06.2006>
207. LaBar, K.S., Cabeza, R., 2006. Cognitive neuroscience of emotional memory. *Nature Reviews Neuroscience*. <https://doi.org/10.1038/nrn1825>
208. Lacy, J.W., Stark, C.E.L., 2012. Intrinsic functional connectivity of the human medial temporal lobe suggests a distinction between adjacent MTL cortices and hippocampus. *Hippocampus*. <https://doi.org/10.1002/hipo.22047>
209. LaFerla, F.M., Green, K.N., Oddo, S., 2007. Intracellular amyloid- β in Alzheimer's disease. *Nature Reviews Neuroscience*. <https://doi.org/10.1038/nrn2168>
210. LaFerla, F.M., Oddo, S., 2005. Alzheimer's disease: A β , tau and synaptic dysfunction. *Trends in Molecular Medicine*. <https://doi.org/10.1016/j.molmed.2005.02.009> Lamprecht, R., LeDoux, J., 2004. Structural plasticity and memory. *Nature Reviews Neuroscience*. <https://doi.org/10.1038/nrn1301>
211. Lanoiselée, H.-M., Nicolas, G., Wallon, D., Rovelet-Lecrux, A., Lacour, M., Rousseau, S., Richard, A.-C., Pasquier, F., Rollin-Sillaire, A., Martinaud, O., Quillard-Muraine, M., de la Sayette, V.,

- Boutoleau-Bretonniere, C., Etcharry-Bouyx, F., Chauviré, V., Sarazin, M., le Ber, I., Epelbaum, S., Jonveaux, T., Rouaud, O., Ceccaldi, M., Félician, O., Godefroy, O., Formaglio, M., Croisile, B., Auriacombe, S., Chamard, L., Vincent, J.-L., Sauvée, M., Marelli-Tosi, C., Gabelle, A., Ozsancak, C., Pariente, J., Paquet, C., Hannequin, D., Campion, D., collaborators of the CNR-MAJ project, 2017. APP, PSEN1, and PSEN2 mutations in early-onset Alzheimer disease: A genetic screening study of familial and sporadic cases. *PLoS Med.* 14, e1002270.
212. Larsen, R.S., Jesper Sjöström, P., 2015. Synapse-type-specific plasticity in local circuits. *Current Opinion in Neurobiology*. <https://doi.org/10.1016/j.conb.2015.08.001> Larson, J., Lynch, G., Games, D., Seubert, P., 1999. Alterations in synaptic transmission and long-term potentiation in hippocampal slices from young and aged PDAPP mice. *Brain Research*. [https://doi.org/10.1016/s0006-8993\(99\)01698-4](https://doi.org/10.1016/s0006-8993(99)01698-4)
213. Lazarov, O., Lee, M., Peterson, D.A., Sisodia, S.S., 2002. Evidence That Synaptically Released β -Amyloid Accumulates as Extracellular Deposits in the Hippocampus of Transgenic Mice. *The Journal of Neuroscience*. <https://doi.org/10.1523/jneurosci.22-22-09785.2002>
214. LeDoux, J., 2007. The amygdala. *Curr. Biol.* 17, R868–74.
215. Lee, H.-M., Giguere, P.M., Roth, B.L., 2014. DREADDs: novel tools for drug discovery and development. *Drug Discov. Today* 19, 469–473.
216. Lee, J.H., Durand, R., Gradinaru, V., Zhang, F., Goshen, I., Kim, D.-S., Fenno, L.E., Ramakrishnan, C., Deisseroth, K., 2010. Global and local fMRI signals driven by neurons defined optogenetically by type and wiring. *Nature* 465, 788–792.
217. Leong, A.T.L., Dong, C.M., Gao, P.P., Chan, R.W., To, A., Sanes, D.H., Wu, E.X., 2018. Optogenetic auditory fMRI reveals the effects of visual cortical inputs on auditory midbrain response. *Sci. Rep.* 8, 8736.
218. Li, D.-P., Chen, S.-R., Pan, H.-L., 2002. Nitric Oxide Inhibits Spinally Projecting Paraventricular Neurons Through Potentiation of Presynaptic GABA Release. *Journal of Neurophysiology*. <https://doi.org/10.1152/jn.00540.2002>
219. Liebsch, F., Kulic, L., Teunissen, C., Shobo, A., Ulku, I., Engelschalt, V., Hancock, M.A., van der Flier, W.M., Kunach, P., Rosa-Neto, P., Scheltens, P., Poirier, J., Saftig, P., Bateman, R.J., Breitner, J., Hock, C., Multhaup, G., 2019. A β 34 is a BACE1-derived degradation intermediate associated with amyloid clearance and Alzheimer's disease progression. *Nature Communications*. <https://doi.org/10.1038/s41467-019-10152-w>
220. Li, J., Yang, R., Xia, K., Wang, T., Nie, B., Gao, K., Chen, J., Zhao, H., Li, Y., Wang, W., 2018. Effects of stress on behavior and resting-state fMRI in rats and evaluation of Telmisartan therapy in a stress-induced depression model. *BMC Psychiatry*. <https://doi.org/10.1186/s12888-018-1880-y>
221. Lin, Y.J., Koretsky, A.P., 1997. Manganese ion enhances T1-weighted MRI during brain activation: an approach to direct imaging of brain function. *Magn. Reson. Med.* 38, 378–388.
222. Lipton, S., Sanz-Blasco, S., 2012. Faculty of 1000 evaluation for Levetiracetam suppresses neuronal network dysfunction and reverses synaptic and cognitive deficits in an Alzheimer's disease model. F1000 -Post-publication peer review of the biomedical literature. <https://doi.org/10.3410/f.717965468.793466480>

- 223.Li, R., Wu, X., Fleisher, A.S., Reiman, E.M., Chen, K., Yao, L., 2012. Attention-related networks in Alzheimer's disease: A resting functional MRI study. *Human Brain Mapping*.
<https://doi.org/10.1002/hbm.21269>
- 224.Livingston, G., Sommerlad, A., Orgeta, V., Costafreda, S.G., Huntley, J., Ames, D., Ballard, C., Banerjee, S., Burns, A., Cohen-Mansfield, J., Cooper, C., Fox, N., Gitlin, L.N., Howard, R., Kales, H.C., Larson, E.B., Ritchie, K., Rockwood, K., Sampson, E.L., Samus, Q., Schneider, L.S., Selbæk, G., Teri, L., Mukadam, N., 2017. Dementia prevention, intervention, and care. *The Lancet*.
[https://doi.org/10.1016/s0140-6736\(17\)31363-6](https://doi.org/10.1016/s0140-6736(17)31363-6)
- 225.Logothetis, N.K., Pauls, J., Augath, M., Trinath, T., Oeltermann, A., 2001. Neurophysiological investigation of the basis of the fMRI signal. *Nature* 412, 150– 157.
- 226.Lozsadi, D.A., Lerner, A.J., 2006. Prevalence and Causes of Seizures at the Time of Diagnosis of Probable Alzheimer's Disease. *Dementia and Geriatric Cognitive Disorders*.
<https://doi.org/10.1159/000093664>
- 227.Lu, H., Golay, X., Pekar, J.J., van Zijl, P.C.M., 2003. Functional magnetic resonance imaging based on changes in vascular space occupancy. *Magnetic Resonance in Medicine*.
<https://doi.org/10.1002/mrm.10519>
- 228.Lu, H., Hua, J., van Zijl, P.C.M., 2013. Noninvasive functional imaging of cerebral blood volume with vascular-space-occupancy (VASO) MRI. *NMR in Biomedicine*.
<https://doi.org/10.1002/nbm.2905>
- 229.Luo, F., Rustay, N.R., Ebert, U., Hradil, V.P., Cole, T.B., Llano, D.A., Mudd, S.R., Zhang, Y., Fox, G.B., Day, M., 2012. Characterization of 7-and 19-month-old Tg2576 mice using multimodal *in vivo* imaging: limitations as a translatable model of Alzheimer's disease. *Neurobiol. Aging* 33, 933– 944.
- 230.Luo, Y., Bolon, B., Kahn, S., Bennett, B.D., Babu-Khan, S., Denis, P., Fan, W., Kha, H., Zhang, J., Gong, Y., Martin, L., Louis, J.-C., Yan, Q., Richards, W.G., Citron, M., Vassar, R., 2001. Mice deficient in BACE1, the Alzheimer's β -secretase, have normal phenotype and abolished β -amyloid generation. *Nature Neuroscience*. <https://doi.org/10.1038/85059>
- 231.Machulda, M.M., Ward, H.A., Borowski, B., Gunter, J.L., Cha, R.H., O'Brien, P.C., Petersen, R.C., Boeve, B.F., Knopman, D., Tang-Wai, D.F., Ivnik, R.J., Smith, G.E., Tangalos, E.G., Jack, C.R., Jr, 2003. Comparison of memory fMRI response among normal, MCI, and Alzheimer's patients. *Neurology* 61, 500–506.
- 232.Magee, J.C., 1997. A Synaptically Controlled, Associative Signal for Hebbian Plasticity in Hippocampal Neurons. *Science*. <https://doi.org/10.1126/science.275.5297.209>
- 233.Maggi, C.A., Meli, A., 1986. Suitability of urethane anesthesia for physiopharmacological investigations in various systems. Part 1: General considerations. *Experientia* 42, 109– 114.
- 234.Mandeville, J.B., Jenkins, B.G., Chen, Y.-C.I., Choi, J.-K., Kim, Y.R., Belen, D., Liu, C., Kosofsky, B.E., Marota, J.J.A., 2004. Exogenous contrast agent improves sensitivity of gradient-echo functional magnetic resonance imaging at 9.4 T. *Magnetic Resonance in Medicine: An Official Journal of the International Society for Magnetic Resonance in Medicine* 52, 1272–1281.
- 235.Mandeville, J.B., Marota, J.J., Kosofsky, B.E., Keltner, J.R., Weissleder, R., Rosen, B.R.,

- Weisskoff, R.M., 1998. Dynamic functional imaging of relative cerebral blood volume during rat forepaw stimulation. *Magn. Reson. Med.* 39, 615–624.
- 236.Mandino, F., Cerri, D.H., Garin, C.M., Straathof, M., van Tilborg, G.A., Chakravarty, M.M., Dhenain, M., Dijkhuizen, R.M., Gozzi, A., Hess, A. and Keilholz, S.D., 2020. Animal Functional Magnetic Resonance Imaging: Trends and Path Toward Standardization. *Frontiers in Neuroinformatics*, 13, p.78.
- 237.Mandino, F., Yeow, L. Y., Gigg, J., Olivo, M., & Grandjean, J., 2019. Preserved functional networks in a hydrocephalic mouse. *ScienceMatters*.
<https://doi.org/10.19185/matters.201905000001>
- 238.Manno, F.A.M., Isla, A.G., Manno, S.H.C., Ahmed, I., Cheng, S.H., Barrios, F.A., Lau, C., 2019. Early Stage Alterations in White Matter and Decreased Functional Interhemispheric Hippocampal Connectivity in the 3xTg Mouse Model of Alzheimer’s Disease. *Frontiers in Aging Neuroscience*.
<https://doi.org/10.3389/fnagi.2019.00039>
- 239.Marchese, M., Cowan, D., Karimi, K., Ashthorpe, V., Head, E., Ma, D., Zhao, H., Davis, P., Kapadia, M., Sakic, B., 2013. Immunological dysfunction and MCI-like behavior in the 3xTgAD mice. *Alzheimer’s & Dementia*. <https://doi.org/10.1016/j.jalz.2013.05.244>
- 240.Maren, S., Fanselow, M.S., 1995. Synaptic plasticity in the basolateral amygdala induced by hippocampal formation stimulation *in vivo*. *The Journal of Neuroscience*.
<https://doi.org/10.1523/jneurosci.15-11-07548.1995>
- 241.Maren, S., Quirk, G.J., 2004. Neuronal signalling of fear memory. *Nat. Rev. Neurosci.* 5, 844–852.
- 242.Marioni, R.E., Harris, S.E., Zhang, Q., McRae, A.F., Hagenaars, S.P., Hill, W.D., Davies, G., Ritchie, C.W., Gale, C.R., Starr, J.M., Goate, A.M., Porteous, D.J., Yang, J., Evans, K.L., Deary, I.J., Wray, N.R., Visscher, P.M., 2018. GWAS on family history of Alzheimer’s disease. *Transl. Psychiatry* 8, 99.
- 243.Martorana, A., Koch, G., 2014. ‘Is dopamine involved in Alzheimer’s disease?’ *Front. Aging Neurosci.* 6, 252.
- 244.Martorana, A., Mori, F., Esposito, Z., Kusayanagi, H., Monteleone, F., Codecà, C., Sancesario, G., Bernardi, G., Koch, G., 2009. Dopamine Modulates Cholinergic Cortical Excitability in Alzheimer’s Disease Patients. *Neuropsychopharmacology*. <https://doi.org/10.1038/npp.2009.60>
- 245.Masters, C.L., Simms, G., Weinman, N.A., Multhaup, G., McDonald, B.L., Beyreuther, K., 1985. Amyloid plaque core protein in Alzheimer disease and Down syndrome. *Proceedings of the National Academy of Sciences*. <https://doi.org/10.1073/pnas.82.12.4245>
- 246.Mastrangelo, M.A., Bowers, W.J., 2008. Detailed immunohistochemical characterization of temporal and spatial progression of Alzheimer’s disease-related pathologies in male triple-transgenic mice. *BMC Neurosci.* 9, 81.
- 247.McGaugh, J.L., 2002. Memory consolidation and the amygdala: a systems perspective. *Trends Neurosci.* 25, 456.
- 248.McKhann, G., Drachman, D., Folstein, M., Katzman, R., Price, D., Stadlan, E.M., 1984. Clinical diagnosis of Alzheimer’s disease: report of the NINCDS-ADRDA Work Group under the auspices

- of Department of Health and Human Services Task Force on Alzheimer's Disease. *Neurology* 34, 939–944.
249. McNaughton, B.L., 1980. Evidence for two physiologically distinct perforant pathways to the fascia dentata. *Brain Res.* 199, 1–19.
250. McQuiston, A.R., 2010. Cholinergic modulation of excitatory synaptic input integration in hippocampal CA1. *J. Physiol.* 588, 3727–3742.
251. Mendez, M., Lim, G., 2003. Seizures in elderly patients with dementia: epidemiology and management. *Drugs Aging* 20, 791–803.
252. Mesulam, M., 2004. The cholinergic lesion of Alzheimer's disease: pivotal factor or side show? *Learn. Mem.* 11, 43–49.
253. Miller, K.L., Alfaro-Almagro, F., Bangerter, N.K., Thomas, D.L., Yacoub, E., Xu, J., Bartsch, A.J., Jbabdi, S., Sotiropoulos, S.N., Andersson, J.L.R., Griffanti, L., Douaud, G., Okell, T.W., Weale, P., Dragonu, I., Garratt, S., Hudson, S., Collins, R., Jenkinson, M., Matthews, P.M., Smith, S.M., 2016. Multimodal population brain imaging in the UK Biobank prospective epidemiological study. *Nat. Neurosci.* 19, 1523–1536.
254. Moechars, D., Dewachter, I., Lorent, K., Reversé, D., Baekelandt, V., Naidu, A., Tesseur, I., Spittaels, K., Van Den Haute, C., Checler, F., Godaux, E., Cordell, B., Van Leuven, F., 1999. Early Phenotypic Changes in Transgenic Mice That Overexpress Different Mutants of Amyloid Precursor Protein in Brain. *Journal of Biological Chemistry*. <https://doi.org/10.1074/jbc.274.10.6483>
255. Montemurro, M.A., Rasch, M.J., Murayama, Y., Logothetis, N.K., Panzeri, S., 2008. Phase-of-firing coding of natural visual stimuli in primary visual cortex. *Curr. Biol.* 18, 375–380.
256. Mori, S., Barker, P.B., 1999. Diffusion magnetic resonance imaging: Its principle and applications. *The Anatomical Record*. [https://doi.org/10.1002/\(sici\)1097-0185\(19990615\)257:3<102::aid-ar7>3.3.co;2-y](https://doi.org/10.1002/(sici)1097-0185(19990615)257:3<102::aid-ar7>3.3.co;2-y)
257. Morris, R.G.M., Moser, E.I., Riedel, G., Martin, S.J., Sandin, J., Day, M., O'Carroll, C., 2003. Elements of a neurobiological theory of the hippocampus: the role of activity-dependent synaptic plasticity in memory. *Philosophical Transactions of the Royal Society of London. Series B: Biological Sciences*. <https://doi.org/10.1098/rstb.2002.1264>
258. Mount, C., Downton, C., 2006. Alzheimer disease: progress or profit? *Nat. Med.* 12, 780–784.
259. Mucke, L., Masliah, E., Yu, G.Q., Mallory, M., Rockenstein, E.M., Tatsuno, G., Hu, K., Kholodenko, D., Johnson-Wood, K., McConlogue, L., 2000. High-level neuronal expression of abeta 1-42 in wild-type human amyloid protein precursor transgenic mice: synaptotoxicity without plaque formation. *J. Neurosci.* 20, 4050–4058.
260. Mueggler, T., Sturchler-Pierrat, C., Baumann, D., Rausch, M., Staufenbiel, M., Rudin, M., 2002. Compromised hemodynamic response in amyloid precursor protein transgenic mice. *J. Neurosci.* 22, 7218–7224.
261. Murphy, K., Birn, R.M., Bandettini, P.A., 2013. Resting-state fMRI confounds and cleanup. *NeuroImage*. <https://doi.org/10.1016/j.neuroimage.2013.04.001>

262. Musiek, E.S., Holtzman, D.M., 2012. Origins of Alzheimer's disease. *Current Opinion in Neurology*. <https://doi.org/10.1097/wco.0b013e32835a30f4>
263. Nagel, G., Szellas, T., Huhn, W., Kateriya, S., Adeishvili, N., Berthold, P., Ollig, D., Hegemann, P., Bamberg, E., 2003. Channelrhodopsin-2, a directly light-gated cation-selective membrane channel. *Proc. Natl. Acad. Sci. U. S. A.* 100, 13940–13945.
264. Nakashiba, T., Cushman, J.D., Pelkey, K.A., Renaudineau, S., Buhl, D.L., McHugh, T.J., Rodriguez Barrera, V., Chittajallu, R., Iwamoto, K.S., McBain, C.J., Fanselow, M.S., Tonegawa, S., 2012. Young dentate granule cells mediate pattern separation, whereas old granule cells facilitate pattern completion. *Cell* 149, 188–201.
265. Nakazono, T., Jun, H., Blurton-Jones, M., Green, K.N., Igarashi, K.M., 2018. Gamma oscillations in the entorhinal-hippocampal circuit underlying memory and dementia. *Neurosci. Res.* 129, 40–46.
266. Nathanson, J.L., Yanagawa, Y., Obata, K., Callaway, E.M., 2009. Preferential labeling of inhibitory and excitatory cortical neurons by endogenous tropism of adeno-associated virus and lentivirus vectors. *Neuroscience*. <https://doi.org/10.1016/j.neuroscience.2009.03.032>
267. Nava-Mesa, M.O., Jimenez-Díaz, L., Yajeya, J., Navarro-Lopez, J.D., 2014. GABAergic neurotransmission and new strategies of neuromodulation to compensate synaptic dysfunction in early stages of Alzheimer's disease. *Frontiers in Cellular Neuroscience*. <https://doi.org/10.3389/fncel.2014.00167>
268. Neitz, A., Mergia, E., Eysel, U.T., Koesling, D., Mittmann, T., 2011. Presynaptic nitric oxide/cGMP facilitates glutamate release via hyperpolarization-activated cyclic nucleotide-gated channels in the hippocampus. *European Journal of Neuroscience*. <https://doi.org/10.1111/j.1460-9568.2011.07654.x>
269. Neitzel, J., Franzmeier, N., Rubinski, A., Ewers, M., Alzheimer's Disease Neuroimaging Initiative (ADNI), 2019. Left frontal connectivity attenuates the adverse effect of entorhinal tau pathology on memory. *Neurology* 93, e347–e357.
270. Nelson, P.T., Abner, E.L., Patel, E., Anderson, S., Wilcock, D.M., Kryscio, R.J., Van Eldik, L.J., Jicha, G.A., Gal, Z., Nelson, R.S., Nelson, B.G., Gal, J., Azam, M.T., Fardo, D.W., Cykowski, M.D., 2018. The Amygdala as a Locus of Pathologic Misfolding in Neurodegenerative Diseases. *J. Neuropathol. Exp. Neurol.* 77, 2–20.
271. Nelson, P.T., Alafuzoff, I., Bigio, E.H., Bouras, C., Braak, H., Cairns, N.J., Castellani, R.J., Crain, B.J., Davies, P., Del Tredici, K., Duyckaerts, C., Frosch, M.P., Haroutunian, V., Hof, P.R., Hulette, C.M., Hyman, B.T., Iwatsubo, T., Jellinger, K.A., Jicha, G.A., Kövari, E., Kukull, W.A., Leverenz, J.B., Love, S., Mackenzie, I.R., Mann, D.M., Masliah, E., McKee, A.C., Montine, T.J., Morris, J.C., Schneider, J.A., Sonnen, J.A., Thal, D.R., Trojanowski, J.Q., Troncoso, J.C., Wisniewski, T., Woltjer, R.L., Beach, T.G., 2012. Correlation of Alzheimer Disease Neuropathologic Changes With Cognitive Status: A Review of the Literature. *Journal of Neuropathology & Experimental Neurology*. <https://doi.org/10.1097/nen.0b013e31825018f7>
272. Nestor, S.M., Rupsingh, R., Borrie, M., Smith, M., Accomazzi, V., Wells, J.L., Fogarty, J., Bartha, R., the Alzheimer's Disease Neuroimaging Initiative, 2008. Ventricular enlargement as a possible measure of Alzheimer's disease progression validated using the Alzheimer's disease neuroimaging initiative database. *Brain*. <https://doi.org/10.1093/brain/awn146>
273. Noebels, J., 2011. A perfect storm: Converging paths of epilepsy and Alzheimer's dementia

- intersect in the hippocampal formation. *Epilepsia* 52 Suppl 1, 39–46.
274. Norman, G., Eacott, M.J., 2004. Impaired object recognition with increasing levels of feature ambiguity in rats with perirhinal cortex lesions. *Behav. Brain Res.* 148, 79–91.
275. Nuriel, T., Angulo, S.L., Khan, U., Ashok, A., Chen, Q., Figueroa, H.Y., Emrani, S., Liu, L., Herman, M., Barrett, G., Savage, V., Buitrago, L., Cepeda-Prado, E., Fung, C., Goldberg, E., Gross, S.S., Abid Hussaini, S., Moreno, H., Small, S.A., Duff, K.E., 2017. Neuronal hyperactivity due to loss of inhibitory tone in APOE4 mice lacking Alzheimer's disease-like pathology. *Nature Communications*. <https://doi.org/10.1038/s41467-017-01444-0>
276. Oakley, H., Cole, S.L., Logan, S., Maus, E., Shao, P., Craft, J., Guillozet-Bongaarts, A., Ohno, M., Disterhoft, J., Van Eldik, L., Berry, R., Vassar, R., 2006. Intraneuronal beta-amyloid aggregates, neurodegeneration, and neuron loss in transgenic mice with five familial Alzheimer's disease mutations: potential factors in amyloid plaque formation. *J. Neurosci.* 26, 10129–10140.
277. Oddo, S., Caccamo, A., Shepherd, J.D., Murphy, M.P., Golde, T.E., Kaye, R., Metherate, R., Mattson, M.P., Akbari, Y., LaFerla, F.M., 2003. Triple-transgenic model of Alzheimer's disease with plaques and tangles: intracellular Abeta and synaptic dysfunction. *Neuron* 39, 409–421.
278. Ogawa, S., Menon, R.S., Tank, D.W., Kim, S.G., Merkle, H., Ellermann, J.M., Ugurbil, K., 1993. Functional brain mapping by blood oxygenation level-dependent contrast magnetic resonance imaging. A comparison of signal characteristics with a biophysical model. *Biophysical Journal*. [https://doi.org/10.1016/s0006-3495\(93\)81441-3](https://doi.org/10.1016/s0006-3495(93)81441-3)
279. Ohara, S., Onodera, M., Simonsen, Ø.W., Yoshino, R., Hioki, H., Iijima, T., Tsutsui, K.-I., Witter, M.P., 2018. Intrinsic Projections of Layer Vb Neurons to Layers Va, III, and II in the Lateral and Medial Entorhinal Cortex of the Rat. *Cell Rep.* 24, 107–116.
280. Palop, J.J., Chin, J., Mucke, L., 2006. A network dysfunction perspective on neurodegenerative diseases. *Nature*. <https://doi.org/10.1038/nature05289>
281. Palop, J.J., Chin, J., Roberson, E.D., Wang, J., Thwin, M.T., Bien-Ly, N., Yoo, J., Ho, K.O., Yu, G.-Q., Kreitzer, A., Finkbeiner, S., Noebels, J.L., Mucke, L., 2007. Aberrant excitatory neuronal activity and compensatory remodeling of inhibitory hippocampal circuits in mouse models of Alzheimer's disease. *Neuron* 55, 697–711.
282. Palop, J.J., Mucke, L., 2016. Network abnormalities and interneuron dysfunction in Alzheimer disease. *Nat. Rev. Neurosci.* 17, 777–792.
283. Palop, J.J., Mucke, L., 2010a. Amyloid-beta-induced neuronal dysfunction in Alzheimer's disease: from synapses toward neural networks. *Nat. Neurosci.* 13, 812–818.
284. Palop, J.J., Mucke, L., 2010b. Synaptic depression and aberrant excitatory network activity in Alzheimer's disease: two faces of the same coin? *Neuromolecular Med.* 12, 48–55.
285. Panksepp, J., Panksepp, J.B., 2013. Toward a cross-species understanding of empathy. *Trends in Neurosciences*. <https://doi.org/10.1016/j.tins.2013.04.009>
286. Paola, M., Macaluso, E., Carlesimo, G.A., Tomaiuolo, F., Worsley, K.J., Fadda, L., Caltagirone, C., 2007. Episodic memory impairment in patients with Alzheimer's disease is correlated with entorhinal cortex atrophy. *Journal of Neurology*. <https://doi.org/10.1007/s00415-006-0435-1>

287. Pawela, C.P., Biswal, B.B., Cho, Y.R., Kao, D.S., Li, R., Jones, S.R., Schulte, M.L., Matloub, H.S., Hudetz, A.G., Hyde, J.S., 2008. Resting-state functional connectivity of the rat brain. *Magn. Reson. Med.* 59, 1021–1029.
288. Paxinos, G., Franklin, K.B.J., 2004. *The Mouse Brain in Stereotaxic Coordinates*. Gulf Professional Publishing.
289. Paz, R., Pare, D., 2013. Physiological basis for emotional modulation of memory circuits by the amygdala. *Curr. Opin. Neurobiol.* 23, 381–386.
290. Paz, R., Pelletier, J.G., Bauer, E.P., Paré, D., 2006. Emotional enhancement of memory via amygdala-driven facilitation of rhinal interactions. *Nat. Neurosci.* 9, 1321–1329.
291. Penfield, W., Milner, B., 1958. Memory deficit produced by bilateral lesions in the hippocampal zone. *AMA Arch. Neurol. Psychiatry* 79, 475–497.
292. Perani, D., Bressi, S., Cappa, S.F., Vallar, G., Alberoni, M., Grassi, F., Caltagirone, C., Cipolotti, L., Franceschi, M., Lenzi, G.L., Fazio, F., 1993. Evidence of multiple memory systems in the human brain. *Brain*. <https://doi.org/10.1093/brain/116.4.903>
293. Petrache, A.L., Rajulawalla, A., Shi, A., Wetzel, A., Saito, T., Saido, T.C., Harvey, K., Ali, A.B., 2019. Aberrant Excitatory–Inhibitory Synaptic Mechanisms in Entorhinal Cortex Microcircuits During the Pathogenesis of Alzheimer’s Disease. *Cerebral Cortex*. <https://doi.org/10.1093/cercor/bhz016>
294. Pikkariainen, M., Rönkkö, S., Savander, V., Insausti, R., Pitkänen, A., 1999. Projections from the lateral, basal, and accessory basal nuclei of the amygdala to the hippocampal formation in rat. *J. Comp. Neurol.* 403, 229–260.
295. Pimplikar, S.W., 2009. Reassessing the amyloid cascade hypothesis of Alzheimer’s disease. *Int. J. Biochem. Cell Biol.* 41, 1261–1268.
296. Pitkänen, A., Tuunanen, J., Kälviäinen, R., Partanen, K., Salmenperä, T., 1998. Amygdala damage in experimental and human temporal lobe epilepsy. *Epilepsy Research*. [https://doi.org/10.1016/s0920-1211\(98\)00055-2](https://doi.org/10.1016/s0920-1211(98)00055-2)
297. Pontecorvo, M.J., Devous, M.D., Navitsky, M., Lu, M., Salloway, S., Schaerf, F.W., Jennings, D., Arora, A.K., McGeehan, A., Lim, N.C., Xiong, H., Joshi, A.D., Siderowf, A., Mintun, M.A., for the 18F-AV-1451-A05 investigators, 2017. Relationships between flortaucipir PET tau binding and amyloid burden, clinical diagnosis, age and cognition. *Brain*. <https://doi.org/10.1093/brain/aww334>
298. Pooler, A.M., Noble, W., Hanger, D.P., 2014. A role for tau at the synapse in Alzheimer’s disease pathogenesis. *Neuropharmacology*. <https://doi.org/10.1016/j.neuropharm.2013.09.018>
299. Poser, B.A., Norris, D.G., 2011. Application of whole-brain CBV-weighted fMRI to a cognitive stimulation paradigm: Robust activation detection in a stroop task experiment using 3D GRASE VASO. *Human Brain Mapping*. <https://doi.org/10.1002/hbm.21083>
300. Price, J.L., Ko, A.I., Wade, M.J., Tsou, S.K., McKeel, D.W., Morris, J.C., 2001. Neuron number in the entorhinal cortex and CA1 in preclinical Alzheimer disease. *Arch. Neurol.* 58, 1395–1402.

301. Radde, R., Bolmont, T., Kaeser, S.A., Coomaraswamy, J., Lindau, D., Stoltze, L., Calhoun, M.E., Jäggli, F., Wolburg, H., Gengler, S. and Haass, C., 2006. A β 42-driven cerebral amyloidosis in transgenic mice reveals early and robust pathology. *EMBO reports*, 7(9), pp.940-946.
302. Rae, E.A. and Brown, R.E., 2015. The problem of genotype and sex differences in life expectancy in transgenic AD mice. *Neuroscience & Biobehavioral Reviews*, 57, pp.238-251.
303. Raichle, M.E., 2015. The Brain's Default Mode Network. *Annual Review of Neuroscience*.
<https://doi.org/10.1146/annurev-neuro-071013-014030>
304. Raichle, M.E., MacLeod, A.M., Snyder, A.Z., Powers, W.J., Gusnard, D.A., Shulman, G.L., 2001. A default mode of brain function. *Proceedings of the National Academy of Sciences*.
<https://doi.org/10.1073/pnas.98.2.676>
305. Rao, J.-S., Liu, Z., Zhao, C., Wei, R.-H., Zhao, W., Tian, P.-Y., Zhou, X., Yang, Z.-Y., Li, X.-G., 2017. Ketamine changes the local resting-state functional properties of anesthetized-monkey brain. *Magn. Reson. Imaging* 43, 144–150.
306. Rawlani, S., Rawlani, S., 2014. Basic Principles of Magnetic Resonance Imaging. Oral and Maxillofacial Imaging Techniques. https://doi.org/10.5005/jp/books/12342_16
307. Razoux, F., Baltes, C., Mueggler, T., Seuwen, A., Russig, H., Mansuy, I., Rudin, M., 2013. Functional MRI to assess alterations of functional networks in response to pharmacological or genetic manipulations of the serotonergic system in mice. *Neuroimage* 74, 326–336.
308. Reynolds, G.P., 1983. Increased concentrations and lateral asymmetry of amygdala dopamine in schizophrenia. *Nature* 305, 527–529.
309. Ringman, J.M., 2005. What the Study of Persons At Risk for Familial Alzheimer's Disease Can Tell Us About the Earliest Stages of the Disorder: A Review. *J. Geriatr. Psychiatry Neurol.* 18, 228–233.
310. Roberson, E.D., Scarce-Levie, K., Palop, J.J., Yan, F., Cheng, I.H., Wu, T., Gerstein, H., - Q. Yu, G., Mucke, L., 2007. Reducing Endogenous Tau Ameliorates Amyloid -Induced Deficits in an Alzheimer's Disease Mouse Model. *Science*. <https://doi.org/10.1126/science.1141736>
Roher, A.E., Weiss, N., Kokjohn, T.A., Kuo, Y.-M., Kalback, W., Anthony, J., Watson, D., Luehrs, D.C., Sue, L., Walker, D., Emmerling, M., Goux, W., Beach, T., 2002. Increased A β Peptides and Reduced Cholesterol and Myelin Proteins Characterize White Matter Degeneration in Alzheimer's Disease†. *Biochemistry*. <https://doi.org/10.1021/bi026173d>
311. Rombouts, S.A.R.B., Serge A R, Barkhof, F., Goekoop, R., Stam, C.J., Scheltens, P., 2005. Altered resting-state networks in mild cognitive impairment and mild Alzheimer's disease: An fMRI study. *Human Brain Mapping*. <https://doi.org/10.1002/hbm.20160>
312. Roozendaal, B., McGaugh, J.L., 2011. Memory modulation. *Behavioral Neuroscience*.
<https://doi.org/10.1037/a0026187>
313. Roth, B.L., 2016. DREADDs for Neuroscientists. *Neuron* 89, 683–694.
314. Rowland, D.C., Weible, A.P., Wickersham, I.R., Wu, H., Mayford, M., Witter, M.P., Kentros, C.G., 2013. Transgenically targeted rabies virus demonstrates a major monosynaptic projection from hippocampal area CA2 to medial entorhinal layer II neurons. *J. Neurosci.* 33, 14889–14898.

315. Roy, D.S., Arons, A., Mitchell, T.I., Pignatelli, M., Ryan, T.J., Tonegawa, S., 2016. Memory retrieval by activating engram cells in mouse models of early Alzheimer's disease. *Nature* 531, 508–512.
316. Rungta, R.L., Osmanski, B.-F., Boido, D., Tanter, M., Charpak, S., 2017. Light controls cerebral blood flow in naive animals. *Nat. Commun.* 8, 14191.
317. Salamone, J.D., Correa, M., Mingote, S.M., Weber, S.M., 2005. Beyond the reward hypothesis: alternative functions of nucleus accumbens dopamine. *Curr. Opin. Pharmacol.* 5, 34–41.
318. Salvadores, N., Sanhueza, M., Manque, P., Court, F.A., 2017. Axonal Degeneration during Aging and Its Functional Role in Neurodegenerative Disorders. *Front. Neurosci.* 11, 451.
319. Sandson, T.A., Felician, O., Edelman, R.R., Warach, S., 1999. Diffusion-Weighted Magnetic Resonance Imaging in Alzheimer's Disease. *Dementia and Geriatric Cognitive Disorders*.
<https://doi.org/10.1159/000017099>
320. Sanz-Arigita, E.J., Schoonheim, M.M., Damoiseaux, J.S., Serge A R, Maris, E., Barkhof, F., Scheltens, P., Stam, C.J., 2010. Loss of 'Small-World' Networks in Alzheimer's Disease: Graph Analysis of fMRI Resting-State Functional Connectivity. *PLoS ONE*.
<https://doi.org/10.1371/journal.pone.0013788>
321. Savander, V., Go, C.G., LeDoux, J.E., Pitkänen, A., 1995. Intrinsic connections of the rat amygdaloid complex: projections originating in the basal nucleus. *J. Comp. Neurol.* 361, 345–368.
322. Scheltens, P., Blennow, K., Breteler, M.M.B., de Strooper, B., Frisoni, G.B., Salloway, S., Van der Flier, W.M., 2016. Alzheimer's disease. *The Lancet*. [https://doi.org/10.1016/s0140-6736\(15\)01124-1](https://doi.org/10.1016/s0140-6736(15)01124-1)
323. Schmid, F., Wachsmuth, L., Albers, F., Schwalm, M., Stroh, A., Faber, C., 2017. True and apparent optogenetic BOLDfMRI signals. *Magnetic Resonance in Medicine*.
<https://doi.org/10.1002/mrm.26095>
324. Schmidt-Hieber, C., Häusser, M., 2013. Cellular mechanisms of spatial navigation in the medial entorhinal cortex. *Nature Neuroscience*. <https://doi.org/10.1038/nn.3340>
325. Schöll, M., Lockhart, S.N., Schonhaut, D.R., O'Neil, J.P., Janabi, M., Ossenkoppele, R., Baker, S.L., Vogel, J.W., Faria, J., Schwimmer, H.D., Rabinovici, G.D., Jagust, W.J., 2016. PET Imaging of Tau Deposition in the Aging Human Brain. *Neuron*. <https://doi.org/10.1016/j.neuron.2016.01.028>
326. Schönheit, B., Zarski, R., Ohm, T.G., 2004. Spatial and temporal relationships between plaques and tangles in Alzheimer-pathology. *Neurobiol. Aging* 25, 697–711.
327. Schulz, K., Sydekum, E., Krueppel, R., Engelbrecht, C.J., Schlegel, F., Schröter, A., Rudin, M., Helmchen, F., 2012. Simultaneous BOLD fMRI and fiber-optic calcium recording in rat neocortex. *Nat. Methods* 9, 597–602.
328. Schwinn, D.A., McIntyre, R.W., Reves, J.G., 1990. Isoflurane-induced vasodilation: role of the alpha-adrenergic nervous system. *Anesth. Analg.* 71, 451–459.
329. Sciolino, N.R., Plummer, N.W., Chen, Y.-W., Alexander, G.M., Robertson, S.D., Dudek, S.M., McElligott, Z.A., Jensen, P., 2016. Recombinase-Dependent Mouse Lines for Chemogenetic

- Activation of Genetically Defined Cell Types. *Cell Reports*.
<https://doi.org/10.1016/j.celrep.2016.05.034>
- 330.Scoville, W. B., & Milner, B., 2000. Loss of recent memory after bilateral hippocampal lesions. 1957. *J Neuropsychiatry Clin Neurosci*, 12, 103-13.
- 331.Segal, M., 2010. Dendritic spines, synaptic plasticity and neuronal survival: activity shapes dendritic spines to enhance neuronal viability. *European Journal of Neuroscience*.
<https://doi.org/10.1111/j.1460-9568.2010.07270.x>
- 332.Selden, N., Mesulam, M.M., Geula, C., 1994. Human striatum: the distribution of neurofibrillary tangles in Alzheimer's disease. *Brain Res*. 648, 327–331.
- 333.Selkoe, D.J., 2011. Alzheimer's Disease. *Cold Spring Harbor Perspectives in Biology*.
<https://doi.org/10.1101/cshperspect.a004457>
- 334.Selkoe, D.J., 2008. Soluble oligomers of the amyloid beta-protein impair synaptic plasticity and behavior. *Behav. Brain Res*. 192, 106–113.
- 335.Selkoe, D.J., 2002. Alzheimer's Disease Is a Synaptic Failure. *Science*.
<https://doi.org/10.1126/science.1074069>
- 336.Selkoe, D.J., 1997. Alzheimer's Disease--Genotypes, Phenotype, and Treatments. *Science* 275, 630–631.
- 337.Serrano-Pozo, A., Frosch, M.P., Masliah, E., Hyman, B.T., 2011. Neuropathological Alterations in Alzheimer Disease. *Cold Spring Harbor Perspectives in Medicine*.
<https://doi.org/10.1101/cshperspect.a006189>
- 338.Sforazzini, F., Schwarz, A.J., Galbusera, A., Bifone, A., Gozzi, A., 2014. Distributed BOLD and CBV-weighted resting-state networks in the mouse brain. *Neuroimage* 87, 403–415.
- 339.Shah, D., Jonckers, E., Praet, J., Vanhoutte, G., Palacios, R.D. y., Bigot, C., D'Souza, D.V., Verhoye, M., Van der Linden, A., 2013. Resting-state fMRI Reveals Diminished Functional Connectivity in a Mouse Model of Amyloidosis. *PLoS ONE*.
<https://doi.org/10.1371/journal.pone.0084241>
- 340.Shah, D., Praet, J., Latif Hernandez, A., Höfling, C., Anckaerts, C., Bard, F., Morawski, M., Detrez, J.R., Prinsen, E., Villa, A., De Vos, W.H., Maggi, A., D'Hooge, R., Balschun, D., Rossner, S., Verhoye, M., Van der Linden, A., 2016. Early pathologic amyloid induces hypersynchrony of BOLD resting-state networks in transgenic mice and provides an early therapeutic window before amyloid plaque deposition. *Alzheimers. Dement*. 12, 964–976.
- 341.Shannon, C.E., 1948. A Mathematical Theory of Communication. *Bell System Technical Journal*.
<https://doi.org/10.1002/j.1538-7305.1948.tb01338.x>
- 342.Sheline, Y.I., Morris, J.C., Snyder, A.Z., Price, J.L., Yan, Z., D'Angelo, G., Liu, C., Dixit, S., Benzinger, T., Fagan, A., Goate, A., Mintun, M.A., 2010. APOE4 Allele Disrupts Resting-state fMRI Connectivity in the Absence of Amyloid Plaques or Decreased CSF A 42. *Journal of Neuroscience*. <https://doi.org/10.1523/jneurosci.3987-10.2010>
- 343.Sheline, Y.I., Raichle, M.E., Snyder, A.Z., Morris, J.C., Head, D., Wang, S., Mintun, M.A., 2010.

- Amyloid Plaques Disrupt Resting State Default Mode Network Connectivity in Cognitively Normal Elderly. *Biological Psychiatry*. <https://doi.org/10.1016/j.biopsych.2009.08.024>
344. Shen, L., 1989. Neural integration by short term potentiation. *Biological Cybernetics*. <https://doi.org/10.1007/bf00203180>
345. Shmuel, A., 2019. On the relationship between functional MRI signals and neuronal activity. *Casting Light on the Dark Side of Brain Imaging*. <https://doi.org/10.1016/b978-0-12-816179-1.00007-4>
346. Silva, A.C., 2012. Using manganese-enhanced MRI to understand BOLD. *Neuroimage* 62, 1009–1013.
347. Singh, V., Chertkow, H., Lerch, J.P., Evans, A.C., Dorr, A.E., Kabani, N.J., 2006. Spatial patterns of cortical thinning in mild cognitive impairment and Alzheimer's disease. *Brain*. <https://doi.org/10.1093/brain/awl256>
348. Šišková, Z., Justus, D., Kaneko, H., Friedrichs, D., Henneberg, N., Beutel, T., Pitsch, J., Schoch, S., Becker, A., von der Kammer, H., Remy, S., 2014. Dendritic structural degeneration is functionally linked to cellular hyperexcitability in a mouse model of Alzheimer's disease. *Neuron* 84, 1023–1033.
349. Small, S.A., Duff, K., 2008. Linking A β and Tau in Late-Onset Alzheimer's Disease: A Dual Pathway Hypothesis. *Neuron*. <https://doi.org/10.1016/j.neuron.2008.11.007>
350. Small, S.A., Perera, G.M., DeLaPaz, R., Mayeux, R., Stern, Y., 1999. Differential regional dysfunction of the hippocampal formation among elderly with memory decline and Alzheimer's disease. *Ann. Neurol.* 45, 466–472.
351. Smitha, K.A., Akhil Raja, K., Arun, K.M., Rajesh, P.G., Thomas, B., Kapilamoorthy, T.R., Kesavadas, C., 2017. Resting state fMRI: A review on methods in resting state connectivity analysis and resting state networks. *Neuroradiol. J.* 30, 305–317.
352. Smith, S.M., Jenkinson, M., Woolrich, M.W., Beckmann, C.F., Behrens, T.E.J., Johansen-Berg, H., Bannister, P.R., De Luca, M., Drobnjak, I., Flitney, D.E., Niazy, R.K., Saunders, J., Vickers, J., Zhang, Y., De Stefano, N., Michael Brady, J., Matthews, P.M., 2004. Advances in functional and structural MR image analysis and implementation as FSL. *NeuroImage*. <https://doi.org/10.1016/j.neuroimage.2004.07.051>
353. Soma, L.R., 1983. ANESTHETIC AND ANALGESIC CONSIDERATIONS IN THE
354. EXPERIMENTAL ANIMAL. *Annals of the New York Academy of Sciences*. <https://doi.org/10.1111/j.1749-6632.1983.tb53483.x>
355. Sorg, C., Riedl, V., Muhlau, M., Calhoun, V.D., Eichele, T., Laer, L., Drzezga, A., Forstl, H., Kurz, A., Zimmer, C., Wohlschlagel, A.M., 2007. Selective changes of resting-state networks in individuals at risk for Alzheimer's disease. *Proceedings of the National Academy of Sciences*. <https://doi.org/10.1073/pnas.0708803104>
356. Sperling, R.A., 2003. fMRI studies of associative encoding in young and elderly controls and mild Alzheimer's disease. *Journal of Neurology, Neurosurgery & Psychiatry*. <https://doi.org/10.1136/jnnp.74.1.44>

357. Sperling, R.A., Aisen, P.S., Beckett, L.A., Bennett, D.A., Craft, S., Fagan, A.M., Iwatsubo, T., Jack, C.R., Jr, Kaye, J., Montine, T.J., Others, 2011. Toward defining the preclinical stages of Alzheimer's disease: Recommendations from the National Institute on Aging-Alzheimer's Association workgroups on diagnostic guidelines for Alzheimer's disease. *Alzheimers. Dement.* 7, 280–292.
358. Spinney, L., 2014. Alzheimer's disease: The forgetting gene. *Nature*.
<https://doi.org/10.1038/510026a>
359. Squire, L., Zola-Morgan, S., 1991. The medial temporal lobe memory system. *Science*.
<https://doi.org/10.1126/science.1896849>
360. Stelzmann, R.A., Norman Schnitzlein, H., Reed Murtagh, F., 1995. An english translation of alzheimer's 1907 paper, ?über eine eigenartige erkankung der hirnrinde? *Clinical Anatomy*.
<https://doi.org/10.1002/ca.980080612>
361. Sturchler-Pierrat, C., Abramowski, D., Duke, M., -H. Wiederhold, K., Mistl, C., Rothacher, S., Ledermann, B., Burki, K., Frey, P., Paganetti, P.A., Waridel, C., Calhoun, M.E., Jucker, M., Probst, A., Staufenbiel, M., Sommer, B., 1997. Two amyloid precursor protein transgenic mouse models with Alzheimer disease-like pathology. *Proceedings of the National Academy of Sciences*.
<https://doi.org/10.1073/pnas.94.24.13287>
362. Sturm, V.E., Yokoyama, J.S., Seeley, W.W., Kramer, J.H., Miller, B.L., Rankin, K.P., 2013. Heightened emotional contagion in mild cognitive impairment and Alzheimer's disease is associated with temporal lobe degeneration. *Proc. Natl. Acad. Sci. U. S. A.* 110, 9944–9949.
363. Tanaka, Y., Meguro, K., Yamaguchi, S., Ishii, H., Watanuki, S., Funaki, Y., Yamaguchi, K., Yamadori, A., Iwata, R., Itoh, M., 2003. Decreased striatal D2 receptor density associated with severe behavioral abnormality in Alzheimer's disease. *Ann. Nucl. Med.* 17, 567–573.
364. Thal, D.R., Rüb, U., Orantes, M., Braak, H., 2002. Phases of A β -deposition in the human brain and its relevance for the development of AD. *Neurology* 58, 1791–1800.
365. Thal, D.R., Rüb, U., Schultz, C., Sassin, I., Ghebremedhin, E., Del Tredici, K., Braak, E., Braak, H., 2000. Sequence of A β -Protein Deposition in the Human Medial Temporal Lobe. *J. Neuropathol. Exp. Neurol.* 59, 733–748.
366. Ting, J.T., Lee, B.R., Chong, P., Soler-Llavina, G., Cobbs, C., Koch, C., Zeng, H., Lein, E., 2018. Preparation of Acute Brain Slices Using an Optimized N-Methyl-D-glucamine Protective Recovery Method. *J. Vis. Exp.* <https://doi.org/10.3791/53825>
367. Toda, T., Parylak, S.L., Linker, S.B., Gage, F.H., 2019. The role of adult hippocampal neurogenesis in brain health and disease. *Mol. Psychiatry* 24, 67–87.
368. Tomás Pereira, I., Agster, K.L., Burwell, R.D., 2016. Subcortical connections of the perirhinal, postrhinal, and entorhinal cortices of the rat. I. afferents. *Hippocampus* 26, 1189–1212.
369. Trzepacz, P.T., Yu, P., Bhamidipati, P.K., Willis, B., Forrester, T., Tabas, L., Schwarz, A.J., Saykin, A.J., Alzheimer's Disease Neuroimaging Initiative, 2013. Frontolimbic atrophy is associated with agitation and aggression in mild cognitive impairment and Alzheimer's disease. *Alzheimers. Dement.* 9, S95–S104.e1.

370. Tsao, A., Moser, M.-B., Moser, E.I., 2013. Traces of experience in the lateral entorhinal cortex. *Curr. Biol.* 23, 399–405.
371. Tulving, E., Markowitsch, H.J., 1998. Episodic and declarative memory: role of the hippocampus. *Hippocampus* 8, 198–204.
372. Tye, K.M., Deisseroth, K., 2012. Optogenetic investigation of neural circuits underlying brain disease in animal models. *Nature Reviews Neuroscience*. <https://doi.org/10.1038/nrn3171>
373. Uludag, K., Ugurbil, K., Berliner, L., 2015. fMRI: From Nuclear Spins to Brain Functions. Springer.
374. Van Essen, D.C., Ugurbil, K., Auerbach, E., Barch, D., Behrens, T.E.J., Bucholz, R., Chang, A., Chen, L., Corbetta, M., Curtiss, S.W., Della Penna, S., Feinberg, D., Glasser, M.F., Harel, N., Heath, A.C., Larson-Prior, L., Marcus, D., Michalareas, G., Moeller, S., Oostenveld, R., Petersen, S.E., Prior, F., Schlaggar, B.L., Smith, S.M., Snyder, A.Z., Xu, J., Yacoub, E., WU-Minn HCP Consortium, 2012. The Human Connectome Project: a data acquisition perspective. *Neuroimage* 62, 2222–2231.
375. van Groen, T., Miettinen, P., Kadish, I., 2003. The entorhinal cortex of the mouse: organization of the projection to the hippocampal formation. *Hippocampus* 13, 133–149.
376. Van Hoesen, G.W., 1995. Anatomy of the medial temporal lobe. *Magnetic resonance imaging*, 13(8), pp.1047-1055.
377. Van Hoesen, G.W., Hyman, B.T., Damasio, A.R., 1991. Entorhinal cortex pathology in Alzheimer's disease. *Hippocampus* 1, 1–8.
378. van Meer, M.P.A., Otte, W.M., van der Marel, K., Nijboer, C.H., Kavelaars, A., van der Sprenkel, J.W.B., Viergever, M.A., Dijkhuizen, R.M., 2012. Extent of Bilateral Neuronal Network Reorganization and Functional Recovery in Relation to Stroke Severity. *Journal of Neuroscience*. <https://doi.org/10.1523/jneurosci.3662-11.2012>
379. van Praag, H., Kempermann, G., Gage, F.H., 1999. Running increases cell proliferation and neurogenesis in the adult mouse dentate gyrus. *Nat. Neurosci.* 2, 266–270.
380. van Strien, N.M., Cappaert, N.L.M., Witter, M.P., 2009. The anatomy of memory: an interactive overview of the parahippocampal–hippocampal network. *Nature Reviews Neuroscience*. <https://doi.org/10.1038/nrn2614>
381. Vemuri, P., Wiste, H.J., Weigand, S.D., Shaw, L.M., Trojanowski, J.Q., Weiner, M.W., Knopman, D.S., Petersen, R.C., Jack, C.R., Jr, Alzheimer's Disease Neuroimaging Initiative, 2009. MRI and CSF biomarkers in normal, MCI, and AD subjects: diagnostic discrimination and cognitive correlations. *Neurology* 73, 287–293.
382. Vermunt, L., Sikkes, S.A.M., van den Hout, A., Handels, R., Bos, I., van der Flier, W.M., Kern, S., Ousset, P.-J., Maruff, P., Skoog, I., Verhey, F.R.J., Freund-Levi, Y., Tsolaki, M., Wallin, Å.K., Olde Rikkert, M., Soininen, H., Spuru, L., Zetterberg, H., Blennow, K., Scheltens, P., Muniz-Terrera, G., Visser, P.J., Alzheimer Disease Neuroimaging Initiative, AIBL Research Group, ICTUS/DSA study groups, 2019a. Duration of preclinical, prodromal, and dementia stages of Alzheimer's disease in relation to age, sex, and APOE genotype. *Alzheimers. Dement.* 15, 888–898.

383. Vermunt, L., van Paasen, A.J.L., Teunissen, C.E., Scheltens, P., Visser, P.J., Tijms, B.M., for the Alzheimer's Disease Neuroimaging Initiative, 2019b. Alzheimer disease biomarkers may aid in the prognosis of MCI cases initially reverted to normal. *Neurology*.
<https://doi.org/10.1212/wnl.0000000000007609>
384. Vinters, H.V., 1987. Cerebral amyloid angiopathy. A critical review. *Stroke* 18, 311–324.
385. Vossel, K.A., Tartaglia, M.C., Nygaard, H.B., Zeman, A.Z., Miller, B.L., 2017. Epileptic activity in Alzheimer's disease: causes and clinical relevance. *Lancet Neurol.* 16, 311–322.
386. Vossel, K.A., Zhang, K., Brodbeck, J., Daub, A.C., Sharma, P., Finkbeiner, S., Cui, B., Mucke, L., 2010. Tau Reduction Prevents A β -Induced Defects in Axonal Transport: Fig. 1. *Science*.
<https://doi.org/10.1126/science.1194653>
387. Vradenburg, G., 2015. A pivotal moment in Alzheimer's disease and dementia: how global unity of purpose and action can beat the disease by 2025. *Expert Review of Neurotherapeutics*.
<https://doi.org/10.1586/14737175.2015.995638>
388. Wang, L., Zang, Y., He, Y., Liang, M., Zhang, X., Tian, L., Wu, T., Jiang, T., Li, K., 2006. Changes in hippocampal connectivity in the early stages of Alzheimer's disease: evidence from resting state fMRI. *Neuroimage* 31, 496–504.
389. Weggen, S., Beher, D., 2012. Molecular consequences of amyloid precursor protein and presenilin mutations causing autosomal-dominant Alzheimer's disease. *Alzheimers. Res. Ther.* 4, 9.
390. Weiner, M.W., Veitch, D.P., 2015. Introduction to special issue: Overview of Alzheimer's Disease Neuroimaging Initiative. *Alzheimer's & Dementia*. <https://doi.org/10.1016/j.jalz.2015.05.007>
391. Weiner, M.W., Veitch, D.P., Aisen, P.S., Beckett, L.A., Cairns, N.J., Green, R.C., Harvey, D., Jack, C.R., Jagust, W., Liu, E., Morris, J.C., Petersen, R.C., Saykin, A.J., Schmidt, M.E., Shaw, L., Shen, L., Siuciak, J.A., Soares, H., Toga, A.W., Trojanowski, J.Q., Alzheimer's Disease Neuroimaging Initiative, 2013. The Alzheimer's Disease Neuroimaging Initiative: a review of papers published since its inception. *Alzheimers. Dement.* 9, e111–94.
392. Weitz, A.J., Fang, Z., Lee, H.J., Fisher, R.S., Smith, W.C., Choy, M., Liu, J., Lin, P., Rosenberg, M., Lee, J.H., 2015. Optogenetic fMRI reveals distinct, frequency-dependent networks recruited by dorsal and intermediate hippocampus stimulations. *Neuroimage* 107, 229–241.
393. Witter, M.P., 2007a. The perforant path: projections from the entorhinal cortex to the dentate gyrus. *Prog. Brain Res.* 163, 43–61.
394. Witter, M.P., 2007b. The perforant path: projections from the entorhinal cortex to the dentate gyrus. *The Dentate Gyrus: A Comprehensive Guide to Structure, Function, and Clinical Implications*.
[https://doi.org/10.1016/s0079-6123\(07\)63003-9](https://doi.org/10.1016/s0079-6123(07)63003-9)
395. Witter, M.P., Amaral, D.G., 1991. Entorhinal cortex of the monkey: V. Projections to the dentate gyrus, hippocampus, and subicular complex. *J. Comp. Neurol.* 307, 437–459.
396. Witter, M.P., Doan, T.P., Jacobsen, B., Nilssen, E.S., Ohara, S., 2017. Architecture of the Entorhinal Cortex A Review of Entorhinal Anatomy in Rodents with Some Comparative Notes. *Front. Syst. Neurosci.* 11, 46.

397. Witter, M.P., Van Hoesen, G.W., Amaral, D.G., 1989. Topographical organization of the entorhinal projection to the dentate gyrus of the monkey. *J. Neurosci.* 9, 216–228.
398. Wolf, R.L., Detre, J.A., 2007. Clinical neuroimaging using arterial spin-labeled perfusion magnetic resonance imaging. *Neurotherapeutics* 4, 346–359.
399. Wu, J.W., Abid Hussaini, S., Bastille, I.M., Rodriguez, G.A., Mrejeru, A., Rilett, K., Sanders, D.W., Cook, C., Fu, H., Rick A C, Herman, M., Nahmani, E., Emrani, S., Helen Figueroa, Y., Diamond, M.I., Clelland, C.L., Wray, S., Duff, K.E., 2016. Neuronal activity enhances tau propagation and tau pathology *in vivo*. *Nature Neuroscience*. <https://doi.org/10.1038/nn.4328>
400. Wu, L.G., Saggau, P., 1994. Presynaptic calcium is increased during normal synaptic transmission and paired-pulse facilitation, but not in long-term potentiation in area CA1 of hippocampus. *The Journal of Neuroscience*. <https://doi.org/10.1523/jneurosci.14-02-00645.1994>
401. Wu, T., Grandjean, J., Bosshard, S.C., Rudin, M., Reutens, D., Jiang, T., 2017a. Altered regional connectivity reflecting effects of different anaesthesia protocols in the mouse brain. *Neuroimage* 149, 190–199.
402. Xu, C., Krabbe, S., Gründemann, J., Botta, P., Fadok, J.P., Osakada, F., Saur, D., Grewe, B.F., Schnitzer, M.J., Callaway, E.M., Lüthi, A., 2016. Distinct Hippocampal Pathways Mediate Dissociable Roles of Context in Memory Retrieval. *Cell*. <https://doi.org/10.1016/j.cell.2016.09.051>
403. Yamamoto, K., Tanei, Z.-I., Hashimoto, T., Wakabayashi, T., Okuno, H., Naka, Y., Yizhar, O., Fenno, L.E., Fukayama, M., Bito, H., Cirrito, J.R., Holtzman, D.M., Deisseroth, K., Iwatsubo, T., 2015. Chronic Optogenetic Activation Augments A β Pathology in a Mouse Model of Alzheimer Disease. *Cell Reports*. <https://doi.org/10.1016/j.celrep.2015.04.017>
404. Yassa, M.A., Muftuler, L.T., Stark, C.E.L., 2010. Ultrahigh-resolution microstructural diffusion tensor imaging reveals perforant path degradation in aged humans *in vivo*. *Proc. Natl. Acad. Sci. U. S. A.* 107, 12687–12691.
405. Yizhar, O., Fenno, L.E., Prigge, M., Schneider, F., Davidson, T.J., O’Shea, D.J., Sohal, V.S., Goshen, I., Finkelstein, J., Paz, J.T., Stehfest, K., Fudim, R., Ramakrishnan, C., Huguenard, J.R., Hegemann, P., Deisseroth, K., 2011. Neocortical excitation/inhibition balance in information processing and social dysfunction. *Nature*. <https://doi.org/10.1038/nature10360>
406. Yoshiyama, Y., Higuchi, M., Zhang, B., Huang, S.M., Iwata, N., Saido, T.C., Maeda, J., Suhara, T., Trojanowski, J.Q. and Lee, V.M.Y., 2007. Synapse loss and microglial activation precede tangles in a P301S tauopathy mouse model. *Neuron*, 53(3), pp.337-351.
407. Zakaria, J.A.D., Dobrowolska Zakaria, J.A., Vassar, R.J., 2018. A promising, novel, and unique BACE 1 inhibitor emerges in the quest to prevent Alzheimer’s disease. *EMBO Molecular Medicine*. <https://doi.org/10.15252/emmm.201809717>
408. Zang, Y., Jiang, T., Lu, Y., He, Y., Tian, L., 2004. Regional homogeneity approach to fMRI data analysis. *NeuroImage*. <https://doi.org/10.1016/j.neuroimage.2003.12.030> Zeng, H., Madisen, L., 2012. Mouse transgenic approaches in optogenetics. *Prog. Brain Res.* 196, 193–213.
409. Zerbi, V., Grandjean, J., Rudin, M., Wenderoth, N., 2015. Mapping the mouse brain with rs-fMRI: An optimized pipeline for functional network identification. *Neuroimage* 123, 11–21.

410. Zhao, F., Zhao, T., Zhou, L., Wu, Q., Hu, X., 2008. BOLD study of stimulation-induced neural activity and resting-state connectivity in medetomidine-sedated rat. *NeuroImage*.
<https://doi.org/10.1016/j.neuroimage.2007.07.063>
411. Ziyatdinova, S., Gurevicius, K., Kutchiashvili, N., Bolkvadze, T., Nissinen, J., Tanila, H., Pitkänen, A., 2011. Spontaneous epileptiform discharges in a mouse model of Alzheimer's disease are suppressed by antiepileptic drugs that block sodium channels. *Epilepsy Res.* 94, 75–85.
412. Zola-Morgan, S., Squire, L.R., Amaral, D.G., 1986. Human amnesia and the medial temporal region: enduring memory impairment following a bilateral lesion limited to field CA1 of the hippocampus. *J. Neurosci.* 6, 2950–2967.
413. Zucker, R.S., 1989. Short-term synaptic plasticity. *Annu. Rev. Neurosci.* 12, 13–31.

~ Appendix 1 ~

Paper # 1 -Published in ScienceMatters, June 2019 DOI: 10.19185/matters.201905000001

Preserved functional networks in a hydrocephalic mouse

Francesca Mandino^{ab}, Ling Yun Yeow^a, John Gigg^b, Malini Olivo^a, Joanes Grandjean^{ac*}

a) Singapore Bioimaging Consortium (SBIC), Agency for Science, Technology and Research (A*STAR)

b) Faculty of Biology, Medicine and Health, The University of Manchester, Manchester, United Kingdom

c) Department of Radiology and Nuclear Medicine & Donders Institute for Brain, Cognition, and Behaviour, Donders Institute, Radboud University Medical Centre

Abstract

Hydrocephalus is a brain condition characterized by enlarged ventricles, due to an excess of cerebrospinal fluid. Although it is known to affect cognition, development, gait, and mood, the impact of hydrocephalus on large-scale functional brain organization is poorly documented. Here, we present results on a single spontaneous occurrence of severe hydrocephalus observed in a 3xTgAD mouse, compared to a control cohort of 3xTgAD littermates. Resting-state functional magnetic resonance imaging analysis, carried out under light anesthesia, revealed the remarkable presence of functional connectivity (FC) resembling the common mouse resting-state networks (RSNs). Four main components were identified in the hydrocephalic mouse, attributable to the Default Mode network, Salience network, and sensorimotor networks. Characteristic features of the RSNs in the hydrocephalic mouse were found to be well preserved, both in spatial distribution and in FC magnitude, despite the severity of the pathology.

This is the first documented case of resting-state fMRI conducted on a mouse affected by severe hydrocephalus. The surprising presence of resting-state networks was found to be comparable to littermate controls, highlighting a remarkable functional resilience in the hydrocephalic brain.

Introduction

Cerebrospinal fluid (CSF) plays an important role in the regulation of the interstitial fluid of the brain parenchyma and in brain development. Compromised CSF dynamics, due either to excess production, reduced resorption, or altered flow of CSF within the ventricles, affect brain development, leading to hydrocephalus. This condition is characterized by an excess of CSF in the ventricles, impaired cognitive and physical development or, when appearing later in life, cognitive decline, gait disturbance, and urinary incontinence^[1]. Congenital hydrocephalus is one of the most common developmental disorders, affecting nearly 1 in 1000 newly born babies^[2].

Magnetic resonance imaging (MRI) is a non-invasive technique for diagnosis of hydrocephalus, due to its excellent soft tissue contrast and ability to resolve multiple imaging parameters^[3]. Beyond anatomical imaging to resolve the extent of CSF distribution and plan for surgeries, diffusion tensor imaging studies have reported lesions in the white matter in hydrocephalic patients^{[4][5][6]}. While the latter provides an insight into the integrity of the structural tracts across the whole brain, the use of functional (f)MRI is an attractive method to assess the functional integrity of underlying neuronal networks. In particular, functional connectivity (FC), estimated in a paradigm-free setting, allows for the imaging of several resting-state networks (RSNs) in parallel across the brain. This provides a comprehensive representation of the functional parcellation of healthy and diseased tissue.

To date, the extent of FC across RSNs in hydrocephalic conditions has been marginally investigated. Patients with idiopathic normal pressure hydrocephalus were shown to have decreased DMN activity relative to healthy controls^[7]. However, the same DMN activity was counterintuitively increased with symptom severity. A more recent clinical study on resting-state fMRI (rs-fMRI) found disrupted interhemispheric FC in hydrocephalic patients compared to healthy subjects^[8]. Currently, there are no established biomarkers for the functional impact of hydrocephalus^[8].

Preclinical imaging, using dedicated high-field MRI systems, offers a unique translational platform to image the rodent brain, using analogous protocols as in human. Recent interest in rodent imaging has focused on FC imaging, using rs-fMRI, with the motivation to understand the functional reorganization taking place in murine models of brain disorders ranging from Alzheimer's disease^{[9][10][11][12]} to autism and depression^{[13][14]}. However, previous research on hydrocephalus has mainly focused on anatomical measures of white matter integrity and myelination^{[15][16]}. To date, there is a lack of research investigating functional consequences in this condition. Preclinical studies on hydrocephalic rodents would contribute to the understanding of the RSNs arrangements in hydrocephalus, and they may help shed a light onto RSNs changes in clinical cases of hydrocephalus^{[7][8]}.

Objective

The spontaneous occurrence of a hydrocephalic mouse, in a cohort of 3xTg Alzheimer's disease model (3xTgAD^[17]) mice, offers a unique opportunity to investigate the functional consequences of this rare condition in a preclinical setting, at the individual level. We report the observation of remarkably preserved FC in a single case study of a hydrocephalic mouse brain, despite the severity of this case.

Results & Discussion

The hydrocephalic mouse belonged to a cohort of transgenic mice used in a resting-state study on early stages of cerebral amyloidosis. No evident behavioural differences could be observed with respect to gait, feeding, grooming, or mood. Stable physiological parameters were observed for all the animals without a noticeable difference, ensuring optimal recording conditions (Fig. S1): heart rate 336.5 ± 42.3 (Fig. S1A) and blood oxygenation mean 95 ± 4.4 (Fig. S1B). Anatomical images acquired for the hydrocephalic brain showed a broad expansion of the CSF volume, extending to 44% of the total brain volume (Fig. 1A). Cortical thickness was reduced to a range of 0.5 - 0.8 mm, compared to 0.9 - 1.5 mm in the control animals. The GE-EPI images acquired at high-field presented minimal geometric distortion, ensuring precise mapping of the functional networks (Fig. 1B).

We referred to rules defined in^[18] to identify relevant mouse RSNs in the ICA. Four plausible anatomically relevant components for RSNs were found in the hydrocephalic mouse (Fig. 1C, D, E, F, bottom panels). In the control cohort, 4.14 ± 1.01 plausible components could be identified. The representative components in one control animal are shown as reference (Fig. 1C, D, E, F, top panels). The incidence map for the four RSNs shows a 70–100% co-occurrence of the major anatomical regions within each RSN investigated, across all control subjects (Fig. S2). This indicates that individual-level RSNs were stable and spatially converged within the control cohort. One network was found to overlap with the cingulate and retrosplenial cortex, together with patterns of anti-correlations with the anterior parietal cortex (Fig. 1C, S2A), therefore, showing a

spatial distribution corresponding to the rodent DMN. The second network identified presented FC extent attributable to the Salience network (SN), specifically, overlapping with the insular and secondary somatosensory cortex (Fig. 1D, S2B). The full extent of the DMN (Fig. 1C, S2A) and SN (Fig. 1D, S2B) are shown together with the 3-dimensional extension of the CSF in both controls (top panels) and hydrocephalic (bottom panels) mice (Fig. S3A, B). The third and fourth networks corresponded, respectively, to the anterior and posterior sensorimotor networks (Fig. 1E, F; S2C, D), including overlaps with the anterior motor and somatosensory (barrel field) cortex (Fig. 1E, S2C), and the posterior somatosensory (front and hindlimb, auditory, and visual) cortex (Fig. 1F, S2D). Only marginal clusters were observed within sub-cortical networks in the hydrocephalic mouse, while a fifth component, presenting a strong sub-cortical basis, could be observed in 8 of the 17 mice comprising the control cohort. We concluded that the RSN found in the hydrocephalic mouse corresponded to the counterparts found in the control cohort.

To validate these qualitative findings, reference components shown in figure 1 were regressed within the hydrocephalus scan or across all scans in the control animals. Z-statistics, denoting FC strength within a RSN, were extracted using two ROIs located within the DMN and two within the SN (Fig. 1G, H, I, J). Specifically, FC within the cingulate cortex and retrosplenial cortex, two key elements of the DMN (red and yellow arrow in Fig. 1C, respectively), ranged 6.16 ± 2.39 and 5.41 ± 2.28 in the control cohort, while it reached 10.71 and 6.85 in the hydrocephalic mouse (Fig. 1G, H). With respect to the SN, the magnitude of FC within the insula and somatosensory cortex (green and cyan arrow in Fig. 1D, respectively) ranged 8.99 ± 3.10 and 8.36 ± 2.13 in the control group and 12.65 and 7.53 in the hydrocephalic mouse (Fig. 1I, J). In summary, network strength in the hydrocephalic mouse was found to be within ± 1 standard deviation of the estimate in the control group in three of the four ROIs, and ± 2 standard deviations in the fourth. We conclude that RSN within the hydrocephalic mouse presented FC strength on par with those found in animals from the control cohort.

This case report showed that, despite a major excess of CSF, the hydrocephalic mouse brain presented a surprising functional resilience. The intrinsic FC organization resembled the characteristics of four RSNs commonly present in the rodent brain, including DMN, SN, and sensorimotor networks. The spatial distribution and the magnitude of the RSNs have been found to be comparable to the littermate controls. Both the DMN and SN have been identified as major hubs underlying neuropathologies and neurodevelopment in human^{[19][20]}. The strong functional resilience to structural insults exhibited, in this case, departs from observations in human reports, where both these networks have been shown to be affected^{[7][8]}.

This first observation, made in a spontaneous hydrocephalus case, offers a rare glimpse into the functional organization of the mouse brain following a severe insult. This was made possible with ultra-high field magnets and advanced cryoprobe receiver coils allowing for high sensitivity of the resting fMRI signal. Moreover, previously optimized anaesthesia^[21] and preprocessing protocols^[18] provide additional sensitivity for the robust and reliable detection of RSNs at the individual level in rodents. This is exemplified by the high reproducibility of the RSNs detected at the individual level in the control cohort.

Conclusions

We present here the first fMRI investigation into a spontaneous case of hydrocephalus in a mouse. Results highlight the preservation of cortical functional networks despite substantial ventricular enlargement. This report, beyond being a rare scientific curiosity, provides the first insight into

RSNs organization following a severe brain insult and could represent an innovative approach for future research aiming to investigate functional resilience in severe pathological conditions.

Limitations

The major limitation of this study is the reliance on a single observation, due to the spontaneous nature of the occurrence. Dedicated animal models presenting increased incidence of hydrocephalus would contribute to understanding the full extent of the functional resilience to brain insults, and the parameters associated with it, in rodents^[22]. Preclinical functional imaging, in targeted mouse models, would offer a unique opportunity to investigate underlying mechanisms in functional resilience in hydrocephalus.

Methods

All applicable international, national, and/or institutional guidelines for the care and use of animals were followed. All procedures performed in studies involving animals were in accordance with the ethical standards of the Institutional Animal Care and Use Committee (A*STAR Biological Resource Centre, Singapore, IACUC #171203). The complete raw dataset for this study can be found on <https://openneuro.org/datasets/ds001890>; Project ID: Mouse_rest_3xTG.

18 animals (3-month-old males; 1 hydrocephalic mouse and 17 controls, 26–30 g) were triple-transgenic mice (3xTgAD, Jackson Laboratory, Bar Harbor, Maine, USA) bred in-house. Animals were prepared as in^[11]. Briefly, anaesthesia was induced with 4% isoflurane (50%–50% medical air and Oxygen mixture) to allow the animals to be endotracheally intubated. They were then positioned on an MRI-compatible cradle and artificially ventilated at 90 breaths per minute (Kent Scientific Corporation, Torrington, Connecticut, USA). A medetomidine bolus (0.05 mg/kg such, Dormitory, Elanco, Greenfield, Indiana, USA) was administered, together with muscle relaxant (Pancuronium Bromide, Sigma-Aldrich Pte. Ltd., Singapore), followed by a maintenance infusion (0.1 mg/kg/h s.c.), while isoflurane was reduced to 0.5%. Functional scans were acquired 20 min following bolus to ensure physiological stability of the animals.

The animal temperature was maintained at 37°C. Physiological parameters were recorded with a MRI-compatible oximeter (Kent Scientific Corporation, Torrington, Connecticut, USA): heart rate (HR) measured in beats per minute (bpm) and oxygen saturation (SpO₂, measured in %). Data were acquired on an 11.75 T (Bruker BioSpin MRI, Ettlingen, Germany) equipped with a BGA-S gradient system, a linear volume resonator coil for transmission and a 2×2 phased-array cryogenic surface receiver coil. Images were acquired using Paravision 6.0.1 software. An anatomical reference scan was acquired using a spin-echo turboRARE sequence: field of view (FOV) = 17×11 mm² (adapted from 17×9 mm² in control mice to account for enlarged brain), FOV saturation slice masking non-brain regions, number of slices = 28, slice thickness = 0.35, slice gap = 0.05 mm, matrix dimension (MD) = 200×100, repetition time (TR) = 2750 ms, echo time (TE) = 30 ms, RARE factor = 8, number of averages = 2. Rs-fMRI was acquired using a gradient-echo echo-planar imaging (GE-EPI) sequence with the same geometry as the anatomical: MD = 90×60, TR = 1000 ms, TE = 15 ms, flip angle = 50°, volumes = 600, bandwidth = 250 kHz. Field inhomogeneity was corrected using MAPSHIM protocol.

Images were processed using a protocol optimized for the mouse^[18]. Images underwent motion correction (*mcflirt*, FMRIB Software Library v5.0, fsl.fmrib.ox.ac.uk), automatic brain masking

(*bet*), smoothing with a 0.45 mm² kernel (*susan*), and a 0.01 Hz high-pass filter (*fslmaths*). Control animals were registered to a representative anatomical scan drawn from within the control cohort (*antsIntroduction*, Advanced Normalization Tools, <http://picsl.upenn.edu/software/ants/>). Lesions in the hydrocephalus brain precluded normalization to the same reference space, instead, an analysis of the hydrocephalus data was carried out in its native space. Within-subject spatial independent component analysis (ICA, *melodic*) was estimated with automatic dimensionality estimation. Automated nuisance removal (*FIX*) was carried out using a classifier trained on an existing dataset acquired previously in-house. Reference components derived from a representative animal were regressed into individual scans using a dual regression framework in order to obtain individual-level representations of these components^[23]. Z-statistic, a parameter indicative of RSN strength, was estimated in the dual regression analysis and was extracted using regions-of-interest (ROI). ROIs were selected to be representative of major anatomical regions within the respective RSN. Descriptive statistics are given as mean \pm 1 standard deviation.

Funding Statement

This work was supported by the University of Manchester and A*STAR Research Attachment Programme (ARAP), which is co-funded through the University of Manchester, Faculty of Biology, Medicine and Health Doctoral Academy, and Singapore Bioimaging Consortium (SBIC), A*STAR, Singapore. Animal work was supported by Laboratory of Bio-optical Imaging (LBOI), SBIC A*STAR, Singapore.

Acknowledgements

The authors would like to thank Richard Clayton for critical reading of the manuscript.

Conflict of interest

The authors declare no conflicts of interest.

Ethics Statement

All applicable international, national, and/or institutional guidelines for the care and use of animals were followed. All procedures performed in studies involving animals were in accordance with the ethical standards of the Institutional Animal Care and Use Committee (A*STAR Biological Resource Centre, Singapore, IACUC #171203).

No fraudulence is committed in performing these experiments or during processing of the data. We understand that in the case of fraudulence, the study can be retracted by ScienceMatters.

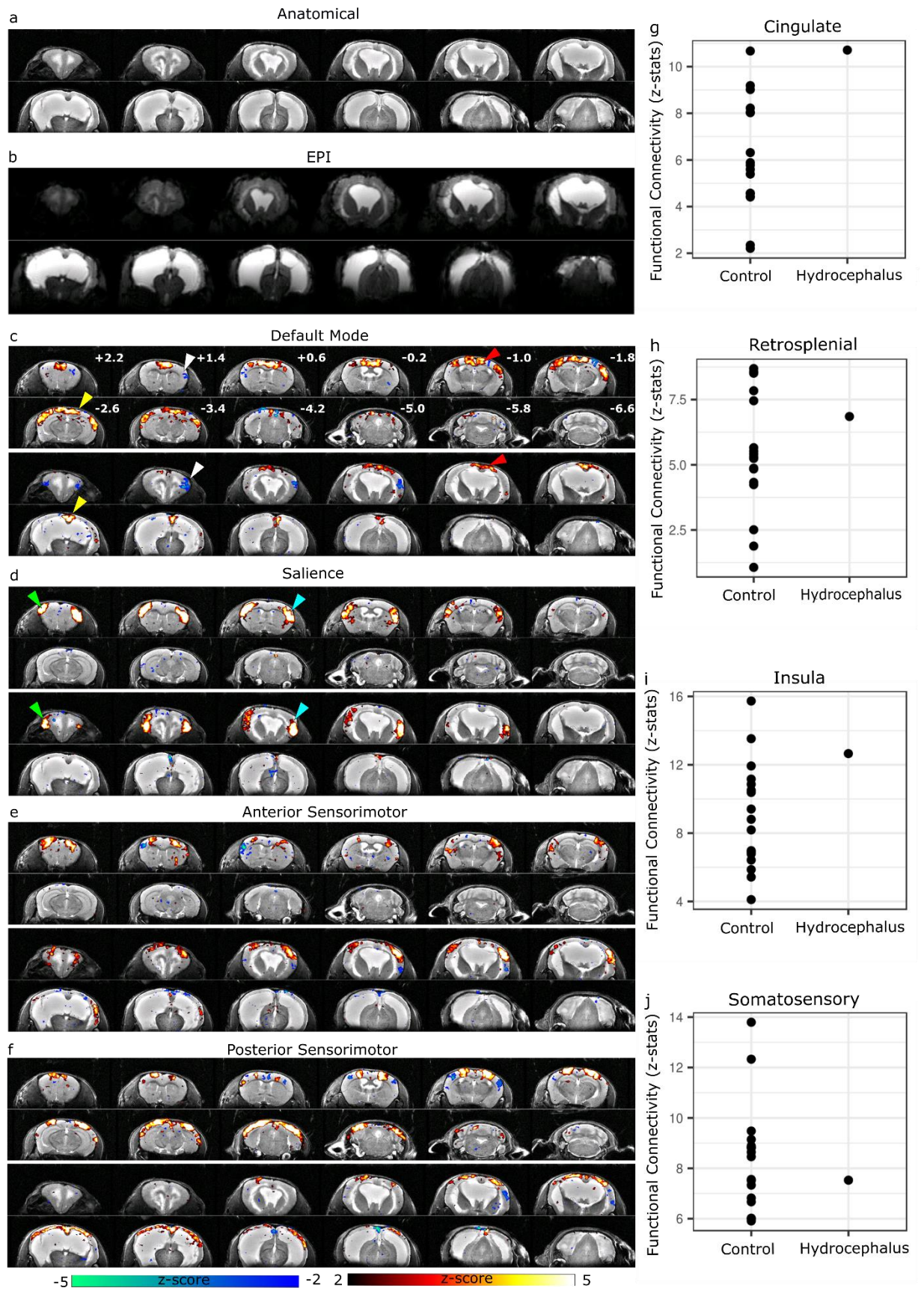


Figure 1. Anatomical and GE-EPI images of the hydrocephalic brain; functional networks in a representative control (top panels) and hydrocephalic mouse (bottom panels) and related Z-statistics. (A) TurboRARE anatomical images acquired with a T2 contrast denote the extent of CSF (bright) with

respect to grey (light grey) and white (dark grey) matter. (B) Single-shot single-echo gradient-echo echo-planar images acquired at 11.75 T present minimal distortions and recapitulate the features of the anatomical images. (C) The mouse Default Mode network (DMN) presents characteristic correlation in the cingulate (red arrows) and retrosplenial cortices (yellow arrows), whilst anti-correlation is found in the insular cortex (white arrows). (D) The Salience network (SN) displays correlation within the insula (green arrow) and secondary somatosensory cortex (cyan arrows). In addition, two sensorimotor networks were observed: (E) the anterior portion encompassing the barrel field somatosensory cortex and anterior motor cortex; and (F) the posterior portion encompassing the front and hindlimb, auditory, and visual cortices. Reference-independent components are shown as color-coded Z-scores overlaid on the respective turboRARE anatomical images. The distance from Bregma of each coronal slice is indicated in mm. (G) Z-statistics for the ROI located in the cingulate cortex, within the DMN: controls 6.16 ± 2.39 and hydrocephalus 10.71. (H) Z-statistics for the ROI located in the retrosplenial cortex, within the DMN: controls 5.41 ± 2.28 and hydrocephalus 6.85. (I) Z-statistics for the ROI located in the insular cortex, within the SN: controls 8.99 ± 3.10 and hydrocephalus 12.65. (J) Z-statistics for the ROI located in the somatosensory cortex, within the SN: controls 8.36 ± 2.13 and hydrocephalus 7.53. $n = 17$ controls, $n = 1$ hydrocephalus.

Citations

- [1] Michael Williams and Jan Malm. “Diagnosis and Treatment of Idiopathic Normal Pressure Hydrocephalus”. In: *CONTINUUM: Lifelong Learning in Neurology* 22.2, Dementia (2016), pp. 579–599. doi: 10.1212/con.0000000000000305. url: <https://doi.org/10.1212/con.0000000000000305>.
- [2] C. Stoll et al. “An epidemiologic study of environmental and genetic factors in congenital hydrocephalus”. In: *European Journal of Epidemiology* 8.6 (1992), pp. 797–803. doi: 10.1007/bf00145322. url: <https://doi.org/10.1007/bf00145322>.
- [3] William G. Bradley Jr. “Magnetic Resonance Imaging of Normal Pressure Hydrocephalus”. In: *Seminars in Ultrasound, CT and MRI* 37.2 (2016), pp. 120–128.
- [4] Y. Assaf et al. “Diffusion Tensor Imaging in Hydrocephalus: Initial Experience”. In: *American Journal of Neuroradiology* 27.8 (2006), pp. 1717–1724.
- [5] Tetsuo KOYAMA et al. “Diffusion Tensor Imaging of Idiopathic Normal Pressure Hydrocephalus: A Voxel-Based Fractional Anisotropy Study”. In: *Neurologia medico-chirurgica* 52.2 (2012), pp. 68–74. doi: 10.2176/nmc.52.68. url: <https://doi.org/10.2176/nmc.52.68>.
- [6] David Hoza et al. “DTI-MRI biomarkers in the search for normal pressure hydrocephalus aetiology: a review”. In: *Neurosurgical Review* 38.2 (2015), pp. 239–244. doi: 10.1007/s10143-014-0584-0. url: <https://doi.org/10.1007/s10143-014-0584-0>.
- [7] Hui Ming Khoo et al. “Default mode network connectivity in patients with idiopathic normal pressure hydrocephalus”. In: *Journal of Neurosurgery JNS* 124.2 (2016), pp. 350–358. doi: 10.3171/2015.1.jns141633. url: <https://doi.org/10.3171/2015.1.jns141633>.
- [8] Yousuke Ogata et al. “Interhemispheric Resting-State Functional Connectivity Predicts Severity of Idiopathic Normal Pressure Hydrocephalus”. In: *Frontiers in Neuroscience* 11 (2017), p. 470. doi: 10.3389/fnins.2017.00470. url: <https://doi.org/10.3389/fnins.2017.00470>.
- [9] Disha Shah et al. “Resting State fMRI Reveals Diminished Functional Connectivity in a Mouse Model of Amyloidosis”. In: *PLOS ONE* 8.12 (2013), e84241. doi: 10.1371/journal.pone.0084241. url: <https://doi.org/10.1371/journal.pone.0084241>.
- [10] Disha Shah et al. “Early pathologic amyloid induces hypersynchrony of BOLD resting-state networks in transgenic mice and provides an early therapeutic window before amyloid plaque deposition”. In: *Alzheimer’s & Dementia* 12.9 (2016), pp. 964–976. doi: 10.1016/j.jalz.2016.03.010. url: <https://doi.org/10.1016/j.jalz.2016.03.010>.

- [11] Joanes Grandjean et al. “Early Alterations in Functional Connectivity and White Matter Structure in a Transgenic Mouse Model of Cerebral Amyloidosis”. In: *Journal of Neuroscience* 34.41 (2014), pp. 13780–13789. doi: 10.1523/jneurosci.4762-13.2014. url: <https://doi.org/10.1523/jneurosci.4762-13.2014>.
- [12] Maxime J. Parent et al. “Multimodal Imaging in Rat Model Recapitulates Alzheimer’s Disease Biomarkers Abnormalities”. In: *Journal of Neuroscience* 37.50 (2017), pp. 12263–12271. doi: 10.1523/jneurosci.1346-17.2017. url: <https://doi.org/10.1523/jneurosci.1346-17.2017>.
- [13] Francesco Sforazzini et al. “Altered functional connectivity networks in a callosal and socially impaired BTBR mice”. In: *Brain Structure and Function* 221.2 (2014), pp. 941–954. doi: 10.1007/s00429-014-0948-9. url: <https://doi.org/10.1007/s00429-014-0948-9>.
- [14] Joanes Grandjean et al. “Chronic psychosocial stress in mice leads to changes in brain functional connectivity and metabolite levels comparable to human depression”. In: *NeuroImage* 142 (2016), pp. 544–552. doi: 10.1016/j.neuroimage.2016.08.013. url: <https://doi.org/10.1016/j.neuroimage.2016.08.013>. 2016.08.013.
- [15] Domenico L. Di Curzio et al. “Memantine treatment of juvenile rats with kaolin-induced hydrocephalus”. In: *Brain Research* 1689 (2018), pp. 54–62. doi: 10.1016/j.brainres.2018.04.001. url: <https://doi.org/10.1016/j.brainres.2018.04.001>.
- [16] Hadijat M. Makinde et al. “Monocyte depletion attenuates the development of posttraumatic hydrocephalus and preserves white matter integrity after traumatic brain injury”. In: *PLOS ONE* 13.11 (2018), e0202722. doi: 10.1371/journal.pone.0202722. url: <https://doi.org/10.1371/journal.pone.0202722>.
- [17] Salvatore Oddo et al. “Amyloid deposition precedes tangle formation in a triple transgenic model of Alzheimer’s disease”. In: *Neurobiology of Aging* 24.8 (2003), pp. 1063–1070. doi: 10.1016/j.neurobiolaging.2003.08.012. url: <https://doi.org/10.1016/j.neurobiolaging.2003.08.012>. 2003.08.012.
- [18] Valerio Zerbi et al. “Mapping the mouse brain with rs-fMRI: An optimized pipeline for functional network identification”. In: *NeuroImage* 123 (2015), pp. 11–21. doi: 10.1016/j.neuroimage.2015.07.090. url: <https://doi.org/10.1016/j.neuroimage.2015.07.090>. 2015.07.090.
- [19] Vinod Menon. “Large-scale brain networks and psychopathology: a unifying triple network model”. In: *Trends in Cognitive Sciences* 15.10 (2011), pp. 483–506. doi: 10.1016/j.tics.2011.08.003. url: <https://doi.org/10.1016/j.tics.2011.08.003>.
- [20] Lucina Q. Uddin et al. “Dynamic Reconfiguration of Structural and Functional Connectivity Across Core Neurocognitive Brain Networks with Development”. In: *Journal of Neuroscience* 31.50 (2011), pp. 18578–18589. doi: 10.1523/jneurosci.4465-11.2011. url: <https://doi.org/10.1523/jneurosci.4465-11.2011>.
- [21] Joanes Grandjean et al. “Optimization of anesthesia protocol for resting-state fMRI in mice based on differential effects of anesthetics on functional connectivity patterns”. In: *NeuroImage* 102 (2014), pp. 838–847. doi: 10.1016/j.neuroimage.2014.08.043. url: <https://doi.org/10.1016/j.neuroimage.2014.08.043>.
- [22] Oliver K. Appelbe et al. “Disruption of the mouse *Jhy* gene causes abnormal ciliary microtubule patterning and juvenile hydrocephalus”. In: *Developmental Biology* 382.1 (2013), pp. 172–185.
- [23] C F Beckmann et al. “Group comparison of resting-state FMRI data using multi-subject ICA and dual regression”. In: *NeuroImage* 47 (2009), S148. doi: 10.1016/s1053-8119(09)71511-3. url: [https://doi.org/10.1016/s1053-8119\(09\)71511-3](https://doi.org/10.1016/s1053-8119(09)71511-3).

Supplementary material

Figures

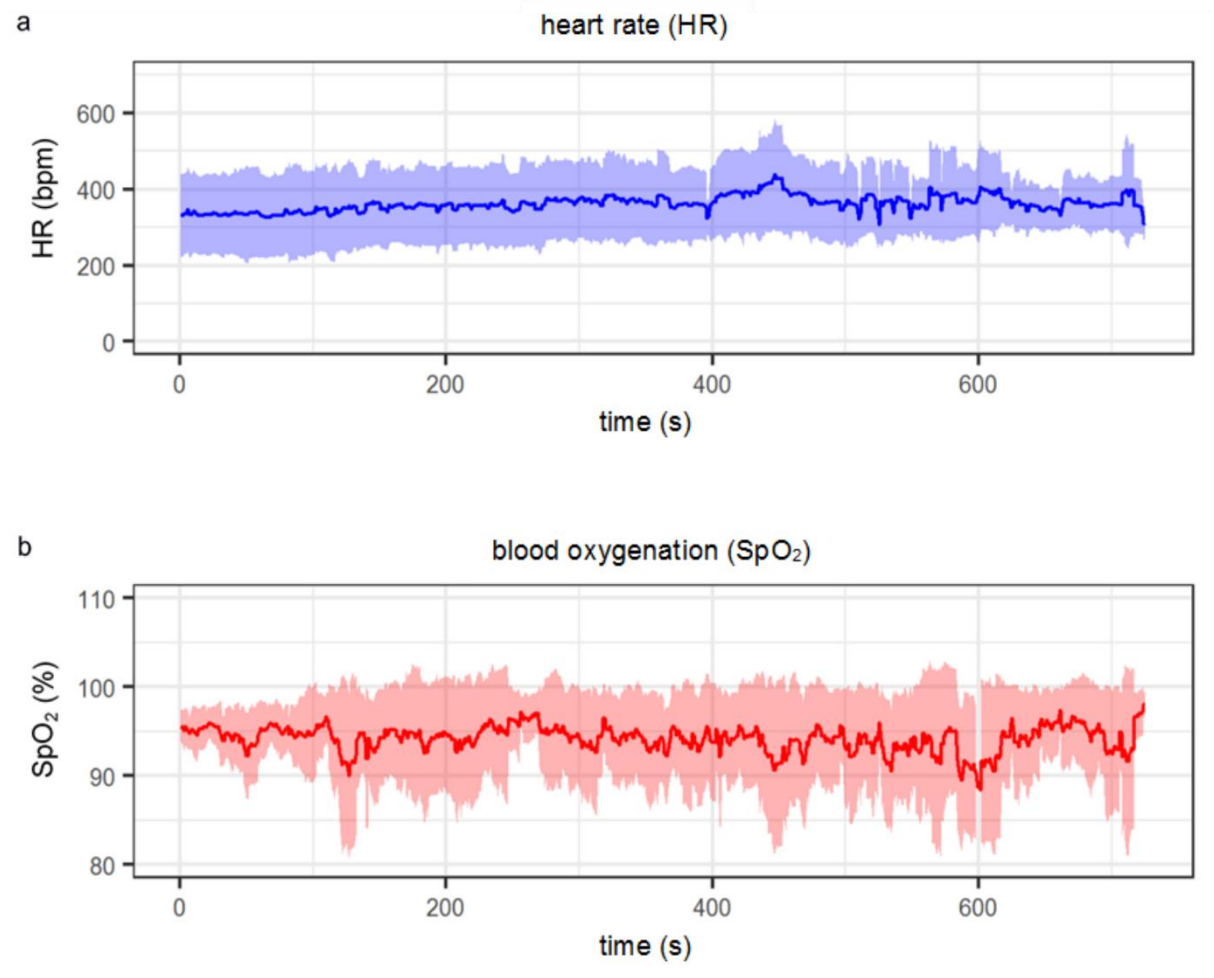


Figure S1. Physiological parameters for fifteen animals belonging to the control group of the animals studied. Parameters were recorded throughout the entire duration of the functional scan. (a) Heart rate (HR), measured in beats per minute (bpm) was reported 336.5 ± 42.3 . (b) The blood oxygenation (SpO₂) was reported 95 ± 4.4 was measured in % change. Overall, the physiological parameters showed little variations across animals. Data from two control animals were not recorded due to a faulty in the device. Both measurements were reported in mean \pm 1 standard deviation over time

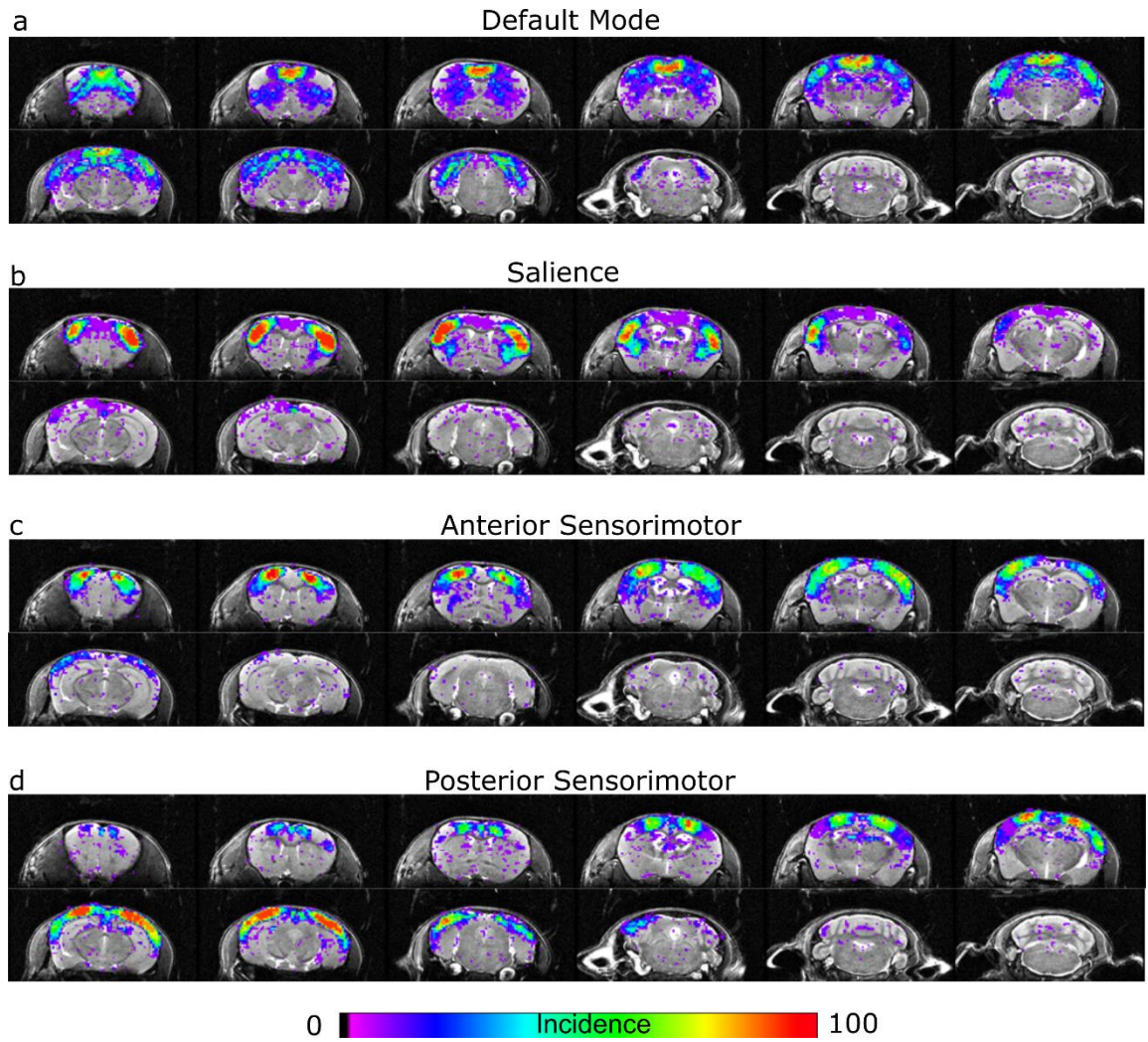


Figure S2. Incidence maps representing the percentage of dataset surviving the significance threshold ($z = 1.9$ corresponding to $p < .05$) in the control group ($n = 17$). Incidence reached 100 % within the main component clusters in all cases, denoting that significant FC could be established across the entire dataset. (a) The mouse DMN presents high incidence within the retrosplenial cortices (yellow arrows in Figure 1c). (b) The Salience network displays highest values within the insula (green arrows in Figure 1d). (c) The anterior sensorimotor areas show high incidence across the subjects, within the barrel field somatosensory cortex and anterior motor cortex; and (d) the posterior somatosensory areas show high overlapping across all subjects, within the front and hindlimb, auditory, and visual cortices, as well as the posterior motor cortex.

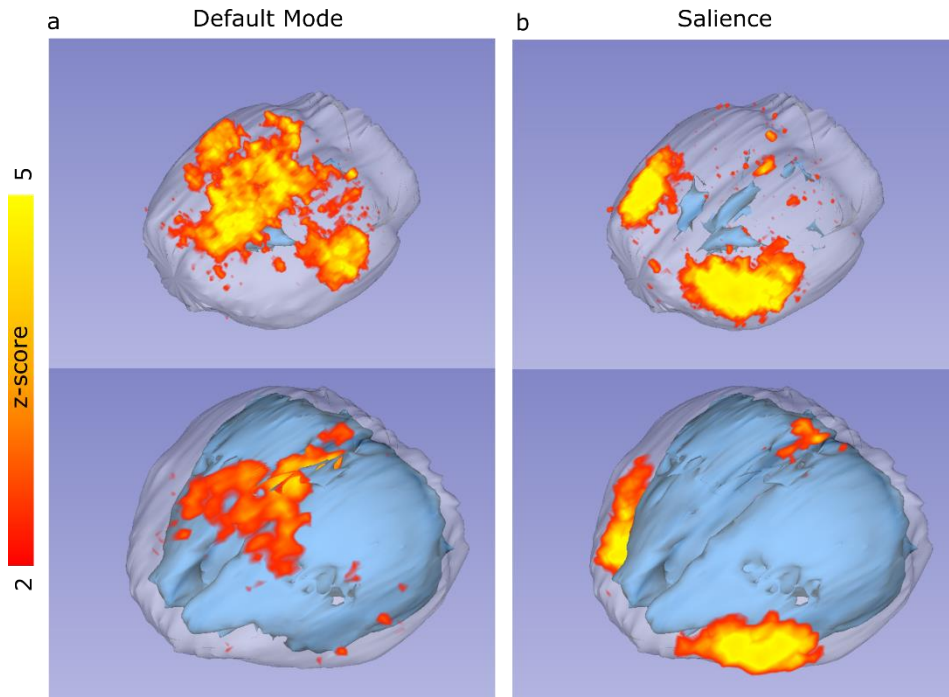


Figure S3. Three-dimensional representations of the DMN and SN. (a) DMN Mode and (b) SN in a representative control (top) and hydrocephalic mouse (bottom) showing the spatial extent of these networks. Individual-level independent components are shown as maximal intensity projections (red-yellow) and CSF volumes are indicated in light blue

~ Appendix 2 ~

Paper #2 – Published in Frontiers of Neuroinformatics

Mandino, F., Cerri, D.H., Garin, C.M., Straathof, M., van Tilborg, G.A., Chakravarty, M.M., Dhenain, M., Dijkhuizen, R.M., Gozzi, A., Hess, A. and Keilholz, S.D., 2020. **Animal Functional Magnetic Resonance Imaging: Trends and Path Toward Standardization.** *Frontiers in Neuroinformatics*, 13, p.78.

Animal functional magnetic resonance imaging: Trends and path toward standardization.

Francesca Mandino^{1,2}, Domenic H. Cerri³, Clement M. Garin⁴, Milou Straathof⁵, Geralda A.F. van Tilborg⁵,

M. Mallar Chakravarty⁶, Marc Dhenain⁴, Rick M. Dijkhuizen⁵, Alessandro Gozzi⁷, Andreas Hess⁸, Shella D. Keilholz⁹, Jason P. Lerch^{1,11}, Yen-Yu Ian Shih³, Joanes Grandjean^{1,12}

1. Singapore Bioimaging Consortium, Agency for Science Technology and Research, Singapore, Singapore
2. Faculty of Biology, Medicine and Health, The University of Manchester, Manchester, United Kingdom
3. Center for Animal MRI, Department of Neurology & Biomedical Research Imaging Center, University of North Carolina, Chapel Hill, NC, USA
4. Commissariat à l'Énergie Atomique et aux Énergies Alternatives (CEA), Direction de la Recherche Fondamentale (DRF), Institut François Jacob, MIRCen, & Centre National de la Recherche Scientifique (CNRS), Université Paris-Sud, Université Paris-Saclay UMR 9199, Neurodegenerative Diseases Laboratory, Fontenay aux roses, France
5. Biomedical MR Imaging and Spectroscopy Group, Center for Image Sciences, University Medical Center Utrecht and Utrecht University, Utrecht, the Netherlands
6. Douglas Mental Health University Institute & Departments of Psychiatry and Biological and Biomedical Engineering, McGill University, Montreal, Quebec, Canada
7. Functional Neuroimaging Laboratory, Istituto Italiano di Tecnologia, Centre for Neuroscience and Cognitive Systems @ UNITN, 38068 Rovereto, Italy
8. Institute of Experimental and Clinical Pharmacology and Toxicology, Friedrich-Alexander University Erlangen-Nürnberg (FAU), Fahrstraße 17, 91054, Erlangen, Germany
9. Department of Biomedical Engineering, Georgia Tech and Emory University, Atlanta, GA, USA
10. Hospital for Sick Children and Department of Medical Biophysics, The University of Toronto, Toronto, Ontario, Canada
11. Wellcome Centre for Integrative NeuroImaging, University of Oxford, Oxford, UK
12. Department of Radiology and Nuclear Medicine & Donders Institute for Brain, Cognition, and Behaviour, Donders Institute, Radboud University Medical Centre, Nijmegen, The Netherlands

Correspondence should be addressed to:

Joanes Grandjean joanes.grandjean@radboudumc.nl

Department of Radiology and Nuclear Medicine & Donders Institute for Brain, Cognition, and Behaviour, Donders Institute, Radboud University Medical Centre, Kappittelweg 29, Nijmegen 6525 EZ, The Netherlands

Abstract

Animal whole-brain functional magnetic resonance imaging (fMRI) provides a non-invasive window into brain activity. A collection of associated methods aims to replicate observations made in humans and to identify the mechanisms underlying the distributed neuronal activity in the healthy and disordered brain. Animal fMRI studies have developed rapidly over the past years, fueled by the development of resting-state fMRI connectivity and genetically-encoded neuromodulatory tools. Yet, comparisons between sites remain hampered by lack of standardization. Recently, we highlighted that mouse resting-state functional connectivity converges across centres, although large discrepancies in sensitivity and specificity remained. Here, we explore past and present trends within the animal fMRI community and highlight critical aspects in study design, data acquisition, and post-processing operations, that may affect the results and influence the comparability between studies. We also suggest practices aimed to promote the adoption of standards within the community and improve between-lab reproducibility. The implementation of standardized animal neuroimaging protocols will facilitate animal population imaging efforts as well as meta-analysis and replication studies, the gold standards in evidence-based science.

1. Introduction

A detailed understanding of the mammalian brain structure and function is one of the greatest challenges of modern neuroscience. Approaching the complexity of the organ and the levels of organization of neuronal circuits across several orders of magnitudes, both spatially and temporally, requires the collective scientific efforts from multiple teams across several disciplines. Neuroimaging, especially by means of magnetic resonance imaging (MRI), is playing a preponderant role in mapping the human and animal brain, due to its non-invasiveness, excellent soft-tissue contrast, and multiple readouts. The human neuroimaging research has accelerated over the past decade, fueled by numerous discoveries about brain structure and function and its relation to disorders. In turn, this has led to population imaging efforts aimed to describe variations in brain structure and function, and their relation to behavioural traits, genetic polymorphisms, and pathology. For instance, since its original description in 1995 (Biswal et al., 1995), resting-state functional connectivity (RS-FC) has been at the centre of numerous population imaging initiatives, such as the 1,000 Functional Connectomes Project (Biswal et al., 2010), the WU-Minn Human Connectome Project (Van Essen et al., 2013; Van Essen and Ugurbil, 2012), and the UK Biobank (Miller et al., 2016). In addition to providing an important baseline of healthy cohorts, these initiatives are complemented with population imaging dedicated to specific psychiatric and neurological disorders, such as the Alzheimer's Disease Neuroimaging Initiative (Petersen et al., 2010; Weiner et al., 2012), the Autism Brain Imaging Data Exchange (Di Martino et al., 2014), or Attention-Deficit Hyperactivity Disorder (HD-200 Consortium, 2012). Collectively, these resources have significantly advanced our understanding of neuro- and psychopathologies, as well as providing an understanding of disorder spectrums at a population level.

In contrast to the above, functional neuroimaging studies in animals have remained mostly confined to single centres, often relying on lab-specific acquisition and processing protocols. There has been little pressure toward standardization within the community, and results from different centres have remained inherently difficult to compare, due to discrepancies related to animal housing and preparation, recording hardware, and analysis methodologies. It is now

emerging that these preparation divergences are at the stem of a number of dissensions within the animal functional neuroimaging community, such as the nature of unilateral vs. bilateral resting-state networks (RSN) in mice (Grandjean et al., 2014; Jonckers et al., 2011; Mechling et al., 2014; Sforazzini et al., 2014), the bilateral BOLD response to non-noxious paw electrical stimulation in mice (Bosshard et al., 2010; Schroeter et al., 2014; Shim et al., 2018), the indirect artefacts emerging in optogenetics fMRI (ofMRI) through either heating or vascular photoactivation (Christie et al., 2013; Rungta et al., 2017; Schmid et al., 2017), or the spatial extent of distributed networks of translational relevance, such as the rodent “default mode network” (DMN) reviewed in (Gozzi and Schwarz, 2016). Only recently did efforts emerge to combine and compare structural and/or functional MRI from multiple centres in monkeys (Milham et al., 2018) and in mice (**Figure 1**) (Grandjean et al., 2019a). These initial studies provide solid grounds for the development of replication studies, meta-analyses, and multi-centre consortia, the gold standards in evidence-based science.

Presently, we aim to describe the current trends in the field and to examine how these impact the results and their comparability with the rest of the literature. We systematically assessed the animal fMRI literature for data acquisition and analysis procedures to provide an overview of the collective directions taken within the animal imaging community. We then reviewed the major considerations taking place in the study design, and how these impact results and their interpretability. Finally, we use this information to provide a road map toward the adoption of standards that will enable animal population studies to inform on the functional mammalian brain.

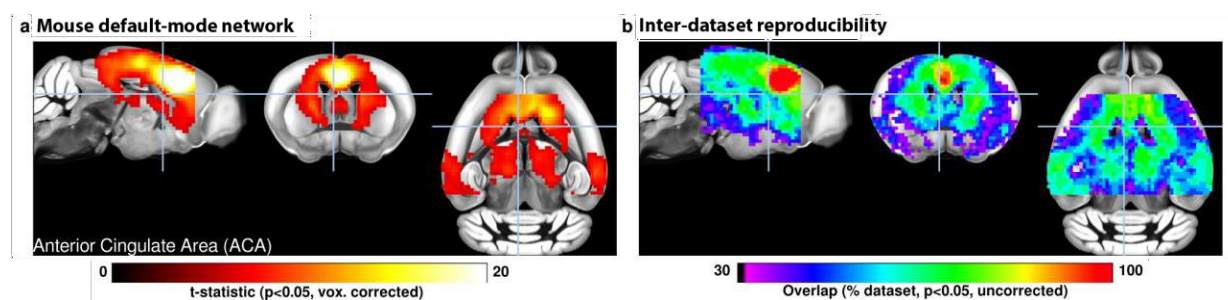


Figure 1 | a) A seed-based analysis of the anterior cingulate area in 98 resting-state fMRI scans reveals the topological distribution of the mouse default-mode network. The regions co-activating with the seed include the dorsal striatum, dorsal thalamus, retrosplenial and posterior parietal areas. b) The reproducibility of the default-mode network was assessed in 17 independent datasets consisting of 15 scans each. Overlapping one- sample t-test maps are summarized in a colour-coded overlay. 12/17 datasets present converging topological features, the remaining 5 failed to present evidence of distal connectivity relative to the seed. Adapted with permission from Grandjean et al (2019a).

2. Methods

We searched the Pubmed database (<https://www.ncbi.nlm.nih.gov/pubmed/>) on 11/02/2019 for the terms “functional magnetic resonance imaging”, “functional MRI”, or “fMRI” within the abstract or title, excluding studies in human and reviews, from 1990 onward, using the following command. “Search ((fMRI[Title/Abstract]) OR functional MRI[Title/Abstract]) OR functional magnetic resonance imaging[Title/Abstract] Sort by: Best Match Filters: Abstract; Publication

date from 1990/01/01 to 2019/12/31; Other Animals”. The query returned 2279 entries. The title and abstract from these were manually screened to exclude studies that did not contain primary research using MRI to assess brain function in animals. In total, 868 research article were considered relevant and could be readily obtained. We recorded the type of study: resting-state or paradigm free RS-FC recordings, pharmacological-evoked, opto- /chemogenetic neuromodulation, deep-brain stimulation (DBS), or stimulus-evoked (including blocks- or events-related designs with sensory stimulation, gas challenge, etc..). We recorded animals species, including strain, gender (male, female, both, N/A), number of animals used, animal preparation (awake, anesthetized free-breathing, anesthetized ventilated), anesthetic used for maintenance during fMRI, field strength, fMRI sequence and contrast, pre-processing software, and noted if the datasets were made available by the authors or in online repositories. The resulting table is made available in the supplementary materials.

3. Results and discussion

3.1 Experimental Design

Animal fMRI presents the opportunity for new and creative directions in study design, but care must be taken to ensure that experimental changes in the fMRI signal are sufficiently robust for detection and that results are not contaminated by procedural artefacts. Here we highlight evidence supporting standards and reporting strategies to optimize data quality, interpretation, and reproducibility for several common animal fMRI paradigms.

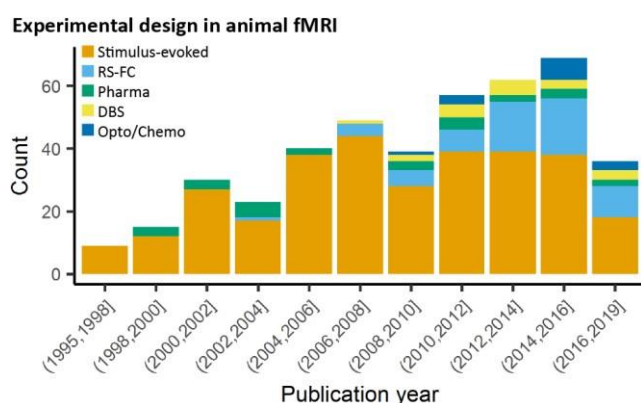


Figure 2 | Study design in animal fMRI over time. Stimulus-evoked fMRI (events or blocks related) remain the major component within animal literature. From 2006 and 2010, resting-state fMRI and opto- / chemogenetics fMRI, respectively, have represented an increasing proportion of the animal fMRI studies.

3.1.1 Stimulus-evoked fMRI

In animal studies, stimulus-evoked fMRI usually refers to externally-applied stimuli during fMRI (e.g. electrical forepaw stimulation), but many principles of study design can be applied to internally delivered stimuli as well, such as with deep-brain stimulation (DBS) and optogenetics. Stimuli can be applied in a block or event-related design. The former alternates between regular stimulation and no-stimulation conditions, while the latter uses brief stimuli presented at varying intervals (Amaro and Barker, 2006). Block designs are best suited to test frequency-related responses and enhance detection power, while event-related designs are best for determining accurate response-time courses and/or frequency-independent functional connectivity (Allen et al., 2015; Amaro and Barker, 2006; Maus and van Breukelen, 2013; Schlegel et al., 2015; Soares et al., 2016; Van der Linden et al., 2007).

Stimulus frequency has a large influence on stimulus-evoked fMRI results. In general, higher frequencies will increase the stimulus input per unit time, thus potentially boosting signal and ability to detect evoked responses (Amaro and Barker, 2006; Kim et al., 2010; Maus and van Breukelen, 2013), but excessive electrical or optical stimulation can cause tissue damage (Acker et al., 2016; Cogan et al., 2016; Kiyatkin, 2007; Lai et al., 2015), heating and related artefacts (Acker et al., 2016; Cardin et al., 2010; Christie et al., 2013; Kiyatkin, 2007; Lai et al., 2015; Stujenske et al., 2015; Zeuthen, 1978), and nonspecific effects (Christie et al., 2013; Rungta et al., 2017; Schlegel et al., 2015; Schroeter et al., 2014; Shih et al., 2014; Tuor et al., 2002). Stimuli may also change basic physiology and therefore alter the fMRI response (Li et al., 2013; Ray et al., 2011; Reimann et al., 2018a; Schroeter et al., 2014; Shih et al., 2014; Tsubota et al., 2012; Tuor et al., 2002), thereby occluding signal from the stimulus itself. These findings highlight the importance of carefully monitoring physiology (see below) and establishing frequency-response curves for the stimuli of choice.

3.1.2 Functional connectivity MRI

Animal fMRI data acquired in the absence of stimulation or modulation, RS-FC, is commonly used to probe synchronization of spontaneously fluctuating signals between combinations of anatomically, functionally, or procedurally defined brain regions (Grandjean et al., 2019a; Guadagno et al., 2018; Lowe et al., 2000; Lu et al., 2007; Lu and Stein, 2014; Pan et al., 2015; van Meer et al., 2010, 2012; Zhao et al., 2008). The use of RS-FC in animal models has rapidly increased over the past decade (**Figure 2**). To collect the most robust and interpretable RS-FC data, a few principles have been proposed. Recent evidence suggests that brain network components may undergo constant dynamic reorganization over several seconds, (Gutierrez-Barragan et al.; Hutchison et al., 2013a; Keilholz et al., 2013; Liang et al., 2015a; Liu and Duyn, 2013; Pan et al., 2015), therefore repetition time should be sufficiently short (e.g. 1 second) to detect these changes, and scan length should produce enough frames (a minimum of about 300) to account for a large number of temporal clusters (Hutchison et al., 2013b; Jonckers et al., 2015; Majeed et al., 2011). Furthermore, if brain modulation/stimulation is included, additional time should be added during the transition periods to and from resting-state to allow for stable connectivity, and subsequent resting periods following each manipulation should be grouped separately to account for potential neuroadaptations (Albaugh et al., 2016; Chan et al., 2017; Chen et al., 2018; Decot et al., 2017; Jonckers et al., 2015; Pawela et al., 2008; Zhao et al., 2008). Importantly, due to the nature of the signal fluctuations on which RS-FC relies, special care must be ensured with regard to physiology and anaesthesia to ensure maximal detection. The effects of animal preparations are further discussed below.

3.1.3 Optogenetics.

Many recent stimulus-evoked animal fMRI studies take advantage of the readily MR-compatible optogenetics toolkit (**Figure 2**) (Abe et al., 2012; Albaugh et al., 2016; Albers et al., 2018; Brocka et al., 2018; Chai et al., 2016; Choe et al., 2018; Desai et al., 2011; Grandjean et al., 2019b; Hinz et al., 2017; Iordanova et al., 2015; Kahn et al., 2013; Lemieux et al., 2015; Leong et al., 2018; Liang et al., 2015b; Lohani et al., 2017; Ryali et al., 2016; Scott and Murphy, 2012; Takata et al., 2015; Weitz et al., 2015; Yu et al., 2016). Optogenetics allows for robust stimulation of specific cellular and/or anatomical populations (Boyden, 2015; Deisseroth, 2015; Fenno et al., 2011; Griessner et al., 2018; Zhang et al., 2010), but despite these advantages this relatively new technique adds layers of complexity over DBS, thereby requiring more rigorous methodology and additional controls.

The light-activated channels/pumps expressed in optogenetics, also known as ‘opsins’, provide a great deal of experimental flexibility (Deisseroth, 2015; Fenno et al., 2011; Guru et al., 2015). There are several opsins to choose from for optical excitation of cells, including the commonly used ChR2 (Atasoy et al., 2008; Boyden et al., 2005; Cardin et al., 2010; Nagel et al., 2003; Zhang et al., 2006) variants activated by penetrating red- shifted light (Klapoetke et al., 2014; Lin et al., 2013; Zhang et al., 2008) and ultra-fast variants capable of frequencies up to 200 Hz (Gunaydin et al., 2010; Hight et al., 2015; Lin et al., 2009). If stable excitation over even longer periods is required in fMRI, issues with a continuous light application can be avoided by using step-function opsins which are temporarily activated by a single pulse of light (Berndt et al., 2009; Ferenczi et al., 2016). Notably, there are also several opsins for cellular inhibition (Berndt et al., 2014; Chuong et al., 2014; Zhang et al., 2007), but their application for fMRI is limited as they require longer periods of illumination prone to heat-related artefacts, and anaesthetized or sedated animals have low baseline levels of activity (Brevard et al., 2003; Lahti et al., 1999; Sicard et al., 2003).

Injection of viral constructs or expression of foreign genes can potentially change brain function (Klein et al., 2006; Lin, 2011; Liu et al., 1999; Miyashita et al., 2013; Zimmermann et al., 2008), and light can induce heating and related MRI artefacts, tissue damage, and nonspecific effects (Christie et al., 2013; Elias et al., 1987; Rungta et al., 2017; Schmid et al., 2016; Stujenske et al., 2015) thus it is critical to characterize opsin expression and activation of the light source with light delivery to empty-vector (e.g. EYFP) controls. It follows that histological confirmation of fibre placement and construct co-localization with targeted promoters is required (Allen et al., 2015; Bernstein and Boyden, 2011; Decot et al., 2017; Gompf et al., 2015; Lin et al., 2016; Madisen et al., 2012; Witten et al., 2011; Zeng and Madisen, 2012). In addition, given the spatial nature of fMRI, the reporting of single-point measurements of light power should be avoided in favour of irradiance (mW/mm^2 ; (Aravanis et al., 2007; Huber et al., 2008; Kahn et al., 2011; Schmid et al., 2017; Yizhar et al., 2011)). Finally, light stimulation at frequencies at or below 20 Hz can produce a visual response by activating the visual-related network, requiring light masking or careful control comparison to view experimental effects (Decot et al., 2017; Ferenczi et al., 2016; Lin et al., 2016; Schmid et al., 2017).

3.1.4 Chemogenetics

Chemogenetics, initially termed “pharmacogenetics”, utilizes pharmacologically-inert ligands to stimulate genetically-encoded designer receptors, with the aim to produce drug-like sustained activation or inhibition of specific neuronal populations. Initial attempts to combine this approach with fMRI have involved the regional re-expression of pharmacologically targetable endogenous G-coupled protein receptors (e.g. Htr1a, (Gozzi et al., 2012)). The recent development of a modular set of evolved G protein-coupled receptors, termed Designer Receptors Exclusively Activated by Designer Drugs (DREADDs) has greatly expanded the capabilities of this approach (Aldrin-Kirk et al., 2018; Alexander et al., 2009; Armbruster et al., 2007; English and Roth, 2015; Lee et al., 2014; Roth, 2016; Sciolino et al., 2016; Smith et al., 2016; Zhu et al., 2016). Like optogenetics, chemogenetics is readily MRI compatible (Chen et al., 2018; Giorgi et al., 2017; Griessner et al., 2018; Markicevic et al.; Roelofs et al., 2017). Despite its potential, there is however an ongoing debate about the specificity of chemogenetics ligands both in neurobehavioural studies, (Gomez et al., 2017; MacLaren et al., 2016; Mahler and Aston-Jones, 2018; Manvich et al., 2018) and in chemo-fMRI applications (Giorgi et al., 2017), thereby requiring rigorous methodology to control for potential off-target effects.

Both hM3Dq and hM4Di DREADDs are classically activated with infusion of the effector clozapine-N-oxide (CNO; (Alexander et al., 2009; Armbruster et al., 2007; Giorgi et al., 2017; Markicevic et al. 2018; Roth, 2016; Smith et al., 2016), but new evidence suggests that CNO does not cross the blood-brain barrier and instead is back-metabolized *in-vivo* into its precursor, clozapine (Gomez et al., 2017; Mahler and Aston- Jones, 2018; Manvich et al., 2018). Importantly, unlike CNO, clozapine is a psychoactive drug, that possesses an affinity for many endogenous receptors. As a result, the use of high CNO doses may result in a plethora of undesirable off-target effects (Ashby and Wang, 1996; MacLaren et al., 2016; Roth, 2016; Selent et al., 2008), including unspecific fMRI response (Giorgi et al., 2017). Overall, it is apparent that chemogenetics effects cannot be interpreted without proper non-DREADD expressing controls. Specifically, the effect of effector administration should be compared between DREADD expressing, and non-DREADD expressing animals and/or hemispheres. Finally, as with optogenetics, validation of DREADD expression and co-localization with target promoters is essential for data interpretation (Aldrin-Kirk et al., 2018; Chen et al., 2018; Farrell et al., 2013; Giorgi et al., 2017; Gomez et al., 2017; Markicevic et al. 2018; Roelofs et al., 2017; Smith et al., 2016).

3.1.5 Pharmacological fMRI

Modulating the brain with pharmacological agents during animal fMRI has a wide variety of traditional applications such as studying the global effects of compounds and their target neurotransmitter systems (Ferrari et al., 2012; Jonckers et al., 2015; Mueggler et al., 2001; Razoux et al., 2013; Shah et al., 2004; van der Marel et al., 2013). This approach does not require surgical methods, and is apt for identifying global or regional changes in function associated with new or existing drug therapies for neurotransmitter-related brain disorders (Bifone and Gozzi, 2012; Canese et al., 2011; Klomp et al., 2012; Leslie and James, 2000; Martin and Sibson, 2008; Medhi et al., 2014; Minzenberg, 2012), or to map the effect of exogenously administered neuromodulators. In addition, pharmacological challenges can be used to probe how targets and neurotransmitter systems modulate BOLD responses evoked by other stimuli or pharmacological agents (Bruinsma et al., 2018; Decot et al., 2017; Griessner et al., 2018; Hess et al., 2007; Knabl et al., 2008; Marota et al., 2000; Rauch et al., 2008; Schwarz et al., 2007; Shah et al., 2016; Shih et al., 2012a; Squillace et al., 2014). However, functional imaging with pharmacological agents may not be ideal for dynamic or repetitive studies as effects are dependent on diffusion and receptor kinetics (Bruinsma et al., 2018; Ferris et al., 2006; Mandeville et al., 2013; Steward et al., 2005), and subject to receptor desensitization and downregulation (Arey, 2014; Berg and Clarke, 2018; Chen et al., 1999); which in some instances may be species-specific (Knabl et al., 2008).

It is important to consider dose-response effects and the pharmacokinetics of each drug used in the experimental design. Ideally several doses of drug, and sufficiently long time series should be included in order to interpret the results according to dose-response and absorption/elimination functions (Bruinsma et al., 2018; Ferris et al., 2006; Jenkins, 2012; Jonckers et al., 2015; Leslie and James, 2000; Marota et al., 2000; Minzenberg, 2012; Mueggler et al., 2001; Rauch et al., 2008; Shah et al., 2015; Steward et al., 2005). Indeed, many pharmacological agents have known systemic effects which can influence animal physiology and the BOLD signal (Ferrari et al., 2012; Klomp et al., 2012; Martin and Sibson, 2008; Shah et al., 2004; Wang et al., 2006), and some drugs have direct effects on the vascular endothelium in the brain, which could alter properties of the hemodynamic response (Gozzi et al., 2007; Luo et al., 2003; Shih et al., 2012b).

It is imperative to closely control and monitor animal physiology, and use appropriate doses in order to control for unwanted side effects. Importantly, vehicle controls are necessary for any pharmacological fMRI study, as increased blood flow/volume and increased blood pressure from systemic infusions can alter the MRI signal (Gozzi et al., 2007; Kalisch et al., 2001; Reimann et al., 2018b; Tuor et al., 2002).

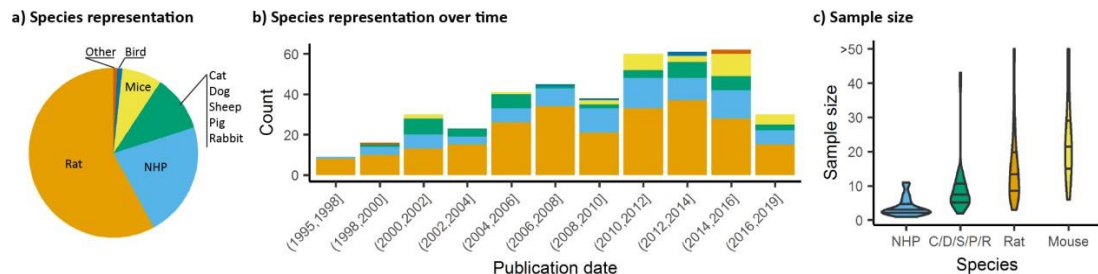


Figure 3 | Species distribution and sample size. A) Animal representation in the documented studies. B) Animal species occurrence in the literature over time. Rats and non-human primate (NHP) represent the major species used, however, since 2008, mice have been used in a growing proportion of animal fMRI studies. C) Number of animals used per fMRI study irrespective of the number of groups or classes. NHP studies are carried out with fewer animals (Percentiles 25, 50, 75 = [2, 3, 5]), whereas studies involving mice involved larger number of animals (Percentiles 25, 50, 75 = [17, 24, 34]).

3.2 Species, sample size, and gender distribution

We assessed studies performed using animals, i.e. all species except homo sapiens. The rat and specifically the Sprague-Dawley strain was the most common species and strain used in fMRI studies, representing 55% of the total studies considered presently (**Figure 3ab**). Non-human primate (NHP) studies were second and mostly relied on the macaques (23%). Studies involving medium-sized domestic mammals (cats, dogs, sheep, pigs, and rabbits) presented 9% of the total literature considered. Studies on males (54%) had a higher incidence than studies in females (14%). A sizable number of studies (22%) omitted to specify the gender. This gender bias reflects a greater trend found throughout neuroscience and other biomedical disciplines (Beery and Zucker, 2011) and should require a greater consideration within the animal neuroimaging community. Finally, the total number of animals was assessed within the studies considered. It should be noted that this was done irrespective of the number of groups. There, we found that nearly half the studies were carried out on ten or fewer subjects (**Figure 3c**). This was particularly marked in studies with NHP (Percentiles 25, 50, 75 = [2, 3, 5]). While sample size depends on the goals of each study and appropriate power calculation, it remains unclear how group sizes were determined in most of these studies. The small group sizes reported here are consistent with general trends in neuroscience toward underpowered studies.

Button et al. estimated that the median power level in neuroscience was at 21% (Button et al., 2013). Hence these trends need to be carefully taken into consideration in the initial stages of study design so that the required animals are used to their full potential.

The wide range of experimental animals available for research offers unique opportunities to study evolutionary trends on distributed neuronal networks. To date, however, interspecies comparisons have remained a difficult task. fMRI has provided numerous descriptions of the network organization in mammals. Specifically, RSNs have been mainly studied in mammals to develop translational models of human diseases and to understand the mechanisms underlying their functional alterations. RSNs' organization has been described in numerous mammalian

species (usually under anesthesia) including rodents (Grandjean et al., 2017b; Hutchison et al., 2010; Jonckers et al., 2011; Sforazzini et al., 2014), ferrets (Zhou et al., 2016), rabbits (Schroeder et al., 2016), dogs (Kyathanahally et al., 2015), prairie vole (Ortiz et al., 2018), and NHP (Belcher et al., 2013; Hutchison et al., 2010; Mantini et al., 2011; Vincent et al., 2007). Particularly active at rest, one of the most widely investigated networks is the DMN (Hampson et al., 2006; Tambini et al., 2010). This network comprises distributed polymodal cortices that are thought to be involved in memory consolidation and higher cognitive functions. Homologues of the human DMN (Raichle et al., 2001) have been identified in a variety of species including NHP (Mantini et al., 2011; Vincent et al., 2007), rats (Lu et al., 2012), mice (Sforazzini et al., 2014; Stafford et al., 2014) and rabbits (Schroeder et al., 2016). The hypothesis of two separated DMNs (anterior and a posterior) has been evoked in dogs (Kyathanahally et al., 2015) and ferrets (Zhou et al., 2016).

The description of each species' functional architectures has been based on a variety of acquisitions, analyses, and anaesthesia or awake protocols. This lack of interspecies standardization is often justified by the variety of brain sizes, different response to anaesthesia, and anatomical organizations observed within mammals. Throughout evolution, brain regions could have duplicated, fused, reorganized or expanded (Hutchison and Everling, 2012). A few studies have compared the connectivity between different species and with similar approaches. Using ICA, Jonckers et al. found that the extracted components, i.e. functional network regions, were more unilateral in mice compared to rats (Jonckers et al., 2011), however this effect failed to be replicated in numerous follow-up studies in mice, e.g. (Grandjean et al., 2014; Sforazzini et al., 2014). In mouse lemur primates and humans, the cortical large-scale networks repertoire presents important similarities but the regional organization into networks highlighted compositional and structural divergences (Garin et al., 2019). Strong interhemispheric functional connectivity (FC) between homotopic regions has been consistently observed in humans and primates suggesting a phylogenetically preserved mammalian characteristic (Hutchison and Everling, 2012). However, lateralized networks (*i.e.* fronto-parietal resting- state network) remain a phenomenon which has only been demonstrated in humans. According to the few comparative studies on mammals functional organization, humans seem to display the strongest variety of functional networks. The complexity and diversity of the animal behaviours are probably related to this large repertoire of networks. This complexity is also reflected by the white matter fibre tracts network (Nadkarni et al., 2018). Moreover, direct evidence is in favour of a close relationship between the structural and functional organization in humans (Damoiseaux and Greicius, 2009), in primates (Miranda-Dominguez et al., 2014) and in mice (Grandjean et al., 2017b; Stafford et al., 2014). However, a recent systematic review showed that structure-function correlations in mammalian brains depend on the connectivity measures, which differ across methods and scales (Straathof et al., 2019). The structure-function correspondence observed in multiple species is an important step in favour of the neural origin underlying the BOLD signal and provides a key to understanding neural network development through the evolution of complex brain structure.

Other universal properties of the brain topology have also emerged recently with graph analysis. One of them is the small-world feature which maximizes the efficiency of information transferred within a network. This network property has been found in multiple species including humans (Bullmore and Sporns, 2009), NHP (Barttfeld et al., 2015; Garin et al., 2019), rodents (Mechling et al., 2014) and ferrets (Zhou et al., 2016).

Moreover, graph-based approaches have clearly revealed a modular nature of human (Sporns and Betzel, 2016), and rodent (Liska et al., 2015) rsfMRI networks, along with evidence of strongly

functionally interconnected polymodal areas, exhibiting hub-like properties (Buckner et al., 2009; Liska et al., 2015). Concerning highly connected regions in human, macaque and mouse lemur, the posterior cingulate cortex was found to be critical in these three species with its major functional hubs located in the DMN (Garin et al., 2019). Interestingly, these areas seem to be instead shifted anteriorly in rodents, in which the anterior cingulate and prefrontal areas exhibit robust hub-like properties (Garin et al., 2019; Gozzi and Schwarz, 2016; Liska et al., 2015). This finding is consistent with rodent species lacking an evolutionary homologue of the primate posterior cingulate cortex (Vogt and Paxinos, 2014). Determining the fine-grained topology and contribution of regions critical for network organization and stability across species and evolution could highlight functional patterns that are especially relevant for network stability. Despite the lack of consensus concerning a standardized methodology in mammals fMRI, cross-species studies could provide essential clues towards a better understanding of brain physiology and evolution.

3.3 Animal preparation and anaesthesia

3.3.1 Animal preparation impact on motion and stress

Functional MRI traditionally relies on temporal changes in haemodynamic parameters, e.g. blood oxygenation level-dependent contrast (BOLD), cerebral blood volume (CBV), or cerebral blood flow (CBF). Functional MRI signals inform on neuronal activity through the evaluation of hemodynamic response *i.e.* the adaptability of local capillaries to deliver oxygen to active neurons at a greater rate than to inactive neurons. BOLD signal, the most commonly used fMRI parameter, is dependent on the relative levels of oxyhemoglobin and deoxyhemoglobin (oxygenated or deoxygenated blood), which is modulated by local blood volumes and flow. In addition, fMRI acquisitions are highly sensitive to subject movement, specifically at tissue boundaries. In humans, several studies showed that small head motions can produce spurious but spatially structured patterns which drastically impacts RS-FC (Power et al., 2014).

In animals, as well, it is critical to control for head motion. As animals are non-compliant species, the most widely used method to control for head stability is to anaesthetize the animals and to stabilize the head with bite bar and ear bars (78%, **Figure 4a**). However, training for awake restraint techniques has been developed in rodents and primates (22%, **Figure 4a**). These procedures may include acclimation in a scanner environment with an increase of the exposure periods of time. Atraumatic devices such as cylindrical head- holder or flat ear bars can be used to fix the head (Liang et al., 2011). Moreover, head fixes attached to the skull with dental cement provide alternatives that do not require lengthy animal training (Yoshida et al., 2016). In primates, individualized plastic helmets have been constructed based on 3D anatomical images for better stabilization of the head (Belcher et al., 2013). The quality of the mechanical set-up to fix the head is critical: according to Kalthoff et al. (Kalthoff et al., 2011), even with carefully fixed heads, motion remains the main source of noise in rat fMRI at 11.75T and it contributes to 30% of the non-neuronal signal variance (60% being attributed to residual noise). This residual motion is related to respiration that represents 5% of the total variance of RS-FC signal (Kalthoff et al., 2011). It can be minimized by artificially-ventilating and paralyzing the animal, a process that results in excellent control of the motion artefacts (Ferrari et al., 2012). Beyond motion, either spontaneous or related to ventilation, cardiac motion induces low-frequency BOLD fluctuations and is another source of noise for fMRI signal interpretation (Murphy et al., 2013). In

some instances, cardiac responses can eclipse the neuronal response, especially in response to potentially stressful stimuli (Schroeter et al., 2014). Hence decisions to mitigate these strong confounding sources and variations between laboratories remain a major obstacle toward the standardization in animal imaging protocols, decisively more so than in human corresponding experiments.

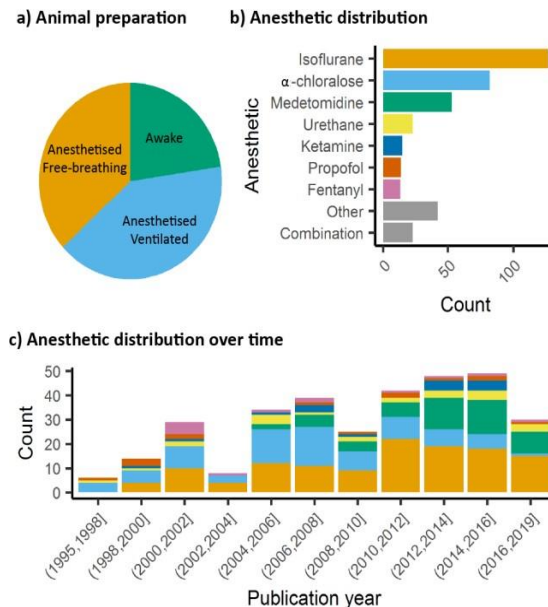


Figure 4 | Animal preparation and anaesthesia trends. A) Animal fMRI relies mainly on anaesthesia to help restrain animals. NHP remain the major species acclimated to awake fMRI. B) Isoflurane is the principal anaesthetic used for maintenance during fMRI recordings. However, the distribution of other agents change with species c) Medetomidine is growing to become the second most used agent behind isoflurane.

3.3.2 Impact of anaesthesia on animal physiology

The global BOLD signal is modulated by heart rate, arterial CO₂ concentration, and temperature. Different anaesthetics modulate various targets in the brain and have different impact on peripheral receptors acting on respiratory or cardiac regulation. Thus, they have different impact on BOLD signal and other haemodynamic readouts. For example, mechanically ventilated rats, for which arterial blood gases (PaCO₂, PaO₂) and pH were maintained constant, showed decreased T2* contrast between veins and parenchyma when anaesthetized with isoflurane 2% as compared to medetomidine or ketamine/xylazine. This was explained by increased CBF and vasodilatation in animals under isoflurane (Ciobanu et al., 2012). The use of mechanical ventilation has the advantage of avoiding hypercapnia (increased paCO₂) which has an impact on fMRI reproducibility (Biswal et al., 1997; Ramos-Cabrer et al., 2005). Hypercapnia also leads to vasodilation and increased CBF (Xu et al., 2011). The modulation of CBF could explain the decrease of the BOLD response specificity to neuronal activity induced by stimuli (Uhrig et al., 2018). Interestingly, Uhrig et al. showed different impacts of various anaesthetics on blood oxygenation in different brain regions. For example, ketamine leads to higher oxygenation in the cortex as compared to the thalamus while the opposite occurs for propofol (Uhrig et al., 2014). This variability may affect the ability to detect networks connecting these regions. The impact of anaesthesia on other physiological parameters, such as body temperature and peripheral cardiovascular activity can modulate the quality of the measured functional connectivity. Both these parameters represent strong benefits to be registered and kept stable to assure normal physiological conditions during the acquisition. The body temperature is usually controlled with a heating cradle, pad or any additional heating system, leading to stable reported temperatures. In light of the above, controlling for the temperature, the paCO₂ and the movement parameters remains essential in assuring the animal stability and the quality of the data. Finally, anaesthesia

can tightly impact CBF autoregulation in response to peripheral blood pressure changes (Gozzi et al., 2007). Peripheral blood pressure recordings, and the presence of autoregulation, are parameters of critical importance for studies of neuromodulation using drugs, optogenetics and/or chemogenetics-fMRI e.g. (Giorgi et al., 2017), as well as in the case of somatosensory stimulation (Schroeter et al., 2014). This is because transmitter-induced peripherally evoked blood pressure changes, in the absence of physiological CBF autoregulation, can give rise to seemingly regionalized fMRI responses (Gozzi et al., 2007; Reimann et al., 2018b). Future research is required to understand to which extent commonly used anaesthetic regimens in rodents do preserve CBF autoregulation. While technically challenging, and invasive, blood pressure recordings can be carried out via femoral arterial cannulation (Ferrari et al., 2015), hence making it possible to understand whether peripheral cardiovascular response and central fMRI activity are temporally correlated.

Several anaesthetics are used for animal studies (**Figure 4b**). They have been classified into several classes according to their targets: GABAA receptors, NMDA receptors, two-pore-domain K^+ channels, and other modes of actions. GABAA receptors are the most widely used targets for anaesthetics. They are chloride channels that hyperpolarize neurons, making them less excitable and thus inhibiting the possibility of an action potential. Widely used anaesthetics as isoflurane, propofol and barbiturates are GABAA receptors agonists (Franks, 2008; Garcia et al., 2010). Each drug within this category displays a subtly unique pharmacological characteristic. For example, isoflurane and sevoflurane have opposite metabolic activities on cerebral blood flow and glucose consumption in various brain regions (Lenz et al., 1998). α -chloralose is widely used in the context of BOLD fMRI because it provides robust metabolic and hemodynamic responses to functional stimulation and is also expected to act on GABAA receptors (Garrett and Gan, 1998). NMDA receptors are other widely used targets. The use of antagonists for these receptors, such as ketamine, is supposed to block excitatory synaptic activity probably leading to anaesthesia. This latter may be related to the fact that ketamine binds preferentially to the NMDA receptors on GABAergic interneurons. Ketamine, however, leads to a "dissociative anaesthesia" during which the perception of pain is dissociated from the perception of noxious stimuli. Besides, it has psychotomimetic effects at low concentrations, leading to auditory and visual hallucinations (Franks, 2008). Ketamine and other NMDA antagonists increase regional brain activity and cerebral blood volume, mainly in the anterior cingulate, the thalamus, the putamen, and the frontal cortex (Bonhomme et al., 2012; Gozzi et al., 2008; Långsjö et al., 2003). Two-pore-domain K^+ channels are targeted by volatile anaesthetics (isoflurane, halothane, nitrous oxide) which have different affinities for subfamilies (TREK-1 or TASK) of these receptors (Patel et al., 1999). These channels modulate the potassium conductance that contributes to the resting membrane potential in neurons. Their opening, therefore, facilitates a hyperpolarizing current, which reduces neuronal excitability and anaesthetizes. Among other targets, α_2 -adrenergic receptor agonists are targeted by xylazine, medetomidine, dexmedetomidine (Sinclair, 2003). The activity of these drugs is related to their action on receptors located in the locus coeruleus and its projections. At this level, they reduce the release of norepinephrine, a neurotransmitter that is necessary for arousal. The anaesthesia induced by these compounds resembles the state of non-REM sleep, i.e. the first four of the five stages of the sleep cycle (Franks, 2008).

3.3.2 *Impact of anaesthetics on neuronal network organization in rodents*

In rodents, isoflurane and medetomidine are currently the most commonly used anaesthetics

(**Figure 4bc**). Importantly, isoflurane is almost systematically used for anaesthesia induction, specifically in rodents.

Variations in the induction time may lead to a lasting effect on brain function, even though anaesthesia is switched to another agent (Magnuson et al., 2014). In addition to their different mechanisms of action (GABAA receptors agonist for isoflurane and alpha2 adrenergic receptor agonists for medetomidine), they have opposite vaso-properties (vasodilatation for isoflurane and vasoconstriction for medetomidine) which could impact neurovascular coupling differently. In rodents, isoflurane seems to preserve the interhemispheric and cortico-cortical FC but only at low doses (~1%) (Bukhari et al., 2017; Grandjean et al., 2014; Uhrig et al., 2014; Wang et al., 2011). Medium to high doses induce burst-suppression effects which are reflected in an increase in the global signal (Grandjean et al., 2014; Liu et al., 2011, 2013).

Medetomidine seems to present opposite effects such as a cortico-cortical disruption and a pronounced striatal FC (Bukhari et al., 2017; Grandjean et al., 2014; Paasonen et al., 2018). The effect of isoflurane and medetomidine and other anaesthetics on the thalamo-cortical FC is still debated. Several studies suggested that a combination of isoflurane and medetomidine (med/iso) at low doses is the best compromise (**Table 1**, med/iso) to preserve FC and to recapitulate network properties of the awake state (Grandjean et al., 2014). However, this combination appears to inhibit thalamo-frontal cortical connectivity, when compared to connectomic estimates of the mouse connectome (Grandjean et al., 2017b). A number of studies in control and transgenic mouse models have been carried out with low doses of halothane (Bertero et al., 2018; Gutierrez-Barragan et al.; Liska et al., 2015, 2018; Pagani et al., 2019; Sforazzini et al., 2014). This inhalational anaesthetic produces stable and long-lasting RS-FC correlation recapitulating patterns of connectivity observed with med/iso combination (Grandjean et al., 2017b), with the advantage of robustly preserving thalamo-frontal connectivity, an effect that makes it especially apt for the investigation of prefrontal circuitry and the rodent default mode network (Bertero et al., 2018). However, the hepatotoxic properties of this compound have led its banning in most countries, preventing widespread use of this anaesthetic regimen. Other anaesthetics used in rodents (propofol, urethane, α -chloralose) are presented in **Table 1**. They are not further discussed here as they showed ambiguous effects on RS-FC and are no longer recommended. Notably, RSNs in mice were shown to converge in a multi-centre comparison (**Figure 1**) (Grandjean et al., 2019a), irrespective of anaesthesia regimen, indicating to some extent that network properties are retained between different conditions.

Anesthetics	Doses	Comparison	Effects	Studies	Species
isoflurane	1%	vs the awake state	preserve interhemispheric FC	(Jonckers et al., 2014)	Mice
		vs anesthetics	cortical and thalamo-cortical FC preserved but disruption of striatal FC	(Grandjean et al., 2014)	
			cortico-cortical FC preserved but disruption of thalamo-cortical FC	(Bukhari et al., 2017)	
	1% to 2%	increasing doses	disruption of interhemispheric FC with increasing doses	(Bukhari et al., 2018)	
	1.3%	vs the awake state	cortico-cortical and striatal FC increase	(Paasonen et al., 2018)	Rats
medetomidine	0.1 mg/kg	vs anesthetics	disruption of thalamo-cortical FC but pronounced striatal FC	(Grandjean et al., 2014)	Mice
			thalamo-cortical FC preserved but disruption cortico-cortical FC	(Bukhari et al., 2017)	Mice
		vs the awake state	cortico-cortical FC decreased	(Paasonen et al., 2018)	Rats
med/iso	0.05 mg/kg; 0.5%	vs anesthetics	preserved FC	(Grandjean et al., 2014)	Mice
				(Bukhari et al., 2017)	
	0.06 mg/kg; 0.5%	vs the awake state	thalamo-cortical and intra-subcortical FC decrease	(Paasonen et al., 2018)	Rats
urethane	2.5 g/kg	vs the awake state	disruption of interhemispheric FC	(Jonckers et al., 2014)	Mice
	1.5 g/kg	vs anesthetics	cortical and thalamo-cortical FC preserved but disruption of striatal FC	(Grandjean et al., 2014)	
	1.25 g/kg	vs the awake state	replication of the awake state	(Paasonen et al., 2018)	Rats
α -chloralose	120 mg/kg	vs the awake state	disruption of interhemispheric FC	(Jonckers et al., 2014)	Mice
	60 mg/kg	vs the awake state	cortico-cortical FC suppression	(Paasonen et al., 2018)	Rats

Table 1 | Anesthetics effects on functional connectivity in rodents. Review of five studies between 2014 and 2018.

3.3.3 Impact of anaesthetics on neuronal network organization in primates

In primates, isoflurane is the most used anaesthetic (Grayson et al., 2016; Hutchison et al., 2013b; Miranda- Dominguez et al., 2014; Vincent et al., 2007). As in rodents, lower dose and shorter anaesthesia duration are associated with an increased ability to detect RS-FC (**Table 2**; (Barttfeld et al., 2015; Uhrig et al., 2018).

Also, one should keep in mind that a direct comparison of the impact of anaesthetics on cerebral networks is difficult because anaesthesia depth also modulates networks and can lead to misinterpretation of the results.

Anesthetics	Doses	Comparison	Effects	Studies	Species
isoflurane	1% to 2.75%	increasing doses	disruption of interhemispheric FC after 1.5%	(Hutchison et al., 2014)	Macaca fascicularis
	0.89% to 1.19%	duration effect	reduction of the DMN FC with a prolonged administration	(Li & Zhang, 2018)	Macaca mulatta
ketamine	20 mg/kg	vs the awake state	preservation of positive FC but average positive FC reduced	(Uhrig et al., 2018)	Macaca mulatta
sevoflurane	2.2 to 4.4 vol%	vs the awake state	average positive FC reduced	(Uhrig et al., 2018)	Macaca mulatta

Table 2 | Anesthetics effects on functional connectivity in primates. Review of five studies between 2014 and 2018.

3.4 Data acquisition

Contrary to human fMRI, which is carried mostly at 1.5T, 3T, and in rarer cases at 7T, animal fMRI is carried at a variety of field strengths, with 7T and 9.4T being the most frequently encountered field strength (26% and 25% respectively, **Figure 5a**). The availability of ultra-high field strength small-bore systems in rodents further increase this range, with fMRI being recorded as high as 15.2T (Jung et al., 2019). While fewer animal MRI system vendors exist compared to human systems, this apparent similarity is compounded with a greater range of coil designs, including home-made coils or cryogenic coils (Baltes et al., 2011), which provide an additional source of variation among the animal studies. Whilst these factors are determined by the centre where the acquisitions are performed, even greater variability comes in in the form of sequence parameters and the resulting contrasts across the different studies. This is exemplified in a report by Grandjean et al. which indicated cortical signal-to-noise ratios ranging from 20 to 400 in mice fMRI acquired at different centres (Grandjean et al., 2019a).

a) Field strength over time

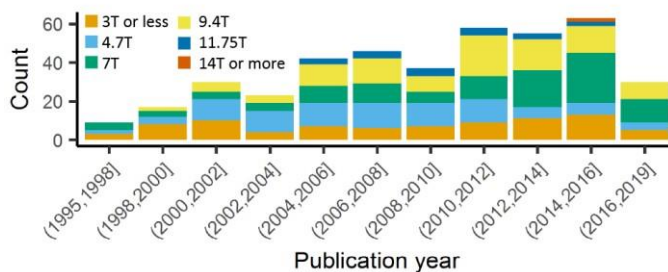
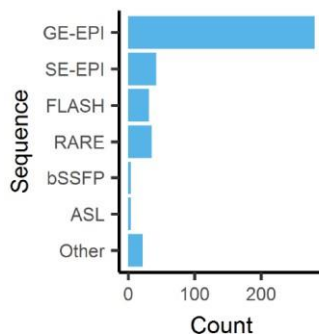
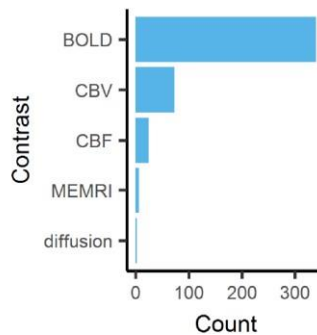


Figure 5 | Data acquisition. a) There is a general trend toward higher strength of the main magnetic field in animal fMRI over time. In the past decade, the majority of studies were performed on 7T and 9.4T systems. b) The acquisitions relied mainly on gradient echo EPI for the acquisition, while older studies either used FLASH or RARE sequences. c) BOLD is the most commonly used contrast in animal studies. The availability of iron nanoparticles in animal studies explains the relatively high incidence of CBV contrasts.

b) Sequence



c) Contrast



Neuronal activity induces vasodilation in surrounding capillaries and arterioles, which may propagate further up- and downstream towards arteries and draining veins. The resulting increase in CBF and CBV and blood oxygenation forms the basis of imaging strategies for fMRI. The most commonly used fMRI method is based on the BOLD contrast (Ogawa et al., 1990). BOLD contrast results from the paramagnetic properties of deoxyhemoglobin, which causes magnetic susceptibility effects inside blood vessels as well as in their surrounding tissue that can be detected with T2- or T2*-weighted sequences (Kim and Ogawa, 2012; Norris, 2006). Deoxyhemoglobin concentration increases dramatically from the arterial (<5%) to the venous side (~40%) of the vascular tree due to the extraction of oxygen in the capillaries (Vovenko and Sokolova, 1998), which makes BOLD imaging particularly sensitive to capillaries, venules and veins. In healthy brain tissue, the neuronal activity typically induces an increase in CBF with resultant increased oxygen delivery that exceeds the decrease in oxygen due to capillary oxygen extraction. As a result, deoxyhemoglobin concentration in the capillaries and veins decreases,

giving rise to a positive BOLD response in T2- or T2*- weighted images.

The most frequently used BOLD-weighted fMRI sequence in rodents is T2*-weighted gradient echo (GE) echo planar imaging (EPI) (**Figure 5b**). GE-EPI provides a relatively high contrast-to-noise ratio (CNR), which increases with field strength. At field strengths $\geq 7\text{T}$, the intravascular contribution to the GE BOLD signal is negligible and signal changes scale almost linearly with echo time (TE) (Han et al., 2019; Yacoub et al., 2003). For optimal BOLD CNR, TE is typically set equal to the average grey matter tissue T2* value (for an overview of brain tissue T2 and T2* values we refer to (Han et al., 2019; Uludağ et al., 2009)). The disadvantage of using GE-EPI for rodent fMRI, however, is its sensitivity to susceptibility artefacts, which are most prominent near air cavities such as the ear canals and around the olfactory bulb, particularly at long TE and high field strength. Furthermore, GE-EPI is highly sensitive to large veins (Uludağ et al., 2009), which makes this sequence spatially non-specific as neurovascular coupling occurs at the level of the capillaries. This has been clearly demonstrated by fMRI studies in rats subjected to electrical stimulation of the forepaws, where the highest GE-EPI BOLD response is observed in the outer layer of the somatosensory cortex where pial vessels are located (Han et al., 2019; Mandeville and Marota, 1999), while neuronal activation mostly occurs in deeper cortical layers. The relative contribution of capillaries to the BOLD signal increases with field strength but remains dominated by the macrovasculature even at 15.2T (Han et al., 2019).

Spatial specificity for neuronal activity can be increased by using spin-echo (SE) EPI for BOLD fMRI (Han et al., 2019; Norris, 2012). SE BOLD is particularly sensitive to small vessels, as signal around large vessels is largely refocused by the 180° pulse. The relative contribution of the microvasculature increases with field strength and TE, and may be further increased by introducing diffusion gradients that reduce the remaining intravascular contribution from large vessels (Kim and Ogawa, 2012). To maintain spatial specificity, EPI train length should be reduced to a minimum to avoid introducing T2* effects (Goense and Logothetis, 2006). In the absence of intravascular contributions to the SE BOLD signal, CNR increases almost linearly with TE, achieving the best contrast when TE equals grey matter tissue T2. SE-EPI images show reduced sensitivity to susceptibility artefacts compared to GE-EPI. However, SE-EPI also comes with lower BOLD CNR, and longer acquisition times.

Since BOLD contrast depends on the TE of the sequence, multi-echo GE sequences have been proposed for BOLD fMRI data acquisition. In multi-echo EPI (ME-EPI), one excitation pulse is followed by acquisition at multiple TEs (Speck and Hennig, 1998). Short TE results in high signal intensity, minimal signal dropout but low CNR, whereas longer TE results in lower signal intensities, more signal dropout but higher CNR. The multi-echo approach has two main applications. First, images acquired at different TE can be combined to optimize the BOLD contrast per region (Poser et al., 2006; Posse et al., 1999), since T2* varies across the brain (Hagberg et al., 2002; Peters et al., 2007). Second, identifying TE-dependent and TE-independent signals can help to separate BOLD T2* signal fluctuations and noise (Kundu et al., 2012). The shortened T2* at high field strength, often used for preclinical imaging, provides less time for image acquisition at additional TEs and limits the time between adjacent TEs. Still, ME-EPI at three different TEs without acceleration is feasible for fMRI in rodents at 9.4T and 11.7T, with a TR of 1.5 to 3 seconds and acceptable spatial resolution (Grandjean et al., 2017a, 2017b; Kundu et al., 2014).

Beside EPI, the balanced steady-state free precession (bSSFP) sequence enables acquiring

BOLD-like contrast images at short TE ($= TR/2$), making these images relatively insensitive to signal dropouts and artefacts often seen in GE-EPI. The origin of the bSSFP contrast is however complex since it does not only depend on T1 and T2 but also on the flip angle, repetition time and off-resonance values (Miller, 2012).

Functional MRI using bSSFP sequences can be performed in the so-called transition-band or the pass-band (Miller 2012). Functional transition-band bSSFP is sensitive to alterations in voxel off-resonances induced by changes in deoxyhemoglobin concentration. At short TE it provides T2-weighted contrast (Scheffler et al., 2001), whereas at long TE the image contrast is mainly T2*-weighted (Miller et al., 2007). Larger signal increases in response to neuronal activation have been measured compared to GE-EPI (Miller et al., 2006; Scheffler et al., 2001). However, transition-band SSFP is also sensitive to field inhomogeneities due to its sensitivity to off-resonances, making whole-brain coverage from anterior to posterior difficult to achieve (Miller, 2012). Furthermore, it is sensitive to physiological and time-varying noise (Miller, 2012). Pass-band bSSFP has been more widely used for fMRI (Miller and Jezzard, 2008; Scheffler and Ehses, 2016). Similar to transition-band bSSFP, its contrast origin shifts from BOLD T2 effects at short TE to BOLD T2* effects at long TE. However, the pass-band SSFP sequence is less sensitive to field inhomogeneities, and sensitivity to physiological noise can be lower than with GE-EPI (Miller et al., 2007). At short TE, an additional advantage is the suppression of BOLD sensitivity in large draining veins, making the sequence more selective to microvasculature contribution compared to GE-EPI (Báez-Yáñez et al., 2017). However, bSSFP sequences have lower BOLD CNR than conventional GE-EPI at short TE (Miller et al., 2007; Zhong et al., 2007), and at long TE, banding-artefacts appear due to field inhomogeneities and macrovascular contributions increase. Consequently, the use of this sequence has so far remained marginal (**Figure 5b**).

Although BOLD contrast is mostly used for fMRI, alternative methods that directly measure CBV or CBF, are available (**Figure 5c**). CBV can be measured with the use of exogenous iron oxide-based contrast agents (Chen et al., 2001; Mandeville et al., 1998). Iron oxide nanoparticles used for CBV contrast exhibit strong r_2 and r_2^* relaxivity, do not cross the intact blood-brain barrier, and have a long blood circulation half-life in the order of hours (Chen et al., 2001). Intravenous administration of nanoparticulate iron oxide introduces magnetic susceptibility effects within the vasculature and its surrounding tissue, which, at sufficiently high dose, are much larger than the effects of deoxyhemoglobin. As a result, intravascular T2*-weighted signal becomes negligible, while the extravascular T2*-weighted signal becomes highly sensitive to changes in CBV (Mandeville, 2012). An increase in CBV, as induced by neuronal activation, increases magnetic susceptibility within the imaging voxel, giving rise to negative CBV-dependent contrast in T2*-weighted images. CBV-dependent contrast is independent of field strength and most optimal when iron oxide injection causes a drop of 40-60% in signal intensity with respect to baseline (Mandeville, 2012). Since baseline signal intensity is strongly dependent on TE, contrast dose should be adjusted to the TE as well. A relatively high dose of contrast agent allows the use of short TE with the advantage of a reduction in susceptibility artefacts (Mandeville et al., 2004). The most commonly used imaging sequence for CBV contrast is GE-EPI, which, in contrast to BOLD GE-EPI, is particularly sensitive to changes in small vessels (arterioles, capillaries and venules). This, which is due to the strong magnetic susceptibility effects of the iron oxide, causes the extravascular signal from tissue surrounding large vessels to be largely eliminated. CBV-weighted fMRI is therefore considered more spatially specific to neuronal activity than GE BOLD fMRI. This has been clearly demonstrated in rats subjected to electrical forepaw, in which a spatial shift in the maximum contrast- to-noise ratio was observed

from the cortical surface with GE BOLD fMRI to deeper layers of the somatosensory cortex with GE CBV-weighted fMRI (Keilholz et al., 2006; Mandeville and Marota, 1999). SE-EPI is typically not used for CBV-weighted fMRI as CNR is lower than with GE-EPI, and CBV changes in small vessels are underestimated (Mandeville et al., 2007).

CBF can be measured non-invasively with Arterial Spin Labelling (ASL), which uses radiofrequency pulse (s) to magnetically label the blood water in major arteries by inverting the longitudinal magnetization (Williams et al., 1992). After a waiting period, the labelled blood water exchanges with brain tissue water, leading to T1 shortening in the imaging plane. Subtracting a second scan without labelling results in an image with only the signal from the labelled inflowing spins. There are two main types of ASL: continuous ASL (cASL) and pulsed ASL (pASL) (Borogovac and Asllani, 2012). cASL sequences include a long labelling pulse and provide high signal-to-noise ratio but low labelling efficiency. In comparison, pASL involves short inversion pulses with high labelling efficiency but low signal-to-noise ratio. A practical advantage of pASL is that short inversion pulses are more easily implemented in ASL protocols. To combine the higher labelling efficiency of pASL and higher sensitivity of cASL, pseudo-continuous ASL (pCASL) was developed (Borogovac and Asllani, 2012; Dai et al., 2008; Silva and Kim, 1999; Wu et al., 2007), and further optimized with multi-phase image acquisitions to tackle rodent-related difficulties with variations in labeling efficiency across different vessels to prevent erroneous calculation of CBF (Larkin et al., 2018). Since EPI is the main read-out for ASL, the presence of a BOLD effect should be taken into account in ASL-based fMRI studies (Lu et al., 2006). Compared to BOLD fMRI, ASL-based fMRI provides about one-third of the contrast-to-noise ratio (Lu et al., 2003), has low temporal resolution and is more challenging to implement (Dette and Wang, 2002). On the other hand, ASL provides stable noise levels - enabling measurement of slow variations in brain function (Aguirre et al., 2002; Wang et al., 2003) - shows less intersubject variability (Tjandra et al., 2005), and is more sensitive to arterioles and microvasculature than to large draining veins (Silva et al., 1999; Tjandra et al., 2005). By far the majority of rodent fMRI studies are executed with one of the abovementioned fMRI approaches that are based on the hemodynamic response to neuronal activation. Alternative fMRI methods aimed at more specific detection of neuronal responses have been developed, such as manganese-enhanced fMRI (Lin and Koretsky, 1997) and diffusion-weighted fMRI (Tsurugizawa et al., 2013) but these approaches have been hampered by non-uniform or limited sensitivity, low temporal resolution and uncertainties about the underlying mechanisms (Rudrapatna et al., 2012; Silva, 2012). Correspondingly, the application of these methods has so far remained marginal (**Figure 5c**). Recent developments in diffusion-weighted fMRI in rodents are likely to give rise to a renewed interest in the method (Abe et al., 2017; Nunes et al., 2019).

3.5 Data analysis

3.5.1 Pre-processing

Image pre- and post-processing are an integral part of every fMRI study. Pre-processing refers to a number of steps to correct for artefacts and normalize data, e.g. motion correction, temporal filtering and co-registration to a reference template. A number of dedicated software packages are designed, usually for human studies, to carry out these functions. With differences in the precision and performance of the various tools available, e.g. motion correction (Morgan et al., 2007) or registration (Klein et al., 2009), the user selection of tools within data analysis is a non-negligible source of bias and variability between studies. Interestingly, an analysis in human fMRI revealed that 223 unique analysis pipelines were used to process data in 241 studies, implying that nearly every study is carried out with an individualized pipeline (Carp, 2012). Efforts to develop unified open-source pre-processing pipelines for human fMRI, e.g. fMRIPrep (Esteban et al., 2019), have yet to reach widespread adoption. In animals, we observed that a large number of studies relied on custom made pre-processing functions (26%,

Figure 6a). SPM was the most common software package used for the analysis (27%). The preponderance of custom made software, as well as the combination of functions from several software suits in animal fMRI research, may be explained by the fact that specific functions were designed for the human brain. The pervasive use of *ad-hoc* pipelines, encouraged by the lack of dedicated animal pipelines, is a major obstacle to results comparisons between centres.

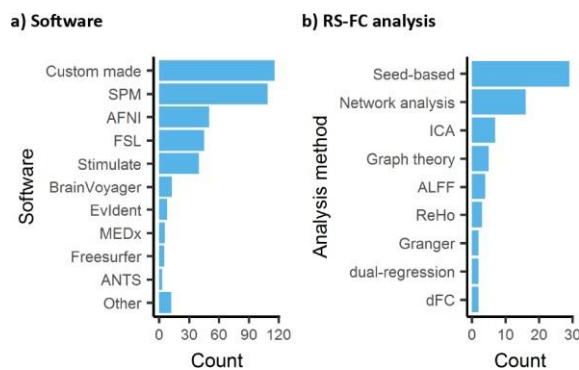


Figure 6 | Software used for data analysis of animal fMRI and functional connectivity analysis. a) Custom made software or combination of existing software pipelines remained the most common approach to animal fMRI data processing, while SPM was the most used software package used. b) Resting-state fMRI in animals is mainly analysed with seed-based analysis.

3.5.2 Templates and atlas selection.

Registration of fMRI results to a common reference space is an integral part of the pre-processing and enables unbiased group-level statistical analysis at a voxel-wise level. In human neuroimaging, standard space and coordinate systems are routinely used to report results in both figures and tables. In animals, we found that the vast majority of the studies did not register fMRI data to standard space (64%) while 24% relied on ad-hoc templates. While this step ensures optimal registration due to similar image contrast, resolution, and orientation, this adds extra challenges in comparing across studies. Contrary to the ubiquitous Montreal Neurological Institute reference space in human (Mazziotta et al., 2001), animal templates have failed to reach a consensus yet, despite efforts to implement standards such as the Waxholm space (Johnson et al., 2010). This is exemplified by the various templates used in animal studies. In rats, five studies relied on (Schweinhart et al., 2003), nine used (Schwarz et al., 2006), five used (Valdés-Hernández et al., 2011), and two used (Nie et al., 2013). In NHP, ten studies were normalized to (Van Essen et al., 2012), ten used (Saleem and Logothetis, 2012), six used (McLaren et al., 2009), and six normalized to (Rohlfing et al., 2012). In mice, seven studies were normalized to (Janke and Ullmann, 2015), four studies used (Lein et al., 2007), and two used (Dorr et al., 2008). More importantly, none of the studies reported three-dimensional coordinates for clusters or slice positions, rendering the precise comparison between studies impractical.

Registration between rodent or NHP brains is, however, a computationally much easier challenge than between human brains due to the simpler and less idiosyncratic cortical folding (NHP) or lissencephalic cortex (rodents). The choice of atlases and the level of parcellations also have large implications for network analysis and graph theory metrics (see below).

3.5.3 Regional and Network Level Analysis of resting-state fMRI.

Stimulus-evoked, pharmacological, DBS, and opto-/chemogenetics fMRI studies are almost systematically analysed with voxel-wise statistics where the time series at every voxel is assessed with an independent model, usually a model of the haemodynamic response to the stimulus/injection paradigms. This is often complemented with ROI analysis of the evoked

response. In comparison, RS-FC is paradigm free, hence often relies on intrinsic models to infer connectivity or associated metrics. Consequently, there are several analysis methods that have been developed primarily in the human literature but which can easily be applied to animals as well (**Figure 6b**). Approaches range from hypothesis-driven (e.g. seed-based analysis) to data-driven (e.g. Independent Component Analysis, ICA) and can be applied at the level of networks or of particular ROI. Some metrics describe the relationship between areas; others are based on features of the low- frequency BOLD fluctuations from a single region. Here we provide a brief overview of some prominent methods.

3.5.4 *Seed-based correlation.*

Seed-based correlation is the most intuitive of the analytical methods and the most commonly used in animals (**Figure 6b**). A seed region can be defined based on function or anatomy and range in size from a few voxels to a parcel from a brain atlas. The time courses from each voxel in the seed are averaged together, and then the correlation is calculated between the averaged seed time course and the time course from every other voxel in the brain. The resulting correlation values can be displayed at the location of each voxel, producing a correlation map (Kalthoff et al., 2011; Liang et al., 2013; Paasonen et al., 2018; Pawela et al., 2008; Sforazzini et al., 2014; Williams et al., 2010; Zerbi et al., 2015). Average values can then be measured for ROIs. Alternatively, the signal from the desired target area can be measured and correlated with the seed time course to directly examine the connection from a particular pair of areas. Seed-based correlation is a low-level metric and thus relatively easy to interpret. As with any measurement, it can be affected by the relative levels of signal and noise. While correlation is robust to differences in amplitude in the two signals, a reduction in BOLD amplitude can go hand in hand with an increase in non-neural noise, which does affect correlation values (Keilholz et al., 2016).

3.5.5 *Independent Component Analysis.*

ICA is a data-driven way to identify networks within the brain. It is widely used in the human neuroimaging community and does not rely on the definition of a seed. Instead, it identifies a number of statistically- independent networks that can be mapped spatially to the brain (Hutchison et al., 2010; Jonckers et al., 2014; Lu et al., 2012; Sforazzini et al., 2014). One of the challenges of the technique is that it is not immediately apparent how many components should be used. As more components are included, the resulting networks fragment into separate areas, and it may sometimes be necessary to combine components to recompose the full network structure. Accordingly, distributed networks of the rodent brain that are robustly identified using seed-based mapping, such as the DMN (Sforazzini et al., 2014), are only detectable with low-dimensional ICA, and are typically segregated into functional sub-portions when a more canonical number of components is selected. As such, the choice of component number is one of the sources of variability across experiments, but it is at least somewhat mitigated by the observation that the same networks can typically be detected in most studies, despite the occasional fragmentation. Other choices that contribute to variability across studies include whether ICA is performed on the entire group of animals at once, or on subgroups (e.g., mutant vs wild type mice). If performed on the whole group, a single set of components is obtained and its strength can be examined in each group. One risk of this approach is that the component structure might be driven by one of the subgroups. If ICA is performed on subgroups, multiple sets of components are obtained with different spatial extents and strengths, making comparisons more difficult. ICA provides spatial maps of components and can be considered a mid-level parameter. Additional analysis is needed to examine the strength of the connectivity within or between networks obtained from ICA and is often calculated using correlation. Strict criterion for the

identification should be encouraged, such as those proposed in (Zerbi et al., 2015), to promote comparable classifications between studies.

3.5.6 Amplitude of low-frequency fluctuations.

The amplitude of low-frequency fluctuations (ALFF; (Zang et al., 2007) and fractional ALFF (Zou et al., 2008) represent the amplitude of the BOLD fluctuations within specific frequency bands, e.g. the 0.01-0.08 Hz range. For fALFF, the amplitude of the fluctuations in the range of interest is normalized by the amplitude of the full frequency range. Both of these measures give an estimate of the strength of the BOLD fluctuations used to map RS-FC, and may include both neural contributions and vascular effects like cerebrovascular reactivity (Golestani et al., 2016). ALFF and fALFF are low-level parameters. In rodents, they are most commonly used to compare across experimental groups (Chang et al., 2018; Wen et al., 2018; Yao et al., 2012).

3.5.7 Regional Homogeneity

Regional Homogeneity (ReHo) is a measure of the local correlation between adjacent voxels (Zang et al., 2004). Similarly to ALFF, and contrary to the majority of the other methods described here, ReHo is a measure that informs on the local signal coherence strength, but not of distal connectivity. The method has been effectively applied in rodents (Li et al., 2018; Wu et al., 2017) and NHP (Rao et al., 2017), such as to describe anaesthesia effects on the mouse brain (Wu et al., 2017). ReHo is also a low-level parameter and is relatively simple to interpret.

3.5.8 Whole-Brain Analysis.

When pursuing a whole brain analysis of RS-FC data, the first question to be answered is that of parcellation. In theory, an analysis could also be performed using each voxel as an independent region, but the signal is noisy and spatially redundant. It is generally agreed upon to group voxels in some way to reduce the dimensionality of the ensuing analysis. The choice of the atlas is often dictated by the level of detail achieved. Parcellation by atlas is an anatomical approach, even though the atlas may be derived from functional information. Another possibility is to perform a functional parcellation, either by clustering or by using a dimensionality reduction algorithm like ICA (Jonckers et al., 2014; Medda et al., 2016). These approaches incorporate information carried by the resting BOLD signal instead of relying on spatial alignment. Following parcellation, other analysis methods are typically applied. One common approach is to calculate the correlation between the average time courses of every possible pairs of ROI. This is similar to seed-based correlation except that the regions of the atlas are used as seeds and targets. Partial volume effects can, therefore, distort the results. The correlation values for the whole brain are often displayed as matrices, where each line shows the correlation for a given ROI with all other possible ROIs. It is then possible to test correlation matrices for differences across groups (although correction for multiple comparisons is essential) or to calculate additional summary metrics using graph theory approaches, described in the next section.

3.5.9 Graph Theory.

The brain can be viewed as a network, with ROI serving as nodes that are connected by edges whose weight is determined by a measure of RS-FC, usually correlation. From this perspective, an entire arsenal of graph- theoretical metrics can be used to describe the network of the brain. These range from mid-level metrics such as degree (the number of edges that connect to a node) to high-level metrics such as modularity that describe the community structure of the brain. For an overview, see (Bullmore and Sporns, 2009). High-level metrics provide a convenient summary of the large-scale functional architecture of the rodent functional connectome, amenable to cross-

species translation (Bertero et al., 2018; Liska et al., 2015; Stafford et al., 2014). They, however, can be influenced by low-level parameters, such as global correlations, and arbitrary parameters such as matrix sparsity whose effects cascade through the analysis and complicate interpretation.

3.5.10 Dynamic Analysis.

In recent years, interest has grown in examining not only average correlation values across groups but dynamic measures of how they vary over time. The simplest approach is to use a windowed version of the image time series to calculate the metrics described above (e.g., correlation) (Keilholz et al., 2013). The window is moved along the time series and the calculation is repeated at different time points. A number of studies have examined the effects of window size, shape, and step size, but the ideal parameters remain difficult to pin down (Grandjean et al., 2017a; Hindriks et al., 2015; Leonardi and Van De Ville, 2015; Shakil et al., 2016, 2018). Windows can be applied to the time courses from a particular ROI or from the whole brain, where they are often summarized as a series of matrices (Allen et al., 2014). Other methods can be used to look at the co-occurrence of the individual events that drive RS-FC (Liu et al., 2018; Petridou et al., 2013) or at large-scale repeated patterns of activity (Belloy et al., 2018; Grandjean et al., 2017a; Majeed et al., 2011), offering the possibility of mapping RS-FC non correlative terms. These represent promising emerging methods to investigate the RS-FC signal beyond the stationary hypothesis which characterizes the methods discussed above.

3.5.11 Functional connectivity metrics and interpretation

Choices of anaesthesia and pre-processing pipeline have the greatest effect on the ability to compare results from different studies (Pan et al., 2015). However, the wide variety of analysis methods available also plays a role in our interpretation of the results. While the choice of analysis is ultimately dictated by the question of interest, there are steps that can be taken to promote standardization across studies. For example, reporting baseline metrics like correlation along with higher-level metrics like modularity would assist with interpretation and comparison to other studies. In human neuroimaging, a test-retest examination of varying RS-FC methods has highlighted reliable methods (Zuo and Xing, 2014), including dual-regression (Filippini et al., 2009). There are a few explicit examinations of test-retest reproducibility in rodents that undergo the same experimental protocols, providing insight into the level of reproducibility that might be expected. Zerbi et al. found an R^2 value of ~ 0.7 for optimally processed data from mice under medetomidine/isoflurane combination (Zerbi et al., 2015). Kalthoff et al. showed that the spatial localization of ICA components shares a common core, particularly under medetomidine sedation (Kalthoff et al., 2013). Nevertheless, substantial variability in the correlation coefficients from different studies is present, depending on pre- processing steps, ROI definition, and other factors.

3.6 Statistics and resource sharing

The statistical analysis carried out by the neuroimaging community has been under increasing scrutiny following reports of inflated false-positive rates in the parametric statistical models traditionally used (Eklund et al., 2016). To assess the emergence of non-parametric voxel-wise statistics, we recorded the occurrence of non-parametric statistics. We found only 12 mentions of such tests out of 868 studies. This low incidence is indicative of comparable trends in the corresponding human neuroimaging field. Differences between studies are accentuated as voxel-wise statistics in animal studies have been corrected with varying degrees of stringency, such as

correcting by arbitrary *ad-hoc* cluster size or p-value threshold. These render the comparison between studies opaque. To overcome these limitations and to permit meta-analysis, NeuroVault (Gorgolewski et al., 2015) offers a resource to publish statistical maps prior to statistical thresholds, leaving the users to explore, reinterpret, and repurpose these results. Unfortunately, such resources are not yet available to animal neuroimaging studies. The advent of RS-FC and network analysis is another source of dissension in the statistical analysis. With fine-grain ROI sets, the number of edges increases dramatically, hence the number of univariate tests and the need to correct for multiple comparisons. There, no consensus currently exists to effectively account for multiple comparisons and the heightened level of false positives ensuing.

The growth of the human neuroimaging community has been fueled by large datasets made publicly available in online repositories (Nichols et al., 2017). Making raw data available is becoming a requirement by the funding bodies, academic centre, and the journals. In spite of these requirements, we only found 15 mentions of data availability, among 868 studies, seven of which upon reasonable request to the senior author.

Publication of datasets on established repositories ensures lasting availability of the dataset and unbiased distribution. Databases such as XNAT (<https://central.xnat.org/>; (Herrick et al., 2016)) and Openneuro (<https://openneuro.org/>; (Poldrack et al., 2013)) are becoming increasingly user-friendly, including standardized formats that allow for the easy organization and retrieval of functional and anatomical data (Gorgolewski et al., 2016). Importantly, potential reticence in human neuroimaging to share material to protect subject privacy do not apply in animal research. Importantly, shared material allows for in-depth scrutiny of published results and hence strengthen the trust in the published results and facilitate meta- analysis.

4 Conclusion and outlooks

With this study, we describe the general trends in animal functional neuroimaging and reflect on emerging collective efforts driving toward larger multi-centre studies and a desire for the adoption of standards and good practices in the field. A general consensus on several acquisition procedures within the community is unlikely to be reached, especially on contentious topics such as anaesthesia and animal preparation.

Nonetheless, we report general trends which indicate some degrees of consensus. For instance, isoflurane and medetomidine and/or their combination represent an increasing proportion of the studies performed in anaesthetized animals, supported with increasing evidence from the literature. Sequences and contrasts are also reaching consensus, as the overwhelming majority of the studies were acquired using GE-EPI and BOLD contrast, predominantly at high fields such as 7T and 9.4T. Importantly, a number of aspects emerge which are currently lacking within our community and which could easily be implemented to greatly ameliorate how results are interpreted. While modest, these first steps will be necessary for the adoption of standards, replication studies, and meta-analysis.

Firstly, the systematic sharing of raw datasets upon publication is the easiest milestone to be achieved within our community. It is often requested by both funding agencies and publishers alike. Yet, less than 1% of the studies were published with its raw data. This represents a severe loss to our community as it prevents the repurposing of material and the critical re-assessment of past results. Arguably, a number of debates regarding methodological aspects of fMRI acquisitions would find a rapid resolution if the material were accessible by the community for in-depth scrutiny. Moreover, a number of variations in data processing highlighted above would be rendered moot as the material could be re-analysed with other pipelines to confirm or compare

results.

The second aspect within acceptable reach in the animal neuroimaging community is the adoption of common reference spaces and the reporting of accurate coordinates in both figures and tables, as is common practice in human studies. Despite several templates being available for mice, rats, and NHP (Bakker et al., 2015), no consensus has yet emerged. The reliance on ad-hoc templates further hinders the adoption of standard templates. While Paxinos and Franklin mice (Paxinos and Franklin, 2012) and Paxinos and Watson rats atlases (The Rat Brain in Stereotaxic Coordinates, 1982) are systematically referred to, activation clusters have not been reported with respect to their three-dimensional coordinates reported in these atlases. Hence, the adoption of exact three-dimensional coordinate systems, together with tools to convert from one system to another would greatly ameliorate how results in animal neuroimaging studies are reported, and would also among other enable meta-analyses.

Finally, contentious areas, specifically anaesthesia and animal preparations, should be approached jointly by multiple laboratories to ensure that the manipulations lead to reproducible results between centres, and to generate a nucleus around which a consensus can emerge. Such efforts will be necessary for the emergence of animal population imaging studies centred on brain function. Such efforts, likewise to human neuroimaging is expected to dramatically accelerate our understanding of the mammalian brain, its evolution, and the pathological mechanisms which affects its function.

Acknowledgements

FM was supported by the University of Manchester and A*STAR Research Attachment Programme (ARAP), which is co-funded through the University of Manchester, Faculty of Biology, Medicine and Health Doctoral Academy, and Singapore Bioimaging Consortium (SBIC), A*STAR, Singapore. JG wishes to acknowledge the SBIC core funds. AG is supported by the European Research Council (ERC, DISCONN, GA 802371), by the Simons Foundation (SFARI 400101), the Brain and Behavior Foundation (NARSAD, Independent Investigator Grant 25861), and the NIH (1R21MH116473-01A1). MS and RMD are supported by the Netherlands Organization for Scientific Research (NWO-VICI 016.130.662). GAFT is supported by the National Institute of Mental Health of the National Institutes of Health under award number R01MH111417.

Author Contributions Statement

JG designed the study, collected and processed the data. All the authors contributed to the manuscript preparation.

Conflict of Interest Statement

The authors have no conflict of interest to declare.

References

- Abe, Y., Sekino, M., Terazono, Y., Ohsaki, H., Fukazawa, Y., Sakai, S., et al. (2012). Opto-fMRI analysis for exploring the neuronal connectivity of the hippocampal formation in rats. *Neurosci. Res.* 74, 248–255. doi:10.1016/j.neures.2012.08.007.
- Abe, Y., Tsurugizawa, T., and Le Bihan, D. (2017). Water diffusion closely reveals neural activity status in rat brain loci affected by anesthesia. *PLoS Biol.* 15, e2001494.

doi:10.1371/journal.pbio.2001494.

Acker, L., Pino, E. N., Boyden, E. S., and Desimone, R. (2016). FEF inactivation with improved optogenetic methods. *Proc. Natl. Acad. Sci. U. S. A.* 113, E7297–E7306. doi:10.1073/pnas.1610784113.

Aguirre, G. K., Detre, J. A., Zarahn, E., and Alsop, D. C. (2002). Experimental design and the relative sensitivity of BOLD and perfusion fMRI. *Neuroimage* 15, 488–500. doi:10.1006/nimg.2001.0990.

Albaugh, D. L., Salzwedel, A., Van Den Berge, N., Gao, W., Stuber, G. D., and Shih, Y.-Y. I. (2016). Functional Magnetic Resonance Imaging of Electrical and Optogenetic Deep Brain Stimulation at the Rat Nucleus Accumbens. *Scientific Reports* 6. doi:10.1038/srep31613.

Albers, F., Schmid, F., Wachsmuth, L., and Faber, C. (2018). Line scanning fMRI reveals earlier onset of optogenetically evoked BOLD response in rat somatosensory cortex as compared to sensory stimulation. *Neuroimage* 164, 144–154. doi:10.1016/j.neuroimage.2016.12.059.

Aldrin-Kirk, P., Heuer, A., Rylander Ottosson, D., Davidsson, M., Mattsson, B., and Björklund, T. (2018). Chemogenetic modulation of cholinergic interneurons reveals their regulating role on the direct and indirect output pathways from the striatum. *Neurobiol. Dis.* 109, 148–162. doi:10.1016/j.nbd.2017.10.010.

Alexander, G. M., Rogan, S. C., Abbas, A. I., Armbruster, B. N., Pei, Y., Allen, J. A., et al. (2009). Remote control of neuronal activity in transgenic mice expressing evolved G protein-coupled receptors. *Neuron* 63, 27–39. doi:10.1016/j.neuron.2009.06.014.

Allen, B. D., Singer, A. C., and Boyden, E. S. (2015). Principles of designing interpretable optogenetic behavior experiments. *Learning & Memory* 22, 232–238. doi:10.1101/lm.038026.114.

Amaro, E., Jr, and Barker, G. J. (2006). Study design in fMRI: basic principles. *Brain Cogn.* 60, 220–232. doi:10.1016/j.bandc.2005.11.009.

Aravanis, A. M., Wang, L.-P., Zhang, F., Meltzer, L. A., Mogri, M. Z., Schneider, M. B., et al. (2007). An optical neural interface: in vivo control of rodent motor cortex with integrated fiberoptic and optogenetic technology. *J. Neural Eng.* 4, S143–56. doi:10.1088/1741-2560/4/3/S02.

Arey, B. J. (2014). An Historical Introduction to Biased Signaling. *Biased Signaling in Physiology, Pharmacology and Therapeutics*, 1–39. doi:10.1016/b978-0-12-411460-9.00001-x.

Armbruster, B. N., Li, X., Pausch, M. H., Herlitze, S., and Roth, B. L. (2007). Evolving the lock to fit the key to create a family of G protein-coupled receptors potently activated by an inert ligand. *Proc. Natl. Acad. Sci. U. S. A.* 104, 5163–5168. doi:10.1073/pnas.0700293104.

Ashby, C. R., Jr, and Wang, R. Y. (1996). Pharmacological actions of the atypical antipsychotic drug clozapine: a review. *Synapse* 24, 349–394. doi:10.1002/(SICI)1098-2396(199612)24:4<349::AID-SYN5>3.0.CO;2-D.

Atasoy, D., Aponte, Y., Su, H. H., and Sternson, S. M. (2008). A FLEX switch targets Channelrhodopsin-2 to multiple cell types for imaging and long-range circuit mapping. *J. Neurosci.* 28, 7025–7030. doi:10.1523/JNEUROSCI.1954-08.2008.

- Báez-Yáñez, M. G., Ehses, P., Mirkes, C., Tsai, P. S., Kleinfeld, D., and Scheffler, K. (2017). The impact of vessel size, orientation and intravascular contribution on the neurovascular fingerprint of BOLDbSSFP fMRI. *Neuroimage* 163, 13–23. doi:10.1016/j.neuroimage.2017.09.015.
- Bakker, R., Tiesinga, P., and Kötter, R. (2015). The Scalable Brain Atlas: Instant Web-Based Access to Public Brain Atlases and Related Content. *Neuroinformatics* 13, 353–366. doi:10.1007/s12021-014- 9258-x.
- Baltes, C., Bosshard, S., Mueggler, T., Ratering, D., and Rudin, M. (2011). Increased blood oxygen level- dependent (BOLD) sensitivity in the mouse somatosensory cortex during electrical forepaw stimulation using a cryogenic radiofrequency probe. *NMR Biomed.* 24, 439–446. doi:10.1002/nbm.1613.
- Barttfeld, P., Uhrig, L., Sitt, J. D., Sigman, M., Jarraya, B., and Dehaene, S. (2015). Signature of consciousness in the dynamics of resting-state brain activity. *Proc. Natl. Acad. Sci. U. S. A.* 112, 887– 892. doi:10.1073/pnas.1418031112.
- Beery, A. K., and Zucker, I. (2011). Sex bias in neuroscience and biomedical research. *Neurosci. Biobehav. Rev.* 35, 565–572. doi:10.1016/j.neubiorev.2010.07.002.
- Belcher, A. M., Yen, C. C., Stepp, H., Gu, H., Lu, H., Yang, Y., et al. (2013). Large-scale brain networks in the awake, truly resting marmoset monkey. *J. Neurosci.* 33, 16796–16804. doi:10.1523/JNEUROSCI.3146-13.2013.
- Belloy, M. E., Shah, D., Abbas, A., Kashyap, A., Roßner, S., Van der Linden, A., et al. (2018). Quasi- Periodic Patterns of Neural Activity improve Classification of Alzheimer’s Disease in Mice. *Sci. Rep.* 8, 10024. doi:10.1038/s41598-018-28237-9.
- Berg, K. A., and Clarke, W. P. (2018). Making Sense of Pharmacology: Inverse Agonism and Functional Selectivity. *Int. J. Neuropsychopharmacol.* 21, 962–977. doi:10.1093/ijnp/pyy071.
- Berndt, A., Lee, S. Y., Ramakrishnan, C., and Deisseroth, K. (2014). Structure-guided transformation of channelrhodopsin into a light-activated chloride channel. *Science* 344, 420–424. doi:10.1126/science.1252367.
- Berndt, A., Yizhar, O., Gunaydin, L. A., Hegemann, P., and Deisseroth, K. (2009). Bi-stable neural state switches. *Nat. Neurosci.* 12, 229–234. doi:10.1038/nn.2247.
- Bernstein, J. G., and Boyden, E. S. (2011). Optogenetic tools for analyzing the neural circuits of behavior. *Trends Cogn. Sci.* 15, 592–600. doi:10.1016/j.tics.2011.10.003.
- Bertero, A., Liska, A., Pagani, M., Parolisi, R., Masferrer, M. E., Gritti, M., et al. (2018). Autism-associated 16p11.2 microdeletion impairs prefrontal functional connectivity in mouse and human. *Brain* 141, 2055–2065. doi:10.1093/brain/awy111.
- Bifone, A., and Gozzi, A. (2012). Neuromapping techniques in drug discovery: pharmacological MRI for the assessment of novel antipsychotics. *Expert Opin. Drug Discov.* 7, 1071–1082. doi:10.1517/17460441.2012.724057.
- Biswal, B. B., Mennes, M., Zuo, X.-N., Gohel, S., Kelly, C., Smith, S. M., et al. (2010). Toward discovery science of human brain function. *Proc. Natl. Acad. Sci. U. S. A.* 107, 4734–4739.

doi:10.1073/pnas.0911855107.

Biswal, B., Hudetz, A. G., Zerrin Yetkin, F., Haughton, V. M., and Hyde, J. S. (1997). Hypercapnia Reversibly Suppresses Low-Frequency Fluctuations in the Human Motor Cortex during Rest Using Echo-Planar MRI. *J. Cereb. Blood Flow Metab.* 17, 301–308. doi:10.1097/00004647-199703000-00007.

Biswal, B., Yetkin, F. Z., Haughton, V. M., and Hyde, J. S. (1995). Functional connectivity in the motor cortex of resting human brain using echo-planar MRI. *Magn. Reson. Med.* 34, 537–541. Available at: <https://www.ncbi.nlm.nih.gov/pubmed/8524021>.

Bonhomme, V., Boveroux, P., Brichant, J. F., Laureys, S., and Boly, M. (2012). Neural correlates of consciousness during general anesthesia using functional magnetic resonance imaging (fMRI). *Arch. Ital. Biol.* 150, 155–163. doi:10.4449/aib.v150i2.1242.

Borogovac, A., and Asllani, I. (2012). Arterial Spin Labeling (ASL) fMRI: advantages, theoretical constraints, and experimental challenges in neurosciences. *Int. J. Biomed. Imaging* 2012, 818456. doi:10.1155/2012/818456.

Bosshard, S. C., Baltes, C., Wyss, M. T., Mueggler, T., Weber, B., and Rudin, M. (2010). Assessment of brain responses to innocuous and noxious electrical forepaw stimulation in mice using BOLD fMRI. *Pain* 151, 655–663. doi:10.1016/j.pain.2010.08.025.

Boyden, E. S. (2015). Erratum: Optogenetics and the future of neuroscience. *Nat. Neurosci.* 18, 1862. doi:10.1038/nn1215-1862b.

Boyden, E. S., Zhang, F., Bamberg, E., Nagel, G., and Deisseroth, K. (2005). Millisecond-timescale, genetically targeted optical control of neural activity. *Nat. Neurosci.* 8, 1263–1268. doi:10.1038/nn1525.

Brevard, M. E., Duong, T. Q., King, J. A., and Ferris, C. F. (2003). Changes in MRI signal intensity during hypercapnic challenge under conscious and anesthetized conditions. *Magn. Reson. Imaging* 21, 995–1001. Available at: <https://www.ncbi.nlm.nih.gov/pubmed/14684202>.

Brocka, M., Helbing, C., Vincenz, D., Scherf, T., Montag, D., Goldschmidt, J., et al. (2018). Contributions of dopaminergic and non-dopaminergic neurons to VTA-stimulation induced neurovascular responses in brain reward circuits. *Neuroimage* 177, 88–97. doi:10.1016/j.neuroimage.2018.04.059.

Bruinsma, T. J., Sarma, V. V., Oh, Y., Jang, D. P., Chang, S.-Y., Worrell, G. A., et al. (2018). The Relationship Between Dopamine Neurotransmitter Dynamics and the Blood-Oxygen-Level-Dependent (BOLD) Signal: A Review of Pharmacological Functional Magnetic Resonance Imaging. *Frontiers in Neuroscience* 12. doi:10.3389/fnins.2018.00238.

Buckner, R. L., Sepulcre, J., Talukdar, T., Krienen, F. M., Liu, H., Hedden, T., et al. (2009). Cortical hubs revealed by intrinsic functional connectivity: mapping, assessment of stability, and relation to Alzheimer's disease. *J. Neurosci.* 29, 1860–1873. doi:10.1523/JNEUROSCI.5062-08.2009.

Bukhari, Q., Schroeter, A., Cole, D. M., and Rudin, M. (2017). Resting State fMRI in Mice Reveals Anesthesia Specific Signatures of Brain Functional Networks and Their Interactions. *Front. Neural Circuits* 11, 5. doi:10.3389/fncir.2017.00005.

Bullmore, E., and Sporns, O. (2009). Complex brain networks: graph theoretical analysis of structural and functional systems. *Nat. Rev. Neurosci.* 10, 186–198. doi:10.1038/nrn2575.

- Button, K. S., Ioannidis, J. P. A., Mokrysz, C., Nosek, B. A., Flint, J., Robinson, E. S. J., et al. (2013). Power failure: why small sample size undermines the reliability of neuroscience. *Nat. Rev. Neurosci.* 14, 365–376. doi:10.1038/nrn3475.
- Canese, R., Marco, E. M., De Pasquale, F., Podo, F., Laviola, G., and Adriani, W. (2011). Differential response to specific 5-Ht (7) versus whole-serotonergic drugs in rat forebrains: a pHMRI study. *Neuroimage* 58, 885–894. doi:10.1016/j.neuroimage.2011.06.089.
- Cardin, J. A., Carlén, M., Meletis, K., Knoblich, U., Zhang, F., Deisseroth, K., et al. (2010). Targeted optogenetic stimulation and recording of neurons in vivo using cell-type-specific expression of Channelrhodopsin-2. *Nature Protocols* 5, 247–254. doi:10.1038/nprot.2009.228.
- Carp, J. (2012). The secret lives of experiments: methods reporting in the fMRI literature. *Neuroimage* 63, 289–300. doi:10.1016/j.neuroimage.2012.07.004.
- Chai, Y., Bi, G., Wang, L., Xu, F., Wu, R., Zhou, X., et al. (2016). Direct detection of optogenetically evoked oscillatory neuronal electrical activity in rats using SLOE sequence. *Neuroimage* 125, 533–543. doi:10.1016/j.neuroimage.2015.10.058.
- Chang, W.-T., Puspitasari, F., Garcia-Miralles, M., Yeow, L. Y., Tay, H.-C., Koh, K. B., et al. (2018). Connectomic imaging reveals Huntington-related pathological and pharmaceutical effects in a mouse model. *NMR in Biomedicine* 31, e4007. doi:10.1002/nbm.4007.
- Chan, R. W., Leong, A. T. L., Ho, L. C., Gao, P. P., Wong, E. C., Dong, C. M., et al. (2017). Low-frequency hippocampal–cortical activity drives brain-wide resting-state functional MRI connectivity. *Proceedings of the National Academy of Sciences* 114, E6972–E6981. doi:10.1073/pnas.1703309114.
- Chen, Y. C., Mandeville, J. B., Nguyen, T. V., Talele, A., Cavagna, F., and Jenkins, B. G. (2001). Improved mapping of pharmacologically induced neuronal activation using the IRON technique with superparamagnetic blood pool agents. *J. Magn. Reson. Imaging* 14, 517–524. Available at: <https://www.ncbi.nlm.nih.gov/pubmed/11747003>.
- Chen, Y. I., Brownell, A. L., Galpern, W., Isacson, O., Bogdanov, M., Beal, M. F., et al. (1999). Detection of dopaminergic cell loss and neural transplantation using pharmacological MRI, PET and behavioral assessment. *Neuroreport* 10, 2881–2886. Available at: <https://www.ncbi.nlm.nih.gov/pubmed/10549790>.
- Chen, Y.-W., Das, M., Oyarzabal, E. A., Cheng, Q., Plummer, N. W., Smith, K. G., et al. (2018). Genetic identification of a population of noradrenergic neurons implicated in attenuation of stress-related responses. *Mol. Psychiatry*. doi:10.1038/s41380-018-0245-8.
- Choe, K. Y., Sanchez, C. F., Harris, N. G., Otis, T. S., and Mathews, P. J. (2018). Optogenetic fMRI and electrophysiological identification of region-specific connectivity between the cerebellar cortex and forebrain. *Neuroimage* 173, 370–383. doi:10.1016/j.neuroimage.2018.02.047.
- Christie, I. N., Wells, J. A., Southern, P., Marina, N., Kasparov, S., Gourine, A. V., et al. (2013). fMRI response to blue light delivery in the naïve brain: implications for combined optogenetic fMRI studies. *Neuroimage* 66, 634–641. doi:10.1016/j.neuroimage.2012.10.074.
- Chuong, A. S., Miri, M. L., Busskamp, V., Matthews, G. A. C., Acker, L. C., Sørensen, A. T., et al. (2014). Noninvasive optical inhibition with a red-shifted microbial rhodopsin. *Nature Neuroscience* 17, 1123–1129. doi:10.1038/nn.3752.

- Ciobanu, L., Reynaud, O., Uhrig, L., Jarraya, B., and Le Bihan, D. (2012). Effects of anesthetic agents on brain blood oxygenation level revealed with ultra-high field MRI. *PLoS One* 7, e32645. doi:10.1371/journal.pone.0032645.
- Cogan, S. F., Ludwig, K. A., Welle, C. G., and Takmakov, P. (2016). Tissue damage thresholds during therapeutic electrical stimulation. *J. Neural Eng.* 13, 021001. doi:10.1088/1741-2560/13/2/021001.
- Dai, W., Garcia, D., de Bazelaire, C., and Alsop, D. C. (2008). Continuous flow-driven inversion for arterial spin labeling using pulsed radio frequency and gradient fields. *Magnetic Resonance in Medicine* 60, 1488–1497. doi:10.1002/mrm.21790.
- Damoiseaux, J. S., and Greicius, M. D. (2009). Greater than the sum of its parts: a review of studies combining structural connectivity and resting-state functional connectivity. *Brain Struct. Funct.* 213, 525–533. doi:10.1007/s00429-009-0208-6.
- Decot, H. K., Namboodiri, V. M. K., Gao, W., McHenry, J. A., Jennings, J. H., Lee, S.-H., et al. (2017). Coordination of Brain-Wide Activity Dynamics by Dopaminergic Neurons. *Neuropsychopharmacology* 42, 615–627. doi:10.1038/npp.2016.151.
- Deisseroth, K. (2015). Optogenetics: 10 years of microbial opsins in neuroscience. *Nat. Neurosci.* 18, 1213–1225. doi:10.1038/nn.4091.
- Desai, M., Kahn, I., Knoblich, U., Bernstein, J., Atallah, H., Yang, A., et al. (2011). Mapping brain networks in awake mice using combined optical neural control and fMRI. *J. Neurophysiol.* 105, 1393–1405. doi:10.1152/jn.00828.2010.
- Detre, J. A., and Wang, J. (2002). Technical aspects and utility of fMRI using BOLD and ASL. *Clin. Neurophysiol.* 113, 621–634. Available at: <https://www.ncbi.nlm.nih.gov/pubmed/11976042>.
- Di Martino, A., Yan, C.-G., Li, Q., Denio, E., Castellanos, F. X., Alaerts, K., et al. (2014). The autism brain imaging data exchange: towards a large-scale evaluation of the intrinsic brain architecture in autism. *Mol. Psychiatry* 19, 659–667. doi:10.1038/mp.2013.78.
- Dorr, A. E., Lerch, J. P., Spring, S., Kabani, N., and Henkelman, R. M. (2008). High resolution three-dimensional brain atlas using an average magnetic resonance image of 40 adult C57Bl/6J mice. *Neuroimage* 42, 60–69. doi:10.1016/j.neuroimage.2008.03.037.
- Eklund, A., Nichols, T. E., and Knutsson, H. (2016). Cluster failure: Why fMRI inferences for spatial extent have inflated false-positive rates. *Proceedings of the National Academy of Sciences* 113, 7900–7905. doi:10.1073/pnas.1602413113.
- Elias, Z., Powers, S. K., Atstupenas, E., and Tony Brown, J. (1987). Hyperthermia from interstitial laser irradiation in normal rat brain. *Lasers in Surgery and Medicine* 7, 370–375. doi:10.1002/lsm.1900070413.
- English, J. G., and Roth, B. L. (2015). Chemogenetics-A Transformational and Translational Platform. *JAMA Neurol.* 72, 1361–1366. doi:10.1001/jamaneurol.2015.1921.
- Esteban, O., Markiewicz, C. J., Blair, R. W., Moodie, C. A., Isik, A. I., Erramuzpe, A., et al. (2019). fMRIPrep: a robust preprocessing pipeline for functional MRI. *Nat. Methods* 16, 111–116. doi:10.1038/s41592-018-0235-4.

- Farrell, M. S., Pei, Y., Wan, Y., Yadav, P. N., Daigle, T. L., Urban, D. J., et al. (2013). A Gas DREADD mouse for selective modulation of cAMP production in striatopallidal neurons. *Neuropsychopharmacology* 38, 854–862. doi:10.1038/npp.2012.251.
- Fenno, L., Yizhar, O., and Deisseroth, K. (2011). The development and application of optogenetics. *Annu. Rev. Neurosci.* 34, 389–412. doi:10.1146/annurev-neuro-061010-113817.
- Ferenczi, E. A., Zalocusky, K. A., Liston, C., Grosenick, L., Warden, M. R., Amatya, D., et al. (2016). Prefrontal cortical regulation of brainwide circuit dynamics and reward-related behavior. *Science* 351, aac9698. doi:10.1126/science.aac9698.
- Ferrari, L., Turrini, G., Crestan, V., Bertani, S., Cristofori, P., Bifone, A., et al. (2012). A robust experimental protocol for pharmacological fMRI in rats and mice. *J. Neurosci. Methods* 204, 9–18. doi:10.1016/j.jneumeth.2011.10.020.
- Ferris, C. F., Febo, M., Luo, F., Schmidt, K., Brevard, M., Harder, J. A., et al. (2006). Functional magnetic resonance imaging in conscious animals: a new tool in behavioural neuroscience research. *J. Neuroendocrinol.* 18, 307–318. doi:10.1111/j.1365-2826.2006.01424.x.
- Filippini, N., MacIntosh, B. J., Hough, M. G., Goodwin, G. M., Frisoni, G. B., Smith, S. M., et al. (2009). Distinct patterns of brain activity in young carriers of the APOE-epsilon4 allele. *Proc. Natl. Acad. Sci. U. S. A.* 106, 7209–7214. doi:10.1073/pnas.0811879106.
- Franks, N. P. (2008). General anaesthesia: from molecular targets to neuronal pathways of sleep and arousal. *Nat. Rev. Neurosci.* 9, 370–386. doi:10.1038/nrn2372.
- Garcia, P., Kolesky, S., and Jenkins, A. (2010). General Anesthetic Actions on GABAA Receptors. *Curr. Neuropharmacol.* 8, 2–9. doi:10.2174/157015910790909502.
- Garin, C. M., Nadkarni, N. A., Landeau, B., Chételat, G., Picq, J.-L., Bougacha, S., et al. (2019). Resting state cerebral networks in mouse lemur primates: from multilevel validation to comparison with humans. *Neuroscience*, 463.
- Garrett, K. M., and Gan, J. (1998). Enhancement of gamma-aminobutyric acidA receptor activity by alpha- chloralose. *J. Pharmacol. Exp. Ther.* 285, 680–686. Available at: <https://www.ncbi.nlm.nih.gov/pubmed/9580613>.
- Giorgi, A., Migliarini, S., Galbusera, A., Maddaloni, G., Mereu, M., Margiani, G., et al. (2017). Brain-wide Mapping of Endogenous Serotonergic Transmission via Chemogenetic fMRI. *Cell Rep.* 21, 910–918. doi:10.1016/j.celrep.2017.09.087.
- Goense, J. B. M., and Logothetis, N. K. (2006). Laminar specificity in monkey V1 using high-resolution SE- fMRI. *Magn. Reson. Imaging* 24, 381–392. doi:10.1016/j.mri.2005.12.032.
- Golestani, A. M., Wei, L. L., and Chen, J. J. (2016). Quantitative mapping of cerebrovascular reactivity using resting-state BOLD fMRI: Validation in healthy adults. *Neuroimage* 138, 147–163. doi:10.1016/j.neuroimage.2016.05.025.
- Gomez, J. L., Bonaventura, J., Lesniak, W., Mathews, W. B., Sysa-Shah, P., Rodriguez, L. A., et al. (2017). Chemogenetics revealed: DREADD occupancy and activation via converted clozapine. *Science* 357, 503–507. doi:10.1126/science.aan2475.
- Gompf, H. S., Budygin, E. A., Fuller, P. M., and Bass, C. E. (2015). Targeted genetic

- manipulations of neuronal subtypes using promoter-specific combinatorial AAVs in wild-type animals. *Front. Behav. Neurosci.* 9, 152. doi:10.3389/fnbeh.2015.00152.
- Gorgolewski, K. J., Auer, T., Calhoun, V. D., Craddock, R. C., Das, S., Duff, E. P., et al. (2016). The brain imaging data structure, a format for organizing and describing outputs of neuroimaging experiments. *Sci Data* 3, 160044. doi:10.1038/sdata.2016.44.
- Gorgolewski, K. J., Varoquaux, G., Rivera, G., Schwarz, Y., Ghosh, S. S., Maumet, C., et al. (2015). NeuroVault.org: a web-based repository for collecting and sharing unthresholded statistical maps of the human brain. *Front. Neuroinform.* 9, 8. doi:10.3389/fninf.2015.00008.
- Gozzi, A., Ceolin, L., Schwarz, A., Reese, T., Bertani, S., Crestan, V., et al. (2007). A multimodality investigation of cerebral hemodynamics and autoregulation in pharmacological MRI. *Magn. Reson. Imaging* 25, 826–833. doi:10.1016/j.mri.2007.03.003.
- Gozzi, A., Jain, A., Giovannelli, A., Bertollini, C., Crestan, V., Schwarz, A. J., et al. (2012). A Neural Switch for Active and Passive Fear. *Neuron* 73, 854. doi:10.1016/j.neuron.2012.02.007.
- Gozzi, A., Large, C. H., Schwarz, A., Bertani, S., Crestan, V., and Bifone, A. (2008). Differential Effects of Antipsychotic and Glutamatergic Agents on the phMRI Response to Phencyclidine. *Neuropsychopharmacology* 33, 1690–1703. doi:10.1038/sj.npp.1301547.
- Gozzi, A., and Schwarz, A. J. (2016). Large-scale functional connectivity networks in the rodent brain. *Neuroimage* 127, 496–509. doi:10.1016/j.neuroimage.2015.12.017.
- Grandjean, J., Canella, C., Anckaerts, C., Ayrancı, G., Bougacha, S., Bienert, T., et al. (2019a). Common functional networks in the mouse brain revealed by multi-centre resting-state fMRI analysis. *bioRxiv*, 541060. doi:10.1101/541060.
- Grandjean, J., Corcoba, A., Kahn, M. C., Upton, A. L., Deneris, E. S., Seifritz, E., et al. (2019b). A brain- wide functional map of the serotonergic responses to acute stress and fluoxetine. *Nat. Commun.* 10, 350. doi:10.1038/s41467-018-08256-w.
- Grandjean, J., Preti, M. G., Bolton, T. A. W., Buerge, M., Seifritz, E., Pryce, C. R., et al. (2017a). Dynamic reorganization of intrinsic functional networks in the mouse brain. *Neuroimage* 152, 497–508. doi:10.1016/j.neuroimage.2017.03.026.
- Grandjean, J., Schroeter, A., Batata, I., and Rudin, M. (2014). Optimization of anesthesia protocol for resting-state fMRI in mice based on differential effects of anesthetics on functional connectivity patterns. *Neuroimage* 102 Pt 2, 838–847. doi:10.1016/j.neuroimage.2014.08.043.
- Grandjean, J., Zerbi, V., Balsters, J. H., Wenderoth, N., and Rudin, M. (2017b). Structural Basis of Large- Scale Functional Connectivity in the Mouse. *J. Neurosci.* 37, 8092–8101. doi:10.1523/JNEUROSCI.0438-17.2017.
- Grayson, D. S., Bliss-Moreau, E., Machado, C. J., Bennett, J., Shen, K., Grant, K. A., et al. (2016). The Rhesus Monkey Connectome Predicts Disrupted Functional Networks Resulting from Pharmacogenetic Inactivation of the Amygdala. *Neuron* 91, 453–466. doi:10.1016/j.neuron.2016.06.005.
- Griessner, J., Pasięka, M., Böhm, V., Grössl, F., Kaczanowska, J., Pliota, P., et al. (2018). Central amygdala circuit dynamics underlying the benzodiazepine anxiolytic effect. *Mol. Psychiatry*. doi:10.1038/s41380- 018-0310-3.

- Guadagno, A., Kang, M. S., Devenyi, G. A., Mathieu, A. P., Rosa-Neto, P., Chakravarty, M., et al. (2018). Reduced resting-state functional connectivity of the basolateral amygdala to the medial prefrontal cortex in preweaning rats exposed to chronic early-life stress. *Brain Struct. Funct.* 223, 3711–3729. doi:10.1007/s00429-018-1720-3.
- Gunaydin, L. A., Yizhar, O., Berndt, A., Sohal, V. S., Deisseroth, K., and Hegemann, P. (2010). Ultrafast optogenetic control. *Nature Neuroscience* 13, 387–392. doi:10.1038/nn.2495.
- Guru, A., Post, R. J., Ho, Y.-Y., and Warden, M. R. (2015). Making Sense of Optogenetics. *Int. J. Neuropsychopharmacol.* 18, yv079. doi:10.1093/ijnp/pyv079.
- Gutierrez-Barragan, D., Albert Basson, M., Panzeri, S., and Gozzi, A. Oscillatory brain states govern spontaneous fMRI network dynamics. doi:10.1101/393389.
- Hagberg, G. E., Indovina, I., Sanes, J. N., and Posse, S. (2002). Real-time quantification of T (2) (*) changes using multiecho planar imaging and numerical methods. *Magn. Reson. Med.* 48, 877–882. doi:10.1002/mrm.10283.
- Hampson, M., Driesen, N. R., Skudlarski, P., Gore, J. C., and Constable, R. T. (2006). Brain Connectivity Related to Working Memory Performance. *Journal of Neuroscience* 26, 13338–13343. doi:10.1523/jneurosci.3408-06.2006.
- Han, S., Son, J. P., Cho, H., Park, J., and Kim, S. (2019). Gradient-echo and spin-echo blood oxygenation level-dependent functional MRI at ultrahigh fields of 9.4 and 15.2 Tesla. *Magnetic Resonance in Medicine* 81, 1237–1246. doi:10.1002/mrm.27457.
- HD-200 Consortium (2012). The ADHD-200 Consortium: A Model to Advance the Translational Potential of Neuroimaging in Clinical Neuroscience. *Front. Syst. Neurosci.* 6, 62. doi:10.3389/fnsys.2012.00062.
- Herrick, R., Horton, W., Olsen, T., McKay, M., Archie, K. A., and Marcus, D. S. (2016). XNAT Central: Open sourcing imaging research data. *Neuroimage* 124, 1093–1096. doi:10.1016/j.neuroimage.2015.06.076.
- Hess, A., Sergejeva, M., Budinsky, L., Zeilhofer, H. U., and Brune, K. (2007). Imaging of hyperalgesia in rats by functional MRI. *European Journal of Pain* 11, 109–109. doi:10.1016/j.ejpain.2006.01.005.
- Hight, A. E., Kozin, E. D., Darrow, K., Lehmann, A., Boyden, E., Brown, M. C., et al. (2015). Superior temporal resolution of Chronos versus channelrhodopsin-2 in an optogenetic model of the auditory brainstem implant. *Hear. Res.* 322, 235–241. doi:10.1016/j.heares.2015.01.004.
- Hindriks, R., Woolrich, M., Luckhoo, H., Joensson, M., Mohseni, H., Kringelbach, M. L., et al. (2015). Role of white-matter pathways in coordinating alpha oscillations in resting visual cortex. *Neuroimage* 106, 328–339. doi:10.1016/j.neuroimage.2014.10.057.
- Hinz, R., Peeters, L., Li, C., Van Der Linden, A., and Keliris, G. (2017). A comparison of BOLD response between optogenetic and visual stimulation of the lateral Geniculate Nucleus. *Frontiers in Neuroscience* 11. doi:10.3389/conf.fnins.2017.94.00059.
- Huber, D., Petreanu, L., Ghitani, N., Ranade, S., Hromádka, T., Mainen, Z., et al. (2008). Sparse optical microstimulation in barrel cortex drives learned behaviour in freely moving mice. *Nature* 451, 61–64. doi:10.1038/nature06445.

- Hutchison, R. M., and Everling, S. (2012). Monkey in the middle: why non-human primates are needed to bridge the gap in resting-state investigations. *Front. Neuroanat.* 6, 29. doi:10.3389/fnana.2012.00029.
- Hutchison, R. M., Mirsattari, S. M., Jones, C. K., Gati, J. S., and Leung, L. S. (2010). Functional networks in the anesthetized rat brain revealed by independent component analysis of resting-state fMRI. *J. Neurophysiol.* 103, 3398–3406. doi:10.1152/jn.00141.2010.
- Hutchison, R. M., Womelsdorf, T., Allen, E. A., Bandettini, P. A., Calhoun, V. D., Corbetta, M., et al. (2013a). Dynamic functional connectivity: promise, issues, and interpretations. *Neuroimage* 80, 360–378. doi:10.1016/j.neuroimage.2013.05.079.
- Hutchison, R. M., Womelsdorf, T., Gati, J. S., Everling, S., and Menon, R. S. (2013b). Resting-state networks show dynamic functional connectivity in awake humans and anesthetized macaques. *Hum. Brain Mapp.* 34, 2154–2177. doi:10.1002/hbm.22058.
- Iordanova, B., Vazquez, A. L., Poplawsky, A. J., Fukuda, M., and Kim, S.-G. (2015). Neural and hemodynamic responses to optogenetic and sensory stimulation in the rat somatosensory cortex. *J. Cereb. Blood Flow Metab.* 35, 922–932. doi:10.1038/jcbfm.2015.10.
- Janke, A. L., and Ullmann, J. F. P. (2015). Robust methods to create ex vivo minimum deformation atlases for brain mapping. *Methods* 73, 18–26. doi:10.1016/j.ymeth.2015.01.005.
- Jenkins, B. G. (2012). Pharmacologic magnetic resonance imaging (phMRI): imaging drug action in the brain. *Neuroimage* 62, 1072–1085. doi:10.1016/j.neuroimage.2012.03.075.
- Johnson, G. A., Badea, A., Brandenburg, J., Cofer, G., Fubara, B., Liu, S., et al. (2010). Waxholm space: an image-based reference for coordinating mouse brain research. *Neuroimage* 53, 365–372. doi:10.1016/j.neuroimage.2010.06.067.
- Jonckers, E., Delgado y Palacios, R., Shah, D., Guglielmetti, C., Verhoye, M., and Van der Linden, A. (2014). Different anesthesia regimes modulate the functional connectivity outcome in mice. *Magn. Reson. Med.* 72, 1103–1112. doi:10.1002/mrm.24990.
- Jonckers, E., Shah, D., Hamaide, J., Verhoye, M., and Van der Linden, A. (2015). The power of using functional fMRI on small rodents to study brain pharmacology and disease. *Front. Pharmacol.* 6, 231. doi:10.3389/fphar.2015.00231.
- Jonckers, E., Van Audekerke, J., De Visscher, G., Van der Linden, A., and Verhoye, M. (2011). Functional connectivity fMRI of the rodent brain: comparison of functional connectivity networks in rat and mouse. *PLoS One* 6, e18876. doi:10.1371/journal.pone.0018876.
- Jung, W. B., Shim, H.-J., and Kim, S.-G. (2019). Mouse BOLD fMRI at ultrahigh field detects somatosensory networks including thalamic nuclei. *Neuroimage*. doi:10.1016/j.neuroimage.2019.03.063.
- Kahn, I., Desai, M., Knoblich, U., Bernstein, J., Henninger, M., Graybiel, A. M., et al. (2011). Characterization of the Functional MRI Response Temporal Linearity via Optical Control of Neocortical Pyramidal Neurons. *Journal of Neuroscience* 31, 15086–15091. doi:10.1523/jneurosci.0007-11.2011.
- Kahn, I., Knoblich, U., Desai, M., Bernstein, J., Graybiel, A. M., Boyden, E. S., et al. (2013). Optogenetic drive of neocortical pyramidal neurons generates fMRI signals that are correlated

with spiking activity. *Brain Res.* 1511, 33–45. doi:10.1016/j.brainres.2013.03.011.

Kalisch, R., Elbel, G. K., Gössl, C., Czisch, M., and Auer, D. P. (2001). Blood pressure changes induced by arterial blood withdrawal influence bold signal in anesthetized rats at 7 Tesla: implications for pharmacologic mri. *Neuroimage* 14, 891–898. doi:10.1006/nimg.2001.0890.

Kalthoff, D., Po, C., Wiedermann, D., and Hoehn, M. (2013). Reliability and spatial specificity of rat brain sensorimotor functional connectivity networks are superior under sedation compared with general anesthesia. *NMR Biomed.* 26, 638–650. doi:10.1002/nbm.2908.

Kalthoff, D., Seehafer, J. U., Po, C., Wiedermann, D., and Hoehn, M. (2011). Functional connectivity in the rat at 11.7T: Impact of physiological noise in resting state fMRI. *Neuroimage* 54, 2828–2839. doi:10.1016/j.neuroimage.2010.10.053.

Keilholz, S. D., Billings, J. C. W., Kai Wang, Abbas, A., Hafenegger, C., Wen-Ju Pan, et al. (2016).

Multiscale network activity in resting state fMRI. *Conf. Proc. IEEE Eng. Med. Biol. Soc.* 2016, 61–64. doi:10.1109/EMBC.2016.7590640.

Keilholz, S. D., Magnuson, M. E., Pan, W.-J., Willis, M., and Thompson, G. J. (2013). Dynamic properties of functional connectivity in the rodent. *Brain Connect.* 3, 31–40. doi:10.1089/brain.2012.0115.

Keilholz, S. D., Silva, A. C., Raman, M., Merkle, H., and Koretsky, A. P. (2006). BOLD and CBV-weighted functional magnetic resonance imaging of the rat somatosensory system. *Magn. Reson. Med.* 55, 316–324. doi:10.1002/mrm.20744.

Kim, S.-G., and Ogawa, S. (2012). Biophysical and Physiological Origins of Blood Oxygenation Level- Dependent fMRI Signals. *Journal of Cerebral Blood Flow & Metabolism* 32, 1188–1206. doi:10.1038/jcbfm.2012.23.

Kim, T., Masamoto, K., Fukuda, M., Vazquez, A., and Kim, S.-G. (2010). Frequency-dependent neural activity, CBF, and BOLD fMRI to somatosensory stimuli in isoflurane-anesthetized rats. *NeuroImage* 52, 224–233. doi:10.1016/j.neuroimage.2010.03.064.

Kiyatkin, E. A. (2007). Physiological and pathological brain hyperthermia. *Prog. Brain Res.* 162, 219–243. doi:10.1016/S0079-6123 (06)62012-8.

Klapoetke, N. C., Murata, Y., Kim, S. S., Pulver, S. R., Birdsey-Benson, A., Cho, Y. K., et al. (2014). Addendum: independent optical excitation of distinct neural populations. *Nat. Methods* 11, 972. Available at: <https://www.ncbi.nlm.nih.gov/pubmed/25317449>.

Klein, A., Andersson, J., Ardekani, B. A., Ashburner, J., Avants, B., Chiang, M.-C., et al. (2009). Evaluation of 14 nonlinear deformation algorithms applied to human brain MRI registration. *Neuroimage* 46, 786–802. doi:10.1016/j.neuroimage.2008.12.037.

Klein, R. L., Dayton, R. D., Leidenheimer, N. J., Jansen, K., Golde, T. E., and Zweig, R. M. (2006). Efficient Neuronal Gene Transfer with AAV8 Leads to Neurotoxic Levels of Tau or Green Fluorescent Proteins. *Molecular Therapy* 13, 517–527. doi:10.1016/j.ymthe.2005.10.008.

Klomp, A., Tremoleda, J. L., Schranter, A., Gsell, W., and Reneman, L. (2012). The use of pharmacological- challenge fMRI in pre-clinical research: application to the 5-HT system. *J. Vis. Exp.* doi:10.3791/3956.

- Knabl, J., Witschi, R., Hösl, K., Reinold, H., Zeilhofer, U. B., Ahmadi, S., et al. (2008). Reversal of pathological pain through specific spinal GABAA receptor subtypes. *Nature* 451, 330–334. doi:10.1038/nature06493.
- Kundu, P., Inati, S. J., Evans, J. W., Luh, W.-M., and Bandettini, P. A. (2012). Differentiating BOLD and non-BOLD signals in fMRI time series using multi-echo EPI. *Neuroimage* 60, 1759–1770. doi:10.1016/j.neuroimage.2011.12.028.
- Kundu, P., Santin, M. D., Bandettini, P. A., Bullmore, E. T., and Petiet, A. (2014). Differentiating BOLD and non-BOLD signals in fMRI time series from anesthetized rats using multi-echo EPI at 11.7 T. *Neuroimage* 102 Pt 2, 861–874. doi:10.1016/j.neuroimage.2014.07.025.
- Kyathanahally, S. P., Jia, H., Pustovyy, O. M., Waggoner, P., Beyers, R., Schumacher, J., et al. (2015). Anterior-posterior dissociation of the default mode network in dogs. *Brain Struct. Funct.* 220, 1063–1076. doi:10.1007/s00429-013-0700-x.
- Lahti, K. M., Ferris, C. F., Li, F., Sotak, C. H., and King, J. A. (1999). Comparison of evoked cortical activity in conscious and propofol-anesthetized rats using functional MRI. *Magnetic Resonance in Medicine* 41, 412–416. doi:10.1002/(sici)1522-2594(199902)41:2<412::aid-mrm28>3.0.co;2-3.
- Lai, H.-Y., Albaugh, D. L., Kao, Y.-C. J., Younce, J. R., and Shih, Y.-Y. I. (2015). Robust deep brain stimulation functional MRI procedures in rats and mice using an MR-compatible tungsten microwire electrode. *Magn. Reson. Med.* 73, 1246–1251. doi:10.1002/mrm.25239.
- Långsjö, J. W., Kaisti, K. K., Aalto, S., Hinkka, S., Aantaa, R., Oikonen, V., et al. (2003). Effects of subanesthetic doses of ketamine on regional cerebral blood flow, oxygen consumption, and blood volume in humans. *Anesthesiology* 99, 614–623. Available at: <https://www.ncbi.nlm.nih.gov/pubmed/12960545>.
- Larkin, J. R., Simard, M. A., Khrapitchev, A. A., Meakin, J. A., Okell, T. W., Craig, M., et al. (2018). Quantitative blood flow measurement in rat brain with multiphase arterial spin labelling magnetic resonance imaging. *J. Cereb. Blood Flow Metab.*, 271678X18756218. doi:10.1177/0271678X18756218.
- Lee, H.-M., Giguere, P. M., and Roth, B. L. (2014). DREADDs: novel tools for drug discovery and development. *Drug Discov. Today* 19, 469–473. doi:10.1016/j.drudis.2013.10.018.
- Lein, E. S., Hawrylycz, M. J., Ao, N., Ayres, M., Bensinger, A., Bernard, A., et al. (2007). Genome-wide atlas of gene expression in the adult mouse brain. *Nature* 445, 168–176. doi:10.1038/nature05453.
- Lemieux, L., Whittingstall, K., and Uludağ, K. (2015). “Combining fMRI with Other Modalities: Multimodal Neuroimaging,” in *fMRI: From Nuclear Spins to Brain Functions* Biological Magnetic Resonance, eds. K. Uludağ, K. Ugurbil, and L. Berliner (Boston, MA: Springer US), 739–768. doi:10.1007/978-1-4899-7591-1_25.
- Lenz, C., Rebel, A., van Ackern, K., Kuschinsky, W., and Waschke, K. F. (1998). Local Cerebral Blood Flow, Local Cerebral Glucose Utilization, and Flow-Metabolism Coupling during Sevoflurane versus Isoflurane Anesthesia in Rats. *Anesthesiology* 89, 1480–1488. doi:10.1097/00000542-199812000-00026.

- Leonardi, N., and Van De Ville, D. (2015). On spurious and real fluctuations of dynamic functional connectivity during rest. *Neuroimage* 104, 430–436. doi:10.1016/j.neuroimage.2014.09.007.
- Leong, A. T. L., Dong, C. M., Gao, P. P., Chan, R. W., To, A., Sanes, D. H., et al. (2018). Optogenetic auditory fMRI reveals the effects of visual cortical inputs on auditory midbrain response. *Sci. Rep.* 8, 8736. doi:10.1038/s41598-018-26568-1.
- Leslie, R. A., and James, M. F. (2000). Pharmacological magnetic resonance imaging: a new application for functional MRI. *Trends Pharmacol. Sci.* 21, 314–318. Available at: <https://www.ncbi.nlm.nih.gov/pubmed/10918638>.
- Liang, Z., King, J., and Zhang, N. (2011). Uncovering intrinsic connective architecture of functional networks in awake rat brain. *J. Neurosci.* 31, 3776–3783. doi:10.1523/JNEUROSCI.4557-10.2011.
- Liang, Z., Li, T., King, J., and Zhang, N. (2013). Mapping thalamocortical networks in rat brain using resting-state functional connectivity. *Neuroimage* 83, 237–244. doi:10.1016/j.neuroimage.2013.06.029.
- Liang, Z., Liu, X., and Zhang, N. (2015a). Dynamic resting state functional connectivity in awake and anesthetized rodents. *Neuroimage* 104, 89–99. doi:10.1016/j.neuroimage.2014.10.013.
- Liang, Z., Watson, G. D. R., Alloway, K. D., Lee, G., Neuberger, T., and Zhang, N. (2015b). Mapping the functional network of medial prefrontal cortex by combining optogenetics and fMRI in awake rats. *Neuroimage* 117, 114–123. doi:10.1016/j.neuroimage.2015.05.036.
- Li, G., Shih, Y.-Y. I., Kiel, J. W., De La Garza, B. H., Du, F., and Duong, T. Q. (2013). MRI study of cerebral, retinal and choroidal blood flow responses to acute hypertension. *Exp. Eye Res.* 112, 118–124. doi:10.1016/j.exer.2013.04.003.
- Li, J., Yang, R., Xia, K., Wang, T., Nie, B., Gao, K., et al. (2018). Effects of stress on behavior and resting-state fMRI in rats and evaluation of Telmisartan therapy in a stress-induced depression model. *BMC Psychiatry* 18. doi:10.1186/s12888-018-1880-y.
- Lin, J. Y. (2011). A user's guide to channelrhodopsin variants: features, limitations and future developments. *Experimental Physiology* 96, 19–25. doi:10.1113/expphysiol.2009.051961.
- Lin, J. Y., Knutsen, P. M., Muller, A., Kleinfeld, D., and Tsien, R. Y. (2013). ReaChR: a red-shifted variant of channelrhodopsin enables deep transcranial optogenetic excitation. *Nat. Neurosci.* 16, 1499–1508. doi:10.1038/nn.3502.
- Lin, J. Y., Lin, M. Z., Steinbach, P., and Tsien, R. Y. (2009). Characterization of Engineered Channelrhodopsin Variants with Improved Properties and Kinetics. *Biophysical Journal* 96, 1803–1814. doi:10.1016/j.bpj.2008.11.034.
- Lin, P., Fang, Z., Liu, J., and Lee, J. H. (2016). Optogenetic Functional MRI. *Journal of Visualized Experiments*. doi:10.3791/53346.
- Lin, Y. J., and Koretsky, A. P. (1997). Manganese ion enhances T1-weighted MRI during brain activation: an approach to direct imaging of brain function. *Magn. Reson. Med.* 38, 378–388. Available at: <https://www.ncbi.nlm.nih.gov/pubmed/9339438>.

- Liska, A., Bertero, A., Gomolka, R., Sabbioni, M., Galbusera, A., Barsotti, N., et al. (2018). Homozygous Loss of Autism-Risk Gene CNTNAP2 Results in Reduced Local and Long-Range Prefrontal Functional Connectivity. *Cereb. Cortex* 28, 1141–1153. doi:10.1093/cercor/bhx022.
- Liska, A., Galbusera, A., Schwarz, A. J., and Gozzi, A. (2015). Functional connectivity hubs of the mouse brain. *Neuroimage* 115, 281–291. doi:10.1016/j.neuroimage.2015.04.033.
- Liu, H.-S., Jan, M.-S., Chou, C.-K., Chen, P.-H., and Ke, N.-J. (1999). Is Green Fluorescent Protein Toxic to the Living Cells? *Biochemical and Biophysical Research Communications* 260, 712–717. doi:10.1006/bbrc.1999.0954.
- Liu, X., and Duyn, J. H. (2013). Time-varying functional network information extracted from brief instances of spontaneous brain activity. *Proc. Natl. Acad. Sci. U. S. A.* 110, 4392–4397. doi:10.1073/pnas.1216856110.
- Liu, X., -H. Zhu, X., Zhang, Y., and Chen, W. (2011). Neural Origin of Spontaneous Hemodynamic Fluctuations in Rats under Burst-Suppression Anesthesia Condition. *Cerebral Cortex* 21, 374–384. doi:10.1093/cercor/bhq105.
- Liu, X., Zhu, X.-H., Zhang, Y., and Chen, W. (2013). The Change of Functional Connectivity Specificity in Rats Under Various Anesthesia Levels and its Neural Origin. *Brain Topography* 26, 363–377. doi:10.1007/s10548-012-0267-5.
- Lohani, S., Poplawsky, A. J., Kim, S.-G., and Moghaddam, B. (2017). Unexpected global impact of VTA dopamine neuron activation as measured by opto-fMRI. *Mol. Psychiatry* 22, 585–594. doi:10.1038/mp.2016.102.
- Lowe, M. J., Dzemidzic, M., Lurito, J. T., Mathews, V. P., and Phillips, M. D. (2000). Correlations in low- frequency BOLD fluctuations reflect cortico-cortical connections. *Neuroimage* 12, 582–587. doi:10.1006/nimg.2000.0654.
- Lu, H., Donahue, M. J., and van Zijl, P. C. M. (2006). Detrimental effects of BOLD signal in arterial spin labeling fMRI at high field strength. *Magn. Reson. Med.* 56, 546–552. doi:10.1002/mrm.20976.
- Lu, H., Golay, X., Pekar, J. J., and van Zijl, P. C. M. (2003). Functional magnetic resonance imaging based on changes in vascular space occupancy. *Magnetic Resonance in Medicine* 50, 263–274. doi:10.1002/mrm.10519.
- Lu, H., and Stein, E. A. (2014). Resting state functional connectivity: Its physiological basis and application in neuropharmacology. *Neuropharmacology* 84, 79–89. doi:10.1016/j.neuropharm.2013.08.023.
- Lu, H., Zou, Q., Gu, H., Raichle, M. E., Stein, E. A., and Yang, Y. (2012). Rat brains also have a default mode network. *Proceedings of the National Academy of Sciences* 109, 3979–3984. doi:10.1073/pnas.1200506109.
- Lu, H., Zuo, Y., Gu, H., Waltz, J. A., Zhan, W., Scholl, C. A., et al. (2007). Synchronized delta oscillations correlate with the resting-state functional MRI signal. *Proc. Natl. Acad. Sci. U. S. A.* 104, 18265–18269. doi:10.1073/pnas.0705791104.
- Luo, F., Wu, G., Li, Z., and Li, S.-J. (2003). Characterization of effects of mean arterial blood pressure induced by cocaine and cocaine methiodide on BOLD signals in rat brain. *Magn. Reson.*

Med. 49, 264–270. doi:10.1002/mrm.10366.

MacLaren, D. A. A., Browne, R. W., Shaw, J. K., Krishnan Radhakrishnan, S., Khare, P., España, R. A., et al. (2016). Clozapine N-Oxide Administration Produces Behavioral Effects in Long-Evans Rats: Implications for Designing DREADD Experiments. *eNeuro* 3. doi:10.1523/ENEURO.0219-16.2016.

Madisen, L., Mao, T., Koch, H., Zhuo, J.-M., Berenyi, A., Fujisawa, S., et al. (2012). A toolbox of Cre- dependent optogenetic transgenic mice for light-induced activation and silencing. *Nat. Neurosci.* 15, 793–802. doi:10.1038/nn.3078.

Magnuson, M. E., Thompson, G. J., Pan, W.-J., and Keilholz, S. D. (2014). Time-dependent effects of isoflurane and dexmedetomidine on functional connectivity, spectral characteristics, and spatial distribution of spontaneous BOLD fluctuations. *NMR Biomed.* 27, 291–303. doi:10.1002/nbm.3062.

Mahler, S. V., and Aston-Jones, G. (2018). CNO Evil? Considerations for the Use of DREADDs in Behavioral Neuroscience. *Neuropsychopharmacology* 43, 934–936. doi:10.1038/npp.2017.299.

Majeed, W., Magnuson, M., Hasenkamp, W., Schwarb, H., Schumacher, E. H., Barsalou, L., et al. (2011). Spatiotemporal dynamics of low frequency BOLD fluctuations in rats and humans. *Neuroimage* 54, 1140–1150. doi:10.1016/j.neuroimage.2010.08.030.

Mandeville, J. B. (2012). IRON fMRI measurements of CBV and implications for BOLD signal. *NeuroImage* 62, 1000–1008. doi:10.1016/j.neuroimage.2012.01.070.

Mandeville, J. B., Jenkins, B. G., Chen, Y.-C. I., Choi, J.-K., Kim, Y. R., Belen, D., et al. (2004). Exogenous contrast agent improves sensitivity of gradient-echo functional magnetic resonance imaging at 9.4 T. *Magn. Reson. Med.* 52, 1272–1281. doi:10.1002/mrm.20278.

Mandeville, J. B., Leite, F. P., and Marota, J. J. A. (2007). Spin-echo MRI underestimates functional changes in microvascular cerebral blood plasma volume using exogenous contrast agent. *Magn. Reson. Med.* 58, 769–776. doi:10.1002/mrm.21380.

Mandeville, J. B., and Marota, J. J. (1999). Vascular filters of functional MRI: spatial localization using BOLD and CBV contrast. *Magn. Reson. Med.* 42, 591–598. Available at: <https://www.ncbi.nlm.nih.gov/pubmed/10467305>.

Mandeville, J. B., Marota, J. J., Kosofsky, B. E., Keltner, J. R., Weissleder, R., Rosen, B. R., et al. (1998). Dynamic functional imaging of relative cerebral blood volume during rat forepaw stimulation. *Magn. Reson. Med.* 39, 615–624. Available at: <https://www.ncbi.nlm.nih.gov/pubmed/9543424>.

Mandeville, J. B., Sander, C. Y. M., Jenkins, B. G., Hooker, J. M., Catana, C., Vanduffel, W., et al. (2013). A receptor-based model for dopamine-induced fMRI signal. *Neuroimage* 75, 46–57. doi:10.1016/j.neuroimage.2013.02.036.

Mantini, D., Gerits, A., Nelissen, K., Durand, J.-B., Joly, O., Simone, L., et al. (2011). Default mode of brain function in monkeys. *J. Neurosci.* 31, 12954–12962. doi:10.1523/JNEUROSCI.2318-11.2011.

Manvich, D. F., Webster, K. A., Foster, S. L., Farrell, M. S., Ritchie, J. C., Porter, J. H., et al. (2018). The DREADD agonist clozapine N-oxide (CNO) is reverse-metabolized to clozapine and produces clozapine-like interoceptive stimulus effects in rats and mice. *Sci. Rep.* 8, 3840.

doi:10.1038/s41598-018-22116-z.

Markicevic, M., Fulcher, B. D., Lewis, C., Helmchen, F., Rudin, M., Zerbi, V., et al. Cortical excitation:inhibition imbalance causes network specific functional hypoconnectivity: a DREADD-fMRI study. doi:10.1101/492108.

Marota, J. J., Mandeville, J. B., Weisskoff, R. M., Moskowitz, M. A., Rosen, B. R., and Kosofsky, B. E. (2000). Cocaine activation discriminates dopaminergic projections by temporal response: an fMRI study in Rat. *Neuroimage* 11, 13–23. doi:10.1006/nimg.1999.0520.

Martin, C., and Sibson, N. R. (2008). Pharmacological MRI in animal models: a useful tool for 5-HT research? *Neuropharmacology* 55, 1038–1047. doi:10.1016/j.neuropharm.2008.08.014.

Maus, B., and van Breukelen, G. J. P. (2013). Optimal Design for Functional Magnetic Resonance Imaging Experiments. *Zeitschrift für Psychologie* 221, 174–189. doi:10.1027/2151-2604/a000145.

Mazziotta, J., Toga, A., Evans, A., Fox, P., Lancaster, J., Zilles, K., et al. (2001). A probabilistic atlas and reference system for the human brain: International Consortium for Brain Mapping (ICBM). *Philos. Trans. R. Soc. Lond. B Biol. Sci.* 356, 1293–1322. doi:10.1098/rstb.2001.0915.

McLaren, D. G., Kosmatka, K. J., Oakes, T. R., Kroenke, C. D., Kohama, S. G., Matochik, J. A., et al. (2009). A population-average MRI-based atlas collection of the rhesus macaque. *Neuroimage* 45, 52– 59. doi:10.1016/j.neuroimage.2008.10.058.

Mechling, A. E., Hübner, N. S., Lee, H.-L., Hennig, J., von Elverfeldt, D., and Harsan, L.-A. (2014). Fine- grained mapping of mouse brain functional connectivity with resting-state fMRI. *Neuroimage* 96, 203– 215. doi:10.1016/j.neuroimage.2014.03.078.

Medda, A., Hoffmann, L., Magnuson, M., Thompson, G., Pan, W.-J., and Keilholz, S. (2016). Wavelet-based clustering of resting state MRI data in the rat. *Magn. Reson. Imaging* 34, 35–43. doi:10.1016/j.mri.2015.10.005.

Medhi, B., Misra, S., Avti, P. K., Kumar, P., Kumar, H., and Singh, B. (2014). Role of neuroimaging in drug development. *Reviews in the Neurosciences* 25. doi:10.1515/revneuro-2014-0031.

Milham, M. P., Ai, L., Koo, B., Xu, T., Amiez, C., Balezeau, F., et al. (2018). An Open Resource for Non- human Primate Imaging. *Neuron* 100, 61–74.e2. doi:10.1016/j.neuron.2018.08.039.

Miller, K. L. (2012). FMRI using balanced steady-state free precession (SSFP). *Neuroimage* 62, 713–719. doi:10.1016/j.neuroimage.2011.10.040.

Miller, K. L., Alfaro-Almagro, F., Bangerter, N. K., Thomas, D. L., Yacoub, E., Xu, J., et al. (2016). Multimodal population brain imaging in the UK Biobank prospective epidemiological study. *Nat. Neurosci.* 19, 1523–1536. doi:10.1038/nn.4393.

Miller, K. L., and Jezzard, P. (2008). Modeling SSFP functional MRI contrast in the brain. *Magn. Reson. Med.* 60, 661–673. doi:10.1002/mrm.21690.

Miller, K. L., Smith, S. M., Jezzard, P., and Pauly, J. M. (2006). High-resolution FMRI at 1.5T using balanced SSFP. *Magn. Reson. Med.* 55, 161–170. doi:10.1002/mrm.20753.

Miller, K. L., Smith, S. M., Jezzard, P., Wiggins, G. C., and Wiggins, C. J. (2007). Signal and

noise characteristics of SSFP fMRI: a comparison with GRE at multiple field strengths. *Neuroimage* 37, 1227–1236. doi:10.1016/j.neuroimage.2007.06.024.

Minzenberg, M. J. (2012). Pharmacological MRI approaches to understanding mechanisms of drug action. *Curr. Top. Behav. Neurosci.* 11, 365–388. doi:10.1007/7854_2011_177.

Miranda-Dominguez, O., Mills, B. D., Grayson, D., Woodall, A., Grant, K. A., Kroenke, C. D., et al. (2014).

Bridging the gap between the human and macaque connectome: a quantitative comparison of global interspecies structure-function relationships and network topology. *J. Neurosci.* 34, 5552–5563. doi:10.1523/JNEUROSCI.4229-13.2014.

Miyashita, T., Shao, Y. R., Chung, J., Pourzia, O., and Feldman, D. E. (2013). Long-term channelrhodopsin-2 (ChR2) expression can induce abnormal axonal morphology and targeting in cerebral cortex. *Front. Neural Circuits* 7, 8. doi:10.3389/fncir.2013.00008.

Morgan, V. L., Dawant, B. M., Li, Y., and Pickens, D. R. (2007). Comparison of fMRI statistical software packages and strategies for analysis of images containing random and stimulus-correlated motion.

Comput. Med. Imaging Graph. 31, 436–446. doi:10.1016/j.compmedimag.2007.04.002.

Mueggler, T., Baumann, D., Rausch, M., and Rudin, M. (2001). Bicuculline-induced brain activation in mice detected by functional magnetic resonance imaging. *Magn. Reson. Med.* 46, 292–298. Available at: <https://www.ncbi.nlm.nih.gov/pubmed/11477632>.

Murphy, K., Birn, R. M., and Bandettini, P. A. (2013). Resting-state fMRI confounds and cleanup.

Neuroimage 80, 349–359. doi:10.1016/j.neuroimage.2013.04.001.

Nadkarni, N. A., Bougacha, S., Garin, C., Dhenain, M., and Picq, J.-L. (2018). Digital templates and brain atlas dataset for the mouse lemur primate. *Data Brief* 21, 1178–1185. doi:10.1016/j.dib.2018.10.067.

Nagel, G., Szellas, T., Huhn, W., Kateriya, S., Adeishvili, N., Berthold, P., et al. (2003). Channelrhodopsin-2, a directly light-gated cation-selective membrane channel. *Proc. Natl. Acad. Sci. U. S. A.* 100, 13940–13945. doi:10.1073/pnas.1936192100.

Nichols, T. E., Das, S., Eickhoff, S. B., Evans, A. C., Glatard, T., Hanke, M., et al. (2017). Best practices in data analysis and sharing in neuroimaging using MRI. *Nat. Neurosci.* 20, 299–303. doi:10.1038/nn.4500.

Nie, B., Chen, K., Zhao, S., Liu, J., Gu, X., Yao, Q., et al. (2013). A rat brain MRI template with digital stereotaxic atlas of fine anatomical delineations in paxinos space and its automated application in voxel-wise analysis. *Hum. Brain Mapp.* 34, 1306–1318. doi:10.1002/hbm.21511.

Norris, D. G. (2006). Principles of magnetic resonance assessment of brain function. *J. Magn. Reson. Imaging* 23, 794–807. doi:10.1002/jmri.20587.

Norris, D. G. (2012). Spin-echo fMRI: The poor relation? *Neuroimage* 62, 1109–1115. doi:10.1016/j.neuroimage.2012.01.003.

Nunes, D., Ianus, A., and Shemesh, N. (2019). Layer-specific connectivity revealed by diffusion-weighted functional MRI in the rat thalamocortical pathway. *Neuroimage* 184, 646–657. doi:10.1016/j.neuroimage.2018.09.050.

- Ogawa, S., Lee, T. M., Kay, A. R., and Tank, D. W. (1990). Brain magnetic resonance imaging with contrast dependent on blood oxygenation. *Proc. Natl. Acad. Sci. U. S. A.* 87, 9868–9872. Available at: <https://www.ncbi.nlm.nih.gov/pubmed/2124706>.
- Ortiz, J. J., Portillo, W., Paredes, R. G., Young, L. J., and Alcauter, S. (2018). Resting state brain networks in the prairie vole. *Scientific Reports* 8. doi:10.1038/s41598-017-17610-9.
- Paasonen, J., Stenroos, P., Salo, R. A., Kiviniemi, V., and Gröhn, O. (2018). Functional connectivity under six anesthesia protocols and the awake condition in rat brain. *NeuroImage* 172, 9–20. doi:10.1016/j.neuroimage.2018.01.014.
- Pagani, M., Bertero, A., Liska, A., Galbusera, A., Sabbioni, M., Barsotti, N., et al. (2019). Deletion of autism risk gene Shank3 disrupts prefrontal connectivity. *J. Neurosci.* doi:10.1523/JNEUROSCI.2529-18.2019.
- Pan, W.-J., Billings, J. C. W., Grooms, J. K., Shakil, S., and Keilholz, S. D. (2015). Considerations for resting state functional MRI and functional connectivity studies in rodents. *Front. Neurosci.* 9, 269. doi:10.3389/fnins.2015.00269.
- Patel, A. J., Honoré, E., Lesage, F., Fink, M., Romey, G., and Lazdunski, M. (1999). Inhalational anesthetics activate two-pore-domain background K⁺ channels. *Nat. Neurosci.* 2, 422–426. doi:10.1038/8084.
- Pawela, C. P., Biswal, B. B., Cho, Y. R., Kao, D. S., Li, R., Jones, S. R., et al. (2008). Resting-state functional connectivity of the rat brain. *Magn. Reson. Med.* 59, 1021–1029. doi:10.1002/mrm.21524.
- Paxinos, G., and Franklin, K. B. J. (2012). *Paxinos and Franklin's the Mouse Brain in Stereotaxic Coordinates*. Academic Press Available at: https://books.google.com/books/about/Paxinos_and_Franklin_s_the_Mouse_Brain_i.html?hl=&id=8RJZLwEACAAJ.
- Peters, A. M., Brookes, M. J., Hoogenraad, F. G., Gowland, P. A., Francis, S. T., Morris, P. G., et al. (2007). T2* measurements in human brain at 1.5, 3 and 7 T. *Magnetic Resonance Imaging* 25, 748–753. doi:10.1016/j.mri.2007.02.014.
- Petersen, R. C., Aisen, P. S., Beckett, L. A., Donohue, M. C., Gamst, A. C., Harvey, D. J., et al. (2010). Alzheimer's Disease Neuroimaging Initiative (ADNI): clinical characterization. *Neurology* 74, 201–209. doi:10.1212/WNL.0b013e3181cb3e25.
- Poldrack, R. A., Barch, D. M., Mitchell, J. P., Wager, T. D., Wagner, A. D., Devlin, J. T., et al. (2013). Toward open sharing of task-based fMRI data: the OpenfMRI project. *Front. Neuroinform.* 7, 12. doi:10.3389/fninf.2013.00012.
- Poser, B. A., Versluis, M. J., Hoogduin, J. M., and Norris, D. G. (2006). BOLD contrast sensitivity enhancement and artifact reduction with multiecho EPI: parallel-acquired inhomogeneity-desensitized fMRI. *Magn. Reson. Med.* 55, 1227–1235. doi:10.1002/mrm.20900.
- Posse, S., Wiese, S., Gembris, D., Mathiak, K., Kessler, C., Grosse-Ruyken, M. L., et al. (1999). Enhancement of BOLD-contrast sensitivity by single-shot multi-echo functional MR imaging. *Magn. Reson. Med.* 42, 87–97. Available at: <https://www.ncbi.nlm.nih.gov/pubmed/10398954>.
- Power, J. D., Mitra, A., Laumann, T. O., Snyder, A. Z., Schlaggar, B. L., and Petersen, S. E.

- (2014). Methods to detect, characterize, and remove motion artifact in resting state fMRI. *Neuroimage* 84, 320–341. doi:10.1016/j.neuroimage.2013.08.048.
- Raichle, M. E., MacLeod, A. M., Snyder, A. Z., Powers, W. J., Gusnard, D. A., and Shulman, G. L. (2001). A default mode of brain function. *Proc. Natl. Acad. Sci. U. S. A.* 98, 676–682. doi:10.1073/pnas.98.2.676.
- Ramos-Cabrer, P., Weber, R., Wiedermann, D., and Hoehn, M. (2005). Continuous noninvasive monitoring of transcutaneous blood gases for a stable and persistent BOLD contrast in fMRI studies in the rat. *NMR Biomed.* 18, 440–446. doi:10.1002/nbm.978.
- Rao, J.-S., Liu, Z., Zhao, C., Wei, R.-H., Zhao, W., Tian, P.-Y., et al. (2017). Ketamine changes the local resting-state functional properties of anesthetized-monkey brain. *Magn. Reson. Imaging* 43, 144–150. doi:10.1016/j.mri.2017.07.025.
- Rauch, A., Rainer, G., Augath, M., Oeltermann, A., and Logothetis, N. K. (2008). Pharmacological MRI combined with electrophysiology in non-human primates: effects of Lidocaine on primary visual cortex. *Neuroimage* 40, 590–600. doi:10.1016/j.neuroimage.2007.12.009.
- Ray, R. S., Corcoran, A. E., Brust, R. D., Kim, J. C., Richerson, G. B., Nattie, E., et al. (2011). Impaired respiratory and body temperature control upon acute serotonergic neuron inhibition. *Science* 333, 637–642. doi:10.1126/science.1205295.
- Razoux, F., Baltes, C., Mueggler, T., Seuwen, A., Russig, H., Mansuy, I., et al. (2013). Functional MRI to assess alterations of functional networks in response to pharmacological or genetic manipulations of the serotonergic system in mice. *Neuroimage* 74, 326–336. doi:10.1016/j.neuroimage.2013.02.031.
- Reimann, C., Brangsch, J., Kaufmann, J. O., Adams, L. C., Onthank, D. C., Robinson, S. P., et al. (2018a). Contrast-Enhanced Magnetic Resonance Angiography Using a Novel Elastin-Specific Molecular Probe in an Experimental Animal Model. *Contrast Media Mol. Imaging* 2018, 9217456. doi:10.1155/2018/9217456.
- Reimann, H. M., Todiras, M., Hodge, R., Huelnhagen, T., Millward, J. M., Turner, R., et al. (2018b). Somatosensory BOLD fMRI reveals close link between salient blood pressure changes and the murine neuromatrix. *Neuroimage* 172, 562–574. doi:10.1016/j.neuroimage.2018.02.002.
- Roelofs, T. J. M., Verharen, J. P. H., van Tilborg, G. A. F., Boekhoudt, L., van der Toorn, A., de Jong, J. W., et al. (2017). A novel approach to map induced activation of neuronal networks using chemogenetics and functional neuroimaging in rats: A proof-of-concept study on the mesocorticolimbic system. *Neuroimage* 156, 109–118. doi:10.1016/j.neuroimage.2017.05.021.
- Rohlfing, T., Kroenke, C. D., Sullivan, E. V., Dubach, M. F., Bowden, D. M., Grant, K. A., et al. (2012). The INIA19 Template and NeuroMaps Atlas for Primate Brain Image Parcellation and Spatial Normalization. *Front. Neuroinform.* 6, 27. doi:10.3389/fninf.2012.00027.
- Roth, B. L. (2016). DREADDs for Neuroscientists. *Neuron* 89, 683–694. doi:10.1016/j.neuron.2016.01.040.
- Rudrapatna, U. S., van der Toorn, A., van Meer, M. P. A., and Dijkhuizen, R. M. (2012). Impact of hemodynamic effects on diffusion-weighted fMRI signals. *Neuroimage* 61, 106–114. doi:10.1016/j.neuroimage.2012.02.050.

- Rungta, R. L., Osmanski, B.-F., Boido, D., Tanter, M., and Charpak, S. (2017). Light controls cerebral blood flow in naive animals. *Nat. Commun.* 8, 14191. doi:10.1038/ncomms14191.
- Ryali, S., Shih, Y.-Y. I., Chen, T., Kochalka, J., Albaugh, D., Fang, Z., et al. (2016). Combining optogenetic stimulation and fMRI to validate a multivariate dynamical systems model for estimating causal brain interactions. *Neuroimage* 132, 398–405. doi:10.1016/j.neuroimage.2016.02.067.
- Saleem, K. S., and Logothetis, N. K. (2012). *A Combined MRI and Histology Atlas of the Rhesus Monkey Brain in Stereotaxic Coordinates*. Academic Press Available at: <https://market.android.com/details?id=book-evc5q5c-EbsC>.
- Scheffler, K., and Ehse, P. (2016). High-resolution mapping of neuronal activation with balanced SSFP at 9.4 tesla. *Magn. Reson. Med.* 76, 163–171. doi:10.1002/mrm.25890.
- Scheffler, K., Seifritz, E., Bilecen, D., Venkatesan, R., Hennig, J., Deimling, M., et al. (2001). Detection of BOLD changes by means of a frequency-sensitive trueFISP technique: preliminary results. *NMR Biomed.* 14, 490–496. Available at: <https://www.ncbi.nlm.nih.gov/pubmed/11746942>.
- Schlegel, F., Schroeter, A., and Rudin, M. (2015). The hemodynamic response to somatosensory stimulation in mice depends on the anesthetic used: Implications on analysis of mouse fMRI data. *Neuroimage* 116, 40–49. doi:10.1016/j.neuroimage.2015.05.013.
- Schmid, F., Wachsmuth, L., Albers, F., Schwalm, M., Stroh, A., and Faber, C. (2017). True and apparent optogenetic BOLDfMRI signals. *Magnetic Resonance in Medicine* 77, 126–136. doi:10.1002/mrm.26095.
- Schmid, F., Wachsmuth, L., Schwalm, M., Prouvot, P.-H., Jubal, E. R., Fois, C., et al. (2016). Assessing sensory versus optogenetic network activation by combining (o)fMRI with optical Ca2 recordings. *Journal of Cerebral Blood Flow & Metabolism* 36, 1885–1900. doi:10.1177/0271678x15619428.
- Schroeder, M. P., Weiss, C., Procissi, D., Disterhoft, J. F., and Wang, L. (2016). Intrinsic connectivity of neural networks in the awake rabbit. *Neuroimage* 129, 260–267. doi:10.1016/j.neuroimage.2016.01.010.
- Schroeter, A., Schlegel, F., Seuwen, A., Grandjean, J., and Rudin, M. (2014). Specificity of stimulus-evoked fMRI responses in the mouse: the influence of systemic physiological changes associated with innocuous stimulation under four different anesthetics. *Neuroimage* 94, 372–384. doi:10.1016/j.neuroimage.2014.01.046.
- Schwarz, A. J., Danckaert, A., Reese, T., Gozzi, A., Paxinos, G., Watson, C., et al. (2006). A stereotaxic MRI template set for the rat brain with tissue class distribution maps and co-registered anatomical atlas: application to pharmacological MRI. *Neuroimage* 32, 538–550. doi:10.1016/j.neuroimage.2006.04.214.
- Schwarz, A. J., Gozzi, A., Reese, T., Heidbreder, C. A., and Bifone, A. (2007). Pharmacological modulation of functional connectivity: the correlation structure underlying the phMRI response to d-amphetamine modified by selective dopamine D3 receptor antagonist SB277011A. *Magn. Reson. Imaging* 25, 811–820. doi:10.1016/j.mri.2007.02.017.
- Schweinhardt, P., Fransson, P., Olson, L., Spenger, C., and Andersson, J. L. R. (2003). A template for spatial normalisation of MR images of the rat brain. *J. Neurosci. Methods* 129, 105–

113. Available at: <https://www.ncbi.nlm.nih.gov/pubmed/14511814>.

Sciolino, N. R., Plummer, N. W., Chen, Y.-W., Alexander, G. M., Robertson, S. D., Dudek, S. M., et al. (2016). Recombinase-Dependent Mouse Lines for Chemogenetic Activation of Genetically Defined Cell Types. *Cell Reports* 15, 2563–2573. doi:10.1016/j.celrep.2016.05.034.

Scott, N. A., and Murphy, T. H. (2012). Hemodynamic Responses Evoked by Neuronal Stimulation via Channelrhodopsin-2 Can Be Independent of Intracortical Glutamatergic Synaptic Transmission. *PLoS ONE* 7, e29859. doi:10.1371/journal.pone.0029859.

Selent, J., López, L., Sanz, F., and Pastor, M. (2008). Multi-Receptor Binding Profile of Clozapine and Olanzapine: A Structural Study Based on the New β 2Adrenergic Receptor Template. *ChemMedChem* 3, 1194–1198. doi:10.1002/cmdc.200800074.

Sforazzini, F., Schwarz, A. J., Galbusera, A., Bifone, A., and Gozzi, A. (2014). Distributed BOLD and CBV- weighted resting-state networks in the mouse brain. *Neuroimage* 87, 403–415. doi:10.1016/j.neuroimage.2013.09.050.

Shah, D., Blockx, I., Guns, P.-J., De Deyn, P. P., Van Dam, D., Jonckers, E., et al. (2015). Acute modulation of the cholinergic system in the mouse brain detected by pharmacological resting-state functional MRI. *Neuroimage* 109, 151–159. doi:10.1016/j.neuroimage.2015.01.009.

Shah, D., Blockx, I., Keliris, G. A., Kara, F., Jonckers, E., Verhoye, M., et al. (2016). Cholinergic and serotonergic modulations differentially affect large-scale functional networks in the mouse brain. *Brain Struct. Funct.* 221, 3067–3079. doi:10.1007/s00429-015-1087-7.

Shah, Y. B., Prior, M. J. W., Dixon, A. L., Morris, P. G., and Marsden, C. A. (2004). Detection of cannabinoid agonist evoked increase in BOLD contrast in rats using functional magnetic resonance imaging. *Neuropharmacology* 46, 379–387. doi:10.1016/j.neuropharm.2003.09.023.

Shakil, S., Billings, J. C., Keilholz, S. D., and Lee, C.-H. (2018). Parametric Dependencies of Sliding Window Correlation. *IEEE Trans. Biomed. Eng.* 65, 254–263. doi:10.1109/TBME.2017.2762763.

Shakil, S., Keilholz, S. D., and Chin-Hui Lee (2016). Adaptive change point detection of dynamic functional connectivity networks. *Conf. Proc. IEEE Eng. Med. Biol. Soc.* 2016, 1135–1138. doi:10.1109/EMBC.2016.7590904.

Shih, Y.-Y. I., Chiang, Y.-C., Shyu, B.-C., Jaw, F.-S., Duong, T. Q., and Chang, C. (2012a). Endogenous opioid-dopamine neurotransmission underlie negative CBV fMRI signals. *Exp. Neurol.* 234, 382–388. doi:10.1016/j.expneurol.2011.12.042.

Shih, Y.-Y. I., Huang, S., Chen, Y.-Y., Lai, H.-Y., Kao, Y.-C. J., Du, F., et al. (2014). Imaging neurovascular function and functional recovery after stroke in the rat striatum using forepaw stimulation. *J. Cereb. Blood Flow Metab.* 34, 1483–1492. doi:10.1038/jcbfm.2014.103.

Shih, Y.-Y. I., Li, G., Muir, E. R., De La Garza, B. H., Kiel, J. W., and Duong, T. Q. (2012b). Pharmacological MRI of the choroid and retina: blood flow and BOLD responses during nitroprusside infusion. *Magn. Reson. Med.* 68, 1273–1278. doi:10.1002/mrm.24112.

Shim, H.-J., Jung, W. B., Schlegel, F., Lee, J., Kim, S., Lee, J., et al. (2018). Mouse fMRI under ketamine and xylazine anesthesia: Robust contralateral somatosensory cortex activation in response to forepaw stimulation. *Neuroimage* 177, 30–44. doi:10.1016/j.neuroimage.2018.04.062.

- Sicard, K., Shen, Q., Brevard, M. E., Sullivan, R., Ferris, C. F., King, J. A., et al. (2003). Regional Cerebral Blood Flow and BOLD Responses in Conscious and Anesthetized Rats Under Basal and Hypercapnic Conditions: Implications for Functional MRI Studies. *Journal of Cerebral Blood Flow & Metabolism*, 472–481. doi:10.1097/00004647-200304000-00011.
- Silva, A. C. (2012). Using manganese-enhanced MRI to understand BOLD. *Neuroimage* 62, 1009–1013. doi:10.1016/j.neuroimage.2012.01.008.
- Silva, A. C., and Kim, S.-G. (1999). Pseudo-continuous arterial spin labeling technique for measuring CBF dynamics with high temporal resolution. *Magnetic Resonance in Medicine* 42, 425–429. doi:10.1002/(sici)1522-2594(199909)42:3<425::aid-mrm3>3.0.co;2-s.
- Silva, A. C., Lee, S. P., Yang, G., Iadecola, C., and Kim, S. G. (1999). Simultaneous blood oxygenation level-dependent and cerebral blood flow functional magnetic resonance imaging during forepaw stimulation in the rat. *J. Cereb. Blood Flow Metab.* 19, 871–879. doi:10.1097/00004647-199908000-00006.
- Sinclair, M. D. (2003). A review of the physiological effects of alpha2-agonists related to the clinical use of medetomidine in small animal practice. *Can. Vet. J.* 44, 885–897. Available at: <https://www.ncbi.nlm.nih.gov/pubmed/14664351>.
- Smith, K. S., Bucci, D. J., Luikart, B. W., and Mahler, S. V. (2016). DREADDS: Use and application in behavioral neuroscience. *Behav. Neurosci.* 130, 137–155. doi:10.1037/bne0000135.
- Soares, J. M., Magalhães, R., Moreira, P. S., Sousa, A., Ganz, E., Sampaio, A., et al. (2016). A Hitchhiker's Guide to Functional Magnetic Resonance Imaging. *Front. Neurosci.* 10, 515. doi:10.3389/fnins.2016.00515.
- Speck, O., and Hennig, J. (1998). Functional imaging by I0- and T2*-parameter mapping using multi-image EPI. *Magn. Reson. Med.* 40, 243–248. Available at: <https://www.ncbi.nlm.nih.gov/pubmed/9702706>.
- Sporns, O., and Betzel, R. F. (2016). Modular Brain Networks. *Annual Review of Psychology* 67, 613–640. doi:10.1146/annurev-psych-122414-033634.
- Squillace, M., Doderio, L., Federici, M., Migliarini, S., Errico, F., Napolitano, F., et al. (2014). Dysfunctional dopaminergic neurotransmission in asocial BTBR mice. *Transl. Psychiatry* 4, e427. doi:10.1038/tp.2014.69.
- Stafford, J. M., Jarrett, B. R., Miranda-Dominguez, O., Mills, B. D., Cain, N., Mihalas, S., et al. (2014). Large-scale topology and the default mode network in the mouse connectome. *Proc. Natl. Acad. Sci. U. S. A.* 111, 18745–18750. doi:10.1073/pnas.1404346111.
- Steward, C. A., Marsden, C. A., Prior, M. J. W., Morris, P. G., and Shah, Y. B. (2005). Methodological considerations in rat brain BOLD contrast pharmacological MRI. *Psychopharmacology* 180, 687–704. doi:10.1007/s00213-005-2213-7.
- Straathof, M., Sinke, M. R., Dijkhuizen, R. M., and Otte, W. M. (2019). A systematic review on the quantitative relationship between structural and functional network connectivity strength in mammalian brains. *J. Cereb. Blood Flow Metab.* 39, 189–209. doi:10.1177/0271678X18809547.
- Stujenske, J. M., Spellman, T., and Gordon, J. A. (2015). Modeling the Spatiotemporal Dynamics of Light and Heat Propagation for In Vivo Optogenetics. *Cell Rep.* 12, 525–534. doi:10.1016/j.celrep.2015.06.036.

Takata, N., Yoshida, K., Komaki, Y., Xu, M., Sakai, Y., Hikishima, K., et al. (2015). Optogenetic activation of CA1 pyramidal neurons at the dorsal and ventral hippocampus evokes distinct brain-wide responses revealed by mouse fMRI. *PLoS One* 10, e0121417. doi:10.1371/journal.pone.0121417.

Tambini, A., Ketz, N., and Davachi, L. (2010). Enhanced Brain Correlations during Rest Are Related to Memory for Recent Experiences. *Neuron* 65, 280–290. doi:10.1016/j.neuron.2010.01.001.

The Rat Brain in Stereotaxic Coordinates (1982). doi:10.1016/c2009-0-63235-9.

Tjandra, T., Brooks, J. C. W., Figueiredo, P., Wise, R., Matthews, P. M., and Tracey, I. (2005). Quantitative assessment of the reproducibility of functional activation measured with BOLD and MR perfusion imaging: Implications for clinical trial design. *NeuroImage* 27, 393–401. doi:10.1016/j.neuroimage.2005.04.021.

Tsubota, T., Ohashi, Y., Tamura, K., and Miyashita, Y. (2012). Optogenetic inhibition of Purkinje cell activity reveals cerebellar control of blood pressure during postural alterations in anesthetized rats. *Neuroscience* 210, 137–144. doi:10.1016/j.neuroscience.2012.03.014.

Tsurugizawa, T., Ciobanu, L., and Le Bihan, D. (2013). Water diffusion in brain cortex closely tracks underlying neuronal activity. *Proc. Natl. Acad. Sci. U. S. A.* 110, 11636–11641. doi:10.1073/pnas.1303178110.

Tuor, U. I., McKenzie, E., and Tomanek, B. (2002). Functional magnetic resonance imaging of tonic pain and vasopressor effects in rats. *Magn. Reson. Imaging* 20, 707–712. Available at: <https://www.ncbi.nlm.nih.gov/pubmed/12591566>.

Uhrig, L., Ciobanu, L., Djemai, B., Le Bihan, D., and Jarraya, B. (2014). Sedation agents differentially modulate cortical and subcortical blood oxygenation: evidence from ultra-high field MRI at 17.2 T. *PLoS One* 9, e100323. doi:10.1371/journal.pone.0100323.

Uhrig, L., Sitt, J. D., Jacob, A., Tasserie, J., Barttfeld, P., Dupont, M., et al. (2018). Resting-state Dynamics as a Cortical Signature of Anesthesia in Monkeys. *Anesthesiology* 129, 942–958. doi:10.1097/ALN.0000000000002336.

Uludağ, K., Müller-Bierl, B., and Uğurbil, K. (2009). An integrative model for neuronal activity-induced signal changes for gradient and spin echo functional imaging. *Neuroimage* 48, 150–165. doi:10.1016/j.neuroimage.2009.05.051.

Valdés-Hernández, P. A., Sumiyoshi, A., Nonaka, H., Haga, R., Aubert-Vásquez, E., Ogawa, T., et al. (2011). An in vivo MRI Template Set for Morphometry, Tissue Segmentation, and fMRI Localization in Rats. *Front. Neuroinform.* 5, 26. doi:10.3389/fninf.2011.00026.

Van der Linden, A., Van Camp, N., Ramos-Cabrera, P., and Hoehn, M. (2007). Current status of functional MRI on small animals: application to physiology, pathophysiology, and cognition. *NMR Biomed.* 20, 522–545. doi:10.1002/nbm.1131.

van der Marel, K., Homberg, J. R., Otte, W. M., and Dijkhuizen, R. M. (2013). Functional and structural neural network characterization of serotonin transporter knockout rats. *PLoS One* 8, e57780. doi:10.1371/journal.pone.0057780.

Van Essen, D. C., Glasser, M. F., Dierker, D. L., and Harwell, J. (2012). Cortical parcellations of

the macaque monkey analyzed on surface-based atlases. *Cereb. Cortex* 22, 2227–2240. doi:10.1093/cercor/bhr290.

Van Essen, D. C., Smith, S. M., Barch, D. M., Behrens, T. E. J., Yacoub, E., Ugurbil, K., et al. (2013). The WU-Minn Human Connectome Project: an overview. *Neuroimage* 80, 62–79. doi:10.1016/j.neuroimage.2013.05.041.

Van Essen, D. C., and Ugurbil, K. (2012). The future of the human connectome. *Neuroimage* 62, 1299–1310. doi:10.1016/j.neuroimage.2012.01.032.

van Meer, M. P. A., Otte, W. M., van der Marel, K., Nijboer, C. H., Kavelaars, A., van der Sprenkel, J. W. B., et al. (2012). Extent of Bilateral Neuronal Network Reorganization and Functional Recovery in Relation to Stroke Severity. *Journal of Neuroscience* 32, 4495–4507. doi:10.1523/jneurosci.3662-11.2012.

van Meer, M. P. A., van der Marel, K., Wang, K., Otte, W. M., El Bouazati, S., Roeling, T. A. P., et al. (2010). Recovery of sensorimotor function after experimental stroke correlates with restoration of resting-state interhemispheric functional connectivity. *J. Neurosci.* 30, 3964–3972. doi:10.1523/JNEUROSCI.5709-09.2010.

Vincent, J. L., Patel, G. H., Fox, M. D., Snyder, A. Z., Baker, J. T., Van Essen, D. C., et al. (2007). Intrinsic functional architecture in the anaesthetized monkey brain. *Nature* 447, 83–86. doi:10.1038/nature05758.

Vogt, B. A., and Paxinos, G. (2014). Cytoarchitecture of mouse and rat cingulate cortex with human homologies. *Brain Struct. Funct.* 219, 185–192. doi:10.1007/s00429-012-0493-3.

Vovenko, E. P., and Sokolova, I. B. (1998). [Oxygen tension in the brain cortex arterioles during spontaneous respiration with the hypoxic gas mixture in rats]. *Russ. Fiziol. Zh. Im. I M Sechenova* 84, 527–535. Available at: <https://www.ncbi.nlm.nih.gov/pubmed/9785420>.

Wang, J., Aguirre, G. K., Kimberg, D. Y., Roc, A. C., Li, L., and Detre, J. A. (2003). Arterial spin labeling perfusion fMRI with very low task frequency. *Magn. Reson. Med.* 49, 796–802. doi:10.1002/mrm.10437.

Wang, K., van Meer, M. P. A., van der Marel, K., van der Toorn, A., Xu, L., Liu, Y., et al. (2011). Temporal scaling properties and spatial synchronization of spontaneous blood oxygenation level-dependent (BOLD) signal fluctuations in rat sensorimotor network at different levels of isoflurane anesthesia. *NMR Biomed.* 24, 61–67. doi:10.1002/nbm.1556.

Wang, R., Foniok, T., Wamsteeker, J. I., Qiao, M., Tomanek, B., Vivanco, R. A., et al. (2006). Transient blood pressure changes affect the functional magnetic resonance imaging detection of cerebral activation. *Neuroimage* 31, 1–11. doi:10.1016/j.neuroimage.2005.12.004.

Weiner, M. W., Veitch, D. P., Aisen, P. S., Beckett, L. A., Cairns, N. J., Green, R. C., et al. (2012). The Alzheimer's Disease Neuroimaging Initiative: a review of papers published since its inception. *Alzheimers. Dement.* 8, S1–68. doi:10.1016/j.jalz.2011.09.172.

Weitz, A. J., Fang, Z., Lee, H. J., Fisher, R. S., Smith, W. C., Choy, M., et al. (2015). Optogenetic fMRI reveals distinct, frequency-dependent networks recruited by dorsal and intermediate hippocampus stimulations. *Neuroimage* 107, 229–241. doi:10.1016/j.neuroimage.2014.10.039.

- Wen, J., Goyal, M. S., Astafiev, S. V., Raichle, M. E., and Yablonskiy, D. A. (2018). Genetically defined cellular correlates of the baseline brain MRI signal. *Proc. Natl. Acad. Sci. U. S. A.* 115, E9727–E9736. doi:10.1073/pnas.1808121115.
- Williams, D. S., Detre, J. A., Leigh, J. S., and Koretsky, A. P. (1992). Magnetic resonance imaging of perfusion using spin inversion of arterial water. *Proc. Natl. Acad. Sci. U. S. A.* 89, 212–216. doi:10.1073/pnas.89.1.212.
- Williams, K. A., Magnuson, M., Majeed, W., LaConte, S. M., Peltier, S. J., Hu, X., et al. (2010). Comparison of α -chloralose, medetomidine and isoflurane anesthesia for functional connectivity mapping in the rat. *Magnetic Resonance Imaging* 28, 995–1003. doi:10.1016/j.mri.2010.03.007.
- Witten, I. B., Steinberg, E. E., Lee, S. Y., Davidson, T. J., Zalocusky, K. A., Brodsky, M., et al. (2011). Recombinase-driver rat lines: tools, techniques, and optogenetic application to dopamine-mediated reinforcement. *Neuron* 72, 721–733. doi:10.1016/j.neuron.2011.10.028.
- Wu, T., Grandjean, J., Bosshard, S. C., Rudin, M., Reutens, D., and Jiang, T. (2017). Altered regional connectivity reflecting effects of different anaesthesia protocols in the mouse brain. *Neuroimage* 149, 190–199. doi:10.1016/j.neuroimage.2017.01.074.
- Wu, W.-C., Fernández-Seara, M., Detre, J. A., Wehrli, F. W., and Wang, J. (2007). A theoretical and experimental investigation of the tagging efficiency of pseudocontinuous arterial spin labeling. *Magn. Reson. Med.* 58, 1020–1027. doi:10.1002/mrm.21403.
- Xu, F., Uh, J., Brier, M. R., Hart, J., Jr, Yezhuvath, U. S., Gu, H., et al. (2011). The influence of carbon dioxide on brain activity and metabolism in conscious humans. *J. Cereb. Blood Flow Metab.* 31, 58–67. doi:10.1038/jcbfm.2010.153.
- Yacoub, E., Duong, T. Q., Van De Moortele, P.-F., Lindquist, M., Adriany, G., Kim, S.-G., et al. (2003). Spin-echo fMRI in humans using high spatial resolutions and high magnetic fields. *Magn. Reson. Med.* 49, 655–664. doi:10.1002/mrm.10433.
- Yao, Q.-L., Zhang, H.-Y., Nie, B.-B., Fang, F., Jiao, Y., and Teng, G.-J. (2012). MRI assessment of amplitude of low-frequency fluctuation in rat brains with acute cerebral ischemic stroke. *Neurosci. Lett.* 509, 22–26. doi:10.1016/j.neulet.2011.12.036.
- Yizhar, O., Fenno, L. E., Davidson, T. J., Mogri, M., and Deisseroth, K. (2011). Optogenetics in neural systems. *Neuron* 71, 9–34. doi:10.1016/j.neuron.2011.06.004.
- Yoshida, K., Mimura, Y., Ishihara, R., Nishida, H., Komaki, Y., Minakuchi, T., et al. (2016). Physiological effects of a habituation procedure for functional MRI in awake mice using a cryogenic radiofrequency probe. *J. Neurosci. Methods* 274, 38–48. doi:10.1016/j.jneumeth.2016.09.013.
- Yu, G., Onodera, H., Aono, Y., Kawano, F., Ueda, Y., Furuya, A., et al. (2016). Optical manipulation of the alpha subunits of heterotrimeric G proteins using photoswitchable dimerization systems. *Sci. Rep.* 6, 35777. doi:10.1038/srep35777.
- Zang, Y.-F., He, Y., Zhu, C.-Z., Cao, Q.-J., Sui, M.-Q., Liang, M., et al. (2007). Altered baseline brain activity in children with ADHD revealed by resting-state functional MRI. *Brain Dev.* 29, 83–91. doi:10.1016/j.braindev.2006.07.002.
- Zang, Y., Jiang, T., Lu, Y., He, Y., and Tian, L. (2004). Regional homogeneity approach to fMRI data analysis. *NeuroImage* 22, 394–400. doi:10.1016/j.neuroimage.2003.12.030.

- Zeng, H., and Madisen, L. (2012). Mouse transgenic approaches in optogenetics. *Progress in Brain Research*, 193–213. doi:10.1016/b978-0-444-59426-6.00010-0.
- Zerbi, V., Grandjean, J., Rudin, M., and Wenderoth, N. (2015). Mapping the mouse brain with rs-fMRI: An optimized pipeline for functional network identification. *Neuroimage* 123, 11–21. doi:10.1016/j.neuroimage.2015.07.090.
- Zeuthen, T. (1978). Potentials and small-signal impedances of platinum microelectrodes in vivo and in vitro. *Med. Biol. Eng. Comput.* 16, 489–499. Available at: <https://www.ncbi.nlm.nih.gov/pubmed/102881>.
- Zhang, F., Gradinaru, V., Adamantidis, A. R., Durand, R., Airan, R. D., de Lecea, L., et al. (2010). Optogenetic interrogation of neural circuits: technology for probing mammalian brain structures. *Nat. Protoc.* 5, 439–456. doi:10.1038/nprot.2009.226.
- Zhang, F., Prigge, M., Beyrière, F., Tsunoda, S. P., Mattis, J., Yizhar, O., et al. (2008). Red-shifted optogenetic excitation: a tool for fast neural control derived from *Volvox carteri*. *Nature Neuroscience* 11, 631–633. doi:10.1038/nn.2120.
- Zhang, F., Wang, L.-P., Boyden, E. S., and Deisseroth, K. (2006). Channelrhodopsin-2 and optical control of excitable cells. *Nature Methods* 3, 785–792. doi:10.1038/nmeth936.
- Zhang, F., Wang, L.-P., Brauner, M., Liewald, J. F., Kay, K., Watzke, N., et al. (2007). Multimodal fast optical interrogation of neural circuitry. *Nature* 446, 633–639. doi:10.1038/nature05744.
- Zhao, F., Zhao, T., Zhou, L., Wu, Q., and Hu, X. (2008). BOLD study of stimulation-induced neural activity and resting-state connectivity in medetomidine-sedated rat. *NeuroImage* 39, 248–260. doi:10.1016/j.neuroimage.2007.07.063.
- Zhong, K., Leupold, J., Hennig, J., and Speck, O. (2007). Systematic investigation of balanced steady-state free precession for functional MRI in the human visual cortex at 3 Tesla. *Magn. Reson. Med.* 57, 67–73. doi:10.1002/mrm.21103.
- Zhou, Z. C., Salzwedel, A. P., Radtke-Schuller, S., Li, Y., Sellers, K. K., Gilmore, J. H., et al. (2016). Resting state network topology of the ferret brain. *Neuroimage* 143, 70–81. doi:10.1016/j.neuroimage.2016.09.003.
- Zhu, H., Aryal, D. K., Olsen, R. H. J., Urban, D. J., Swearingen, A., Forbes, S., et al. (2016). Cre-dependent DREADD (Designer Receptors Exclusively Activated by Designer Drugs) mice. *Genesis* 54, 439–446. doi:10.1002/dvg.22949.
- Zimmermann, D., Zhou, A., Kiesel, M., Feldbauer, K., Terpitz, U., Haase, W., et al. (2008). Effects on capacitance by overexpression of membrane proteins. *Biochemical and Biophysical Research Communications* 369, 1022–1026. doi:10.1016/j.bbrc.2008.02.153.
- Zou, Q.-H., Zhu, C.-Z., Yang, Y., Zuo, X.-N., Long, X.-Y., Cao, Q.-J., et al. (2008). An improved approach to detection of amplitude of low-frequency fluctuation (ALFF) for resting-state fMRI: fractional ALFF. *J. Neurosci. Methods* 172, 137–141. doi:10.1016/j.jneumeth.2008.04.012.
- Zuo, X.-N., and Xing, X.-X. (2014). Test-retest reliabilities of resting-state FMRI measurements in human brain functional connectomics: a systems neuroscience perspective. *Neurosci.*

Biobehav. Rev. 45, 100–118. doi:10.1016/j.neubiorev.2014.05.009.

Curriculum Vitae ~ **FRANCESCA MANDINO**

236, Park Street – New Haven 06511 CT, USA

+1 (203) 809-7438 – twitter: @francimandi

Email: mandino.francesca@gmail.com // francesca.mandino@yale.edu

EDUCATION AND TRAINING

01/2020 – present

Postgraduate associate with Prof T. Constable and Assistant Prof E. Lake

Radiology and biomedical imaging - Yale School of Medicine

Main projects: combination of mesoscopic calcium imaging with high field functional Magnetic Resonance Imaging (fMRI).

Preclinical neuroimaging research

09/2015 – 12/2019

Ph.D. Student (ARAP Scheme) with Dr J. Gigg and Prof M. Olivo

University of Manchester (UK) and A*STAR (Singapore)

Main projects: *In vivo* electrophysiology, opto-functional Magnetic Resonance Imaging (fMRI), calcium fiber photometry to investigate brain changes in a transgenic mouse model for Alzheimer's disease (AD)-like pathology.

Thesis title: Functional mapping of the entorhinal cortex reveals a hub for synaptic excitability in young 3xTg mouse model for Alzheimer's disease

Alzheimer's Disease Research

06/2018 – 07/2018

Building and Mining Brain Cell Atlases and Connectomes Summer School

Suzhou (China)

03/2015 – 07/2015

Visiting researcher with Prof F. Casamenti and Prof A.M. Pugliese

Universita' degli Studi di Firenze (Italy)

In vitro electrophysiology, brain slices preparation.

Alzheimer's Disease Research

10/2012 – 09/2013

Master's Degree (MSc) in Cognitive Neuroscience

University of York (UK) – *Upper Second (2:1, Merit)*

Main topics: Research design in neuroimaging, basic principles in neuroimaging, data acquisition and analysis in neuroimaging, topics in cognitive neuroscience, research design and statistics, topics in psychological research.

Thesis title: Influence of a cognitive load on speech perception: towards a reallocation of the resources.

Magneto-encephalography (MME), Electro-encephalography (EEG) and fMRI techniques

10/2012 – 09/2013

Bachelor's degree (BSc) in Biology

Universita' degli Studi di Firenze (Italy) – *First (106/110)*

Thesis title: Study of NAGPA, GNPTAB and GNPTG genes in Homo sapiens, non-human Primates, lower Mammals and other Vertebrates.

Gene sequences alignment for mutations in mammals

WORK EXPERIENCE

04/2017 – 09/2017

Postgraduate tutor at Singapore BioImaging Consortium (SBIC), A*STAR (Singapore)

Supervising and teaching postgraduate students: stereotaxic surgery and opto-fMRI animal preparation, data acquisition, processing and analysis.

01/2014 – 03/2015

Employee for IMASAF and GSG Toscana (Calenzano, Firenze)

06/2011 – 01/2012

Employer: Mr. Oscar Mandino

Finance Accounting and Management for the family company IMASAF and GSG Toscana.

02/2012 – 05/2012

Volunteer in Museo di Storia Naturale (Firenze)

Employer: Mr. Lorenzo Rook

Organisation of exhibitions and management of exhibition halls.

09/2010 – 04/2011

Private tutor (Firenze)

Self-employed

Tutoring Primary school students in maths, English, Italian, biology, history and geography.

PUBLICATIONS

- **Mandino, F., et al.**, (2019). Preserved functional networks in a hydrocephalic mouse. (*Published ScienceMatters*).
- **Mandino, F., et al.**, (2020). Animal functional magnetic resonance imaging: Trends and path toward standardization. (*Published Frontiers of Neuroinformatics*)
- Grandjean, J., et al., (2019). Common functional networks in the mouse brain revealed by multi-centre resting-state fMRI analysis. *BioRxiv*, 541060.
- **Mandino, F. et al.**, 3xTgAD mice express early in vivo synaptic hyperexcitability in amygdala and dentate gyrus following activation of lateral entorhinal cortex.
- **Mandino, F. et al.**, Brain-wide functional mapping of the entorhinal cortex in young 3xTg mouse model for Alzheimer's disease. (*BioRxiv* <https://doi.org/10.1101/2020.04.03.022590>)
- **Mandino, F., & Yeow, LY., et al.**, Triple network activity regulation mediated by the insular cortex in the mouse brain. (*in preparation*)
- Bell, G., et al., (2019). Functionalised iron oxide nanoparticles for multimodal optoacoustic and magnetic resonance imaging. *Journal of Materials Chemistry B*.

CONFERENCE CONTRIBUTIONS

Oral presentations:

- May 2019 – **ISMRM2019** – *Montreal (Quebec)*
- August 2018 – **SBIC&CAI joint symposium** – *Singapore*

Poster presentations:

- June 2018 – **OHBM2018** – *Singapore*
- March 2016 – **ARUK2016** – *Manchester (UK)*
- July 2016 – **FENS2016** – *Copenhagen (Denmark)*
- August 2016 – Limits of Perception – *Warwick (UK)*
- 04/2016 – Neurodegeneration Meeting – *Manchester (UK)*

AWARDS AND FUNDING

12/2017

SBIC research award – SGD 100,000

Title: Direct and indirect neuronal activity: a multi-modal approach.

CERTIFICATION

2015 and 2017

Home Office Personal Licence for operating on animals.

Responsible care and use of laboratory animals course,
Biological Resource Centre (*UK, Singapore*)

2018

Python and tensorflow training.

RELEVANT TECHNICAL SKILLS

- Windows - Python (Notepad – Pycharm – PsychoPy) – Mac OS X – PERL – Bash.
- Competent with Microsoft Office, Macintosh, Linux/Unix/Fedora/Ubuntu
- Outstanding scientific written and verbal skills
- Competent in using SQL, FSL, Presentation[®] MATLAB, SPSS, FSL, Bioedit, DmDX fMRI, MEG, TMS.
- Biological lab techniques (DNA extraction, PCR, electrophoresis) CLUSTAL W (FASTA, BLAST), statistical software for multiple alignments R ESOLVER, ERGON, mricron.
- *In vivo* electrophysiology: confident in animal preparation, stereotaxic surgery, data acquisition, brain fixation, electrophysiological data analysis with Spike2[®], NeuroExplorer[®], Origin, Prism.
- Neuroimaging: expert in stereotaxic surgery, viral injection, animal intubation, fMRI acquisition, data pre-processing and analysis, statistics, immunohistochemistry and histology.

COMMUNICATION SKILLS

During my MSc, I had the chance to learn how to express myself in a scientific environment, in a non-native language, therefore improving my social and communication skills, and learning how to adapt according to a lay or specific audience. I learnt how to work within a team, share and discuss ideas in a constructive way, deal with individual's needs and visions of the project and integrate them for the benefit of the team.

During my PhD, the fundamental growth I experienced was on how to distinguish primary tasks from secondary ones and stay focused under pressure. Presenting posters and talks to diverse conference types has taught me how to better deliver the key findings of my research, and how to network and seek advice from researchers within and outside my field of expertise. I have had the chance to establish collaborations with external institutes and to supervise postgraduate students, teach about animal preparation, surgery techniques, data acquisition.

ORGANIZATIONAL/MANAGERIAL SKILLS

With my PhD, I experienced the transition between being a student and creating my own independent project. I have learnt how to plan ahead, especially for time-point experiments, and how to start breeding colonies of mice, implementing the 3R principles. Within the research institute in Singapore, I have had the chance to apply for, and be awarded with, a within-institute award, therefore experiencing how to write a proposal for a research grant and how to manage the costs of that project.

REFERENCES

Dr John Gigg

(Ph.D. Supervisor)

University of Manchester (UK)

john.gigg@manchester.ac.uk

Prof Olivo Malini

(Ph.D. Co-Supervisor)

Singapore BioImaging Consortium

A*STAR (Singapore)

malini_olivo@sbic.a-star.edu.sg

Dr Joanes Grandjean

Singapore BioImaging Consortium

A*STAR (Singapore)

joanes_grandjean@sbic.a-star.edu.sg